Analysis and Enhancements of ESA/ESOC Multi-GNSS Solutions

Master Thesis Report

MSc. Aerospace Engineering - TU Delft
Iván Sermanoukian Molina

Analysis and Enhancements of ESA/ESOC Multi-GNSS Solutions

Master Thesis Report

by

Iván Sermanoukian Molina

to obtain the degree of Master of Science in Aerospace Engineering
at the Delft University of Technology,
to be defended publicly on Tuesday November 26, 2024 at 09:30 AM.

Student number:	5781531	
Project duration:	February, 2024 - October, 2024	
Supervisors:	Dr. Ir. J.A.A. (Jose) van den IJssel	TU Delft
	Dr.-Ing. Francesco Gini	ESA
	Dr.-Ing. Erik Schönemann	ESA
Thesis committee:	Dr. Ir. P.N.A.M. (Pieter) Visser	TU Delft, Chair
	Dr. Ir. J.A.A. (Jose) van den IJssel	TU Delft, Supervisor
	Dr. Ir. Wouter van der Wal	TU Delft, Examiner
	Dr.-Ing. Francesco Gini	ESA, External
	Dr.-Ing. Erik Schönemann	ESA, External

TU Delft

esa

Abstract

Over the past decade, there have been significant advancements in both the availability and diversity of satellite navigation systems, on both regional and global scales. The growing significance of GNSS across various fields has led not only to the modernisation of existing systems like the GPS and GLONASS, but also to the creation of new ones such as Galileo. The Navigation Support Office (NSO) operates as a vital component within the European Space Agency, specialising in the precise utilisation of navigation satellite systems. In 2024, NSO underwent a revision of its GNSS processing system, which resulted in a state-of-the-art GNSS processing framework known as CHAMP, Consolidated High Accuracy Multi-GNSS Processing, which is based on constellation-wise data processing and normal equation stacking to efficiently generate GNSS products for all major navigation constellations. This new approach enables internal comparisons between individual constellation solutions and the consolidated multi-GNSS solution, revealing unique characteristics of each constellation and demonstrating the enhanced impact of combining them in critical ways.

This thesis explores and addresses key inconsistencies in the processing of multi-GNSS solutions within the Navigation Support Office, with a particular focus on producing accurate single-constellation solutions that can be reliably combined into a coherent multi-constellation framework. To tackle these inconsistencies, a comprehensive Python-based programme has been developed as an extension of the CHAMP framework, enabling a more efficient and structured approach for analysing large-scale GNSS data. As a result, this new tool provides the basis needed to identify anomalies, track trends, and address inconsistencies across various constellations during the combination process, as a post-processing analysis or within the operational pipeline. The core of this research involves a detailed examination of the parameters estimated in the NSO GNSS precise orbit determination, both in terms of individual and combined multi-GNSS solutions, including Earth orientation parameters, satellite state vectors, ground station positions, clock biases, and empirical accelerations, among others.

The investigation lead to significant inconsistencies in the Length of Day estimates of the individual GPS constellation, affecting the accuracy of the combined multi-GNSS solution. These issues are compounded by the combination of the large weight given to the GPS constellation in the combination due to its low variability, and the GPS non-gravitational a priori models, specially regarding forces like solar radiation pressure, which have been demonstrated to be not as refined as those for other constellations. Additionally, the tuning of empirical accelerations has shown that there is room for improvement to better reflect satellite dynamics.

In conclusion, several key enhancements were identified and proposed to improve the overall performance and reliability of the combined multi-GNSS solution, and subsequently improve the quality of the NSO GNSS products. These mainly comprise the comparison of different non-gravitational a priori models combined with the fine-tuning of empirical accelerations, allowing for a more robust integration of single-constellation solutions into a cohesive multi-constellation framework. Ultimately, recommendations on the way forward are given to create new models based on the results shown on this thesis.

Contents

Nomenclature

List of Acronyms

Acronym	Definition
ANTEX	Antenna Exchange Format
ARP	Antenna Reference Point
AU	Astronomical Unit
BCRS	Barycentric Celestial Reference System
BDS	BeiDou Navigation Satellite System
BDT	Beidou Time
BIH	Bureau International de l'Heure
BLS	Bayesian Least Squares
C/A	Coarse/Acquisition
CCB	Change Control Board
CDMA	Code Division Multiple Access
CHAMP	Consolidated High Accuracy MGNSS Processing
CI/CD	Continuous Integration/Continuous Deployment
CIO	Celestial Intermediate Origin
CIP	Celestial Intermediate Pole
CPR	Cycle-Per-Revolution accelerations
CPU	Central Processing Unit
DAILY	Daily Outputs
DCBIAS	Differential Code Bias
DORIS	Doppler Orbitography and Radiopositioning Integrated by Satellite
EAP	Earth Albedo Radiation Pressure
EARP	Earth Albedo Radiation Pressure
EC	European Commission
ECOM	Empirical CODE Orbit Model
EGNOS	European Geostationary Navigation Overlay Service
EGON	ESA's GNSS Observation Network (EGON)
EIP	Earth Infrared Radiation Pressure
EIRP	Earth Infrared Radiation Pressure
EOP	Earth Orientation Parameter
EPNS	European Space Agency Precise Navigation System
ERA	Earth Rotation Angle
ERP	Earth Rotation Parameter
ESA	European Space Agency
ESOC	European Space Operations Centre
E-TAC	EPNS Test Cases Automatic Comparison
FDMA	Frequency Division Multiple Access
FOC	Full Operational Capability
G2G	Galileo Second Generation
GCRS	Geocentric Celestial Reference System
GEO	Geostationary Orbits
GLONASS	Global'naya Navigatsionnaya Sputnikovaya Sistema
GLST	GLONASS Time

Acronym	Definition
GNSS	Global Navigation Satellite System
GPS	Global Positioning System
GPST	GPS Time
GST	Galileo System Time
IAU	International Astronomical Union
IB	Integer Bootstrapping
ICB	Interchannel Bias
ICRF	International Celestial Reference Frame
ICRS	International Celestial Reference System
IERS	International Earth Rotation and Reference Systems Service
IGS	International GNSS Service
IGSO	Inclined Geosynchronous Orbits
ILS	Integer Least-Squares
IMU	Inertial Measurement Unit
IOC	Initial Operating Capability
IONO	Ionospheric Modelling and Corrections
IOV	In-Orbit Validation
IR	Integer Rounding
IRNSS	Indian Regional Navigation Satellite System
IRP	International Reference Pole
ISB	Inter-System Bias
ITRF	International Terrestrial Reference Frame
ITRS	International Terrestrial Reference System
JPL	Jet Propulsion Laboratory
LEO	Low Earth Orbit
LOD	Length of Day
LS	Least-Squares
MEO	Medium Earth orbit
MGNSS	Multi-constellation GNSS
MSD	Mean Solar Day
MW	Melbourne-Wübbena
NAPEOS	NAvigation Package for Earth Observation Satellites
NavIC	Navigation with Indian Constellation
NEQ	Normal Equation
NL	Narrow-Lane
NNR	No-Net-Rotation
NNT	No-Net-Translation
NSO	Navigation Support Office
PCO	Phase Centre Offset
PCV	Phase Centre Variation
PNT	Positioning
POD	Precise Orbit Determination
PPS	Precise Positioning Service
PRN	Pseudorandom Noise
QZO	Quasi-Zenith Orbit
QZSS	Quasi-Zenith Satellite System
RAM	Random-Access Memory
RINEX	Receiver Independent Exchange Format
RMS	Root Mean Square
RNSS	Regional Navigation Satellite System
SBAS	Satellite-Based Augmentation Systems
SINEX	Solution Independent Exchange
SLR	Satellite Laser Ranging
SOD	Satellite Orbit Determination
SP3	Standard Product #3
SPS	Standard Positioning Service
SRP	Solar Radiation Pressure
STD	Slant Tropospheric Delay

Acronym	Definition
TAI	International Atomic Time
TEC	Total Electron Content
TRF	Terrestrial Reference Frame
TT	Terrestrial Time
TUM	Technical University of Munich
UNOOSA	United Nations Office for Outer Space Affairs
UTC	Coordinated Universal Time
VLBI	Very Long Baseline Interferometry
WL	Wide-Lane
XPO	X Polar motion
XPOR	X Polar motion rate
YPO	Y Polar motion
YPOR	Y Polar motion rate
ZTD	Zenith Tropospheric Delay

List of Symbols

Symbol	Definition
c	Speed of light
C_R	Radiation Pressure Coefficient
dt^s	Clock offsets of the emitter
dt_r	Clock offsets of the receiver
f	Frequency
H	Jacobian
$I^s_{r,f}$	Ionospheric delay
J	Loss function
$k_{r,f}$	Instrumental delays of the emitter for carrier phase
$k_{s,f}$	Instrumental delays of the receiver for carrier phase
K^s_f	Instrumental delays of the emitter for pseudorange
$K_{r,f}$	Instrumental delays of the receiver for pseudorange
m	Mass
m_f	Multipath errors effect for carrier phase
M_f	Multipath errors effect for pseudorange
n	Refractive index of air
N	Normal matrix
$N^s_{r,f}$	Integer ambiguity in the carrier phase
$p^s_{r,f}$	Pseudorange
$P_\odot$	Solar flux
P_x	Variance-covariance matrix of the a priori parameters
Q_{yy}	Variance-covariance matrix of the observations
r_{sat}	Satellite Orbital Position vector
t	Time
t^{AB}	System time offset
T^s_r	Tropospheric delay
t_{tog}	Time of generation
t_{tom}	Time of measurement
u	Argument of latitude
v	Satellite Orbital Velocity
v_{sat}	Satellite Orbital Velocity vector
W	Weight matrix
w^s_r	Phase wind-up effect
x	State vector
y	Vector of measurements

Symbol	Definition
α_{vis}	Visible absorption coefficient
$\Delta\delta^s_{r,f}$	Phase interchannel bias
$\Delta d^s_{r,f}$	Code interchannel bias
ΔU	Gravitational Potential
δ_{rel}	Relativistic effect due to space-time curvature
δ_{vis}	Visible diffuse reflection coefficient
η	Shadow function
λ_f	Wavelength of the carrier signal
μ	Gravitational Parameter
ϕ	Wave phase
ρ^s_r	True geometric range between the emitter and receiver
ρ_{vis}	Visibe specular reflection coefficient
σ	Standard deviation
τ	Signal time-travel between the emitter and the receiver
τ^s	Satellite time scale
τ_r	Receiver time scale
θ	True anomaly
$\varepsilon^s_{r,f}$	Receiver noise and other smaller effects
$\varphi^s_{r,f}$	Phase range
$\xi^s_{r,f}$	PCO correction of the transmitting/receiving antennas for pseudorange
$\zeta^s_{r,f}$	PCO correction of the transmitting/receiving antennas for carrier phase

1 Introduction

Global Navigation Satellite Systems (GNSS) have become a vital component of modern life, enabling a diverse array of applications. These range from everyday navigation systems, which require accuracy within a few meters, to highly specialised applications that demand extreme precision at the millimetre level. As a result, GNSS satellites play a critical role in space-related industries, supporting current uses such as satellite navigation, precise orbital tracking, and space debris monitoring. Looking ahead, future applications include supporting lunar missions, coordinating deep-space navigation, assisting in asteroid mining, and enabling human exploration on Mars and beyond. Over the past decade, there have been significant advancements in both the availability and diversity of satellite navigation systems, on regional and global scales. The growing significance of GNSS across various fields has led not only to the modernisation of existing systems like the Global Positioning System (GPS) and the *Global'naya Navigatsionnaya Sputnikovaya Sistema* (GLONASS), but also to the creation of new systems such as Galileo, the BeiDou Navigation System (BeiDou), the Quasi-Zenith Satellite System (QZSS) and the Indian Regional Navigation Satellite System (IRNSS), also called NavIC (acronym for Navigation with Indian Constellation). Consequently, for GNSS analysis centres, there is a continuous need to upgrade and evolve their software in order to continuously improve its computational performance and accuracy, handling new observations, models and algorithms for each constellation.

The Navigation Support Office (NSO) is as a vital component of the European Space Agency (ESA), specialising in the precise utilisation of navigation satellite systems. NSO is located in the European Space Operations Centre (ESOC), which serves as the nerve centre for the operation of ESA's spacecraft, overseeing mission planning, execution, and control. Established with the primary objective of contributing to ESA missions, third-party activities, and Europe's pivotal navigation initiatives, NSO plays a central role in advancing the Galileo programme, among others. Founded as a centre of expertise, NSO has evolved into a cornerstone of ESA's navigation capabilities, and taken the role of an International GNSS Service analysis centre. At the forefront of its responsibilities is the management and development of the European Space Agency Precise Navigation System (EPNS), a cutting-edge software system designed for the processing of GNSS data. As the successor of NAPEOS, the Navigation Package for Earth Orbiting Satellites, EPNS stands as a testament to NSO's commitment to maintaining and advancing state-of-the-art technologies in the field of satellite navigation.

With the growing diversification of constellations and end-user applications, an enhancement of NSO's operational methodology was required. One of the main issues of the existing NSO GNSS processing was the inefficient data handling for the different product solutions. Additionally, with the addition of the latest GNSS constellations, the computational requirements of the multi-GNSS solution were becoming too large, compromising the efficiency of the operational pipeline. Thus, dividing the combined multi-GNSS process into smaller processes, e.g. constellation wise, would allow to reduce the memory load of the processes dramatically, in terms of CPU, disk space and RAM, while speeding things up by relying on parallel computations. As a result, in 2024, the Navigation Support Office underwent a revision of the GNSS processing system, which resulted in a novel GNSS processing framework called CHAMP, *Consolidated High Accuracy Multi-GNSS Processing*. The redesigned software, which relies on EPNS in the background, is based on constellation-wise data processing and normal equation stacking to efficiently generate GNSS products for all the current major navigation systems except NavIC, which will be added in the near future now that a secondary frequency is available for civil uses. CHAMP optimises the individual processes and eliminates the aforementioned duplications, making efficient use of resources and improving the reliability, maintainability and timeliness of the whole sequence from the data insertion to the publication of the products, which is only possible thanks to a new modular system that allows to streamline reconfiguration.

This new approach, which reduces the overall daily computation time of NSO processing pipelines by several hours, enables internal comparisons between individual constellation solutions and the consolidated multi-GNSS solution, revealing unique characteristics of each constellation and demonstrating the enhanced impact of combining them. By allowing cross-constellation quality checks and comparisons with the combined solution, this method provides a more nuanced understanding of the distinct contributions and performance of each system. This setup distances itself from more widely adopted methods that process all constellations together, opting instead for a more modular and comparative framework that enhances the granularity of the analysis.

1.1 Problem Description

An initial analysis comparing the new individual and subsequently stacked GNSS constellation solutions with respect to the precursor always-combined solutions showed noticeable differences, even if within similar error scales for each constellation. While these differences were mostly concentrated in the radial direction for the GPS constellation, reaching up to several centimetre differences in daily satellite orbit overlaps, Galileo showed differences in both the radial and along-track directions, revealing inconsistencies between the different techniques. At the same time, it was found that GLONASS results were degraded as they were dominated by two very poorly behaving satellites, namely GLO-706 and GLO-719. Moreover, the individual GLONASS solution seemed to perform better than the combined solution. In terms of the newly-added BeiDou constellation, it was seen that adding the BEI-GEO and the BEI-IGSO satellite blocks may negatively influence the results.

Even if all constellations were given the same weight on the first step of the new multi-GNSS processing approach, further testing concluded that downweighting GLONASS data in comparison to the other constellations in the combined solution resulted in improved results in terms of satellite orbit overlaps, reducing the large variability induced by the individual GLONASS data. However, even if overall overlap results were closer to the legacy accuracy, there were still noticeable differences in the GPS and Galileo along-track direction, among smaller differences for other constellations. Among the new discoveries, it was seen that GLONASS results improved when BeiDou was included in the combination, whereas BeiDou performed a bit better if GLONASS was not. Thus, the analysis concluded that the loss of accuracy for the new methodology could be either due to the new constellation-wise approach and/or due to inclusion of BeiDou in the combined solution. The poor performance of GLONASS could also be a contributing factor, but this was not expected to affect the combined solution significantly once the observations were downweighted.

Consequently, this thesis focuses on the need for the Navigation Support Office to perform an in-depth analysis of the differences between the individual and combined solutions within the CHAMP framework in order to analyse the possible inconsistencies found for all estimated parameters, while analysing the effects of specific constellations into the combination. Previous analyses focused primarily on differences in orbit overlaps, overlooking other estimated variables that could serve as valuable performance indicators. This limitation stems from the fact that the estimated parameters are not regularly stored in easily readable files, due to operational disk space constraints. To address this issue, a new toolset was required to efficiently extract and store all relevant parameters from both intermediate and final products, without altering the current operational workflow or introducing additional outputs or dependencies into the system. This solution ensures the comprehensive analysis of all key performance indicators while maintaining the integrity of the existing methodology.

1.2 Research Proposal

This section introduces the research proposal, detailing the primary objectives and key research questions that will be explored in this study. Conducted in collaboration with the European Space Agency and TU Delft, the study aims to make significant contributions to the ongoing development of advanced navigation processing technologies by providing a thorough analysis of existing challenges and proposing targeted solutions to the Navigation Support Office GNSS processing methodology. In addition to developing tools for deeper operational insights, the research will address current inconsistencies in the multi-GNSS processing and recommend future steps for improving accuracy while maintaining computational efficiency. Through this comprehensive approach, the study will benefit all users relying on enhanced precision for a diverse range of applications.

1.2.1 Research Objective

The research objective of this thesis is to delve into the ongoing efforts of the ESA Navigation Support Office to refine the accuracy while maintaining the computational efficiency of the multi-GNSS processing products. The focus will be on identifying and resolving inconsistencies that arise from the combination of individual GNSS constellations using normal equation stacking, as well as analysing inconsistencies across all individual constellations. The ultimate goal is to produce seamless and reliable navigation products that meet the high precision and performance demands of ESA's operations.

1.2.2 Research Questions

The main research question for this project is:

How can the Navigation Support Office refine its multi-GNSS processes to achieve enhanced accuracy, ensuring the consistency and reliability of the individual and combined GNSS navigation products on an operational basis?

The sub-questions that arise from this are:

- What specific inconsistencies exist in the intermediate and final GNSS products generated by NSO's current two-step methodology, and can these inconsistencies be quantified?
- What are the root causes of the identified inconsistencies within the operational context of NSO?
- To what extent do the observed inconsistencies deviate from established standards and performance metrics, and how do these deviations impact the overall reliability and accuracy of NSO's navigation products?
- Which modifications or enhancements can be implemented in NSO's two-step methodology to effectively address and resolve the identified inconsistencies, and how might these changes impact the overall efficiency of the navigation processes?

1.3 Thesis Outline

This thesis is structured into several chapters to systematically address the research objective and provide the necessary information to answer the research questions. Chapter 2 introduces the reader to GNSS technology, providing an overview of its architecture, available constellations, single- and multi-GNSS observables, as well as signal perturbations and combinations, with an emphasis on practical applications. Chapter 3 follows with a detailed exploration of Precise Orbit Determination (POD), beginning with algorithm fundamentals and moving through the setup of coordinate systems and time, before explaining both gravitational and non-gravitational perturbations, along with other dynamic model uncertainties. Subsequently, Chapter 4 outlines the computational methodology that is used for the NSO GNSS processing. The computational framework of the GNSS processing is based on two software tools, ESA's Precise Navigation System (EPNS) and the Consolidated High Accuracy MGNSS Processing (CHAMP), for which the general specifications are introduced along with the applied physical and numerical models. Chapter 5 provides an analysis of all relevant estimated parameters in the NSO GNSS processing and identifies which parameters show inconsistencies in the different processing steps. Building on these inconsistencies, Chapter 6 details the improvements made to the CHAMP tool, including modifications to the combination process, analysis of a priori models, and proposed solutions. The thesis concludes with a summary of the key findings and recommendations for future work in Chapter 7.

2 Global Navigation Satellite Systems

A Global Navigation Satellite System (GNSS) can be described as a constellation of satellites orbiting a celestial body and continuously transmitting electromagnetic signals that enable both ground and space global coverage applications. The basic principle of positioning with GNSS is based on the concept of multilateration, where the location of a user is determined by the measurement of distances to multiple GNSS satellites for which the position is precisely known. In this chapter, the GNSS architecture is described in Section 2.1, the main navigation constellations available are presented in Section 2.2, and followed by the different types of single- and multi-constellation GNSS observations in Section 2.3 and 2.4, respectively. Subsequently, the primary GNSS signal perturbations are summarised in Section 2.5, while the methodologies to mitigate some of these errors using combinations of observations are introduced in Section 2.6.

2.1 GNSS Architecture

A GNSS basically consists of three main segments: the space segment, which comprises the satellites; the ground or control segment, which manages the proper operation of the system; and the user segment, which includes the GNSS receivers providing positioning, velocity and precise timing capabilities to users. While the user segment is mostly shared among different GNSS, each system has its own dedicated ground and space segment. The space segment of the GNSS systems analysed in this thesis is formed by satellite constellations orbiting the Earth, so that there are at least four satellites in view simultaneously from any point of the surface at any time. These satellites generate and transmit electromagnetic waves modulated with navigation information on different carrier frequencies for each constellation, as seen in Section 2.2. The ground or control segment is responsible for the operation and maintenance of the GNSS satellites. It typically includes two control centres (master and backup), a globally distributed network of Telemetry, Tracking, and Command (TT&C) stations to monitor spacecraft, a network of sensor stations that track navigation signals sent by the satellites, and a series of globally distributed uplink antennas to relay navigation messages, including ephemerides and clock corrections, to the GNSS satellites. Overall, its primary functions include regulating the status and configuration of satellites, predicting changes in satellite positions and clock accuracy, maintaining synchronisation with the GNSS time scale using atomic clocks, and updating navigation messages for all satellites within the constellation (Sanz Subirana et al., 2013). The user segment is composed of GNSS receivers which measure the signals, determine pseudoranges and other observables and use them to solve the navigation equations for Positioning, Navigation and Timing (PNT) purposes.

2.2 GNSS and RNSS Constellations

Global Navigation Satellite Systems are typically deployed in medium-altitude Earth orbits (MEO) to achieve comprehensive global coverage. These systems may also incorporate satellites in inclined geosynchronous orbits (IGSO) and geostationary orbits (GEO) to provide additional coverage and enhance performance in specific regions. In contrast, Regional Navigation Satellite Systems (RNSS) are designed to function similarly to GNSS but are limited to providing navigation services within a specific, predefined geographical area. Presently, there are four operational GNSS systems: GPS, operated by the United States; GLONASS, by Russia; Galileo, by the European Union; and BeiDou, by China. Additionally, there are two RNSS systems in operation: the Quasi-Zenith Satellite System (QZSS) operated by Japan, and the Indian Regional Navigation Satellite System (IRNSS), also known as the Navigation with Indian Constellation (NavIC), operated by India. A comprehensive overview of each system is presented in the following subsections.

In addition to GNSS and RNSS, there are also Satellite-Based Augmentation Systems (SBAS) that enhance GNSS performance. SBAS leverages geostationary communication satellites to deliver differential correction data and integrity information to GNSS users, significantly improving the accuracy and reliability of the signals. This enhancement is particularly valuable for applications requiring high precision, such as satellite positioning for Earth observation, space debris tracking, satellite constellation management, and precise orbit determination. Although SBAS is a critical component in augmenting GNSS capabilities, it is beyond the scope of this project. Further information on SBAS and its functionalities can be found in Teunissen and Montenbruck (2017).

2.2.1 GNSS/RNSS Specifications

An overview of GNSS and RNSS configurations is provided in Table 2.1. The GLONASS, Galileo and BeiDou systems rely on Walker constellation designs, which are a specific type of satellite distribution across orbital planes intended to provide uniform global coverage while ensuring that a minimum number of satellites is always visible from any location on Earth. In a Walker constellation, satellites are evenly spaced across multiple orbital planes that consist of circular orbits at the same altitude. These satellites are synchronised in their orbital periods to maintain a consistent geometric configuration relative to one another over time. The Walker notation, denoted as $t/p/f$ with an inclination i and mean altitude h, describes this configuration: t represents the total number of satellites, p denotes the number of equally spaced orbital planes, and f indicates the relative phasing between satellites in adjacent planes. The phasing is such that the change in true anomaly, θ, (in degrees) for equivalent satellites in neighbouring planes is $\theta = f \cdot 360/t$. The Galileo Walker constellation 3D orbital planes are shown in Figure 2.1b, while the orbital satellite pattern design is shown in Figure 2.1a. Additionally, the satellite arrangement of other constellations can be seen in Figure 4.2, evidencing the different orbit designs.

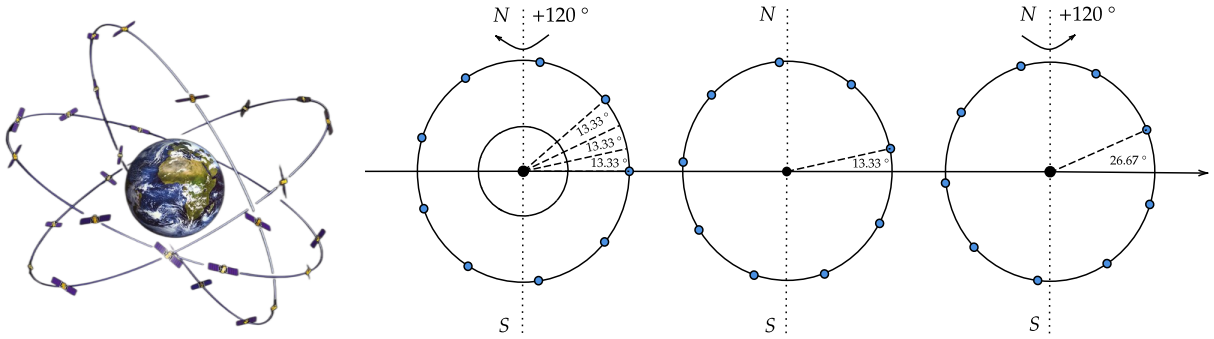

(a) 3D orbital planes

(b) 2D orbital planes and satellite distribution

Figure 2.1: Galileo Walker constellation 56° : 27/3/1 (European Space Agency, 2024a)

Table 2.1: Overview of global and regional satellite-based navigation systems (Updated from Teunissen and Montenbruck, 2017)

System	GPS	GLONASS	GALILEO	BeiDou	QZSS	NavIC
Orbits	MEO	MEO	MEO	MEO, IGSO, GEO	IGSO, GEO	IGSO, GEO
Nominal # satellites	24	24	30	27, 3, 5	3, 1	4, 3
MEO design	Six planes h = 20200 km i = 55 °	Walker (24/3/1) h =19100 km i = 64.8 °	Walker (27/3/1)) h = 23222 km i = 56 °	Walker (24/3/1) h = 21528 km i =55 °	-	-
IGSO design	-	-	-	i =55 °	i = 43 °	i = 29 °
GEO design	-	-	-	h = 35,786 km	h = 35,786 km	h = 35,786 km
FOC date	1993	1996	2024	RNSS-2012 GNSS-2020	2017	2016
Origin	USA	Russia	Europe	China	Japan	India
Coverage	Global	Global	Global	Global	East Asia Oceania region	-30 ° < ϕ <50 ° 30 ° < λ <130 °
Frequencies MHz	L1 1575.42 L2 1227.60 L5 1176.45	L1 1602.00 L2 1246.00 L3 1202.025	E1 1575.42 E5a 1176.45 E5b 1207.14 E6 1278.75	B1 1561.098 B2a 1176.45 B2b 1207.14 B3 1268.52	L1 1575.42 L2 1227.60 L5 1176.45 E6 1278.75	L1 1575.42 L5 1176.45 S 2492.028

The signals from different GNSS are widely spread over the L-band, with multiple constellations transmitting on overlapping frequencies, as illustrated in Figure 2.2. This shared use of frequencies enhances interoperability among the systems, improving the functionality of multi-GNSS receivers. However, it also introduces the potential for interference, particularly if the signal modulations are not properly designed.

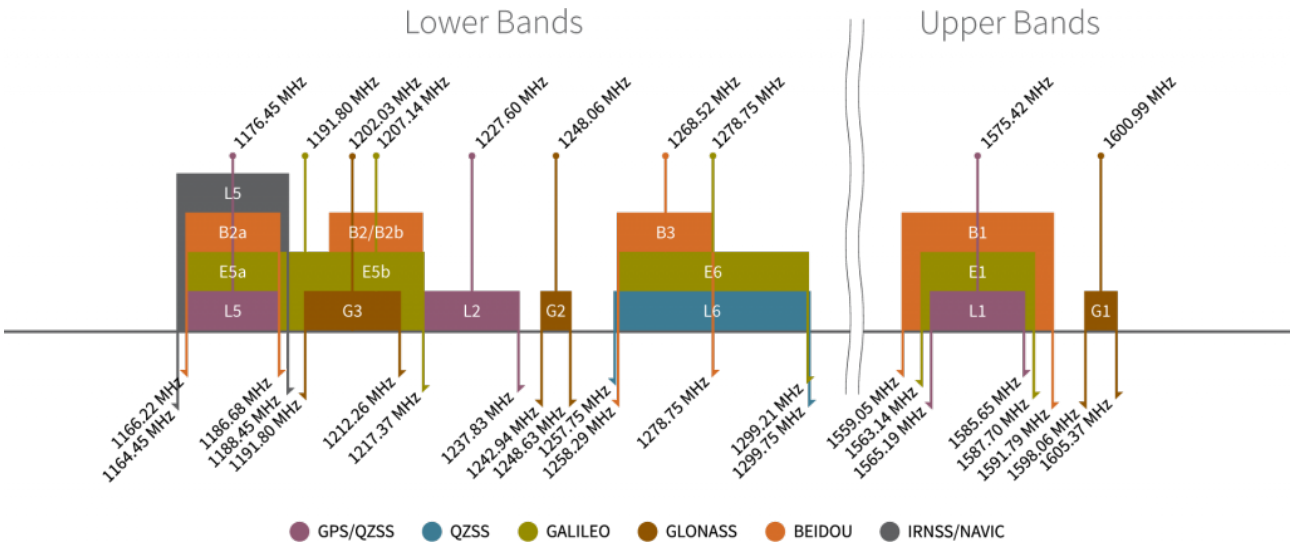

Figure 2.2: GNSS Constellations - Radio Frequencies (Calian Group, 2024)

2.2.2 GPS

The Global Positioning System (GPS) is a space-based GNSS operated by the United States of America, delivering global positioning, navigation, and timing services to civilian and military users, albeit with distinct service provisions for each category. The launch of the first Block I Navstar GPS satellite in February 1978 marked the beginning of the system, with Initial Operating Capability (IOC) declared in December 1993. Subsequently, Full Operational Capability (FOC) was reached in June 1995, following the deployment of a 24-satellite constellation. The GPS space segment has since undergone continuous development, progressing through eight satellite blocks across three generations: Block I (1978), Block II (1989), Block IIA (1990), Block IIR (1997), Block IIR-M (2005), Block IIF (2010), Block IIIA (2018), and the anticipated Block IIIF (scheduled for 2026).

GPS offers two distinct positioning services: the Precise Positioning Service (PPS) and the Standard Positioning Service (SPS). The PPS, available on the GPS L1 (1575.42 MHz) and L2 (1227.6 MHz) frequencies, utilises an encrypted precision code, referred to as the Y-code, along with a navigation message for authorised users. In contrast, the SPS operates on the GPS L1 frequency, using a coarse/acquisition (C/A) code and a navigation data message intended for civilian use. Following the launch of the Block IIR-M satellites, a new civilian signal, L2C, was introduced, alongside an enhanced military signal (M-code) on the L1 and L2 frequencies, offering improved resistance to jamming compared to the older Y-code. The subsequent Block IIF generation added the L5 frequency (1176.45 MHz), which is specifically designed for aviation safety and other civilian applications. This generation also facilitated interoperability with other GNSS systems, such as GALILEO, QZSS, and NavIC, by standardising signal structures and frequencies, thereby enhancing multi-constellation navigation capabilities (Teunissen and Montenbruck, 2017).

2.2.3 GLONASS

The *Global'naya Navigatsionnaya Sputnikovaya Sistema*, normally referred to as GLONASS, is another GNSS currently operated by the Russian Federation and initially developed by the former Soviet Union to provide the same services as GPS. Following the launch of its first satellite in October 1982, GLONASS achieved full operational status in early 1996 with a constellation of 24 satellites. In the same way as GPS, GLONASS has undergone development through three generations: GLONASS I/II (1982), GLONASS-M (2003), and GLONASS-K (2011). GLONASS is based on frequency division multiple access (FDMA) for its signals, unlike GPS, which uses code division multiple access (CDMA). In FDMA, all channel users transmit simultaneously but occupy different sub-bands of the total available bandwidth. In contrast, with CDMA, all users also transmit simultaneously, but they use the entire available bandwidth, separated by unique codes. Initially, GLONASS was designed to transmit within the L1 band (1602-1615.5 MHz) and the L2 band (1246-1256.5 MHz), with frequency spacings of 0.5625 MHz and 0.4375 MHz, respectively. The latest GLONASS-K generation, however, supports CDMA signals on a new L3 frequency (1202.025 MHz), in addition to the legacy FDMA signals, thereby enhancing compatibility and interoperability with other GNSS systems.

2.2.4 Galileo

The Galileo system is a GNSS which is developed as a joint initiative of the European Commission (EC) and the European Space Agency to provide a highly accurate global positioning service under European civilian control. The first fully-operational satellite was launched in August 2014, starting a constellation of 30 satellites of which 24 are designated as primary with 6 spares. By October 2024, 29 are already in Full Operational Capability and 2 are In Orbit Validation (IOV). This deployment has been executed in three phases, while a new parallel initiative, the Galileo Second Generation (G2G), is currently under development (European Space Agency, 2021).

Galileo satellites transmit across three frequency bands with right-hand circularly polarised signals, using code division multiple access to offer three levels of service that support the various functions provided by Galileo and EGNOS, the European Geostationary Navigation Overlay Service, a Satellite-Based Augmentation System designed to enhance satellite navigation systems to comply with safety-critical application requirements. These frequency bands are E1 (1575,42 MHz), E6 (1278.75 MHz) and E5, which is further divided into E5a (1176.45 MHz) and E5b (1207.14 MHz), being able to track each component separately or in combination. The E1 band, in particular, facilitates interoperability with other GNSS constellations, significantly increasing the number of GNSS signals available to a given user and allowing higher accuracy for precise orbit determination, among other performance enhancements (United Nations Office for Outer Space Affairs, 2018).

2.2.5 BeiDou

The BeiDou Navigation Satellite System (BeiDou or BDS), operated by the People's Republic of China, has been developed in three distinct phases: BDS-1 (1994), which began as an RNSS, and later expanded into a GNSS with the subsequent phases, BDS-2 (2004) and BDS-3 (2009). The initial constellation, comprising three GEO satellites, was completed in 2003, and the system was declared to have reached FOC in December 2012, providing global coverage as of 2020. As of 2024, the operational constellation includes five GEO satellites, 27 MEO satellites, and three IGSO satellites, providing global users with high-quality services including navigation, positioning and data communication (China Satellite Navigation Office, 2019). BeiDou transmits two levels of service, an open and an authorised service, using signals based on the CDMA technique. The current constellation transmits circularly polarised signals with three distinct radio frequencies in the L band, referred to as B1 (1561.098 MHz), B2 (1207.14 MHz), and B3 (1268.52 MHz). Both the open and authorised services are available across these three frequency bands, providing flexibility and robustness in various applications (Sanz Subirana et al., 2013).

2.2.6 QZSS

The Quasi-Zenith Satellite System (QZSS) is a RNSS operated by the Japanese Government, and characterised by the use of multiple satellites in inclined orbits to ensure that at least one satellite is always positioned near the zenith above Japan. This configuration is particularly effective for overcoming signal obstructions caused by tall buildings in densely populated cities, where signals can often be blocked. Consequently, the design provides additional coverage across nearly the entire country, while also supporting interoperability with other GNSS constellations such as GPS and Galileo (Teunissen and Montenbruck, 2017). The first QZSS satellite was launched in September 2010, while the RNSS was fully completed on 2017. The constellation consists of three Quasi-Zenith Orbit (QZO) and one GEO satellites that transmit on four different frequency bands: L1 (1575.42 MHz), L2 (1227.60 MHz), L5 (1176.45 MHz), and L6 (128.75 MHz) (QZSS Cabinet Office, 2020).

2.2.7 IRNSS/NavIC

The Indian Regional Navigation Satellite System (IRNSS), known since 2016 as Navigation with Indian Constellation (NavIC), has been developed by the Indian government to serve India and the surrounding area, from 30° south to 50° north in latitude and 30° east to 130° east in longitude. The NavIC constellation consists of 3 GEO satellites and 4 IGSO satellites, aiming to provide a real-time pseudorange-based position accuracy of better than 20 m in the main service area (Teunissen and Montenbruck, 2017). The first satellite was launched on October 2014 and the constellation was completed in 2016. NavIC provides two types of service: an open service for civilian use and a restricted service for authorised users. Both services are available on the L5 (1176.45 MHz) and S (2492.028 MHz) frequency bands. This dual-band configuration enhances signal reliability and robustness, ensuring effective navigation coverage within the intended service region. In May 2024, NavIC added the L1 frequency for civilian use, aligning it with other GNSS constellations like GPS, Galileo, and GLONASS.

2.3 GNSS Observations

This section provides an introduction to GNSS signals and explains the two primary types of one-way ranging GNSS observations: pseudorange and carrier phase. The observation equations for these measurements are presented in detail, providing the mathematical framework for calculating distances between satellites and receivers. Additionally, the key factors that influence the ideal ranging are briefly introduced, with further elaboration provided in Section 2.5.

2.3.1 Signal Structure and Modulation

To ease the fundamental distance measurement required for GNSS positioning, a key characteristic of these signals, which propagate at the speed of light, is the modulation of the harmonic radio wave, commonly referred to as the *carrier*, by a distinct pseudorandom noise (PRN) code. The carrier wave represents a sinusoidal signal at a specific frequency, while the PRN sequence, consisting of binary digits, serves as a unique identifier for each satellite operating on the same frequency for most GNSS receivers. This modulation scheme is primarily relevant for GNSS systems using CDMA, while FDMA systems, like GLONASS, employ different methods for satellite distinction. In addition to the PRN code, the navigation information is embedded within the GNSS carrier wave, as depicted in Figure 2.3. This navigation message contains critical data, including satellite ephemeris, clock bias parameters, almanac, satellite health status, and other supplementary information, depending on the GNSS constellation.

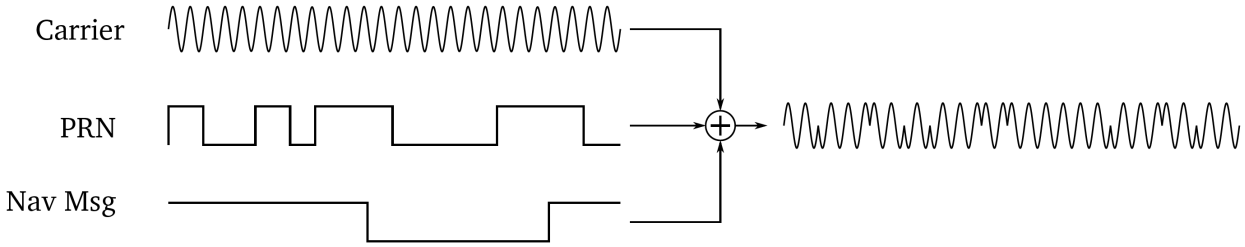

Figure 2.3: GNSS signal structure (Reckeweg, 2020)

2.3.2 Code Phase Measurements

The GNSS receiver determines the time difference between the receiver clock at signal reception and the transmitting satellite clock at signal transmission. This time difference is then multiplied by the speed of light to compute the apparent range between the satellite and the receiver, or more specifically, the distance between the antenna phase centres of the emitting and receiving antennas, referred to as the pseudorange. This process is based on measuring the code phase, which is achieved by aligning the PRN code of the receiver-generated replica signal with the received satellite signal. The ambiguity in the PRN code phase is subsequently resolved by utilising the information embedded within the broadcast navigation message.

The measured code phase of the replica signal is used to establish the signal time of generation t_{tog} in the satellite time scale τ^s, measured at the time of measurement t_{tom} in it own receiver time scale τ_r. This relationship forms the basis of the pseudorange measurement as presented in Equation 2.1, and depicted in Figure 2.4a.

$$p^s_{r,f,ideal} = c \cdot \left[\tau_r(t_{tom}) - \tau^s(t^{tog})\right] = ||r_r(t) - r_s(t-\tau)|| \quad , \tag{2.1}$$

where t is the generalised time of measurement at the receiver, and τ is the signal time-travel between the emitter and the receiver.

However, this measurement is referred to as pseudorange because it does not match the true geometric distance between the satellite and the receiver. This discrepancy arises primarily due to the asynchrony between the satellite and receiver clocks, along with various other factors that affect the signal during its transmission. Therefore, multiple error sources that must be taken into account and modelled within the Observation Equation 2.2 in order to accurately derive the true range (Teunissen and Montenbruck, 2017; Sanz Subirana et al., 2013). In this context, the notation s denotes the emitting satellite, r represents the receiver, and f indicates the frequency-dependent nature of the variable.

Code Phase Observation Equation

$$\begin{aligned} p^s_{r,f}(t) = \rho^s_r(t, t-\tau) + \xi^s_{r,f}(t) + c \cdot [dt_r(t) - dt^s(t-\tau) + \Delta d^s_{r,f}(t)] \\ + T^s_r(t) + I^s_{r,f}(t) + \delta_{rel}(t) + K_{r,f}(t) + K^s_f(t-\tau) \\ + M_f(t) + \varepsilon^s_{r,f}(t) \end{aligned} \quad , \tag{2.2}$$

where

- $p^s_{r,f}(t)$ represents the measured pseudorange, as defined in Equation 2.1.
- $\rho^s_r(t, t-\tau)$ denotes the true geometric distance between the transmitting satellite and the receiver.
- $\xi^s_{r,f}(t)$ is the correction term accounting for phase-centre offsets of the transmitting and receiving antennas.
- c refers to the speed of light, used to convert the measured time delay into distance.
- $dt_r(t)$ is the clock offset of the receiver with respect to the GNSS time scale.
- $dt^s(t-\tau)$ is the clock offset of the transmitting satellite with respect to the GNSS time scale.
- $\Delta d^s_{r,f}(t)$ accounts for the code interchannel bias, addressing discrepancies between different frequency channels.
- $T^s_r(t)$ is the tropospheric delay, which is a non-dispersive effect.
- $I^s_{r,f}(t)$ is the ionospheric delay, which is a frequency-dependent distortion.
- $\delta_{rel}(t)$ captures the relativistic effect due to space-time curvature.
- $K_{r,f}(t)$ is the instrumental delay of the receiver.
- $K^s_f(t-\tau)$ is the instrumental delay of the emitting satellite.
- $M_f(t)$ includes the effects of multipath errors.
- $\varepsilon^s_{r,f}(t)$ accounts for receiver noise and other minor effects influencing the measurement.

2.3.3 Carrier Phase Measurements

In addition to the pseudorange measurements, the changes in carrier phase over time can also fulfil the same purpose with a substantially larger precision, around two orders of magnitude higher. This increased accuracy is achieved by measuring the instantaneous beat phase and the accumulated number of zero crossings acquired after mixing with a specific reference signal of the nominal frequency (Teunissen and Montenbruck, 2017). However, this methodology comes at the expense of ambiguity due to an unknown integer number of wavelengths (λN), which can vary arbitrarily every time the receiving device loses the signal lock, resulting in phase jumps or range discontinuities (Sanz Subirana et al., 2013). The idealised carrier phase range measurement is presented in Equation 2.3, and depicted in Figure 2.4b:

$$\varphi^s_{r,f,ideal} = \lambda_f \cdot [\phi_r(t_{tom}) - \phi^s(t_{tom}) + N^s_r(t_{tom}, t_{init})] = \lambda_f \cdot [\Delta\phi^s_r(t_{tom}) + N^s_r] = ||r_r(t) - r_s(t-\tau)|| \quad , \tag{2.3}$$

where $\Delta\phi^s_r(t_{tom})$ represents the fractional phase measurement, and N^s_r denotes the full cycle count of the measured replica carrier signal phase since initial signal acquisition at t_{init}.

Equation 2.4 presents the carrier phase observation equation, in which several terms are identical to those in the pseudorange counterpart, including the true geometric range, the emitter and receiver clock offsets, and the tropospheric propagation delay. In both equations, the ionospheric term has the same magnitude; however, there is a sign change in the carrier phase equation. This occurs because while the carrier phase is advanced as it propagates through the ionosphere, the code measurement experiences a corresponding delay of equal magnitude (Teunissen and Montenbruck, 2017; Schutz et al., 2004).

Carrier Phase Observation Equation

$$\begin{aligned} \varphi^s_{r,f}(t) = \rho^s_r(t, t-\tau) + \zeta^s_{r,f}(t) + c \cdot [dt_r(t) - dt^s(t-\tau) + \Delta\delta^s_{r,f}(t)] \\ + T^s_r(t) - I^s_{r,f}(t) + \delta_{rel}(t) + k_{r,f}(t) + k^s_f(t-\tau) \\ + \lambda_f \cdot [N^s_{r,f} + \cdot w^s_r(t)] \\ + m_f(t) + \varepsilon^s_{r,f}(t) \end{aligned} \quad , \tag{2.4}$$

where the new terms are

- $\varphi^s_{r,f}(t)$ represents the measured phase range for the specified frequency, as the fractional phase measurement of Figure 2.4b.
- $\zeta^s_{r,f}(t)$ accounts for corrections due to the phase-centre offset and variations, influenced by the antenna phase-pattern and signal frequency.
- $\Delta\delta^s_{r,f}(t)$ represents the phase interchannel bias, addressing discrepancies between frequency channels.
- $k_{r,f}(t)$ and $k_{s,f}(t)$ are the carrier phase instrumental delays of the receiver and the emitting satellite, respectively.
- λ_f is the wavelength of the carrier signal.
- $N^s_{r,f}$ denotes the integer ambiguity in the carrier phase, expressed in cycles.
- $w^s_r(t)$ refers to the phase wind-up effect caused by the circular polarisation of the electromagnetic signal.
- $m_f(t)$ captures the impact of multipath errors on the carrier phase measurements.
- $\varepsilon^s_{r,f}(t)$ accounts for receiver noise and other minor effects influencing the carrier phase measurement.

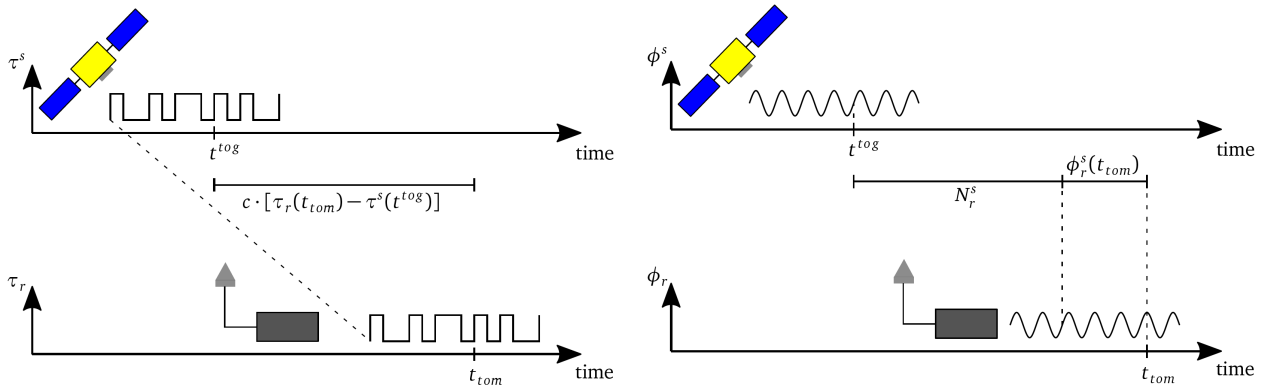

(a) Code phase measurement

(b) Carrier phase measurement

Figure 2.4: GNSS measurements (Reckeweg, 2020)

2.3.3.1 Carrier Phase Integer Ambiguity Resolution

Carrier phase integer ambiguity resolution is essential for achieving fast and high-precision GNSS parameter estimation. This process involves determining the unknown cycle ambiguities in the carrier-phase measurements as integers, which is crucial for precise GNSS positioning, specially in scenarios requiring centimetre-level accuracy. The general steps for ambiguity resolution in GNSS processing are as follows (Teunissen and Montenbruck, 2017):

The resolution process begins with the float solution, where the integer nature of the ambiguities is initially ignored. A standard least-squares estimation is performed, resulting in float ambiguities that represent continuous values. This initial float solution provides a baseline for further refinement. Next, the integer solution is obtained by mapping the float ambiguities to their nearest integer values. This can be achieved through various methods, including integer rounding (IR), integer bootstrapping (IB), or integer least-squares (ILS). Integer rounding involves simply rounding the float ambiguities to the nearest integer values, though this method is not always reliable. Integer bootstrapping sequentially fixes each ambiguity to its nearest integer, offering improved performance over integer rounding. The most rigorous and widely preferred approach is integer least-squares, which searches for the integer ambiguity set that minimises the squared difference between the float ambiguities and their integer estimates. ILS provides the optimal solution in terms of the probability of correctly resolving the ambiguities. Finally, the fixed solution is obtained by readjusting the float solution after the integer ambiguities have been resolved. In this step, the state estimates are updated based on the now-known integer ambiguity values. Once the ambiguity is resolved as an integer, GNSS systems can achieve sub-centimetre positioning accuracy. This is essential for various high-precision applications such as geodesy, surveying, and space missions. However, reliably resolving ambiguities can be challenging, particularly in situations with poor satellite geometry or high measurement noise.

The basic principle of the integer ambiguity resolution scheme implemented in the NSO GNSS processing is structured in two levels: baseline and network (European Space Agency, 2009). At the baseline level, the process starts by forming all double difference Melbourne-Wübbena wide-lane ambiguities. These wide-lane ambiguities are then sorted and fixed according to their fixing probability. Once fixed, the corresponding narrow-lane ambiguities are formed, sorted similarly by their fixing probability. From this set, the independent fixable narrow-lane ambiguities are selected. At the network level, all fixable ambiguities from the baseline level are sorted based on their fixing probability, and again an independent set of fixable ambiguities is selected. After this, the normal equation system is resolved, and the process either moves to the next iteration or concludes depending on whether additional refinement is needed.

In operational GNSS networks, advanced methods like integer least-squares are often used to maximise the success rate of ambiguity resolution and ensure robustness in the solution. The double-difference and Melbourne-Wübbena combinations play a key role in enhancing ambiguity resolution. Challenges arise when dealing with large distances between receivers or in cases of signal interruptions, which complicate the ambiguity resolution process. Therefore, resolving these ambiguities efficiently is a critical aspect of precise GNSS applications (European Space Agency, 2009).

2.4 Multi-Constellation GNSS Observation Equations

Multi-constellation GNSS, commonly referred to as multi-GNSS or MGNSS, has introduced a new set of capabilities, significantly expanding data collection and product generation strategies. By utilising signals from multiple GNSS constellations, MGNSS achieves higher positional accuracy compared to relying on a single constellation. This is particularly advantageous in challenging environments where signals from one constellation may be insufficient. The increased number of satellite signals enhances the success rate of positioning, even in conditions where signal obstruction or degradation is prevalent. Additionally, multi-GNSS offers improved robustness against interference by leveraging multiple frequency bands across different constellations. It is important to note that this section does not address multi-frequency GNSS, which involves tracking signals on more than two frequencies. While multi-frequency observations offer additional benefits such as better ionospheric error correction and improved accuracy, this approach is not within the scope of the current analysis. Therefore, multi-frequency GNSS will not be explored in detail, and the focus will remain on dual-frequency observations, which aligns with the current methodology employed by the Navigation Support Office.

To derive the observation equations for multiple constellations, it is assumed that a MGNSS receiver tracks signals of two or more constellations. The most simple example considers two constellations, denoted as **A** and **B** (Teunissen and Montenbruck, 2017). This approach can be extended to multiple constellations by aligning all systems to a common system time. As previously discussed, when the observations from constellation **A** are recorded at receiver time t_r (the timestamp found in the RINEX observation file), the receiver time differs from the unknown system time of constellation **A**, t^A, as expressed by the receiver clock error dt_r. In the same way, observations from constellation **B**, also collected at receiver time t_r, are based on a different physical clock for its GNSS system time. However, the observations from **B** can be expressed in terms of the receiver clock error relative to constellation **A**'s system time, which is used as a reference.

The system of equations describing the relationship between the receiver time and the system times of constellations **A** and **B** is given as

$$\begin{aligned} t_r(t^A) &= t^A + dt_r(t^A) \\ t_r(t^B) &= t^B + dt_r(t^B) = t^B + dt_r(t^A) - t^{AB} \end{aligned} \quad , \tag{2.5}$$

with the system time offset $t^{AB} = t^B - t^A$, so that $t_r(t^A) = t_r(t^B)$.

With this offset, the pseudorange equations for both satellites can be expressed as

Code Phase Observation Equation - Constellation A

$$\begin{aligned} p^s_{r,f}(t^A) &= c \cdot [t_r(t^A) - t^s(t^A - \tau^s_r)] \\ &= \rho^s_r(t^A, t^A - \tau^s_r) + \xi^s_{r,f}(t^A) + c \cdot [dt_r(t^A) - dt^s(t^A - \tau^s_r) + \Delta d^s_{r,f}(t^A)] \\ &\quad + T^s_r(t^A) + I^s_{r,f}(t^A) + \delta_{rel}(t^A) + K^A_{r,f}(t^A) + K^s_f(t^A - \tau^s_r) \\ &\quad + M_f(t^A) + \varepsilon^s_{r,f}(t^A) \end{aligned} \quad \text{, and,} \tag{2.6}$$

Code Phase Observation Equation - Constellation B

$$\begin{aligned} p^q_{r,f}(t^B) &= c \cdot [t_r(t^B) - t^q(t^B - \tau^q_r)] \\ &= \rho^q_r(t^B, t^B - \tau^q_r) + \xi^q_{r,f}(t^B) + c \cdot [dt_r(t^A) - t^{AB} - dt^q(t^B - \tau^q_r) + \Delta d^q_{r,f}(t^B)] \\ &\quad + T^q_r(t^B) + I^q_{r,f}(t^B) + \delta_{rel}(t^B) + K^B_{r,f}(t^B) + K^q_f(t^B - \tau^q_r) \\ &\quad + M_f(t^B) + \varepsilon^q_{r,f}(t^B) \end{aligned} \quad , \tag{2.7}$$

where $\Delta d^s_{r,f}(t^A)$ and $\Delta d^q_{r,f}(t^B)$ represent the code interchannel biases (ICBs), measured in seconds, which arise in constellations that use FDMA technology, as each channel operates at a different frequency. In contrast, for constellations that employ CDMA technology, all channels share the same frequency, allowing the satellite index to be omitted, and no ICBs are present.

Similar to the system time offset described in Equation 2.5, the receiver hardware bias in the observations of constellation **B** can be defined relative to a reference, following the definition of the intersystem bias (ISB), as

$$ISB^{AB}_{r,f}(t^A, t^B) = \frac{1}{c} \cdot \left[K^B_{r,f}(t^B) - K^A_{r,f}(t^A)\right] + \left[\Delta d^q_{r,f}(t^B) - \Delta d^s_{r,f}(t^A)\right] \quad . \tag{2.8}$$

The ISB is always receiver dependent, and can also be satellite dependent when either one or more satellites in the constellations use FDMA technology. The advantage of formulating the observation equations with these parameters is that, under certain conditions, it becomes possible to calibrate the ISBs. By substituting Equation 2.8 into Equation 2.7, the new code-observation equation for constellation B can be reformulated as

$$\begin{aligned} p^q_{r,f}(t^B) &= c \cdot [t_r(t^B) - t^q(t^B - \tau^q_r)] \\ &= \rho^q_r(t^B, t^B - \tau^q_r) + \xi^q_{r,f}(t^B) + c \cdot [dt_r(t^A) - dt^q(t^B - \tau^q_r) + \Delta d^s_{r,f}(t^A)] \\ &\quad + c \cdot [ISB^{AB}_{r,f}(t^A, t^B) - t^{AB}] \\ &\quad + T^q_r(t^B) + I^q_{r,f}(t^B) + \delta_{rel}(t^B) + K^A_{r,f}(t^A) + K^q_f(t^B - \tau^q_r) \\ &\quad + M_f(t^B) + \varepsilon^q_{r,f}(t^B) \end{aligned} \quad . \tag{2.9}$$

Similarly, the carrier phase observation equation for multi-GNSS can be written as

Carrier Phase Observation Equation - Constellation A

$$\begin{aligned} p^s_{r,f}(t^A) &= \lambda_f \cdot [\phi_r(t^A) - \phi^s(t^A) + N^s_{r,f}] \\ &= \rho^s_r(t^A, t^A - \tau^s_r) + \zeta^s_{r,f}(t^A) + c \cdot [dt_r(t^A) - dt^s(t^A - \tau^s_r) + \Delta\delta^s_{r,f}(t^A)] \\ &\quad + T^s_r(t^A) + I^s_{r,f}(t^A) + \delta_{rel}(t^A) + k^A_{r,f}(t^A) + k^s_f(t^A - \tau^s_r) \\ &\quad + \lambda_f \cdot [N^s_{r,f} + w^s_r(t^A)] \\ &\quad + m_f(t^A) + \varepsilon^s_{r,f}(t^A) \end{aligned} \quad \text{, and,} \tag{2.10}$$

Carrier Phase Observation Equation - Constellation B

$$\begin{aligned} p^q_{r,f}(t^B) &= \lambda_f \cdot [\phi_r(t^A) - \phi^q(t^A) + N^q_{r,f}] \\ &= \rho^q_r(t^B, t^B - \tau^q_r) + \zeta^q_{r,f}(t^B) + c \cdot [dt_r(t^A) - dt^q(t^B - \tau^q_r) + \Delta\delta^s_{r,f}(t^A)] \\ &\quad + c \cdot [ISB^{AB}_{r,f}(t^A, t^B) - t^{AB}] \\ &\quad + T^q_r(t^B) + I^q_{r,f}(t^B) + \delta_{rel}(t^B) + k^A_{r,f}(t^A) + k^q_f(t^B - \tau^q_r) \\ &\quad + m_f(t^B) + \varepsilon^q_{r,f}(t^B) \end{aligned} \quad , \tag{2.11}$$

using the ISB definition for a carrier-phase defined as

$$ISB_{r,f}^{AB}(t^A, t^B) = \frac{1}{c} \cdot \left[k_{r,f}^B(t^B) - k_{r,f}^A(t^A)\right] + \left[\Delta\delta_{r,f}^q(t^B) - \Delta\delta_{r,f}^s(t^A)\right] \quad . \tag{2.12}$$

When both the ISB and the system time offset, t^{AB}, are known, the data from both constellations can be treated as though they come from a unified system. Additionally, for most GNSS constellations, the time system differences (e.g., between their respective clocks) are typically small enough to be negligible in some applications. However, t^{AB} must be considered in the observation equations for the second constellation because it is scaled by the speed of light. For instance, the time offset between GPS Time (GPST) and Galileo System Time (GST) can reach several tens of nanoseconds, which translates into positional differences of several tens of metres. These offsets are typically broadcast as part of the navigation messages and can also be estimated as an unknown parameter during processing. Furthermore, the variability of the ISB and t^{AB} should also be considered. While t^{AB} may remain relatively stable over short periods, it can fluctuate over time, necessitating continuous adjustment or estimation. Similarly, the ISB may vary depending on the receiver and satellite configuration, and must be recalibrated regularly to maintain accuracy in multi-constellation processing.

Besides each constellation's system time, each GNSS system broadcasts satellite positions defined within its own coordinate system. Thus, to solve multi-constellation positioning models, all satellite positions must be converted into a common reference frame. This is the case with precise IGS orbits, where satellite positions from different constellations are all defined relative to a unified reference frame, such as the International Terrestrial Reference Frame (ITRF).

2.5 GNSS Signal Perturbations

As shown in the previous section, several factors in the observation equation can influence the precision of GNSS observations. This section provides an overview of these parameters, along with an example of the proposed methodology for modelling them. The parameters discussed include atmospheric delays, relativistic effects, signal biases, antenna phase-centre offset and variation, carrier phase wind-up, multipath effects, and receiver noise.

2.5.1 Troposphere Delay

GNSS signals have to travel through the Earth´s atmosphere to reach the receivers located on or near the ground. As they propagate, the signals are refracted, causing changes both in terms of speed and direction of travel. Delving deeper into the atmosphere layers, the atmospheric propagation delays can be grouped into those caused by the electrically charged layers and those caused by the neutral layers.

The neutral atmosphere consists of the electrically neutral layers which are stretched from ground level up to a height that varies with the time of day, averaging around 50 km at its lowest point (Kelly, 2012). Since the majority of the effects occur in the lowest region of the atmosphere, the troposphere, the effects are normally referred to as tropospheric propagation delays. These effects of the troposphere on the GNSS signals appear as an additional delay that depends on factors such as temperature, pressure, humidity, and the locations of the transmitter and receiver antennas. A key characteristic of the troposphere is that, for electromagnetic waves with frequencies up to 15 GHz, its effects are non-dispersive, meaning they are not frequency-dependent for GNSS signals. Thus, the pseudorange and carrier phase measurements are affected by the same delay, and this tropospheric refraction cannot be eliminated through dual-frequency measurement combinations (Sanz Subirana et al., 2013). Consequently, the only way to mitigate the tropospheric effect consists on using models or estimates based on observational data (Sanz Subirana et al., 2013). This delay can be written as

$$T = \int (n-1)dl = 10^{-6} \int N dl \quad , \tag{2.13}$$

where n represents the refractive index of air, and N, defined as $N = 10^6(n-1)$, is the refractivity. The refractivity can be further divided into two components: hydrostatic, which accounts for the dry gases (primarily N_2 and O_2), and wet, which considers water vapour, such that $N = N_{hyd} + N_{wet}$.

Moreover, pressure profiles of water vapour differ significantly from those of dry air, which exhibit more deterministic behaviour and account for approximately 90% of the total refraction (Leick et al., 2015). While the delay due to the hydrostatic component varies by less than 1% over a few hours, resulting in errors of around 2.3 m in the zenith direction and up to 10 m for lower elevations, the delay caused by the wet component only affects a few tens of centimetres. However, the wet component changes much more rapidly and randomly, making it difficult to model accurately (Sanz Subirana et al., 2013). Therefore, for high-accuracy positioning, the wet component is estimated along with the receiver coordinates. For this estimation, the Navigation Support Office relies on an hydrostatic a priori model based on Saastamoinen (1972), as well as pressure and temperature values from the empirical GPT (Global Pressure and Temperature) model from Boehm, Heinkelmann, and Schuh (2007). Mapping functions and gradient models are required to map the zenith tropospheric delay (ZTD) to the slant total tropospheric delay (STD) along a signal path. The hydrostatic and wet gradient mapping functions are sourced from Boehm, Werl, and Schuh (2006).

2.5.2 Ionosphere Delay

The ionosphere is the ionised layer of the Earth's atmosphere, extending from approximately 60 km up to more than 2000 km (Sanz Subirana et al., 2013), formed due to the interaction of solar radiation and other charged particles such as cosmic rays. The effect of the ionosphere on the GNSS signal propagation depends on its electron density, which is primarily driven by the geometrical position of the local atmosphere with respect to the Sun, thereby defining the local time of day. During the daytime, solar radiation ionises neutral atoms into free electrons and ions, while at night, the recombination process prevails, leading to a reduction in electron density. Additionally, electron density varies with altitude (Sanz Subirana et al., 2013). Unlike the troposphere, the ionosphere is a dispersive medium, which means that the phase and code of the signal propagate at different velocities. This leads to a delay in pseudorange measurements and an advancement in the carrier phase (Teunissen and Montenbruck, 2017). An approximation of the frequency-dependent delay can be written as

$$I = 40.3\frac{TEC}{f^2} \quad , \tag{2.14}$$

where TEC denotes the total electron content in electrons/m^2, obtained as the total number of electrons in a column of one-meter-square cross-section centred on the signal raypath and ranging from the transmitter to the receiver, and f is the signal frequency in hertz (Teunissen and Montenbruck, 2017).

As seen in Equation 2.14, the ionospheric effect can be accurately modelled as an approximation that is inversely proportional to the square of the signal frequency. Consequently, the linear combination of simultaneous measurements, which can either be pseudoranges or carrier phases, on two different frequencies, such as Galileo E1 and E6, can account for a virtually free observation of ionospheric effects for position determination when using dual- or multi-frequency receivers (Teunissen and Montenbruck, 2017). However, higher-order ionospheric terms, which are not fully mitigated by such combinations, can still be relevant, especially for ground stations requiring precise positioning, and may need to be considered in certain high-precision applications.

2.5.3 Relativistic Effects

GNSS technology has long advanced to a state where the precision of the measurements has reached the nanosecond level, making it essential to account for corrections imposed by relativistic effects to achieve high-accuracy positioning. The rate at which two identical clocks advance depends on their relative positions with respect to gravitational bodies and their motion. For instance, when comparing the clock of a satellite in Earth orbit to one on the Earth's surface, differences arise due to two main relativistic effects: gravitational potential differences, as described by general relativity, and velocity differences, as explained by special relativity. The effect of general relativity can be tackled by modifying the clock's oscillating frequency of the satellite. This adjustment is achieved by applying a constant correction, which depends on the satellite's nominal semi-major axis and can be calculated using

$$\frac{\Delta f_0}{f_0} = \frac{1}{2}\left(\frac{v}{c}\right)^2 + \frac{\Delta U}{c^2} \quad , \tag{2.15}$$

where $\Delta f_0/f_0$ represents the fractional frequency shift of the satellite clock, v is the satellite's orbital velocity, c is the speed of light, and ΔU is the difference in gravitational potential between the satellite and the Earth's surface.

The second effect, often referred to as the periodic relativistic effect, is caused by the orbital eccentricity. This effect induces a periodic time offset that can be corrected using

$$\Delta_{rel} = -2\frac{r_{sat} \cdot v_{sat}}{c^2} \quad , \tag{2.16}$$

with r_{sat} and v_{sat} being the satellite position and velocity vectors, respectively, in the inertial system. Although the periodic relativistic effect is not commonly applied in GNSS observation equations, as it tends to cancel out in the single difference between stations due to its satellite-dependent nature, it becomes important when station and/or satellite clocks are estimated, particularly in undifferenced processing techniques or for absolute navigation, as it can reach up to 50 nanoseconds (European Space Agency, 2009).

Once the clock corrections have been applied, it is necessary to address the Euclidean range correction due to the space-time curvature caused by the Earth's gravitational field, known as the Shapiro signal propagation delay. This effect is computed using

$$\Delta_{rel,shapiro} = \frac{2\mu}{c^2} ln\left(\frac{r_s + r_r + \rho}{r_s + r_r - \rho}\right) \quad , \tag{2.17}$$

where μ denotes Earth's gravitational constant, r_s and r_r are the distances between the satellite and the Earth, and the receiver and the Earth, respectively, and ρ represents the range between the satellite and receiver.

2.5.4 Antenna Phase Centre Offset and Variation

In high-precision GNSS applications, the measured range between the satellite emitter and the receiver is more accurately defined as the distance between the electrical phase centres of the transmitting and receiving antennas. These phase centres are not fixed points; they vary with azimuth, elevation, and frequency, which affects both code and phase observations (Teunissen and Montenbruck, 2017). To account for these variations, the ANTEX format is used to distribute the necessary corrections. The IGS20 ANTEX file, provided by the International GNSS Service (IGS), is widely used, but the Navigation Support Office employs a customised ANTEX file that includes updates specifically related to the Galileo constellation. This customised file defines the phase centre offsets (PCOs) from the Antenna Reference Point (ARP), as well as the elevation- and azimuth-dependent phase centre variations (PCVs).

Accurate positioning relies heavily on accurate PCO and PCV information. Historically, PCOs were estimated due to the absence of manufacturer-provided values, which limited GNSS contributions to the International Terrestrial Reference Frame (ITRF) scale. However, since December 2016, Galileo has been the first GNSS provider to publish official PCO and PCV values, significantly improving observation model accuracy. The Galileo metadata is regularly updated as new satellites are declared operational, ensuring continuous improvements in navigation performance (Schoenemann et al., 2024).

2.5.5 Carrier Phase Wind-Up

Considering a receiver with fixed coordinates, the wind-up effect is related to right-hand circularly polarised waves typically emitted by GNSS signals. These polarised waves determine how the electrical field vector changes over time. As the satellite moves along its orbital path, it continuously rotates to keep its solar panels oriented toward the Sun for optimal energy extraction while maintaining its antenna pointed toward nadir. This rotation causes a phase variation that the receiver interprets as a range variation (Sanz Subirana et al., 2013). As a result, the wind-up effect impacts only the carrier phase measurements, as seen in Equation 2.4, and is dependent on the relative orientation of the emitter and receiver antennas, as well as the direction of the line of sight. For instance, the potential maximum range error using GPS can reach approximately 19 cm for L1 and 25 cm for the L5 frequencies (Teunissen and Montenbruck, 2017). The wind-up correction for a crossed dipole antenna, caused by the satellite's motion, is computed by the expressions derived from Wu et al. (1993).

2.5.6 Instrumental Delays

Instrumental delays, also referred to as signal biases, arise from the imperfect synchronisation of signals as they travel from generation to reception. These instrumental delays, often denoted as K_f in the observation equations, can arise from several sources, including transmission delays through cables or the internal filters of the GNSS receiver. These delays can be divided into satellite-dependent and receiver-dependent components. While these biases are generally assumed to be time-invariant, they can slowly vary due to external factors, such as temperature changes, and typically drift over the course of days. Instrumental delays affect both code and carrier phase measurements, and for a single constellation, the receiver-dependent delays are considered constant across all signals of the same type tracked by a single receiver (Teunissen and Montenbruck, 2017). Since the receiver clock delay is common to all satellites in the constellation, it is usually included in the receiver clock estimate. When considering multi-GNSS systems, the receiver-dependent delays for signals from different constellations are unlikely to be the same. Therefore, it becomes essential to estimate this intersystem bias (ISB) as a separate parameter for each additional GNSS constellation or apply external corrections (Sanz Subirana et al., 2013).

2.5.7 Multipath Errors

Multipath errors arise in both pseudorange and carrier phase observations when a GNSS receiver picks up the same signal through multiple paths, typically due to reflections from nearby surfaces such as the ground or buildings. This effect is particularly important when the signal comes from low-altitude satellites, where the likelihood of encountering reflective surfaces increases. The magnitude of these errors varies across frequencies, typically reaching up to two or three metres for pseudocode measurements, and less than one centimetre for carrier phase observations, such as those from GPS C1 and GPS L1 or L2, respectively (Sanz Subirana et al., 2013). Contrary to measurement noise, multipath errors cannot be characterised as random errors as the temporal variation depends on variational aspects such as the geometry between the satellite, the reflecting surface, and the receiver. For this reason, multipath effects often exhibit periodic behaviour, with timescales ranging from several seconds to several minutes. Since these errors do not average out over time and lack a mean null value, they remain a persistent source of bias in GNSS measurements (Teunissen and Montenbruck, 2017).

2.5.8 Receiver Noise

Receiver noise is caused by imperfections in various electrical components within the signal processing chain, as well as from natural or artificial sources in the surrounding environment (Teunissen and Montenbruck, 2017). This noise introduces random errors into both the pseudorange and the carrier phase observations, although the magnitudes differ significantly. The noise in pseudorange measurements is generally larger than in carrier phase measurements, typically ranging from 1% of the pseudorange value to 1% of the carrier phase wavelength. While receiver noise affects both types of observations, the noise in pseudorange is generally larger than in carrier phase measurements. Receiver noise can often be modelled as a white-noise-like error, which can be reduced by applying a low-pass filter. However, while smoothing can be applied to both code and phase observations, it is more effective for code noise. Smoothing the carrier phase noise is less straightforward due to its much smaller magnitude and higher precision requirements (Sanz Subirana et al., 2013).

2.6 GNSS Combinations of Observations

The combination of GNSS observations is a powerful tool for eliminating nuisance parameters such as ionospheric delays and for isolating specific errors of interest, including multipath effects and ambiguity parameters. These combinations not only improve the precision of GNSS measurements but also enhance error correction capabilities. This section provides an overview of the main types of observation combinations and discusses the use of raw, or uncombined, observations, outlining their benefits and limitations.

2.6.1 Single-Satellite and Single-Receiver Observations

This section introduces observation combinations based on measurements from a single receiver and a single satellite, across one or more frequencies. These combinations allow for improved error mitigation and more precise positioning results by leveraging the unique properties of multi-frequency observations.

2.6.1.1 Narrow- and Wide-Lane Combinations

When two or more carrier-phase observations are combined, they produce a new signal with a different frequency and wavelength. If the combined wavelength is longer than the longest individual wavelength, the combination is referred to as *wide-lane* combination. Conversely, if the combined wavelength is shorter than the shortest individual wavelength, the combination is known as *narrow-lane* combination (Teunissen and Montenbruck, 2017).

The most common dual-frequency wide-lane (WL) and narrow-lane (NL) combinations, using only carrier-phase measurements on the frequencies f_A and f_B, can be written as the carrier-phase measurements ϕ_r^s between receiver r and satellite s on frequencies f_A and f_B, with corresponding wavelengths λ_A and λ_B. This can be expressed as

$$\Phi^s_{r,WL} = \Phi^s_{r,A} - \Phi^s_{r,B} = \frac{\varphi^s_{r,A}}{\lambda_A} - \frac{\varphi^s_{r,B}}{\lambda_B} \quad \text{, and,} \tag{2.18}$$

$$\Phi^s_{r,NL} = \Phi^s_{r,A} + \Phi^s_{r,B} = \frac{\varphi^s_{r,A}}{\lambda_A} + \frac{\varphi^s_{r,B}}{\lambda_B} \quad , \tag{2.19}$$

with the combined wavelengths defined as

$$\lambda_{WL} = \frac{c}{f_A - f_B} \quad \text{and} \quad \lambda_{NL} = \frac{c}{f_A + f_B} \quad , \tag{2.20}$$

where c corresponds to the speed of light. In this manner, the wide- and narrow-lane carrier phase combinations can be constructed, preserving the geometric properties of the signal, as

$$\varphi^s_{r,WL} = \frac{f_A}{f_A - f_B} \cdot \varphi^s_{r,A} - \frac{f_B}{f_A - f_B} \cdot \varphi^s_{r,B} \quad \text{, and,} \tag{2.21}$$

$$\varphi^s_{r,NL} = \frac{f_A}{f_A - f_B} \cdot \varphi^s_{r,A} + \frac{f_B}{f_A - f_B} \cdot \varphi^s_{r,B} \quad . \tag{2.22}$$

Due to their long wavelength, wide-lane combinations are particularly useful for resolving integer ambiguities, which involve determining the integer number of carrier-phase cycles in the observations. In this case, wide-lane combinations are applied to the double-differenced observations, which are explained in Equation 2.32 based on Teunissen and Montenbruck (2017). However, it should be noted that the carrier phase noise in the wide-lane combination is amplified, making it several times larger than in the original signals (Sanz Subirana et al., 2013).

Similarly, narrow-lane and wide-lane combinations can also be formed using pseudorange measurements instead of carrier-phase observations. This is exemplified by the Melbourne–Wübbena combination (MW), which is derived from the difference between narrow-lane pseudorange and wide-lane carrier-phase observations:

$$MW = \varphi^s_{r,WL} - p^s_{r,NL} = \frac{f_A}{f_A - f_B} \cdot \varphi^s_{r,A} - \frac{f_B}{f_A - f_B} \cdot \varphi^s_{r,B} - \frac{f_A}{f_A - f_B} \cdot p^s_{r,A} - \frac{f_B}{f_A - f_B} \cdot p^s_{r,B} \tag{2.23}$$

While the narrow- and wide-lane combinations described here are limited to using two frequencies, similar combinations can be constructed by utilising observations on three or more frequencies simultaneously.

2.6.1.2 Ionospheric-Free Combination

As discussed in the Ionosphere Delay Section 2.5.2, the ionospheric delay is frequency-dependent, which allows for its effective removal when signals are transmitted at different frequencies. By using a linear combination of range measurements at two distinct frequencies, f_A and f_B, the ionospheric delay can be eliminated to a high degree of accuracy. Based on Teunissen and Montenbruck (2017), given the range measurements p^s_{r,f_A} and p^s_{r,f_B} transmitted at these frequencies, the ionospheric-free combinations for pseudorange and carrier phase observations are given as

$$p^s_{r,IF} = \frac{f_A^2}{f_A^2 - f_B^2} \cdot p^s_{r,f_A} - \frac{f_B^2}{f_A^2 - f_B^2} \cdot p^s_{r,f_B} \quad \text{, and,} \tag{2.24}$$

$$\varphi^s_{r,IF} = \frac{f_A^2}{f_A^2 - f_B^2} \cdot \varphi^s_{r,f_A} - \frac{f_B^2}{f_A^2 - f_B^2} \cdot \varphi^s_{r,f_B} \quad . \tag{2.25}$$

While this combination increases the noise in the measurements compared to single-frequency observations, it allows for the elimination of systematic ionospheric effects with an accuracy typically within a few centimetres, depending on the ionospheric conditions and signal frequencies. This is crucial for achieving high precision in applications requiring centimetre- or sub-centimetre-level accuracy. This approach is employed by the Navigation Support Office to ensure accurate and reliable positioning in high-precision applications. Additional techniques, such as smoothing filters, can be employed to mitigate the increased noise introduced by the ionospheric-free combination (Schutz et al., 2004).

2.6.2 Multi-satellite and Multi-Receiver Observations

In the previous section, observations combinations have only been formed from measurements of a single satellite tracked by a single receiver. This section now extends the concept by demonstrating how combinations can also be formed between two satellites, two receivers, or a mixture of both. However, it is important to note that the Navigation Support Office primarily utilises undifferenced observations in its analysis and processing for certain high-accuracy positioning applications. While undifferenced observations are the preferred method for these cases, all possible observation combinations are available and supported within the EPNS software, providing flexibility for various GNSS applications.

2.6.2.1 Single Difference

The pseudorange measurements from a specific satellite, observed at two different receivers, can be differenced to produce:

$$p^s_{12} = p^s_1 - p^s_2 \quad \text{and} \quad \varphi^s_{12} = \varphi^s_1 - \varphi^s_2 \quad , \tag{2.26}$$

where s identifies the satellite, and *1* and *2* denote the two receivers, as shown in Figure 2.5a. The notation $X^s_{12} = X^s_1 - X^s_2$ has been used for brevity in the following explanations. Alternatively, a single difference could be formed using measurements from one receiver observing two different satellites, as represented by Equation 2.27. In this case, t identifies the second satellite, as seen in Figure 2.5b, and based on Schutz et al. (2004).

$$p^{st}_1 = p^s_1 - p^t_1 \quad \text{and} \quad \varphi^{st}_1 = \varphi^s_1 - \varphi^t_1 \quad . \tag{2.27}$$

Expanding the previous equations for two stations and one satellite using the complete observation equations for both pseudorange (Equation 2.2) and carrier phase measurements (Equation 2.4) yields the following expressions:

$$p^s_{12} = \rho^s_{12} + \xi^s_{12} + c \cdot dt_{12} + T^s_{12} + I^s_{12} + \delta^s_{rel,12} + K^s_{12} + M^s_{12} + \varepsilon^s_{12} \tag{2.28}$$

$$\varphi^s_{12} = \rho^s_{12} + \zeta^s_{12} + c \cdot dt_{12} + T^s_{12} - I^s_{12} + \delta^s_{rel,12} + k^s_{12} + \lambda_s \cdot (N^s_{12} + w^s_{12}) + m^s_{12} + \varepsilon^s_{12} \quad . \tag{2.29}$$

This procedure eliminates the residual satellite clock offset, which is identical for two time-synchronised observations at different receivers irrespective of the antenna distance.

Similarly, expanding the equations for one station observing two satellites results in the following expressions, where the residual receiver clock offset is eliminated:

$$p_1^{st} = \rho_1^{st} + \xi_1^{st} + c \cdot dt^{st} + T_1^{st} + I_1^{st} + \delta_{rel,1}^{st} + K_1^{st} + M_1^{st} + \varepsilon_1^{st} \tag{2.30}$$

$$\varphi_1^{st} = \rho_1^{st} + \zeta_1^{st} + c \cdot dt^{st} + T_1^{st} - I_1^{st} + \delta_{rel,1}^{st} + k_1^{st} + \lambda_t \cdot (N_1^t + w_1^t) - \lambda_s \cdot (N_1^s + w_1^s) + \varepsilon_1^{st} \quad . \tag{2.31}$$

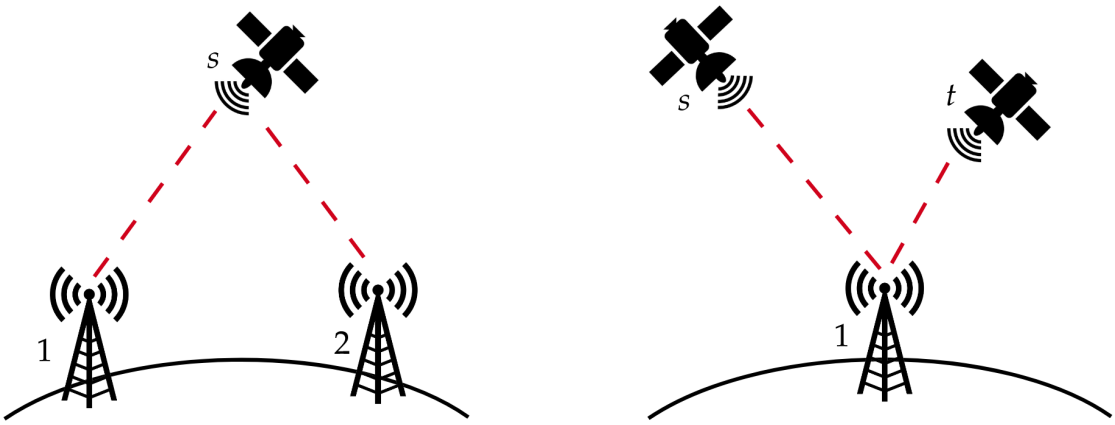

(a) Two stations and one satellite

(b) One station and two satellites

Figure 2.5: Single differencing operations

While single differences are generally formed between identical signals, they do not have to be limited to basic single observations. For instance, an ionosphere-free observable could be combined with any other signal combination in the single difference, depending on the application.. However, as with previous combinations, eliminating parameters from the measurement equations leads to increased noise, which can be modelled as $\sigma_{12} = \sigma^{st} = \sqrt{2}\sigma$, assuming identical standard deviation σ for the uncombined observables.

2.6.2.2 Double Difference

The aforementioned single differences can be further differenced to eliminate additional common errors. By first differencing the measurements between receivers and then applying the differencing to the resulting values between satellites, the double difference is obtained and can be expressed as (Schutz et al., 2004):

$$p_{12}^{st} = p_{12}^{s} - p_{12}^{t} = p_1^{st} - p_2^{st} \tag{2.32}$$

$$\varphi_{12}^{st} = \varphi_{12}^{s} - \varphi_{12}^{t} = \varphi_1^{st} - \varphi_2^{st} \quad . \tag{2.33}$$

Following this approach, the double-difference complete observation equations can be expressed as:

$$p_{12}^{st} = \rho_{12}^{st} + \xi_{12}^{st} + T_{12}^{st} + I_{12}^{st} + K_{12}^{st} + M_{12}^{st} + \varepsilon_{12}^{st} \tag{2.34}$$

$$\varphi_{12}^{st} = \rho_{12}^{st} + \zeta_{12}^{st} + T_{12}^{st} - I_{12}^{st} + k_{12}^{st} + \lambda \cdot (N_{12}^{st} + w_{12}^{st}) + m_{12}^{st} + \varepsilon_{12}^{st} \quad . \tag{2.35}$$

The double-difference process is illustrated in Figure 2.6a. In this formulation, both the receiver and satellite clock errors are effectively eliminated, significantly reducing common systematic errors. However, this comes at the cost of increased measurement noise, which can be modelled as $\sigma_{12}^{st} = \sqrt{2}\sigma_{12} = \sqrt{2}\sigma^{st} = 2\sigma$.

2.6.2.3 Triple Difference

Another method to further reduce errors is to exploit temporal correlation by taking the difference of observations at successive epochs. This time-differencing technique, often referred to as the triple difference, involves subtracting the double-difference observations recorded at two different times. The triple difference can be expressed as:

$$\partial p_{12}^{st} = p_{12}^{st}(t_i) - p_{12}^{st}(t_{i-1}) \quad . \tag{2.36}$$

The corresponding complete observation equations for pseudorange and carrier phase in triple-difference form are:

$$\partial p_{12}^{st} = \partial \rho_{12}^{st} + \partial \xi_{12}^{st} + \partial T_{12}^{st} + \partial I_{12}^{st} + \partial M_{12}^{st} + \partial \varepsilon_{12}^{st} \quad , \tag{2.37}$$

$$\partial \varphi_{12}^{st} = \partial \rho_{12}^{st} + \partial \zeta_{12}^{st} + \partial T_{12}^{st} - \partial I_{12}^{st} + \partial w_{12}^{st} + \partial m_{12}^{st} + \partial \varepsilon_{12}^{st} \quad . \tag{2.38}$$

The triple-difference concept is illustrated in Figure 2.6b. This approach effectively eliminates biases such as K_{12}^{st} and k_{12}^{st}, as well as the carrier phase double-difference ambiguity N_{12}^{st} as long as no cycle slip occurs. Similar to the previous cases, the measurement error can be modelled as $\sigma_{\partial_{12}^{st}} = \sqrt{2}\sigma_{12}^{st} = \sqrt{8}\sigma$.

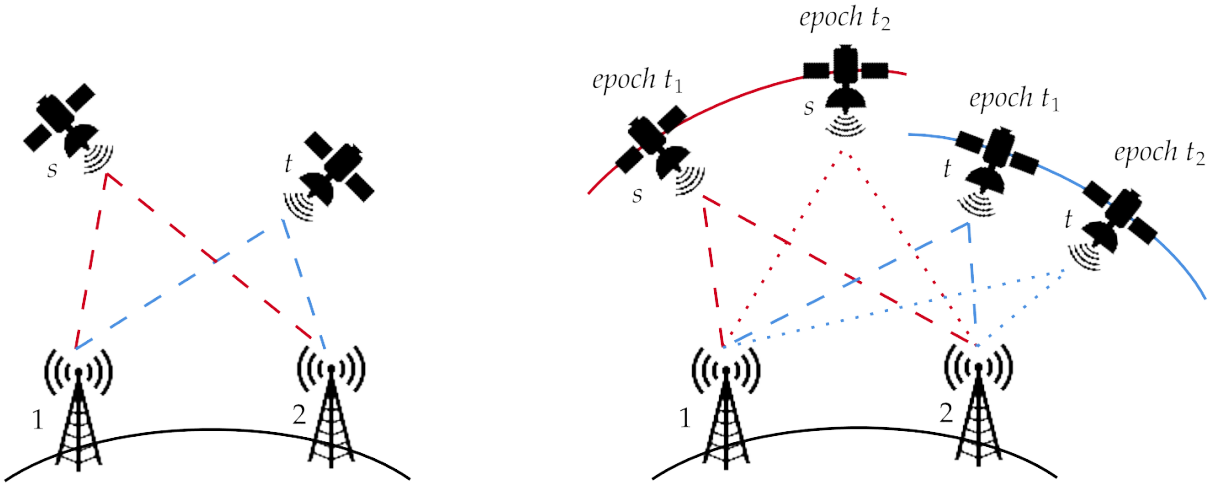

(a) Double differencing operations

(b) Triple differencing operations

Figure 2.6: Types of operations between two stations and two satellites

2.6.3 Undifferenced or RAW Approach

Despite the benefits of using linear combinations of observations, explained in the previous section, using the undifferenced, or also called raw, observations can also have distinct benefits. One of the primary advantages is the preservation of the original physical observation characteristics of the observations, allowing for a more detailed analysis of individual effects, biases, and components. While linear combinations tend to amplify measurement errors by increasing noise levels, the use of raw observables maintains the original error and noise characteristics. However, this approach requires careful treatment of all underlying effects and biases. As shown in Figure 2.7, the raw processing approach provides enhanced analytical capabilities by allowing a more precise examination of each signal component. The figure illustrates the residuals of code and phase observations for different Galileo signals, where the residuals represent the difference between observed and modelled values after various corrections (e.g., satellite positions, clock biases, atmospheric delays). The standard deviation of these residuals demonstrates that the noise level in raw code and phase observations can be significantly lower than in the ionospheric-free linear combination. For instance, in the case of the Galileo E5 signal, the phase

residuals from raw observations show nearly an order of magnitude improvement compared to the ionospheric-free combination, highlighting the potential accuracy gains from using raw data (Schönemann, 2014).

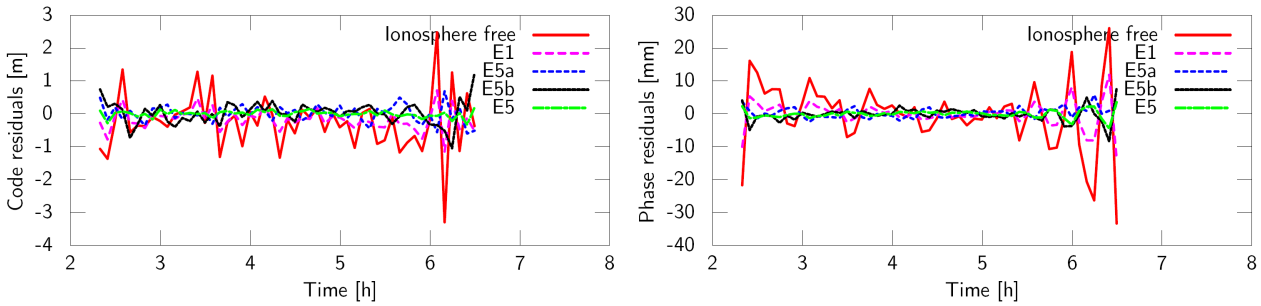

Figure 2.7: Standard deviation of code and phase residuals for different Galileo signals (Schönemann, 2014)

The ability to treat all observations equally, regardless of their GNSS constellation, signal modulation frequency, or the number of measurements, makes raw observations a promising approach for any kind of GNSS analysis. This approach eliminates the need for constellation-specific adjustments, such as intersystem biases. However, a key challenge in processing raw observations is the strong correlation between clock offsets, ionospheric delays, and other variables, which complicates the separation of individual effects. This can result in rank deficiencies in the normal equation system, requiring advanced techniques to resolve (Schönemann, 2014).

3 Precise Orbit Determination

In this chapter, the foundational concepts of Precise Orbit Determination (POD) are introduced in Section 3.1, detailing the essential parameters required to describe a satellite motion. Then, Section 3.2 elaborates on the Least-Squares Algorithm, including its linearisation and the formulation of normal equations, as well as the application of weighting techniques to enhance estimation accuracy. Section 3.3 covers the various coordinate systems and time references critical for GNSS operations, with subsections on time systems and reference frames, including celestial and terrestrial reference frames and their transformations.

An introduction into perturbations is given in Section 3.4, followed by Section 3.5, which focuses on gravitational perturbations affecting satellite orbits, discussing Earth's gravitational potential, third-body effects, and relativistic corrections. Non-gravitational perturbations, such as Solar Radiation Pressure, are examined in Section 3.6, where both physical and empirical models are described. Finally, Section 3.7 addresses the uncertainties inherent in dynamical models.

3.1 POD Concept

For the Precise Orbit Determination problem, the state of the dynamical system is described by a set of parameters required to accurately determine the satellite's current and future positions. This set of parameters is represented by the state vector, $\mathbf{x}(t)$, which includes not only the position and velocity of the satellite at a given time but also potentially other relevant parameters, such as those related to dynamic and measurement models. These additional parameters can help refine the orbit determination process by accounting for various forces and errors that affect the satellite's motion. Given the minimal initial conditions of the satellite state $\mathbf{x_0}$ at time t_0, if the differential equations governing the vehicle's motion are known, these equations can be integrated to estimate the vehicle's state at any future time.

As the initial state is never perfectly known, and certain physical constants and mathematical models are just an approximation to reality, an additional corrective measure is needed to ensure the best estimate is obtained. Consequently, the observations from tracking stations whose positions are precisely known can be used to achieve a better estimate, which will still be subject to both random and systematic errors. Normally these observations comprise measurements such as the range, azimuth or elevation, and the state variables (position, velocity and other model parameters) are not directly observed but obtained as a non-linear relationship with these observations (Schutz et al., 2004).

Precise Orbit Determination can be performed using different approaches—kinematic, dynamic, or reduced-dynamic—depending on the goals of the analysis and the available data. The kinematic method relies exclusively on observational data, without considering the satellite's dynamics, making it suitable for real-time and post-facto analyses. The dynamic method, in contrast, uses a comprehensive model of the forces acting on the satellite to numerically integrate its trajectory, combining observed and modelled data, often through least-squares fitting, for post-facto processing. The reduced-dynamic method integrates elements of both kinematic and dynamic approaches, using observational data while accounting for certain dynamic effects to enhance accuracy. The methodology used by this thesis will follow the reduced-dynamic approach, which aligns with the operational NSO GNSS processing.

POD can be based both on batch and sequential estimators, which are powerful techniques that have been successfully applied to various orbit determination problems in the past. The classical batch estimator works by improving an initial state estimate through the processing of a set of observations all at once, allowing for a comprehensive adjustment of the satellite's orbit based on the entire dataset. In contrast, the sequential estimator, or filter, processes observations one at a time—or multiple measurements at once if available—updating the state vector incrementally at each step. Thus, the Kalman filter is a fast and efficient method well-suited for onboard and real-time applications, whereas the batch method is used where execution time and memory considerations do not pose severe restrictions (Montenbruck and Gill, 2001). As this thesis is mainly focused on data post-processing, the batch estimator is to be used.

3.2 Least-Squares Algorithm

In an environment in which GNSS observations are subject to uncertainty and redundancy, with more observations available than are strictly required to estimate the parameters of interest, the least-squares (LS) estimation algorithm is introduced. The principle for LS is to be able to solve over-determined systems, where there are redundant measurements, in a way that guarantees a unique solution. This is achieved by enforcing the criterion that the sum of the squared residuals (the differences between observed and modelled values) is minimised. Without this criterion, different subsets of inconsistent observations could lead to varying solutions, making it impossible to determine a single best-fit model.

The idea behind LS estimation is to find the state vector, composed by the satellite's trajectory and the model parameters, such that the square of the differences between the modelled observations and the actual measurements is minimised. The result is normally referred to as the trajectory which best fits the observations in a least-squares of the residuals. Additionally, a weighting factor can be applied to each observation, accounting for the fact that not all observations have the same accuracy, allowing higher-quality measurements to have a greater influence on the final solution. More information on the observation weighting is given in Section 3.2.2.

Initially, a general m-dimensional time-dependent state vector can be considered such that

$$\mathbf{x}(t) = \begin{bmatrix} \mathbf{r}(t) & \mathbf{v}(t) & \mathbf{p} & \mathbf{q} \end{bmatrix}^T \quad , \tag{3.1}$$

where $\mathbf{r}$ is the satellite's position and $\mathbf{v}$ is the velocity, $\mathbf{p}$ denotes the environmental parameters (such as atmospheric drag, solar radiation pressure, and gravitational perturbations), and $\mathbf{q}$ represents the control parameters (such as thrust, attitude control inputs, or any active manoeuvres). Model errors can also be accounted for within this framework, typically as part of the environmental or control parameters if they influence the state vector over time. The time-evolution of the state vector $x(t)$ may always be described by an ordinary differential equation of the form

$$\dot{\mathbf{x}} = \frac{\mathrm{d}\mathbf{x}}{\mathrm{d}t} = f(\mathbf{x}, t) \quad . \tag{3.2}$$

Additionally, an n-dimensional vector of measurements or observations taken at times $t_1, \ldots, t_n$ is defined as:

$$\mathbf{y}(t) = \begin{bmatrix} y_1 \\ \vdots \\ y_n \end{bmatrix} \quad . \tag{3.3}$$

In general, in order to avoid a non-unique determination of x, the number of observations n must be equal to or larger than the number of unknowns m. The observations are described by:

$$\mathbf{y} = \mathbf{h}(\mathbf{x}) + \epsilon \quad , \tag{3.4}$$

where $\mathbf{h}$ denotes the modelled value of the observations as a function of the state $\mathbf{x_0}$ at the reference epoch t_0, and ϵ are the differences between the actual and modelled observations, also known as residuals, which result from measurement errors typically assumed to be randomly distributed with a zero mean value.

Consequently, the least-squares orbit determination problem involves as finding the state $\hat{\mathbf{x}}$ that minimises the loss function $J(\mathbf{x_0})$, defined as the squared sum of the residuals ϵ for a given set of measurements y, as represented in Equation 3.5.

$$J(\mathbf{x}) = \epsilon^T \cdot \epsilon = (\mathbf{y} - \mathbf{h}(\mathbf{x}))^T \cdot (\mathbf{y} - \mathbf{h}(\mathbf{x})) \tag{3.5}$$

3.2.1 Linearisation and Normal Equations

A critical aspect of the least-squares orbit determination problem is that $\mathbf{h}$ is a highly non-linear function of the unknown state vector $\mathbf{x}$, as discussed in the various models in Section 2.3. This non-linearity makes it challenging, and in some cases impossible, to directly locate the minimum of the loss function without additional information. Typically, this additional information comes in the form of an initial estimate of the state vector at the reference epoch, as shown in Figure 3.1a. This approximate reference state vector serves as a starting point and simplifies the least-squares problem by providing a first guess for the current state, which is then refined iteratively.

To address the non-linearity, the observation equation can be linearised around the reference state $\mathbf{x_0}$ by using a Taylor series expansion, leading to the following approximation:

$$\mathbf{y} = \mathbf{h}(\mathbf{x}) + \epsilon = \mathbf{h}(\mathbf{x_0}) \quad , \tag{3.6}$$

such that when $\mathbf{x_0}$ is close to $\mathbf{x}$, then $\mathcal{O}(|\mathbf{x} - \mathbf{x_0}|^2) \approx 0$, as seen in Figure 3.1b.

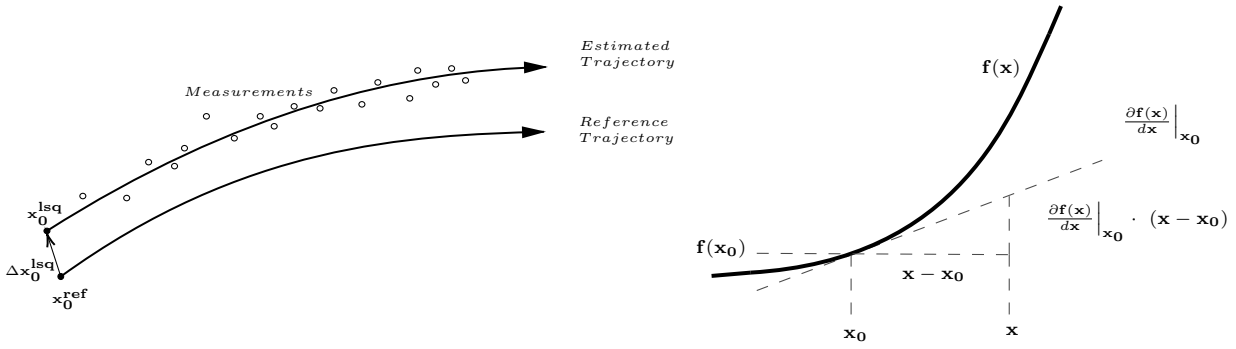

(a) Parameter correction approach to find the best estimate

(b) Linearisation process

Figure 3.1: Least-squares orbit determination

The residual vector can then be expressed by

$$\epsilon = \mathbf{y} - \mathbf{h}(\mathbf{x}) = \mathbf{y} - \mathbf{h}(\mathbf{x_0}) - \left.\frac{\partial \mathbf{h}(\mathbf{x})}{\partial \mathbf{x}}\right|_{\mathbf{x}=\mathbf{x_0}} (\mathbf{x} - \mathbf{x_0}) = \Delta\mathbf{y} - \mathbf{H}\Delta\mathbf{x} \quad , \tag{3.7}$$

where

$$\Delta\mathbf{y} = \mathbf{y} - \mathbf{h}(\mathbf{x_0}), \quad \mathbf{H} = \left.\frac{\partial \mathbf{h}(\mathbf{x})}{\partial \mathbf{x}}\right|_{\mathbf{x}=\mathbf{x_0}}, \text{ and } \quad \Delta\mathbf{x} = \mathbf{x} - \mathbf{x_0} \quad . \tag{3.8}$$

While $\Delta\mathbf{y}$ contains the difference between the actual observations and the observations predicted by the reference trajectory, $\Delta\mathbf{x}$ denotes the difference between $\mathbf{x}$ and the reference state. Additionally, $\mathbf{H}$ corresponds to the Jacobian, which gives the partial derivatives of the modelled observations with respect to the state vector $\mathbf{x}$ at the reference epoch t_i.

As a result, the linearised loss function from Equation 3.5 can be expressed as

$$J(\mathbf{x}) = (\Delta\mathbf{y} - \mathbf{H}\Delta\mathbf{x}) \cdot (\Delta\mathbf{y} - \mathbf{H}\Delta\mathbf{x}) \quad , \tag{3.9}$$

so that the predicted loss function becomes a minimum after applying the correction $\Delta\mathbf{x}$. This minimum can be uniquely determined when the partial derivatives of $J(\mathbf{x})$ with respect to $\Delta\mathbf{x}$ are null, resulting in a general solution estimate of the linearised least-squares problem which can be written as

$$\Delta\hat{\mathbf{x}} = (\mathbf{H}^T\mathbf{H})^{-1}(\mathbf{H}^T\Delta\mathbf{y}) \quad . \tag{3.10}$$

3.2.2 Observation Weighting

In practice, not all observations $\mathbf{y}$ have the same precision, so it is often beneficial to apply weights to the observations based on their estimated accuracy. The principle of *weighted least-squares* is to minimise the weighted sum of squared residuals, assigning higher weights to more accurate observations. This ensures that more reliable data has a greater influence on the final solution. The weighted least-squares solution is defined as

$$\hat{\mathbf{x}} = \arg\min_{\mathbf{x}\in\mathbb{R}^n} \left[(\Delta\mathbf{y} - \mathbf{H}\Delta\mathbf{x})^T \cdot \mathbf{W} \cdot (\Delta\mathbf{y} - \mathbf{H}\Delta\mathbf{x})\right] \quad , \tag{3.11}$$

while corresponding loss function for this minimisation problem is expressed as

$$J(\mathbf{x}) = (\Delta\mathbf{y} - \mathbf{H}\Delta\mathbf{x})^T\mathbf{W}(\Delta\mathbf{y} - \mathbf{H}\Delta\mathbf{x}) \quad , \tag{3.12}$$

where $\Delta\mathbf{y}$ is the vector of residuals between the observed and modelled values, $\Delta\mathbf{x}$ is the correction to the estimated state vector, and $\mathbf{W}$ is the weight matrix, typically defined as $\mathbf{W} = \mathbf{Q}_{\mathbf{yy}}^{-\mathbf{1}}$, where $\mathbf{Q}_{\mathbf{yy}}$ is the variance-covariance matrix of the observations.

The variance-covariance matrix of the observations, $\mathbf{Q}_{\mathbf{yy}}$, represents the uncertainties associated with each observation and is typically diagonal if the observations are uncorrelated. For example:

$$\mathbf{Q}_{\mathbf{yy}} = \begin{bmatrix} \sigma_1^2 & 0 & 0 \\ 0 & \ddots & 0 \\ 0 & 0 & \sigma_n^2 \end{bmatrix} \quad . \tag{3.13}$$

where σ_i^2 is the variance of the i-th observation. The weight matrix $\mathbf{W}$ is then given by:

$$\mathbf{W} = \mathbf{Q}_{\mathbf{yy}}^{-\mathbf{1}} = \begin{bmatrix} \sigma_1^{-2} & 0 & 0 \\ 0 & \ddots & 0 \\ 0 & 0 & \sigma_n^{-2} \end{bmatrix} \quad . \tag{3.14}$$

This formulation ensures that observations with smaller variances (higher precision) receive larger weights, thus contributing more to the final solution. The solution to the weighted least-squares problem is obtained by minimising the loss function. The weighted least-squares estimate of the correction to the state vector $\Delta\hat{\mathbf{x}}$ is:

$$\Delta\hat{\mathbf{x}} = (\mathbf{H}^T\mathbf{W}\mathbf{H})^{-1}(\mathbf{H}^T\mathbf{W}\Delta\mathbf{y}) \quad . \tag{3.15}$$

Here, the matrix $\mathbf{H}^T\mathbf{W}\mathbf{H}$ is referred to as the normal matrix:

$$\mathbf{N} = \mathbf{H}^T\mathbf{W}\mathbf{H} \quad . \tag{3.16}$$

The inverse of the normal matrix ($\mathbf{N}^{-1}$) gives the variance-covariance matrix of the estimated parameters, providing an estimate of the precision of the solution. In cases where the normal matrix is positive-definite, it is computationally more efficient to solve the normal equations:

$$\mathbf{N}\Delta\hat{\mathbf{x}} = \mathbf{H}^T\mathbf{W}\Delta\mathbf{y} \quad . \tag{3.17}$$

This system of equations can be solved using standard techniques for positive-definite systems, such as the Cholesky decomposition.

Due to the non-linear nature of the observation function $\mathbf{h}$, the linearised least-squares solution may not fully capture the true solution. In such cases, an iterative procedure is employed. The initial state vector $\mathbf{x_0}$ is updated with the newly obtained correction $\Delta\hat{\mathbf{x}}$, and the process is repeated until the change in the solution falls below a predefined tolerance:

$$\hat{\mathbf{x}} = \mathbf{x_0} + \Delta\hat{\mathbf{x}} \quad . \tag{3.18}$$

This iterative approach ensures that the solution converges to the true minimum of the loss function.

3.2.2.1 Bayesian Extension

In cases where a priori knowledge of the parameters is available, Bayesian Least Squares can be used to improve the solution. The Bayesian approach incorporates the a priori information into the least-squares framework by modifying the loss function. The modified loss function becomes:

$$J(\mathbf{x}) = (\Delta\mathbf{y} - \mathbf{H}\Delta\mathbf{x})^T\mathbf{W}(\Delta\mathbf{y} - \mathbf{H}\Delta\mathbf{x}) + (\Delta\mathbf{x} - \mathbf{x_0})^T{\mathbf{P_x}}^{-1}(\Delta\mathbf{x} - \mathbf{x_0}) \quad , \tag{3.19}$$

where $\mathbf{x_0}$ is the a priori estimate of the state vector, and $\mathbf{P_x}$ is the variance-covariance matrix of the a priori parameters. This approach balances the contribution of new observations with the prior knowledge, based on the uncertainties of both. The solution to the Bayesian least-squares problem is:

$$\Delta\hat{\mathbf{x}} = (\mathbf{H}^T\mathbf{W}\mathbf{H} + {\mathbf{P_x}}^{-1})^{-1}(\mathbf{H}^T\mathbf{W}\Delta\mathbf{y} + {\mathbf{P_x}}^{-1}\mathbf{x_0}) \quad . \tag{3.20}$$

This allows the final estimate to be influenced both by the new measurements and the prior information, making Bayesian Least Squares particularly valuable in cases where reliable a priori information is available and can improve the robustness of the solution.

3.2.3 Normal Equation Stacking and Multi-Arc Methods

Normal equation stacking and multi-arc methods are efficient approaches to estimate parameters that span multiple arcs while maintaining consistency across them. These methods allow for the estimation of both arc-specific and common parameters across different arcs, reducing computational complexity and enabling the combination of observations over long periods.

The normal equations for each arc i are written as:

$$N_i\Delta\mathbf{x}_i = \mathbf{b}_i \quad , \tag{3.21}$$

where N_i is the normal matrix for arc i, $\Delta\mathbf{x}_i$ is the correction to the parameters for the specific arc, and $\mathbf{b}_i$ is the right-hand side corresponding to the observations of arc i.

In multi-arc estimation, the parameters are divided into arc-specific parameters (such as satellite positions) and global parameters (such as station coordinates or geopotential coefficients). For each arc, both types of parameters are estimated, but the global parameters must remain consistent across all arcs. The stacked normal equations combine the information from each arc into a single system, ensuring that the common parameters are the same across all arcs.

The stacking of normal equations across multiple arcs results in a set of combined equations for the global parameters:

$$\left(\sum_{i=1}^{k} N_{i,g}\right)\Delta\mathbf{x}_g = \sum_{i=1}^{k}\mathbf{b}_{i,g} \quad , \tag{3.22}$$

where $N_{i,g}$ are the submatrices corresponding to the global parameters from each arc, and $\mathbf{b}_{i,g}$ are the corresponding right-hand sides. The global parameter updates $\Delta\mathbf{x}_g$ are obtained by solving this stacked system. Once the global parameters are updated, the arc-specific parameters can be adjusted accordingly by solving the normal equations for each arc.

This method ensures that the estimates of common parameters are consistent across all arcs, providing a more accurate and robust solution over long time spans, while reducing the computational burden typically associated with handling large datasets (European Space Agency, 2009).

This approach allows independent solutions for each GNSS constellation (e.g., GPS, Galileo, GLONASS), enabling separate processing of each constellation's data. The normal equations for these independent solutions can then be combined, making this method highly effective for MGNSS processing.

3.3 Coordinate Systems and Time

Precise and well-defined time references and coordinate frames are crucial in GNSS, where positioning results rely on signal travel time measurements. This section introduces the reader into the fundamentals of time and coordinate systems and frames, providing the necessary foundation for the subsequent chapters of this thesis.

3.3.1 Time Systems

Several time references have been created depending on the intended usage, each based on different periodic processes linked to Earth's rotation, celestial mechanics, or transitions between energy levels in atomic oscillators. Universal and sidereal times are tied to Earth's daily rotation. While Universal Time (UT) uses the Sun as a reference, Sidereal time relies on the vernal equinox, also known as Aries point. Overall, this leads to a 24-hour difference throughout a year, which translates into the sidereal day being shorter than the solar day by $3^m56.5554^s$. The reason is that for the Sun to return to the observer's meridian, Earth must rotate slightly more due to its orbital motion. Universal Time is not completely uniform, as the Earth's rotation is not uniform either due to the varying distribution of Earth's mass introducing fluctuations. The most relevant component today is UT1, determined with respect to the meridian attached to the Earth's spin axis. Historically, UT0 referred to observations with respect to the meridian fixed to the reference pole, and UT2 was a seasonal correction to UT1, but these are now largely obsolete (Teunissen and Montenbruck, 2017).

In order to achieve a more uniform time scale, the International Atomic Time (TAI, from its French name *Temps Atomique International*) was introduced. Atomic time refers to the time scale defined and realised by measuring the oscillations in the energy states of the Caesium-133 atom. However, solar time is still of interest for civilian usage and evolved into the Coordinated Universal Time (UTC). UTC is derived from atomic clocks and hydrogen masers located around after applying a set of algorithms to ensure a uniform time. In accord with the Recommendation TF.460 of the International Telecommunication Union, the UTC scale is adjusted by the insertion or deletion of seconds, known as leap seconds, to account for the accumulated drift over time between TAI and UT1, ensuring that $|UT1 - UTC| < 0.9s$. Leap seconds are determined by the International Earth Rotation and Reference Systems Service (IERS). Additionally, Terrestrial Time (TT) is a time scale established by the International Astronomical Union (IAU) to serve primarily for time measurements of astronomical observations made from the surface of Earth. Its relation with TAI is such that $TT = TAI + 32.184s$. All the relationships between atomic time scales are shown in Figure 3.2b. In terms of the SI second, the length of the mean solar day (MSD) is given by the following expression, representing the difference between UT1 and dynamic time over a period of n days. Historical records show that the length-of-day variation has been increasing by approximately 1.4 milliseconds per century. (Teunissen and Montenbruck, 2017).

$$1MSD = 86400s - \frac{\Delta\tau}{n} \qquad \text{where} \qquad \Delta\tau = UT1 - TT \quad . \tag{3.23}$$

In this equation, 1 MSD represents the length of one mean solar day, which varies slightly due to irregularities in the Earth's rotation. $\Delta\tau$ denotes the difference between UT1 and Terrestrial Time, and the correction $\frac{\Delta\tau}{n}$ accounts for the variation in the length of the mean solar day over a period of n days. The variation is shown in Figure 3.2a

To fulfill the requirements for internal timekeeping and dissemination, each GNSS system operates on a specific system time. These are GPS Time and Galileo Time (GST), which have a permanent negative offset of 19 s with respect to TAI, GLONASS Time, which is always 3 h ahead of UTC, and BeiDou Time (BDT), which has a permanent negative offset of 33 s with respect to TAI. Similarly, the QZSS and NaVIC time systems have the same offset from TAI as GPST and GST.

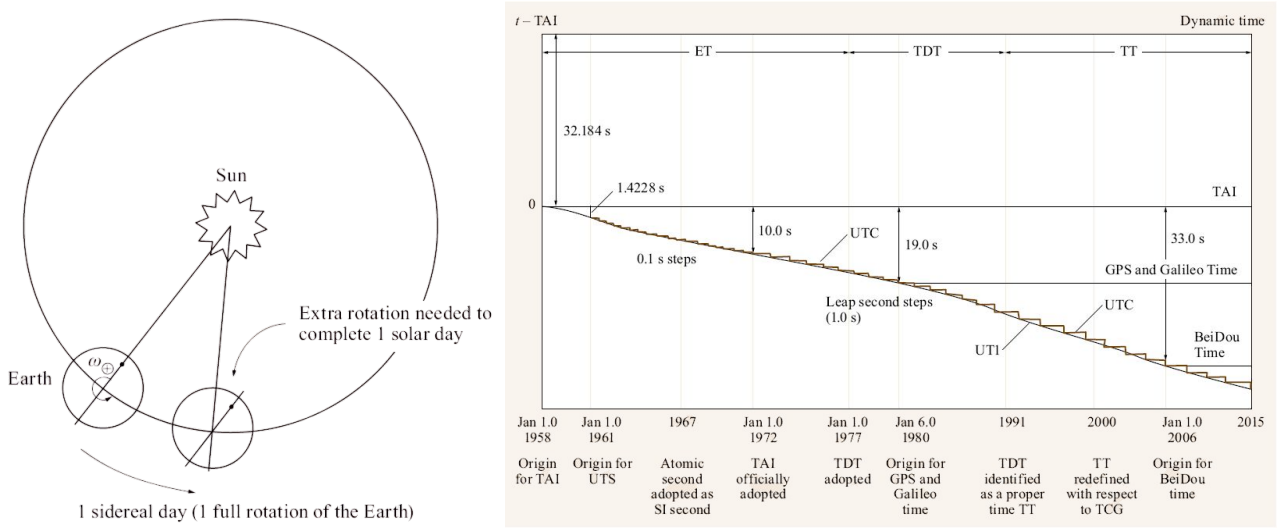

(a) Geometry of sidereal and solar days (b) Relationships between atomic time scales and dynamic time

Figure 3.2: Time Scales (Teunissen and Montenbruck, 2017)

3.3.2 Reference Systems and Frames

Accurate satellite orbit determination requires a well-defined understanding of various reference systems and frames, which provide the mathematical foundation for expressing satellite positions and velocities. These reference systems are crucial for modelling the satellite's motion relative to the Earth, space, and other celestial bodies.

3.3.2.1 Body Reference Frame

The Body Reference Frame is a local frame arbitrarily attached to the satellite or vehicle. For instance it can have its origin coinciding with the origin of the navigation frame, typically defined by the location of the Inertial Measurement Unit (IMU). The axes of this frame are aligned with the directions front, right, and down, as seen from the vehicle, and are assumed to align with the sensitive axes of the onboard sensors. This frame is essential for onboard navigation and control, allowing for precise measurements of the satellite's attitude and orientation. In addition to the Body Reference Frame, specific components attached to the spacecraft, such as antennas or instruments, may require their own local reference frames for precise alignment and pointing. The Antenna Reference Frame, for instance, is defined for these components to ensure accurate orientation relative to both the satellite body and external targets, supporting optimal communication and data collection capabilities.

For example, the axes of the Galileo FOC body-fixed coordinate system, as shown in Figure 3.3, are defined so that the origin is located in the geometrical centre of the dispenser mounting plane on the access panel ($-Z_B$ side). Due to the yaw steering motion, the Sun direction moves in the $X_B - Z_B$ plane of the spacecraft. Thus, Sun incidence on both Y_B-panels and on the $+X_B$-panel is avoided.

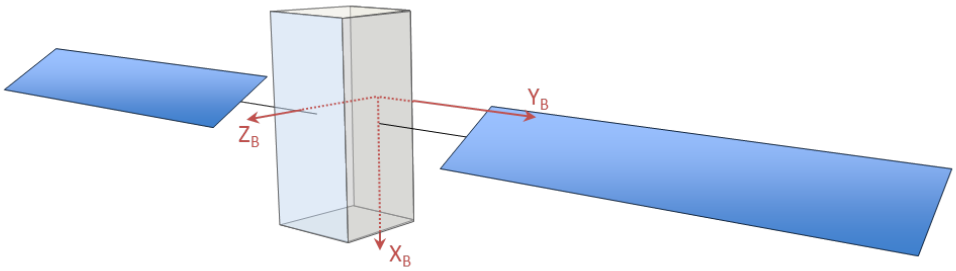

Figure 3.3: Galileo FOC body-fixed coordinate system

3.3.2.2 Celestial Reference System

The Celestial Reference System is a quasi-inertial system where the laws of physics, as described by general relativity, apply without needing to account for rotations over short periods of time. Depending on the system reference origin, the IAU defined the Barycentric Celestial Reference System (BCRS) and the Geocentric Celestial Reference System (GCRS), also known as Earth-Centred Inertial. The BCRS is a global reference system with its origin in the barycenter of the solar system, making it suitable for solving equations of motion for solar system bodies as well as other galactic and extra-galactic objects. Conversely, the GCCRS serves as a local reference system for Earth-based measurements and solving motion equations for bodies in the near-Earth environment (Kaplan, 2006). Thus, the GCRS will be of interest for terrestrial GNSS purposes.

The practical implementation of GCRS is called the Geocentric Celestial Reference Frame, which is determined from precise coordinates of extragalactic radio sources, such as quasars, unlike previous definitions of the frame axes which relied on the equinox and equator (Charlot et al., 2020). The IERS officially established the International Celestial Reference System (ICRS) based on a set of defining sources, which also serve as the realisation of the system, the International Celestial Reference Frame (ICRF).

3.3.2.3 Terrestrial Reference Frame

The Terrestrial Reference Frame, also known as Earth-Centered, Earth-Fixed (ECEF), is a rotating reference system with its origin at the Earth's centre of mass. The International Terrestrial Reference System (ITRS) is defined as a geocentric coordinate system, oriented by the directions of the International Reference Pole (IRP) and the reference meridian as established by the *Bureau International de l'Heure* (BIH) in 1984. The practical realization of the ITRS is the International Terrestrial Reference Frame (ITRF), which involves the determination of three origin parameters, three orientation parameters, and a scale parameter to align with actual geophysical measurements.

3.3.3 Earth Orientation Parameters

The Earth Orientation Parameters (EOPs) are crucial for understanding how Earth's orientation and rotation change over time. These parameters are necessary for making precise transformations between the International Celestial Reference Frame and the International Terrestrial Reference Frame. The key EOPs include UT1-UTC, the Length of Day, pole coordinates and their rates, and celestial pole offsets.

Closely related to UT1-UTC, previously explained in Section 3.3.1, is the Length of Day offset, which measures variations in the actual length of a day compared to the standard 86,400 seconds. LOD fluctuations arise from changes in the Earth's rotational speed, caused by atmospheric winds, ocean currents, and interactions between the Earth's core and mantle. These variations directly affect UT1-UTC and are expressed in milliseconds. LOD monitoring helps maintain synchronisation between Earth's rotation and atomic time, which is critical for high-precision applications in satellite navigation and astronomical observations.

Pole coordinates, denoted as x_p and y_p, describe the position of the Earth's rotational axis in the ITRF. These coordinates, expressed in arcseconds, track the gradual movement of the rotational pole due to factors like mantle convection and external gravitational forces from the Moon and Sun. Polar motion is characterised by two components: the Chandler wobble (a small, circular oscillation with a period of approximately 433 days) and an annual motion due to seasonal variations. Additionally, the pole coordinate rates, denoted $\dot{x}_p$ and $\dot{y}_p$, describe how the pole coordinates change over time, expressed in arcseconds per day. These rates provide insights into how quickly the Earth's rotational axis is shifting, which is vital for predicting future pole positions.

Celestial pole offsets, represented as dX and dY, refer to deviations in the position of the Celestial Intermediate Pole (CIP) relative to its predicted position, based on the precession-nutation models. These offsets, expressed in arcseconds, arise due to the limitations in the accuracy of models that predict the Earth's long-term orientation changes. These celestial pole offsets ensure the correct alignment between the celestial and terrestrial reference frames by accounting for deviations that would otherwise lead to positioning errors.

3.3.3.1 Transformation between ICRF and ITRF

The transformation between the ICRF and ITRF, accounting for the Earth's orientation and rotation, can be expressed as:

$$\vec{r}_{ITRS} = Q(t) \cdot R(t) \cdot W(t) \cdot \vec{r}_{GCRS} = Q(dX, dY, s) \cdot R(ERA) \cdot W(x_p, y_p, s') \cdot \vec{r}_{GCRS} \quad . \tag{3.24}$$

where $Q(t)$ accounts for the motion of the celestial pole in the ICRF, $R(t)$ describes the Earth's rotation around the axis associated with the pole (related to UT1-UTC and LOD), and $W(t)$ corrects for polar motion based on the pole coordinates x_p and y_p. Additionally, while maintaining the magnitudes such that $||\vec{r}_{ITRS}|| = ||\vec{r}_{GCRS}||$. These transformations ensure that satellite positioning and geodetic systems are properly synchronised with the Earth's dynamic rotation and orientation based on the resolutions and recommendations by Petit and Luzum (2010). The transformation matrix related to polar motion is given by

$$W(t) = R_3(-s') \cdot R_2(x_p) \cdot R_1(y_p) \quad , \tag{3.25}$$

where the Terrestrial Intermediate Origin locator s' accounts for a small correction in the Earth's orientation and is a function of the pole coordinates (x_p, y_p) and their time derivatives, which can be computed as

$$s'(t) = \frac{1}{2} \int_{t_0}^{t} (x_p \dot{y}_p - \dot{x}_p y_p) dt \quad . \tag{3.26}$$

The transformation matrix arising from the Earth's rotation around the axis of the Celestial Intermediate Pole can be expressed as:

$$R(t) = R_3(-ERA) \tag{3.27}$$

where ERA is the Earth Rotation Angle, typically defined in radians. ERA corresponds to sidereal time, which is related to the mean solar time UT1 by a simple linear relation. For this reason, UT1 is often reported instead of ERA.

Finally, the transformation matrix arising from the motion of the CIP in the GCRS can be expressed as:

$$Q(t) = R_3(-E) \cdot R_2(-d) \cdot R_3(E) \cdot R_3(s) \quad , \tag{3.28}$$

where E and d are the longitude and latitude of the CIP, respectively, in the celestial frame. The celestial pole offsets, dX and dY, represent corrections to the predicted motion of the CIP based on precession-nutation models. These offsets adjust the position of the CIP by shifting the theoretical longitude and latitude values such that:

$$E' = E + dX, \quad d' = d + dY \quad . \tag{3.29}$$

These corrected values are then incorporated into $Q(t)$ to account for the deviations in the CIP's actual position, ensuring accurate alignment between the celestial and terrestrial reference frames. The coordinates of the CIP in the Geocentric Celestial Reference System are:

$$X = \sin(d) \cdot \cos(E), \qquad Y = \sin(d) \cdot \sin(E), \qquad Z = \cos(d) \quad . \tag{3.30}$$

The Celestial Intermediate Origin (CIO) locator s is a function of the coordinates X and Y, and is computed as:

$$s(t) = -\int_{t_0}^{t} \frac{X(t)\dot{Y}(t) - Y(t)\dot{X}(t)}{1 + Z(t)} dt - (\sigma_0 N_0 - \Sigma_0 N_0) \quad , \tag{3.31}$$

where σ_0 and Σ_0 represent the positions of the CIO at J2000, and N_0 denotes the ascending node of the equator at J2000 in the equator of the GCRS.

3.4 Orbital Perturbations

Keplerian orbits are the closed-form solutions of the two-body problem, which addresses the motion of two point-masses influenced solely by their mutual gravitational attraction. This assumption requires the bodies of the satellite m and attracting body $M_{\oplus}$, in this case the Earth, to be spherically symmetrical, with uniform density. Any factor that causes the motion of a celestial body to deviate from its idealised Keplerian path is considered a perturbation. As a result, the motion of a perturbed body can be written as (Curtis, 2013):

$$\ddot{\vec{r}} + \mu \frac{\vec{r}}{r^3} = \frac{\sum \vec{F}_{perturbation}}{m} \quad , \tag{3.32}$$

where μ is called the Gravitational Parameter and defined as $\mu = G \cdot (M_{\oplus} + m)$, for which G corresponds to the universal gravitational constant.

These perturbing forces, which generally depend on the satellite's position, velocity, and time, influence the satellite's motion in complex ways.. The main natural disturbances are the result of a complex mass distribution of the attracting body which varies under the influence of tidal deformations, additional celestial bodies such as the Sun and the Moon exerting gravitational forces, radiation pressure impacting the satellite, and atmospheric drag dissipating orbit energy for low-altitude orbits, among others. Additionally, the most common artificial perturbation is caused by propulsive thrust, which can be used for orbit maintenance and manoeuvring as well as attitude control. Figure 3.4 shows the order of magnitude of various perturbations of a satellite in several GNSS orbit heights.

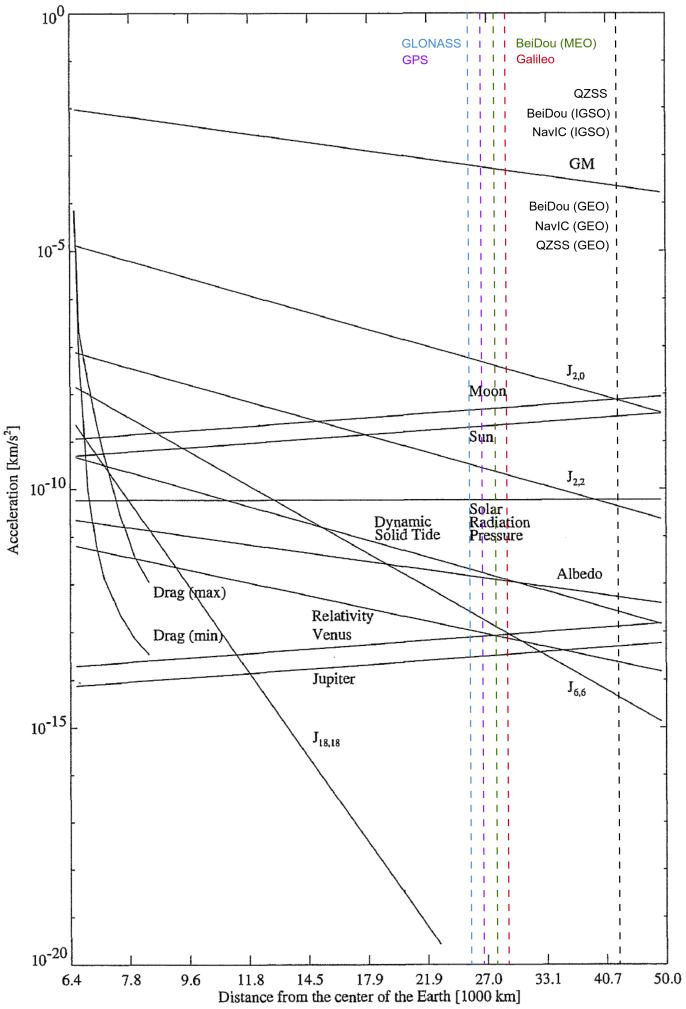

Figure 3.4: Order of magnitude of various perturbations of a satellite in a GNSS orbit. Modified from Montenbruck and Gill, 2001.

3.5 Gravitational Perturbations

This section focuses on the perturbative forces that deviate satellite motion from ideal Keplerian orbits. These perturbations arise from Earth's irregular shape and mass distribution, the gravitational effects of external bodies, temporal changes in Earth's mass, and relativistic influences. A comprehensive understanding of these factors is essential for precise orbit determination and satellite navigation accuracy.

3.5.1 Earth's Gravitational Potential

The ideal Keplerian orbits assume perfectly spherical, homogeneous central bodies. However, Earth is a celestial body characterised as an asymmetric spheroid, bulging at the equator, flattened at the poles, and with additional mass distribution variations. Earth's gravitational acceleration may be described by the gradient $\nabla U(\vec{r})$ of the gravitational potential $U(\vec{r})$ which can be represented in terms of a spherical harmonic series in the form

$$U(\vec{r}) = \frac{\mu}{r} \cdot \sum_{n=0}^{\infty} \sum_{m=0}^{n} \left(\frac{R}{r}\right)^n P_{nm}(sin\phi)(C_{nm} \cdot cos(m\lambda) + S_{nm} \cdot sin(m\lambda)) \quad , \tag{3.33}$$

where r, λ, and ϕ represent the spherical coordinates (radius, geocentric longitude, and latitude) of the position $\vec{r}$ in the Earth-fixed reference frame, R is the equatorial radius of the Earth, P_{nm} stands for the associated Legendre polynomials of degree n and order m, and C_{nm} and S_{nm} are tknown as Stokes coefficients.

The Navigation Support Office relies on a GNSS processing strategy based on a gravity field of degree and order $n = m = 12$. The Stokes coefficients are selected from the EIGEN-GRGS.RL04 gravity field model (Lemoine et al., 2021), a high-resolution global gravity field model which includes GOCE, GRACE and SLR data. While satellites in Low Earth Orbit (LEO) might use a gravity field model with a higher degree and order, perturbations from potential terms above degree 12 cause accelerations smaller than 10^{-11} m/s^2 at GNSS altitudes. These perturbations result in orbit errors at the sub-millimetre level, which can be safely neglected compared to other dominant perturbations (Teunissen and Montenbruck, 2017). More information on the gravitational models used can be found in Section 4.2.7

3.5.2 Third-body Effects

An artificial satellite orbiting Earth is also influenced by the gravitational attraction of the Sun, the Moon, and, to a lesser extent, the planets and other bodies in the Solar System. Assuming that all celestial bodies are point masses, the perturbing force contribution to the equations of motion can be described as:

$$\vec{f}_{3B} = \sum_{j=1}^{n_p} \mu_j \left(\frac{\vec{r}_j - \vec{r}}{||\vec{r}_j - \vec{r}||^3} - \frac{\vec{r}_j}{||\vec{r}_j||^3} \right) \quad , \tag{3.34}$$

where n_p represents the number of additional bodies, j represents a specific body, $\mu_J = G{\cdot}M_J$ is the gravitational parameter of body j, $\vec{r}_j$ is the geocentric position vector of this body, and $\vec{r}$ is the geocentric position vector of the perturbed satellite.

As the perturbing accelerations are represented in the geocentric frame, which is not inertial but accelerated due to the influence of additional perturbing celestial bodies, the second term in Equation 3.34 is necessary. This term represents the perturbing acceleration of third bodies, also known as direct tides, which accounts for the negative perturbing acceleration of the celestial body acting on the Earth.

The Navigation Support Office relies on the Jet Propulsion Laboratory Development Ephemeris 405 (JPL DE405), which include both nutations and librations referred to the International Celestial Reference Frame for all Solar System planets, the Sun, and the Moon as point masses. For modelling the lunar gravity, in addition, also its own J2 effect is considered.

3.5.2.1 Mass Distribution Temporal Changes

For perfectly rigid bodies, the mass distribution remains constant over time in a coordinate system fixed within the body. However, the Earth is not rigid, and the luni-solar gravitational forces induce tidal deformations that redistribute mass in both the solid Earth and the oceans. These mass redistributions result in variations in the Earth's mass property coefficients over time and are referred to as solid Earth tides and ocean tides.

To account for these effects, ocean tide models, such as hydrodynamic finite element models or models derived from satellite altimetry observations, are employed. Specifically, the NSO relies on the EOT11a model, a Global Empirical Ocean Tide model derived in 2011 by residual analysis of multi-mission satellite altimeter data. This model captures tidal variations in the Earth's oceans, including two annual and two semi-annual coefficients, and plays a key role in compensating for the time-variable nature of the mass distribution caused by ocean tides. In addition to ocean tides, the solid Earth tide contributes to these temporal variations. The deformation of the Earth's crust, caused by gravitational forces, shifts the mass within the solid Earth, altering its gravitational potential and introducing time-variable perturbations to the gravity field.

Furthermore, the asymmetry in the Earth's mass distribution resulting from these tidal effects leads to the precession and nutation of the Earth's rotation axis, which causes pole tides. Both solid Earth pole tides and ocean pole tides are modelled according to the IERS 2010 conventions. These pole tides capture the oscillations in the Earth's rotational axis as it shifts relative to the geographic poles. The EIGEN-GRGS.RL04 gravity field model incorporates time-variable gravity content, primarily driven by the redistribution of mass within the Earth system. This includes contributions from hydrology (such as water storage changes in river basins and ice sheets) in addition to tides. The model includes coefficients up to degree and order 90, with bias and trend terms accounting for longer-term variations. However, the temporal validity of this model is limited to the period covered by its underlying data, meaning its use must be contextualised within this timeframe.

By combining these models, it is possible to account for the complex interactions between solid Earth, ocean tides, and pole tides in gravity field modelling, thus improving the accuracy of satellite orbit determination.

3.5.2.2 Relativistic effects

As the equation of motion Equation 3.32 is formulated in Euclidean space, relativistic corrections are needed as perturbing accelerations to account for the curvature of space-time. These are the Schwarzschild effect, the Lense-Thirring effect, and the de-Sitter effect. The Schwarzschild term describes the main relativistic effects, which represent the space curvature caused by the mass of the Earth. For LEO satellites, this effect is on the order of $2 \cdot 10^{-8}\,\mathrm{m/s^2}$, while for geosynchronous orbits, it reaches $7 \cdot 10^{-11}\,\mathrm{m/s^2}$, resulting in a secular shift in the argument of perigee for GNSS satellites (Teunissen and Montenbruck, 2017). The Lense-Thirring effect, also known as the frame-dragging effect, causes a precession of the reference frame and is modelled by Coriolis accelerations. This effect is caused by Earth's rotation, with an impact on the order of $4 \cdot 10^{-13}\,\mathrm{m/s^2}$ for GEO satellites. Finally, the de-Sitter term causes a precession of the geocentric reference frame relative to the fixed stars due to the space-time curvature induced by the Sun's mass as Earth orbits the Sun.(Teunissen and Montenbruck, 2017).

3.6 Non-Gravitational Perturbations

In addition to the gravitational perturbations discussed in the previous section, the motion of satellites is also influenced by non-gravitational forces, also known as surface forces, because they act on the surface of the satellite body instead of its mass. They are the result of the interaction of particles or radiation with the satellite, either by atoms and ions causing drag forces or by photons transferring momentum to the satellite.

Atmospheric drag acceleration is caused by atmospheric particles at satellite orbit height and is proportional to the air mass density. However, as seen in Figure 3.4, air drag is irrelevant for GNSS satellite orbits. In comparison, solar radiation pressure maintains almost the same acceleration effects for any orbit, slightly increasing for higher orbits.

3.6.1 Solar Radiation Pressure

Solar radiation pressure (SRP) is the largest non-gravitational perturbation acting on GNSS satellites. It is produced by the photons impacting the surface of the satellite, which results in a momentum transfer. The effect mainly depends on the satellite geometry, the area-to-mass ratio, the reflective properties, the attitude, and the eclipse factor of the orbit, which accounts for periods when the satellite passes through the Earth's shadow, reducing or eliminating the SRP force.

Compared to gravitational perturbations, SRP is significantly more challenging to model due to the lack of publicly available information about satellite geometry and surface properties. Consequently, two main classes of GNSS radiation pressure models exist: physical models derived from satellite surface properties, and empirical models based on orbit analysis. Physical radiation pressure models provide the perturbing acceleration vector for a given satellite orientation using mathematical formulations that approximate the accelerations based on detailed space vehicle models. These models may also include an adjustable scale factor to account for uncertainties or missing details about the satellite's surface properties, which can be estimated during orbit determination. Empirical radiation pressure models, on the other hand, include parameters that are adjusted during the orbit determination process to best fit the observed satellite motion. One of the most widely used empirical models is the Empirical CODE Orbit Model (ECOM), which is employed by the International GNSS Service, NSO, and other organisations for GNSS satellite orbit determination. Both physical and empirical radiation pressure models are explained in more detail in the following subsections.

3.6.1.1 Analytical Cannonball SRP Model

In its simplest form, solar radiation pressure can be modelled using a cannonball geometry for the satellite, resulting in the following equation for the acceleration:

$$\ddot{\vec{r}} = -\eta C_R \frac{A}{m} P_\odot \left(\frac{1AU}{||\vec{r_\odot}||} \right)^2 \frac{\vec{r_\odot} - \vec{r}}{||\vec{r_\odot} - \vec{r}||} \quad , \tag{3.35}$$

where η is the shadow function that models the illumination conditions, varying between one in full sunlight and zero in total eclipse (umbra), with intermediate values when the satellite is in penumbra. C_R is the radiation pressure coefficient, which depends on the satellite's reflectivity; A/m is the surface-to-mass ratio; $P_\odot$ is the solar flux at a mean distance of 1 Astronomical Unit, $||\vec{r_\odot}||$ is the geocentric position vector of the Sun, and $\vec{r_\odot} - \vec{r}$ is the vector from the satellite to the Sun (Teunissen and Montenbruck, 2017).

3.6.1.2 Analytical Box-Wing SRP Model

While the cannonball model provides a simple approach, real spacecraft are usually designed with more complex geometries that deviate significantly from the spherical shape. For GNSS satellites, a more accurate approximation is the Box-Wing Model, which represents the satellite's main structure as a rectangular box with two large solar panels attached, free to rotate to optimise exposure to sunlight. This model requires detailed knowledge of the surface area, material properties, and orientation of each component relative to the Sun to accurately compute the non-gravitational forces. The interaction of incoming solar radiation with a surface depends on its optical properties, determining whether the radiation is absorbed, specularly reflected, or diffusely reflected. Under the assumption of zero surface transmissivity, all incident radiation is either absorbed or reflected. The fraction of the radiation that is absorbed is denoted by α, while the specularly and diffusely reflected fractions are represented by ρ and δ, respectively. These fractions are also referred to as the absorption, reflection, and diffusion coefficients, and are related by the equation $\alpha + \rho + \delta = 1$.

For modelling SRP, the main focus is on the visible (optical) band, as the Sun emits most of its energy in this spectrum. Therefore, the visible absorption α_{vis}, specular reflection ρ_{vis}, and diffuse reflection δ_{vis} coefficients are used for SRP calculations. For each satellite surface i, the resulting acceleration due to the absorbed, specularly reflected, and diffusely reflected solar radiation is:

$$\ddot{\vec{r}}_{\alpha_i} = \alpha_{vis_i} \cdot C_{R_i} \vec{e}_{sat,\odot} \tag{3.36}$$

$$\ddot{\vec{r}}_{\rho_i} = \rho_{vis_i} \cdot 2\cos\theta_i C_{R_i} \vec{e}_{n_i} \tag{3.37}$$

$$\ddot{\vec{r}}_{\delta_i} = \delta_{vis_i} \cdot C_{R_i} \left(\vec{e}_{sat,\odot} + \frac{2}{3} \vec{e}_{n_i} \right) \quad , \tag{3.38}$$

with $\vec{e}_{sat,\odot} = \frac{\vec{r_\odot} - \vec{r}}{||\vec{r_\odot} - \vec{r}||}$ being the unit vector pointing from the satellite to the Sun, e_{n_i} as the unit vector perpendicular to the satellite's surface i, and θ is the angle between the incident radiation and the normal to the surface i. The radiation pressure coefficient for each surface C_{R_i} is given by:

$$C_{R_i} = -\frac{AU^2}{|r_\odot - r_{sat}|^2} \cdot P_\odot \frac{A_i}{m} \quad . \tag{3.39}$$

Additionally, for a cylindrical surface, the equations can be modified to become:

$$\ddot{\vec{r}}_{\alpha_i} = \alpha_{vis_i} \cdot C_{R_i} \vec{e}_{sat,\odot} \tag{3.40}$$

$$\ddot{\vec{r}}_{\rho_i} = \rho_{vis_i} \cdot \frac{4}{3} \cos\theta_i C_{R_i} \vec{e}_{n_i} \tag{3.41}$$

$$\ddot{\vec{r}}_{\delta_i} = \delta_{vis_i} \cdot C_{R_i} \left(\vec{e}_{sat,\odot} + \frac{\pi}{6} \vec{e}_{n_i} \right) \quad . \tag{3.42}$$

Finally, the total perturbing acceleration due to SRP is the sum over all satellite surfaces:

$$\ddot{\vec{r}}_{SRP} = \sum_{i=1}^{m} \ddot{\vec{r}}_{SRP_i} \quad , \tag{3.43}$$

where m is the number of satellite surfaces considered. For GNSS satellites, the Box-Wing Model is often used with multiple surfaces (+X, -X, +Y, -Y, +Z, -Z, +SA, -SA) to better approximate the spacecraft's interaction with solar radiation. The nominal spacecraft attitude typically aligns the Z-axis toward the Earth, and the remaining axes align with the corresponding satellite surfaces, allowing SRP to be modelled effectively in the GCRS.

For further detail, it can be considered that, over time, spacecraft materials degrade due to exposure to ultraviolet radiation and atomic oxygen, causing changes in the optical properties. The optical coefficients, therefore, evolve from their beginning-of-life (bol) to end-of-life (eol) values over the mission duration T, and this can be interpolated using the equation:

$$\alpha_t = \alpha_{bol} + \frac{\alpha_{eol} - \alpha_{bol}}{\ln(T+1)} \ln(t+1) \quad . \tag{3.44}$$

3.6.1.3 Analytical Box-Wing TRP Model

For solar panels, most absorbed solar radiation is conducted away, but for the spacecraft bus, the energy is diffusely reradiated as heat. This instantaneous thermal reradiation pressure (TRP) can be modelled by adding an acceleration along the surface normal to the solar radiation pressure model:

$$\ddot{\vec{r}}_{TRP} = \alpha_{vis_i} \cdot \frac{2}{3} C_{R_i} \vec{e}_{n_i} \quad . \tag{3.45}$$

However, thermal reradiation is not an instantaneous effect but changes very slowly. This means that there is some form of phase lag between SRP and TRP, also known as thermal inertia. Thus, if the temperature and emissivity of the radiating spacecraft surface i are known, the force from thermal reradiation can be more accurately computed as:

$$\vec{f}_{TRP_i} = -\frac{2 \cdot \sigma \cdot \epsilon_i \cdot A_i \cdot T_i^4}{3 \cdot c} \vec{e}_{n_i} \quad . \tag{3.46}$$

where σ is the Stefan-Boltzmann constant, ϵ_i is the emissivity, A_i is the surface area, T_i is the temperature, and c is the speed of light.

3.6.1.4 Reduced Empirical CODE Orbit Model (ECOM1)

The reduced Empirical CODE Orbit Model (ECOM1) developed by Springer et al. (1999) has become a quasi-standard for SRP modelling of GNSS satellites within and outside the IGS community. ECOM1 is a five-parameter model that estimates accelerations in a Sun-oriented reference frame. This frame includes three constant accelerations: one along the direct line from the spacecraft to the Sun (denoted by the D-axis), one along the spacecraft's Y-axis around which the solar panels rotate (denoted by the Y-axis), and one along a third axis (denoted by the B-axis), which is perpendicular to both D and Y, forming a right-handed coordinate system. Figure 3.5 shows the reference frame illustrating the orientation of the D, Y, and B axes. Additionally, once-per-orbit sine and cosine terms are estimated in the B-direction to accommodate unmodelled accelerations.

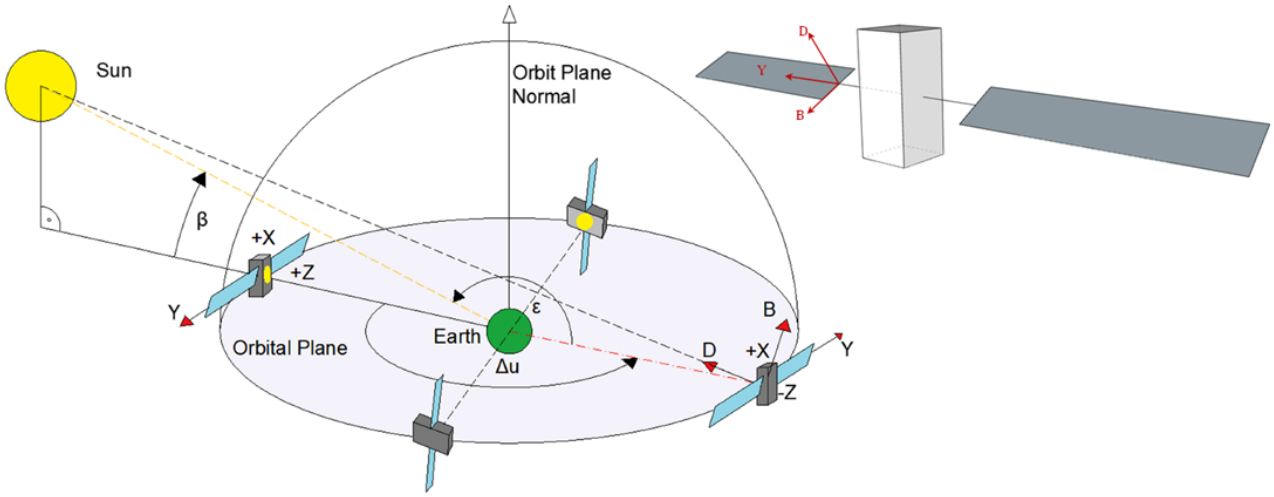

Figure 3.5: Sun-oriented DYB reference frame. Modified from Bury et al. (2020)

The accelerations in ECOM1 can be expressed as:

$$D(\Delta u) = D_0 \tag{3.47}$$
$$Y(\Delta u) = Y_0 \tag{3.48}$$
$$B(\Delta u) = B_0 + B_C \cdot \cos(\Delta u) + B_S \cdot \sin(\Delta u) \quad , \tag{3.49}$$

where D_0, Y_0, and B_0 are the constant accelerations in the D, Y, and B directions, respectively. The terms B_C and B_S represent the once-per-orbit cosine and sine terms in the B-axis, and the variable Δu represents the orbit angle measured between the projected Earth-Sun line and the satellite's position in the orbit plane.

The total acceleration due to SRP in ECOM1 is then expressed as:

$$\vec{\ddot{r}} = \vec{\ddot{r}}_0 + D(\Delta u) \cdot \vec{e}_D + Y(\Delta u) \cdot \vec{e}_Y + B(\Delta u) \cdot \vec{e}_B \quad , \tag{3.50}$$

where $\vec{\ddot{r}}_0$ is the acceleration from an a priori model, if such a model is available and used.

3.6.1.5 Extended Empirical CODE Orbit Model (ECOM2)

The extended Empirical CODE Orbit Model (ECOM2) was introduced by Arnold et al. (2015) to improve SRP modelling, particularly for satellites with non-cubic shapes, such as Galileo, QZSS, and GLONASS. While ECOM1 is effective for many GNSS satellites, the assumption of constant accelerations in the D, Y, and B directions does not always account for the varying cross-section of satellites relative to the Sun. ECOM2 extends the original five-parameter model by introducing additional harmonics in the D-direction to better account for these variations.

The ECOM2 model adds second- and fourth-order harmonic terms in the D-axis:

$$D(\Delta u) = D_0 + D_{2,C} \cdot \cos(2\Delta u) + D_{2,S} \cdot \sin(2\Delta u) + D_{4,C} \cdot \cos(4\Delta u) + D_{4,S} \cdot \sin(4\Delta u) \tag{3.51}$$

$$Y(\Delta u) = Y_0 \tag{3.52}$$

$$B(\Delta u) = B_0 + B_C \cdot \cos(\Delta u) + B_S \cdot \sin(\Delta u) \quad . \tag{3.53}$$

In this extended model, the additional terms $D_{2,C}$, $D_{2,S}$, $D_{4,C}$, and $D_{4,S}$ represent the second- and fourth-order harmonics in the D-axis. These harmonics allow for a more accurate representation of SRP for satellites with a complex geometry, by accounting for the varying cross-section as the satellite moves through its orbit.

The total acceleration due to SRP in ECOM2 is written following the same pattern as in Equation 3.50. Using the nine-parameter ECOM2 instead of ECOM1 has shown significant improvements in several areas, such as radial orbit accuracy, better agreement with SLR (Satellite Laser Ranging) measurements, smaller satellite clock residuals, and a tighter distribution of narrow-lane fractionals. However, the benefits are more pronounced for satellites with non-cubic shapes (e.g., Galileo, QZSS, and GLONASS) and only when no a priori model is available to describe the SRP force with sufficient accuracy. In case no a priori model is used, the ECOM model captures the entire SRP accelerations, instead of a correction to the a priori model. However, using an a priori model can reduce the number of estimated parameters and improves the accuracy, particularly for well-characterized satellites.

3.6.1.6 Empirical ROCK Orbit Model

Special solar radiation pressure models were developed for GPS satellites by Rockwell International, taking into account the spacecraft's material properties. These models became known as the GPS ROCK-models (European Space Agency, 2009). Following a development similar to JPL's GSPM approach, the modified Empirical ROCK Orbit Model, introduced by Dilssner and Springer (2024b), generalises empirical radiation pressure models for GNSS satellites, including solar radiation pressure, Earth radiation pressure, thermal re-radiation, and antenna thrust forces. The model uses Fourier series expansions to efficiently capture non-gravitational perturbations, making it suitable for multi-GNSS processing without needing detailed satellite metadata, such as geometry or surface properties.

The ROCK model defines perturbing accelerations as a truncated harmonic series in a satellite-centred frame, with accelerations parametrised in the X, Y, and Z directions based on the Sun-satellite geometry, as shown in Figure 3.6. For Galileo satellites, the model employs 11 parameters for groups of satellites, estimated from one year of daily GNSS orbits through CODE MGEX processing. However, these coefficients are currently determined for each individual satellite, and not generalised per block, allowing only to use the satellites available on the specific processing year when propagating forwards or backwards in time.

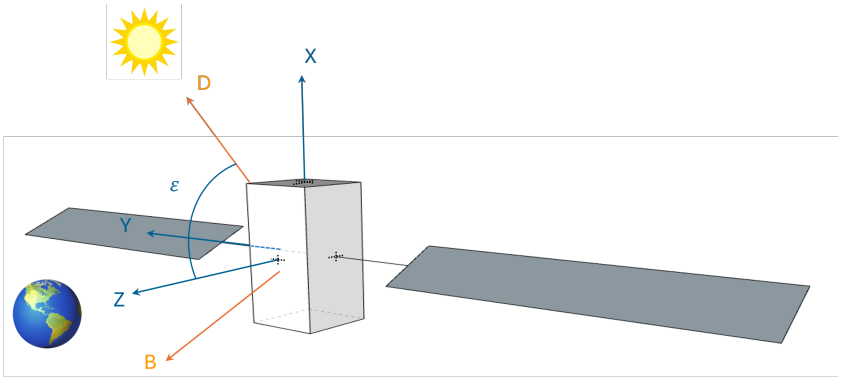

Figure 3.6: Overlap of Sun-fixed (DYB) and spacecraft-fixed (XYZ) reference frames. Modified from Dilssner and Springer (2024b).

The accelerations for Galileo satellites are expressed as follows:

$$X(\varepsilon) = X_{S1} \cdot \sin(\varepsilon) + X_{S2} \cdot |\sin(2\varepsilon)| + X_{S3} \cdot \sin(3\varepsilon) + X_{S4} \cdot \sin(4\varepsilon) \tag{3.54}$$

$$Y(\varepsilon) = Y_0 + Y_{S1} \cdot \sin(\varepsilon) + Y_{C1} \cdot \cos(\varepsilon) \tag{3.55}$$

$$Z(\varepsilon) = Z_0 + Z_{C1} \cdot \cos(\varepsilon) + Z_{S2} \cdot \sin(2\varepsilon) + Z_{S4} \cdot \sin(4\varepsilon) \quad , \tag{3.56}$$

where X_{S1}, X_{S2}, X_{S3}, Y_0, Y_{S1}, Y_{C1}, Z_0, Z_{C1} and Z_{S2} are the empirical ROCK coefficients, and ε is the Sun-satellite angle, or Sun-elongation.

For other GNSS constellations, the model is slightly extended to include a 12-parameter satellite-specific version, adding a fifth-order sine term in the X-direction:

$$X(\varepsilon) = X_{S1} \cdot \sin(\varepsilon) + X_{S2} \cdot \sin(2\varepsilon) + X_{S3} \cdot \sin(3\varepsilon) + X_{S4} \cdot \sin(4\varepsilon) + X_{S5} \cdot \sin(5\varepsilon) \tag{3.57}$$

$$Y(\varepsilon) = Y_0 + Y_{S1} \cdot \sin(\varepsilon) + Y_{C1} \cdot \cos(\varepsilon) \tag{3.58}$$

$$Z(\varepsilon) = Z_0 + Z_{C1} \cdot \cos(\varepsilon) + Z_{S2} \cdot \sin(2\varepsilon) + Z_{S4} \cdot \sin(4\varepsilon) \quad . \tag{3.59}$$

Here, X_{S1} through X_{S5} represent additional harmonic terms in the X-direction to account for the varying cross-section of the satellite relative to the Sun. The ROCK model's flexibility makes it applicable to different GNSS constellations without needing an a priori model, with the parameters adjusted iteratively from observational data. The force in the Y-direction, which has a thermal origin, applies both inside and outside eclipse periods.

3.6.2 Earth Albedo and Infrared Radiation Pressure

Satellites in orbit around Earth are subject to non-gravitational forces from Earth Albedo Radiation Pressure (EARP) and Earth Infrared Radiation Pressure (EIRP). These forces arise from solar radiation that is either reflected by the Earth's surface and atmosphere or absorbed and later re-emitted as thermal radiation. Although these effects are generally smaller than solar radiation pressure, they still contribute perturbations to the satellite's orbit and must be accounted for in precise orbit determination.

3.6.2.1 Earth Albedo Radiation Pressure

Earth albedo radiation pressure refers to the force exerted on a satellite by the fraction of solar radiation reflected by the Earth's surface and atmosphere. Modelling EARP is complex due to the variability of Earth's surface properties, including land and ocean reflectivity, cloud cover, and atmospheric conditions.

A simplified approach assumes a spherical Earth divided into $n \times m$ surface elements, each with equal area. The reflected radiation from each element is modelled using Lambert's law for diffuse reflection, where the re-radiated energy is proportional to the surface area and the Sun's zenith angle with respect to that element. For each flat satellite surface i the perturbing acceleration acting on the satellite and caused by the EARP of a surface element ds may be written in an analogous way as to the equations developed for the solar radiation pressure:

$$\ddot{\vec{r}}_{EARP_i} = C_{EARP_i} \left[(\alpha_{vis_i} + \delta_{vis_i}) \vec{e}_{sat,ds} + \left(2\rho_{vis_i} \cos\theta_i + \frac{2}{3}\delta_{vis_i} \right) \vec{e}_{n_i} \right] \quad , \tag{3.60}$$

where C_{EARP_i} represents the Earth albedo radiation pressure coefficient for each surface element, $\vec{e}_{sat,ds}$ is the unit vector pointing from the satellite to the Earth's surface element ds, $\vec{e}_{n_i}$ is the unit vector normal to the satellite's surface i, and $\cos\theta_i$ is the angle between $\vec{e}_{sat,ds}$ and $\vec{e}_{n_i}$. Finally, the total acceleration due to EARP is derived by summing the contributions from all visible Earth surface elements and the satellite's illuminated surfaces.

3.6.2.2 Earth Infrared Radiation Pressure

In addition to reflected solar radiation, the Earth absorbs some of the solar energy and re-emits it as long-wave infrared radiation, generating a force on satellites known as Earth infrared radiation pressure. The EIRP model follows a similar approach to EARP. For each flat satellite surface i the perturbing acceleration of the satellite due to EIRP of the Earth's surface element ds can be written as

$$\ddot{\vec{r}}_{EIRP_i} = C_{EIRP_i} \left[(\varepsilon_{ir_i} + \delta_{ir_i}) \vec{e}_{sat,ds} + \left(2\rho_{ir_i} \cos\theta_i + \frac{2}{3}\delta_{ir_i} \right) \vec{e}_{n_i} \right] \quad , \tag{3.61}$$

where ε_{ir_i} is the emissivity of the satellite surface in the infrared band, and all other variables have the same definitions as in the EAP model but applied in the infrared band. As with EARP, the total acceleration due to EIRP is derived by summing the contributions from all visible Earth surface elements and the satellite's illuminated surfaces.

3.6.3 Antenna Thrust

Antenna thrust is a non-gravitational perturbation that results from the momentum transfer due to the continuous emission of radio signals from the satellite's communication antennas. As GNSS satellites transmit signals to Earth, the reaction force caused by the emission of electromagnetic waves generates a small but steady thrust on the satellite. While this force is relatively weak compared to other non-gravitational forces such as solar radiation pressure, it can have a cumulative effect over time, gradually altering the satellite's orbit.

The magnitude of the antenna thrust depends on the power of the transmitted signals and the configuration of the satellite's antennas. Though typically ignored in many simpler models, antenna thrust becomes a significant factor in precise orbit determination, particularly for GNSS satellites where long-term stability and accuracy are critical.

3.7 Other Dynamical Model Uncertainties

Non-conservative force models are critical in achieving accurate orbit determination for GNSS and other satellite systems. These models are inherently limited by uncertainties stemming from various factors, such as satellite orientation, material properties, and surface temperature, all of which are time-dependent (Montenbruck and Gill, 2001). When not properly accounted for, these uncertainties can lead to significant errors in precise orbit determination. Although improvements in satellite modelling have reduced these errors, residual forces caused by thermal effects, such as solar and terrestrial heating, continue to present challenges. These thermal forces arise from asymmetric heating of satellite components, resulting in anisotropic radiation forces, which are typically not directly modelled (Schutz et al., 2004).

To address these unmodelled effects, empirical accelerations are often introduced to compensate for residuals forces that are not properly accounted for by the models. In GNSS satellite orbit models, these empirical accelerations are usually decomposed into three directional components corresponding to the satellite's natural motion dynamics: radial, along-track, and cross-track directions. The empirical accelerations are generally expressed as a combination of constant and periodic terms, as follows (European Space Agency, 2009):

$$\vec{\ddot{r}}_r(u) = [a_{r_0} + a_{r_c}\cos(u) + a_{r_s}\sin(u))\,\vec{e}_r \tag{3.62}$$

$$\vec{\ddot{r}}_t(u) = [a_{t_0} + a_{t_c}\cos(u) + a_{t_s}\sin(u))\,\vec{e}_t \tag{3.63}$$

$$\vec{\ddot{r}}_n(u) = [a_{n_0} + a_{n_c}\cos(u) + a_{n_s}\sin(u))\,\vec{e}_n \quad . \tag{3.64}$$

In this representation, u is the argument of latitude of the satellite, and a_{r_0}, a_{t_0}, and a_{n_0} are the constant accelerations in the radial, along-track, and cross-track directions, respectively. The terms a_{r_c}, a_{r_s}, a_{t_c}, a_{t_s}, a_{n_c}, and a_{n_s} represent the periodic variations in acceleration, which are described by cosine and sine functions of the argument of latitude. These periodic terms help model the complex interactions with non-conservative forces, such as solar radiation pressure and Earth's infrared radiation, that systematically change with the satellite's position in its orbit. The Cycle-Per-Revolution (CPR) terms are essential for modelling accelerations that repeat with the satellite's orbital period, compensating for residual forces that cannot be captured by simplified models. By incorporating these constant and periodic components, the CPR accelerations allow for effective compensation of unmodelled accelerations, improving the overall accuracy of the satellite orbit determination process.

4 Computational Methodology

This chapter delves into the computational frameworks and methodologies employed by the Navigation Support Office for satellite navigation and precise orbit determination. Initially, the European Space Agency's Precise Navigation System (EPNS), its architecture and evolution are introduced in Section 4.1 to elucidate the backbone of the Consolidated High Accuracy MGNSS Processing (CHAMP) framework. The CHAMP framework in Section 4.2 is divided into the space segment, showing the different constellations used in the processing in Section 4.2.1, and the ground segment, which relies on a smart selection of ground stations in Section 4.2.2. Once these are defined, the hierarchical software architecture is described from the input files in Section 4.2.3 to the output products in Section 4.2.5, with an emphasis on the multi-GNSS products and the GNSS orbit quality assessment in Section 4.2.6. Finally, the general physical models and settings regarding the observations, normal equation stacking and orbit integration are summarised in Section 4.2.7

4.1 ESA's Precise Navigation System

The European Space Agency's Precise Navigation System (EPNS) is a state of the art software programme for GNSS data processing the last version of which was officially launched in 2024 (Gini et al., 2024). It is the direct successor of NAPEOS, the NAvigation Package for Earth Observation Satellites, which has been the navigation software used by ESOC for orbit propagation and orbit determination in Earth orbiting missions (European Space Agency, 2009). The first versions of NAPEOS were developed in the second half of the 1990s, and were used for Flight Dynamics support to LEO missions. Envisat was ESOC's first operational mission to rely on NAPEOS after its launch in 2002. This initial version setup was founded very heavily on the experience gained during the operations and maintenance of space systems at ESOC during the previous decade. Subsequently, in 2001 the Navigation Support Office was established and a new branch of NAPEOS diverged to specialise in GNSS data processing (PosiTim, 2012). Since January 2008, and until EPNS debut, the Navigation Support Office at ESOC has used the NAPEOS software for all its GNSS operational activities, including the generation of products for the International GNSS Service, which can be found in European Space Agency (2024b).

EPNS, as well as NAPEOS, has been written in Fortran 90/95 programming language, an Object-based language, and is well known for its quality, efficiency and impressive processing speed. Furthermore, it allows a wide variety of GNSS processing applications, among which Precise Point Positioning and Global GNSS solutions are highlighted. EPNS allows the execution of simple and complex programmes, both in sequence and in parallel, using configuration settings that have to be prepared in advance with the GUI, or directly with configuration files. EPNS is fundamentally executed in batch mode, where all programmes are started as binary executables which read data from input files, and write the results to output files. While some of the input files require the user to prepare them beforehand, a large set of common input parameters are contained in the EPNS database. Both the source code and the database updates are protected under strict Change Control Board in order to ensure the reliability of the programme within deployed versions.

Additionally, EPNS changes are monitored using a set of test cases to analyse how modifications of the code affect the overall computations, ranging from basic satellite propagation tests to complex MGNSS simulations. For this purpose, E-TAC, acronym for EPNS Test Cases Automatic Comparison, was developed. This programme allows to compare the results of EPNS against a set of references which should not diverge beyond a set tolerance for each variable. It has been built to be able to run on any platform, accommodating to the user needs running on a local machine to debug custom changes of the source code, or as part of a GitLab CI/CD pipeline which creates everything from scratch, compiling every time the software changes and testing them automatically with every new commit, ensuring the long-term validity of the results (Sermanoukian, 2024). The EPNS source code folder is divided into different sub-folders depending on its functionalities. The main functionalities that are used throughout this thesis are highlighted in Table A.6, and are used as the building blocks of the complete process.

4.2 CHAMP

The Consolidated High Accuracy MGNSS Processing (CHAMP), as first presented in Gini et al. (2024), is the novel system of the ESA/ESOC Navigation Support Office for routinely generating GNSS-based POD and geodetic products for all five navigation systems: GPS, Galileo, GLONASS, BeiDou, QZSS. CHAMP is primarily based on the latest version of EPNS and runs on ESOC's Mission Operational Infrastructure. Thus, CHAMP acts as a wrapper over the EPNS software, providing the initialisation and finalisation scripts that run before and after the main EPNS sequence, respectively.

In terms of constellation-wise processing, instead of processing all constellations (up to 130 satellites in 2024) in one massive run, the CHAMP framework is processing all constellations individually and relying on normal equation stacking to combine the constellations in a flexible manner, leading to substantial savings in CPU power, RAM usage and storage requirements, while improving reliability, maintainability and timeliness. In addition, data consistency is enhanced by aligning satellite orbits and station coordinates to the *Institut Géographique National* (IGN)'s latest cumulative ITRF-IGS20 realisation, while aligning the clock products to UTC based on ESA's UTC realisation UTC(ESA). This is a achieved by an advanced reference clock selection algorithm, which is based on a prioritised list of calibrated stations.

4.2.1 GNSS Constellations

Following on the general constellation information in chapter 2 and the POD perturbations in chapter 3, a detailed comparison of key attributes and parameters for the GNSS constellations included in the CHAMP processing, namely GPS, GLONASS, Galileo, BeiDou, and QZSS is provided in Table 4.1. It covers satellite blocks, selected signal frequencies, orbit estimation methods, centres of mass, phase centre offsets (PCO), phase centre variations (PCV), attitude models, a priori models for solar radiation pressure, albedo, and infrared influences, power thrust, and code biases. The orbital paths of the GNSS constellations individual products on April 19, 2023, are shown in Figure 4.2 to illustrate the spatial distribution and coverage of each constellation on the same scale. Due to the low number of satellites in the current QZSS constellation, QZSS is combined with the GPS satellites as input data into one additional group, allowing to process the combined constellation in the same way as the others.

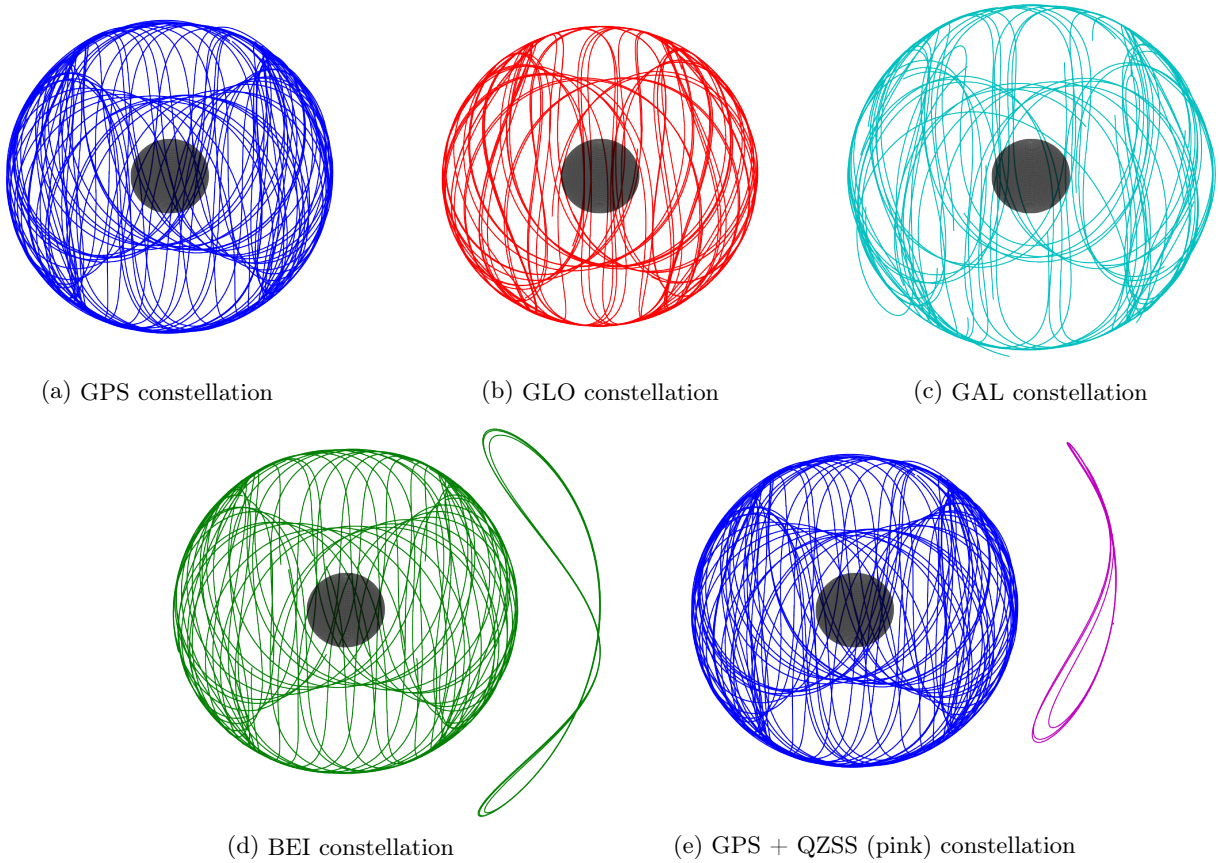

(a) GPS constellation (b) GLO constellation (c) GAL constellation

(d) BEI constellation (e) GPS + QZSS (pink) constellation

Figure 4.2: GNSS constellations according to CHAMP data (19/04/2023) [Same scale]

Table 4.1: CHAMP Constellation specifications - Modelling and data sources

Constellation	GPS	GLONASS	Galileo	BeiDou	QZSS
Block	IIA / IIR / IIF /IIIA	GLONASS-K GLONASS-M	IOV FOC	BeiDou-3	QZSS-1R, QZSS-2I QZSS-2G
Signals	L1W-L2W	L1P-L2P	E1C-E5Q	L1P-L5P	L1C-L2L
Orbit estimation	Independent				Combined GPS+QZSS
Centre of Mass	IGS Satellite Metadata	IGS Satellite Metadata	European GNSS Service Centre	IGS Satellite Metadata	Cabinet Office Metadata
PCO & PCV	Transmitting antenna: esa23.atx / Receiving antenna: igs20.atx				
Attitude model	Nominal yaw steering with noon/night turn model				
A priori model (SRP, Albedo, IR)	Box-Wing model IGS Satellite Metadata	Box-Wing model IGS Satellite Metadata	Box-Wing model European GNSS Service Centre	Box-Wing model ESOC estimates	Box-wing model Cabinett Office Metadata
Power Thrust	IGS Satellite Metadata	IGS Satellite Metadata	IGS Satellite Metadata	ESOC estimates	Cabinett Office Metadata
Code Bias	P1C1 correction (internal CODE.BIA)	-	-	-	-

The Galileo metadata is extracted from the European GNSS Service Centre (2024), while other constellations rely on the IGS and Cabinet Office metadata extracted from International GNSS Service (2024b). Additionally, the nominal attitude model is a combination from Kouba (2009), Dilssner (2010) and Dilssner and Springer (2024a), with modifications for GLONASS based on Dilssner and Springer (2011).

4.2.2 Ground Station Network

The CHAMP framework relies on a smart selection of the best stations for each processing within a set of more than 500 stations, based on ESOC's Optimised Global Station Selection algorithm. On the DAILY level, each constellation can use observations from up to 200 ground stations, while the combined MGNSS product uses the same maximum for the whole stacked solution. As a result, the stations selected for the MGNSS processing are the ones that better suit all the individual constellations. An example can be seen for a 1-day reprocessing of 2023 in Figure 4.3. This map contains a smart selection of 150 stations of ESA's GNSS Observation Network (EGON) combined with other stations from the global IGS network, providing a comprehensive and optimised global distribution of tracking stations. The strategic placement of these stations enhances the robustness and accuracy of the CHAMP mission's data products.

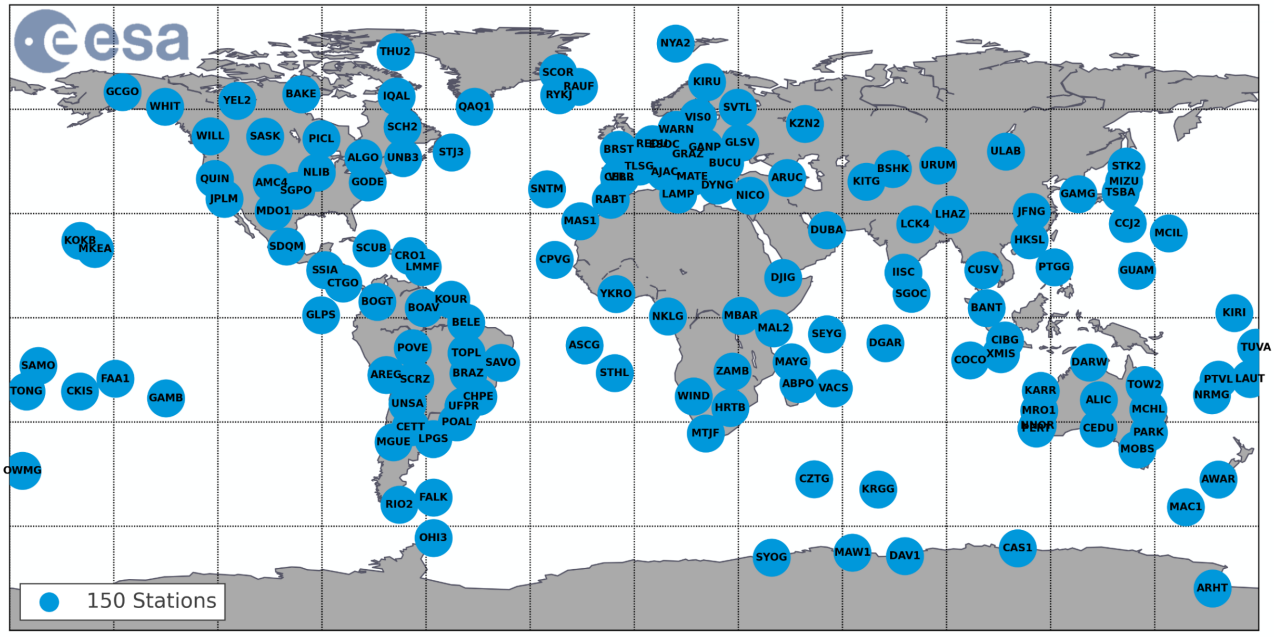

Figure 4.3: Smart station selection in MGNSS processing (ESA Navigation Support Office, 2023)

4.2.3 Software Architecture

CHAMP's software architecture can be depicted as a hierarchical tree structure that outlines the flow and processing of input data. This structure begins with the input data, which is represented as the roots of the tree. The main inputs include the EPNS configuration files, which are combined in the EPNS database, and the navigation RINEX files, which incorporate the broadcast ephemeris data, containing satellite positions and clock information, and the GNSS observations from the geographically distributed station network. Additionally, the roots encompass the ANTEX file, which describes antenna phase centre corrections, which are crucial for precise positioning. Then, Earth Orientation Parameters, which are necessary for accurate orbit calculations and transformations between celestial and terrestrial reference frames, can also be introduced.

Building on these roots, the trunk represents the core GNSS processing stages of the CHAMP framework. This level involves several phases of GNSS data processing, starting with the broadcast fitting, where broadcasted orbits are merged and transformed into SP3 files, to get an a priori orbit for every satellite and clock estimate. The results are then interpolated without considering the clocks to match the defined time step Δt, which is normally defined to either 30 or 300 seconds, depending on the intended purpose. This is done in the Bahn programme, which stands for batch least squares. Then, the transmitted clock biases are cumulated with the previously processed estimates. The processing continues cataloguing the GNSS observations from the RINEX file, screening the data based on code observations and meta information, for which priority is given to IGS20, ESOC UTC and TSD stations. As a result, the best 200 stations for each constellation are selected. Then the orbits are estimated with a time step Δt of 300 seconds, prior to the determination of the reference station clock, based on internal data statistics for the processed day. It then advances to the FLOAT solution Bahn programme, where the estimation of satellite, station, earth orientation and other GNSS parameters including ambiguities is performed ignoring the integer nature of the ambiguities. Subsequently, the integer ambiguity resolution of the previously obtained GNSS phase ambiguities is performed along the estimation of uncalibrated phase delays. Once these are obtained, the sequence advances to the FIX solution Bahn programme, where both code and phase measurements are combined with floating ambiguity resolutions to produce highly precise solutions. These core processing stages result in daily independent outputs for each constellation, referred to as DAILY. The last step of the DAILY sequence is to perform the ITRF alignment of single-constellation solutions. As the single-constellation solutions do not share the same reference frame, this strategy is needed prior to combining all the results. This task is performed in the multiarc programme, which provides the individual station alignments to each constellation.

As the data progresses through the system, it reaches the branches, which represent the aggregation and refinement of individual constellation solutions. This stage involves normal equation stacking, where individual solutions from the different constellations are combined using the independently obtained normal equations of each constellation at the end of the DAILY sequence. A Helmert transformation is performed ensuring no-net translation and rotation, without any constraints to the individual constellation scaling. The branches include an additional Bahn run for the stacked data, which integrates both code and phase data with 30-second clock corrections to achieve high precision solutions. Among others, the processing stage results in combined output for all constellations, referred to as MGNSS.

At the highest level, the leaves symbolise the final products and advanced processes derived from the trunk and branch outputs. These products are often highly specialised and complex, tailored to specific applications, and are compared to orchids due to their complexity and specialisation. Examples of these advanced products include IONO, which relates to ionospheric modelling and corrections, and DCBIAS, which involves Differential Code Bias products to correct biases in GNSS signals. However, these products are out of the scope of this thesis.

As an overall result, the CHAMP framework MGNSS sequence processes 24h-long arcs with simultaneously 200 ground stations and 5 GNSS constellations, enforcing that only high-quality stations are included in the process. It provides products with 3 different latencies: Ultra-Rapid, Rapid, and Final solutions based on the user needs and the available data at each date. In such a way, it enables cross-constellation comparisons, which allow to monitor, analyse, and continuously investigate the intermediate and final constellation products to improve the models and products' quality. The tree analogy summary is shown in Table 4.2. Additionally, the step by step programme information regarding the DAILY and MGNSS sequences can be found in Table A.7 and Table A.8, respectively.

Table 4.2: CHAMP framework structure structure

Level	Programme	Description	Product ID
Leaves	CmdLine	Product generation and advanced processes (orchids)	IONO, DCBIAS
Branches	MultiArc	NEQ-stacking of individual constellations ITRF-IGS20 alignment of each constellation	ULTRA MGNSS
	Bahn	Batch LS, Code and Phase, 30s-clock solution	
Trunk	Broadcast Fit	Pre-processing and a priori orbits	HOURLY DAILY
	GnssObs	Observations processing, Code-only solution	
	Bahn	Batch LS, Code and Phase, FLOAT solution	
	AmbFix	Ambiguity fixing	
	Bahn	Batch LS, Code and Phase, FIX solution	
	MultiArc	ITRF-IGS20 alignment of each constellation	
Roots	CmdLine	Input data files (brdc, RNX, ATX, EOP)	-

4.2.4 Clock Analysis

The DAILY ClockRef run is a process designed to determine new reference clock ensembles for each individual constellation, with a particular focus on GPS. GPS is a critical reference, as many branches use it as the a priori reference for their 30-second clock estimations in the Bahn Clock runs. This process relies on rejecting incomplete or inconsistent stations based on previous steps, ensuring only reliable and continuous clock data is used for GPS and the other constellations. The order of processing is important, with GPS positioned last to leverage the most complete list of rejected reference stations identified in earlier steps. The process begins with an analysis of stations based on their code-only performance. This initial step inspects the receiver clock bias file, identifying stations with poor code-only data at 30-second intervals. Though this step does not produce any direct output, it adds these stations to a list of rejected reference stations, ensuring that subsequent requests for clock ensemble determination only consider stations that perform well.

Next, the process moves on to assess GLONASS, examining its clock bias performance. Similar to the first step, the GLONASS request only checks the receiver clock bias file and does not output data directly but identifies stations with poor GLONASS-only performance. These stations are also added to the rejected list to improve the quality of clock ensemble selection for subsequent constellations. The system then determines and applies the reference clock ensemble for Galileo. By this stage, stations that underperformed in the previous analyses have already been filtered out, meaning that only reliable stations contribute to the Galileo clock ensemble. The same process is then repeated for BeiDou, ensuring that the reference clock ensemble for this constellation is also based on the best-performing stations. Finally, the GPS reference clock ensemble is determined. Since GPS is used as the main reference for many downstream processes, this step benefits from the most complete list of rejected stations. By the time the GPS clock ensemble is calculated, all stations with poor performance in code-only, GLONASS, Galileo, and BeiDou processing have already been excluded, resulting in a highly accurate GPS ensemble. The process concludes with the combination of GPS and QZSS, creating a joint clock ensemble for these constellations.

Then, in the MGNSS scenario, the Bahn Clock run includes all constellations in the processing branch in order to combine them into a single solution, allowing for the estimation of station and satellite clocks along with intersystem biases. GPS serves as the primary reference constellation in this combined clock solution. At 30-second intervals, the process estimates a bias parameter between GPS and each secondary constellation. If discrepancies arise between the observed signals for a station, either specific observations or, in some cases, the entire signal for that station may be rejected. The station statistics from this step are organized by constellation, providing insights into the performance of each system.

4.2.5 MGNSS Products

The following Table 4.3 presents an overview of the selected MGNSS FINAL products which result from the published combined constellation solutions based on the CHAMP framework processing, detailing their standardised formats, sampling intervals, data periods, latency of publication, and general description. Additional products from the other branches such as the HOURLY ULTRA are also available, but out of the scope for this project. All the products can be found in the Navigation Support Office website.

Table 4.3: CHAMP MGNSS published products

Format	Description	Sampling	Period [h]	Latency [days]
SP3	Satellite orbits and clock corrections	5 min	24	10
Clock RINEX	High-resolution clock data	30 s	24	10
SINEX	Normal equation solution	1 day	24	10
Tropo SINEX	Tropospheric delay estimates	1 day	24	10
ERP	Earth rotation parameters	1 day	24	10
Summary File	Analysis report summary	1 day	24	10

In addition to the published products outlined in Table 4.3, a range of intermediate files is generated, each containing some of the estimated parameters for both the DAILY and MGNSS scenarios. The different GNSS processing formats are listed in Table 4.4.

Table 4.4: EPNS Intermediate formats

Type	Format	Description
Clock	tcb	Transmitter Clock Bias
	rcb	Receiver Clock Bias
Normal Equation	neq	NEQ file output from Bahn
	fneq	Special NEQ file intended to be used only in AmbFix
	pneq	NEQ file containing only parameters
	mneq	NEQ file output from Multiarc
	sneq	NEQ file containing only station coordinates and EOPs
	upd	Uncalibrated Phase Delays
Observations file	ntdf	EPNS Observations file
Output	esta	Estimated Parameters (ASCII Format)
	res	Residuals

4.2.6 GNSS Orbit Quality Assessment

In GNSS processing, day boundary orbit differences are crucial for assessing orbit quality and ensuring continuity in satellite positioning data. This metric, focusing on overlaps between consecutive 24-hour orbit arcs, highlights potential discrepancies and serves as a "worst-case" test for orbit consistency, as it reveals cumulative modelling errors or inaccuracies. Minimising these differences is essential for maintaining high accuracy in positioning and timing applications, which are sensitive to even minor deviations.

For example, day boundary orbit differences are utilised in the initial analysis of CHAMP, as noted in Gini et al. (2024), where overlap statistics provide performance insights for individual satellites and entire constellations. In this analysis, the constellation-wise plot shows the strong performance of the GPS, Galileo, and BeiDou constellations. In contrast, GLONASS displays a lower performance, mainly due to the lack of integer ambiguity resolution, less accurate orbital models, and hardware issues affecting some satellites. Similarly, BeiDou and QZSS IGSO and GEO satellites perform less robustly, with results influenced by their unique observation geometries and varying altitudes. For these satellites, the 24-hour arcs are sub-optimal, as this period matches their orbital cycle, complicating performance assessment.

However, in the CHAMP processing, various estimated parameters beyond orbit overlaps are also essential for a comprehensive analysis, and should be checked on a regular basis to analyse the products accuracy and ensure consistency throughout the different constellations and methodologies. These can include Earth Orientation Parameters, station and satellite coordinates, tropospheric and ionospheric delays, phase centre variations and receiver clock offsets, among others.

4.2.7 Models and Settings

The CHAMP framework relies on advanced mathematical and physical models to ensure precise satellite navigation and geodesy. These models account for gravitational and non-gravitational perturbations, atmospheric influences, changes in reference frames and other relativistic effects. As a result, these include comprehensive adjustments for Earth orientation, clock synchronisation, satellite orbits, and empirical SRP accelerations. A summary of the CHAMP framework observations, NEQ stacking weights and orbit integration are shown in Table 4.5. Additionally, based on the relevance of Earth Orientation Parameters in the global parameter analysis of Chapter 5, the conventions and sources used for each EOP model are highlighted in Table 4.6. A summary of the models used for relativity, gravitational perturbations, terrestrial reference frame definitions and atmospheric mapping can be found in Appendix A.1.

Table 4.5: CHAMP observations, NEQ stacking and orbit integration settings

Category	Topic	Description
Observations	Observation type	Undifferenced ionosphere-free linear combination of dual-frequency
	First order ionospheric effect	Accounted for by dual-frequency observations in linear combination
	Data sampling	30 s
	Elevation cutoff angle	10 degrees
	Weighting	$1/(\sin(elevation))$
NEQ Stacking Weights	Weight Sigma Code	1 m (All constellations)
	Weight Sigma Phase	10 mm (GPS, GAL, BEI, QZS), 20 mm (GLO)
Orbit Integration	Integrator	Adams-Bashforth/Adams-Moulton 8th order Multistep prediction-correction method
	Initialisation	Runge–Kutta–Fehlberg 8th order
	Integrator step size	120 steps per revolution
	Arc length	24h

Table 4.6: CHAMP Earth Orientation Parameters model descriptions and sources

Category	Topic	Description
Earth Orientation Parameters	Precession-Nutation	Applied IAU 2000A/2006 model
	Celestial Pole offset	Applied IAU 2000A/2006 model Applied daily dx and dy corrections from IERS Bulletin A
	Celestial Pole rates	Interpolation between given offsets with the 4 neighbouring points numerical derivative
	Subdaily nutation	Prograde diurnal and semi-diurnal nutations in polar motion applied using IERS routine PMSDNUT2.F (Petit and Luzum, 2010)
	UT1 - UTC	Interpolation from IERS Bulletin A (IERS rapids)
	UT1 libration	Semi-diurnal UT1 libration applied using IERS routine UT1LIBR.F (Petit and Luzum, 2010)
	Subdaily pole/UT1	Tide model from (Desai and Sibois, 2016)
	Secular pole	Applied IERS 2010 model
	Terrestrial Pole offset	Interpolation from IERS Bulletin A (IERS rapids)

5 CHAMP Parameter Analysis

This chapter provides an in-depth exploration of the parameters that are estimated during the NSO GNSS processing, along with the parameter extraction procedure applied in the CHAMP framework. These parameters are checked to unveil inconsistencies in the individual and combined solutions, relying on additional external solutions for comparison. The chapter begins with an overview of the new CHAMP parameter extraction procedure in Section 5.1, detailing the methodology to extract the parameters of interest from both intermediate and final products. Section 5.2 presents an overview of all estimated parameters in the CHAMP GNSS processing for the DAILY and MGNSS sequences. In Section 5.3, the focus shifts to the analysis of the Earth Orientation Parameters which influence satellite navigation, in particular UT1-UTC, Length of Day, the X and Y components of polar motion and their rates. Section 5.4 discusses the role of ground stations in the CHAMP processing, highlighting their alignment with the ITRF and the calculation of precise station coordinates. Section 5.5 presents a detailed analysis of the satellite-specific parameters for each constellation, mainly using orbit overlaps. Then, the analysis of the ECOM1 empirical model parameters is found in Section 5.5.2, while the additional Cycle-Per-Revolution empirical accelerations are discussed in Section 5.5.3. Finally, Section 5.6 addresses the clock-related parameters such as clock biases, providing insights for further research.

5.1 Parameter Extraction Procedure

Given that CHAMP was designed as an operational tool where resource optimisation is paramount, most intermediate and final results not intended for publication are routinely deleted. This approach, while efficient in conserving resources, poses significant challenges when attempting to retrieve all estimated variables and results for in-depth analysis. To address this issue, a method was developed to regularly access the necessary data using the files that are retained, ensuring that detailed analysis can still be conducted within the existing operational constraints.

The first step in this process is to analyse the parameters of interest for the project, alongside identifying the files in which they are saved. A summarised list of these parameters is provided in Section 5.2. Ideally, the most straightforward approach for users would be to work with the esta file, which already contains all relevant parameters in ASCII format. However, this file is not routinely saved within the operational pipeline due to its large size, which complicates storage during large-scale reprocessing efforts spanning multiple years. As a result, the decision was made to work with the intermediate files, which are stored in binary format, and extract the final outputs using custom Python parsers.

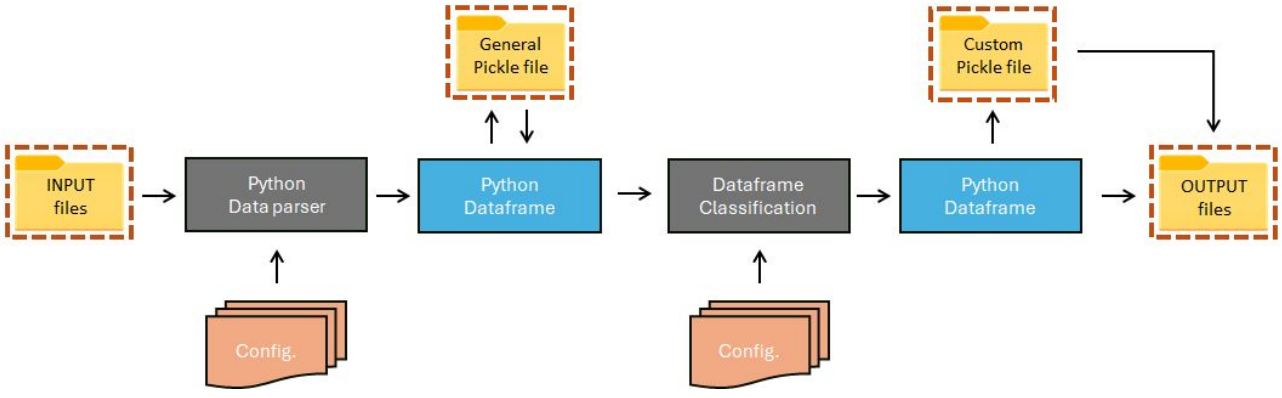

Figure 5.1: CHAMP estimated parameter extraction pipeline

The list of parsers is adapted from a recent research project undertaken by the Navigation Support Office, modified to meet the specific needs of this project. Additionally, new parsers were developed to cover any remaining gaps. The overall data transformation pipeline is outlined in Figure 5.1. These parsers convert the binary data into Python dataframes, with each file producing a unique dataframe containing a comprehensive table of all relevant data. Since this process can be time-consuming, especially for parsers dealing with less structured data, it is advisable to store the extracted data into pickle files. These files significantly reduce the size of the data, compressing it by a factor of 10 to 100 times, which facilitates easier storage of large datasets. Furthermore, loading these compressed pickle files is almost instantaneous, whereas certain parsers can take up to a minute for each file, with processing time increasing linearly for larger datasets during reprocessing operations.

However, despite the efficiency of this process, the resulting dataframes, which aggregate all file data into a single massive table, are not well-suited for detailed analysis. Iterating over a large table to extract a single parameter is inefficient and time-consuming. To address this, the next step involves classifying the data into dictionaries, which allow for more structured access to specific data. This approach enables the creation of groups and subgroups based on attributes like date, satellite constellation, or specific parameters, among others. By organising the data in this manner, smaller, more focused dataframes can be quickly extracted and utilised for large-scale statistical analysis or plotting, reducing processing time to just a few seconds, even for complex datasets. As a result, these steps can be seamlessly integrated into the entire CHAMP DAILY and MGNSS processing pipelines to automate the extraction and organisation of variables of interest. By incorporating this approach, the relevant data can be saved in an easy-to-use format, streamlining subsequent analysis tasks. This automation not only reduces manual effort but also ensures that key parameters are consistently available in an organised and compressed format, optimising both storage and retrieval efficiency across large-scale reprocessing efforts. The enhanced pipelines will facilitate rapid access to high-quality data, allowing users to focus on detailed analysis without being encumbered by time-intensive data handling processes.

5.2 Overview of Estimated Parameters

This section introduces the parameters that are estimated during the DAILY and MGNSS sequences, both before and after the stacking process, as summarised in Table 5.1. The estimated parameters for the individual constellations can be extracted before the ITRF alignment from the normal equation file resulting from the batch least-squares adjustment (Bahn), or after the ITRF alignment from the constellation-specific log (MultiArc). For the combined solution, the data is extracted from the ITRF-aligned normal equation stacking log files (MultiArc). Additionally, on both scenarios the solar radiation, albedo and infra-red radiation coefficients are fixed. A notable distinction exists regarding the SBIAS variable in the DAILY and MGNSS scenarios. In the DAILY scenario, SBIAS is used to account for interfrequency biases in constellations like GLONASS, which employ frequency division multiple access. In contrast, in the MGNSS scenario, the same variable is repurposed to represent the inter-constellation biases, highlighting its flexibility in multi-GNSS processing. Additionally, the ambiguities are only solved in the DAILY sequence and fixed for the MGNSS sequence.

Table 5.1: CHAMP estimated parameters

				DAILY	**MGNSS**
Parameter	**Acronym**	**Units**	**Frequency**	**Source**	
X polar motion	XPO	*mas*	1 day	Bahn NEQ file or MultiArc log	Bahn SNEQ file or MultiArc log
Y polar motion	YPO				
X polar motion rate	XPOR	*mas/day*			
Y polar motion rate	YPOR				
Delta time UT1-UTC	UT	*ms*			
Length of day	LOD				
Parameter	**Acronym**	**Units**	**Frequency**	**Source**	
Station X coordinate	STAX	*km*	1 day	Bahn NEQ file or MultiArc log	Bahn SNEQ file or MultiArc log
Station Y coordinate	STAY				
Station Z coordinate	STAZ				
Parameter	**Acronym**	**Units**	**Frequency**	**Source**	
Satellite X coordinate	SAT__X	*km*	300 s	SP3 file	SP3 file
Satellite Y coordinate	SAT__Y				
Satellite Z coordinate	SAT__Z				
Satellite X velocity	SAT_VX	*km/s*	300 s		
Satellite Y velocity	SAT_VY				
Satellite Z velocity	SAT_VZ				
Parameter	**Acronym**	**Units**	**Frequency**	**Source**	
Satellite Antenna X offset	SATA_X	*m*	1 day	Bahn NEQ file or MultiArc log	Bahn SNEQ file or MultiArc log
Satellite Antenna Y offset	SATA_Y				
Satellite Antenna Z offset	SATA_Z				
Parameter	**Acronym**	**Units**	**Frequency**	**Source**	
Atmosphere zenith delay	ZENDEL	*km*	60 min	Bahn NEQ file or MultiArc log	MultiArc log
Atmosphere gradient East	TGETOT		1 day		
Atmosphere gradient North	TGNTOT				

Table 5.1: CHAMP estimated parameters (continuation)

				DAILY	MGNSS
Parameter	**Acronym**	**Units**	**Frequency**	**Source**	
CPR along constant	CPRAO	km/s^2	1 day	Bahn NEQ file or MultiArc log	MultiArc log
CPR along cosine	CPRAC				
CPR along sine	CPRAS				
Parameter	**Acronym**	**Units**	**Frequency**	**Source**	
CODE d-vec constant	CODEDO	km/s^2	1 day	Bahn NEQ file or MultiArc log	MultiArc log
CODE y-vec constant	CODEYO				
CODE b-vec constant	CODEBO				
CODE b-vec cosine term	CODEBC				
CODE b-vec sine term	CODEBS				
Parameter	**Acronym**	**Units**	**Frequency**	**Source**	
Station GNSS Clock Bias	TBIAS	μs	300 s	RCB file	RCB file
Satellite GNSS Clock Bias	TBIAS	μs		TCB file	TCB file
GNSS Intersystem Bias	SBIAS	μs		-	BIAS SNX file
Ambiguities	AMBIG	km		Bahn NEQ file	Bahn SNEQ file

In the CHAMP GNSS processing framework, various constraints are applied to ensure the accuracy and stability of the estimated parameters. These constraints serve as limits, effectively controlling how much the parameters can deviate from predefined a priori values. The σ constraint values, given in Table 5.2, represent the maximum allowable standard deviation from the apriori values. These constraints are critical in maintaining the accuracy of the computed parameters, and can defined differently for the individual constellation batch least squares estimation (Bahn) or the ITRF alignment (MultiArc). To further ensure the stability and consistency of the reference frame during MultiArc computations, the No-Net-Translation (NNT) and the No-Net-Rotation (NNR) constraints are set to control the translational and rotational movements, safeguarding the integrity of the reference frame and preventing distortions during the stacking process.

Table 5.2: CHAMP estimated parameter constraints

Earth Orientation Parameters	**Units**	**Bahn σ**	**MultiArc σ**
XPO, YPO, XPOR, YPOR, LOD	$mas, mas/day, ms$	10^3	
UT1-UTC	ms	10^{-6}	
Station/Satellite Parameters	**Units**	**Bahn σ**	**MultiArc σ**
STAX, STAY, STAZ	km	10^{-5}	10^{-3}
SATX, SATY, SATZ	km	1	
SATVX, SATVY, SATVZ	km/s	1	
SATAX, SATAY, SATAZ	m	10^{-6}	10^{-8}
Atmosphere Parameters	**Units**	**Bahn σ**	**MultiArc σ**
ZENDEL	km	10^{-3}	
TGETOT, TGNTOT	km	$5 \cdot 10^{-4}$	
Empirical Parameters	**Units**	**Bahn σ**	**MultiArc σ**
CPRAO, CPRAC, CPRAS	km/s^2	10^{-13}	
CODEDO, CODEYO, CODEBO, CODEBC, CODEBS	km/s^2	1	
Clock Parameters	**Units**	**Bahn σ**	**MultiArc σ**
TBIAS	μs	1 (DAILY) 10 (MGNSS)	-
SBIAS	μs	0.01 (DAILY GLO) 0.1 (MGNSS GLO) 1 (MGNSS General)	10^{-9}

An initial analysis shows that certain variables did not require further analysis in terms of the DAILY versus MGNSS differences. For instance, the satellite antenna parameters are highly constrained to the a priori values, preventing any deviation between the two sequences. The following sections show the in-depth analysis of the relevant estimated parameters within the operational products from the Navigation Support Office.

5.3 Earth Orientation Parameters

The absolute evolution of the Earth Orientation Parameters estimated with the individual Galileo constellation or the combined MGNSS solutions is shown in Figure 5.2, comprising all data from the beginning of 2017 until the end of 2023. The main variation comes at the beginning of 2021, when the BeiDou constellation is added to the whole MGNSS solution, as shown by the change in colour. Overall, the Galileo constellation is a representative solution of all the individual constellations. As such, it is superposed to both MGNSS solutions, evidencing that the absolute differences between the estimated parameters of the individual constellations and the combined solution are not clearly visible except for the slight peaks in the daily pole rates in Figure 5.2d and Figure 5.2f.

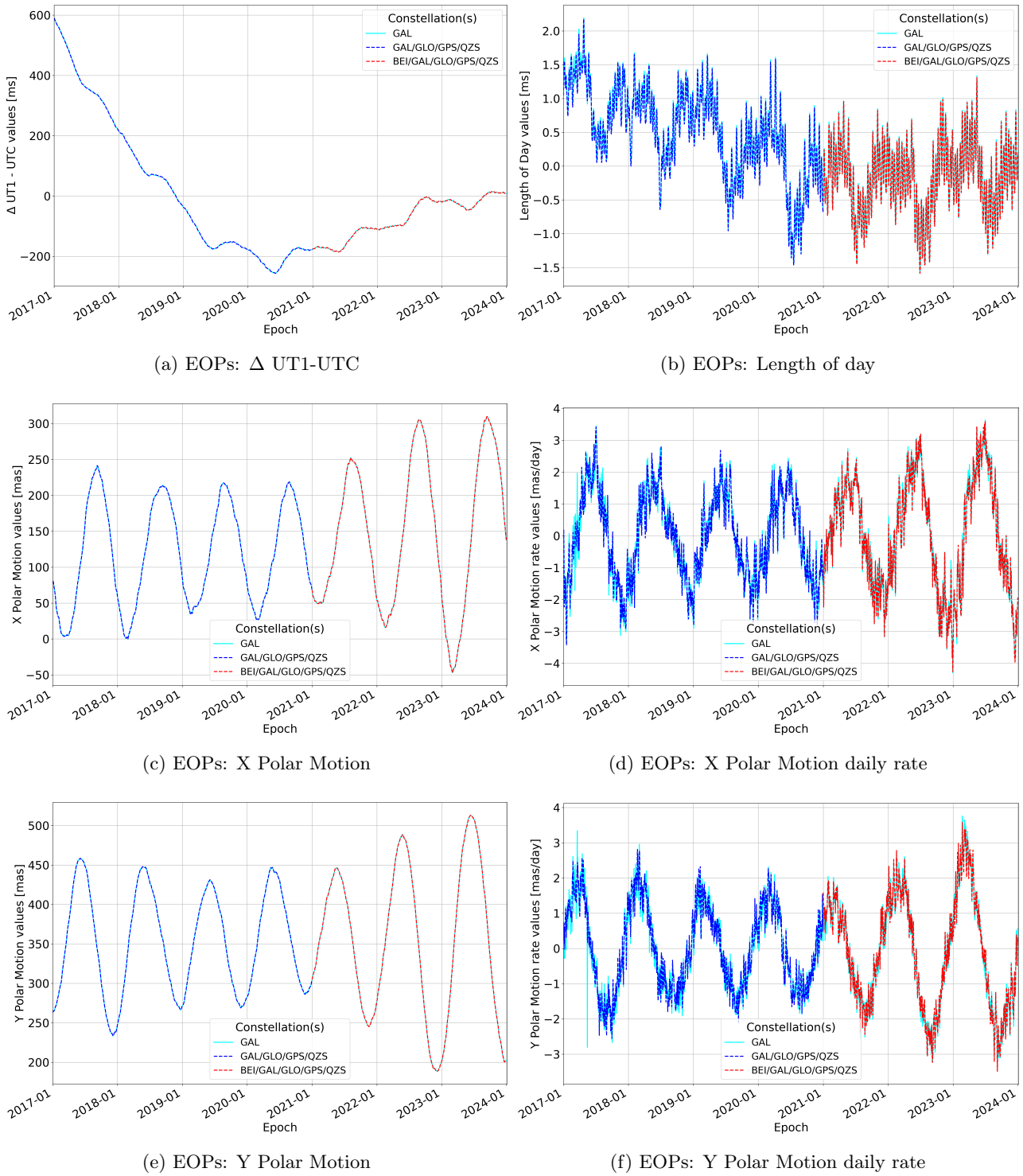

(a) EOPs: Δ UT1-UTC

(b) EOPs: Length of day

(c) EOPs: X Polar Motion

(d) EOPs: X Polar Motion daily rate

(e) EOPs: Y Polar Motion

(f) EOPs: Y Polar Motion daily rate

Figure 5.2: DAILY and MGNSS Earth Orientation Parameter evolution with time

The historical connection between timekeeping and Earth's rotation has led to Coordinated Universal Time being closely aligned with this rotation (McCarthy and Seidelmann, 2018). As Earth's rotation rate is not constant, UTC contains discontinuities to keep this alignment. Since 1972, all UTC discontinuities have required that a leap second is added (Nelson et al., 2001); almost annually at first, with 23 times between 1972 and 1999, and with a much slower pace during the last 24 years, where there have been only four adjustments. This evolution is most probably due to the slowing of the core at a constant rate since 1972, which has caused the solid Earth to rotate more rapidly, and it is possibly influenced by global warming according to Agnew (2024). Extrapolating the trends of the latest research, it is predicted that UTC as now defined will require a negative discontinuity by 2029. This can be seen at the end of Figure 5.2a, with the slope change from 2021 onwards. Furthermore, the length of day has exhibited significant fluctuations over the observed period, as shown in Figure 5.2b. These fluctuations correspond to changes in the Earth's angular velocity. As seen in Na et al. (2012), seasonal ice mass redistribution on the polar or nearby regions can result in significant LOD variations. However, expanding the time domain backwards with data from IERS EOP20C04 from 1962 onwards, it can be seen that the latest years reflect a decrease in LOD, reaching the lowest values ever, aligning with the increase in Earth's angular velocity.

In addition to LOD, polar motion values are also influenced by periodic perturbations, which can provide critical insights into Earth's rotational dynamics. Figure 5.2c and 5.2e display the X and Y components of polar motion, respectively. These plots reveal the regular oscillations in the position of Earth's rotation axis relative to its crust, influenced by various geophysical and environmental factors. Additionally, space geodetic observations of polar motion indicate that around 2005, the average annual pole position began shifting eastward, marking a significant change from the previous century's drift direction (Chen et al., 2013). The daily rates of change for both X and Y polar motion, depicted in Figure 5.2d and 5.2f, show significant variability, indicating the dynamic nature of Earth's rotational behaviour.

To accurately assess the CHAMP EOP solution, an external high-precision EOP solution can serve as a reliable reference point. For this purpose, the IERS EOP20C04 solution is selected as the main external reference due to its high accuracy, consistency, and comprehensive integration of data from multiple measurement techniques (Rotation and (IERS), 2024). The EOP20C04 solution incorporates information from Very Long Baseline Interferometry (VLBI), Satellite Laser Ranging (SLR), Global Navigation Satellite Systems, and Doppler Orbitography and Radiopositioning Integrated by Satellite (DORIS), ensuring a robust and well-rounded dataset. Additionally, it is aligned with the International Terrestrial Reference Frame 2020. In addition to EOP20C04, IERS Bulletin A and Bulletin B are also used as complementary external references. Bulletin A provides rapid solutions for EOPs, updated weekly, making it suitable for near-real-time comparisons, while Bulletin B offers monthly, more stable values based on longer-term observations. Bulletin B's emphasis on stability through monthly data averages makes it especially suitable for identifying gradual trends and minimising short-term variability, providing a reliable baseline for long-term comparisons. To complete the comparative framework, an internal reference from ESOC as shown in Bruni et al. (2022) is included, which combines CHAMP data with other data sources like ILRS (International Laser Ranging Service), IDS (International DORIS Service), and VLBI. This internal reference allows for an in-depth evaluation by incorporating CHAMP-specific information into the combination, further enhancing the reliability of the comparisons across various constellations and datasets.

5.3.1 Δ UT1 - UTC

The differences in the estimated value of Δ UT1-UTC between the individual GNSS constellations and the combined MGNSS solution are illustrated in Figure 5.3. The values are smoothed with a moving average of ten days for the representative three-year period to reduce short-term fluctuations and highlight longer-term trends. The plot indicates no clear patterns in the differences between individual DAILY GNSS constellations and the combined MGNSS solution. All constellations exhibit similar behaviour, with differences consistently staying within the femtosecond level (around 0.3 micrometers), even when the Δ UT1-UTC constraint allows deviations from the a priori values up to the nanosecond level. This suggests that despite minor variations, the performance of each constellation in estimating Δ UT1-UTC is comparable, with no single constellation significantly deviating from the others.

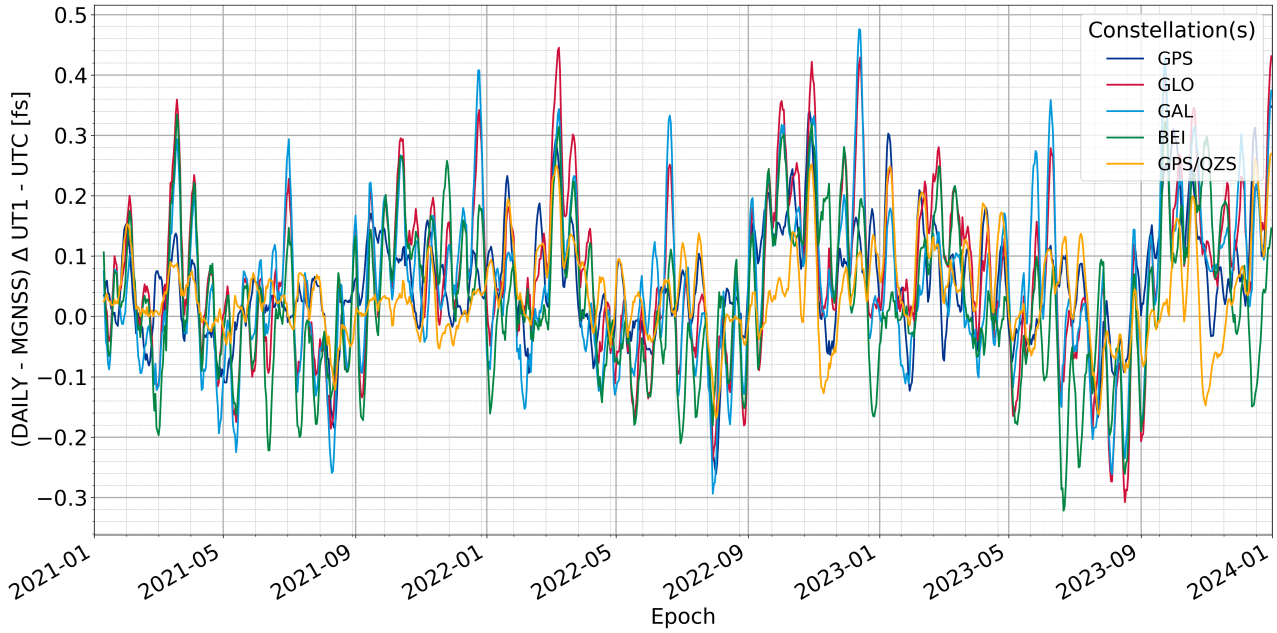

Figure 5.3: DAILY individual Δ UT1-UTC differences wrt. the combined MGNSS solution

The Δ UT1-UTC differences between the individual and combined GNSS constellations and the IERS EOP20C04 reference are shown in Figure 5.4. These mostly remain within a relatively narrow range of ±100 microseconds, except for some outliers. These values represent differences nine orders of magnitude larger than the internal DAILY vs. MGNSS values, indicating a high degree of consistency between these sequences. Additionally, when comparing the IERS EOP20C04 reference with the other multi-technique methodologies in Figure 5.5, a similar variability can be seen in the internal ESOC and external Bulletin B values. This figure only shows the largest difference for each day, enabling to highlight if a specific reference diverges from the IERS EOP20C04 values. When combining the CHAMP MGNSS data with other techniques, the ESOC reference is mostly in line with IERS20C04, slightly reducing the CHAMP differences and removing the outliers. However, during the second half of 2023, the differences are always larger than in Bulletin B. In contrast, Bulletin B seems to have several outliers mostly concentrated in the central months of 2022, which could probably come from the data of the non-GNSS methodologies. These results show that there is no inconsistency in the estimation of Δ UT1-UTC the individual and combined solutions, with differences several orders of magnitude below both the external comparison and the selected constraint.

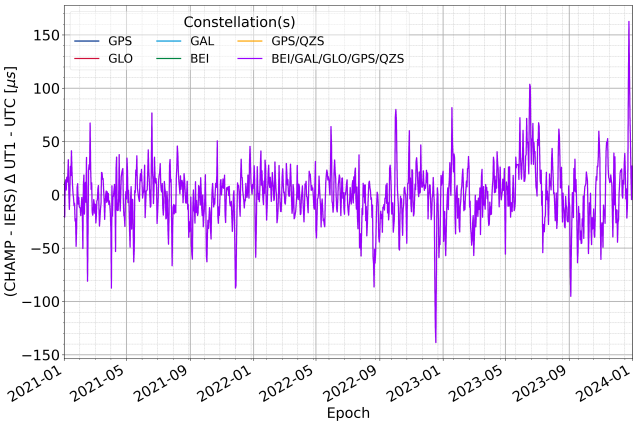

Figure 5.4: Δ UT1-UTC estimated differences wrt. IERS EOP20C04

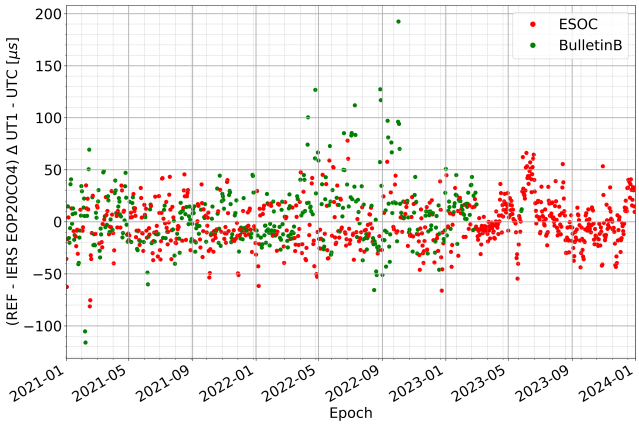

Figure 5.5: Comparison of internal and external references wrt. IERS EOP20C04

5.3.2 Length of Day

The differences in the estimated values of Length of Day between the individual GNSS constellations and the combined MGNSS solution are illustrated in Figure 5.6. The values are smoothed with a moving average of seven days over a three-year period to reduce short-term fluctuations and highlight longer-term trends. The plot highlights significant LOD estimate differences between the individual GNSS constellations, with two distinct groups of behaviour. The first group consists of GLONASS, Galileo and BeiDou, which show a clear yearly periodic pattern, indicating that the differences are influenced by seasonal variations or Earth's rotational effects that repeat on an annual cycle. The second group consists of GPS, both alone and in conjunction with QZSS, which shows a similar yearly periodic pattern but with a completely different sign. This change in sign shows clear inconsistencies between GPS and all other constellations, as the effect of QZSS on the GPS and QZSS combination is not enough to significantly modify the LOD estimates. Notably, the weighted sum of both groups results in the combined MGNSS solution, already evidencing that GPS's weight in the combination is larger than all other constellations.

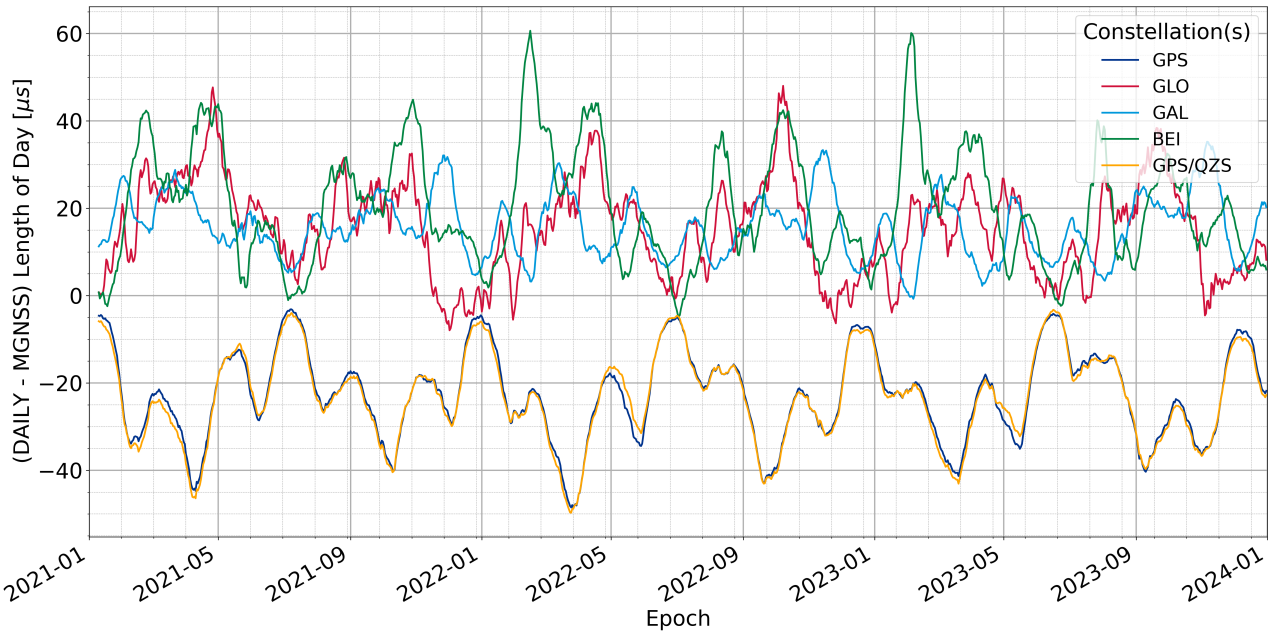

Figure 5.6: DAILY individual LOD differences wrt. the combined MGNSS solution

To further analyse the results, the standard deviations of the individual and combined LOD solutions are presented in Figure 5.7, where a consistent yearly period is observed across all constellations, with variations in amplitude and shape specific to each constellation. In the Bayesian LSQ approach, the weights in the a priori variance-covariance matrix $\mathbf{P_x}^{-1}$ are influenced by the standard deviations of each constellation's LOD estimates. As shown in the figure, GPS has the lowest standard deviations, indicating higher reliability, while GLONASS has the highest standard deviation, suggesting greater variability. Consequently, in the Bayesian framework, GPS receives a higher weight in the variance-covariance matrix, giving it more influence in the combined MGNSS solution. The standard deviation of the combined MGNSS solution reflects a significant reduction in LOD variability, effectively smoothing out inconsistencies present in individual constellations. This reduction in variability is primarily shaped by GPS and Galileo, whose periodicity aligns closely in terms of peak and trough patterns, thereby stabilising the combined LOD estimate. This Bayesian-weighted combination achieves an optimal balance, leveraging the strengths of the more reliable constellations while minimising the influence of noisier constellations.

While the LOD estimates come from the ITRF-aligned MultiArc programme, the a priori values used by MultiArc are taken from the last iteration of the previous fixed Bahn programme for the same constellation, and the fixed Bahn values are initialised based on IERS Bulletin B values. At the same time, the MGNSS a priori values come from the weighted stacking of the fixed Bahn solutions of all individual constellations. As a result, the differences between the estimated and a priori values are shown in Figure 5.8, showing the influence of the reference frame alignment, the NEQ stacking process and the specific parameter constraints. The combined solution reveals significant periodic differences, suggesting a notable divergence from the a priori values. This pronounced discrepancy may point to underlying issues in the data combination process, where errors or biases

from individual constellations are amplified when merged. Additionally, the pattern seems to be influenced by the changes in the GPS constellation, as other constellations remain close to the a priori values. While GPS DAILY values are smaller than in the combined MGNSS, according to Figure 5.6, Figure 5.8 shows that the individual GPS estimates increase with respect to the Bahn a priori values. As these a priori values are stacked in the MGNSS, an even larger change results from the combination.

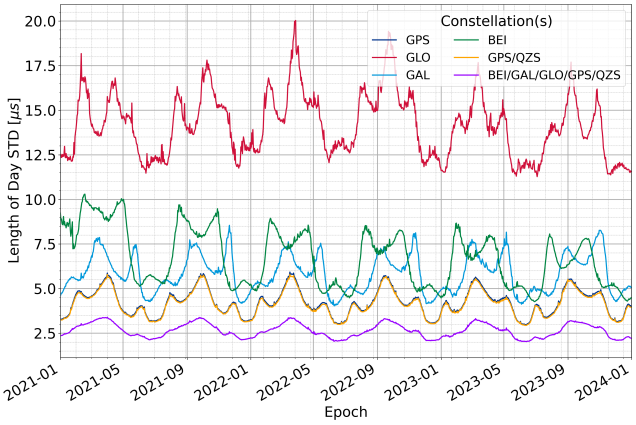

Figure 5.7: LOD standard deviations

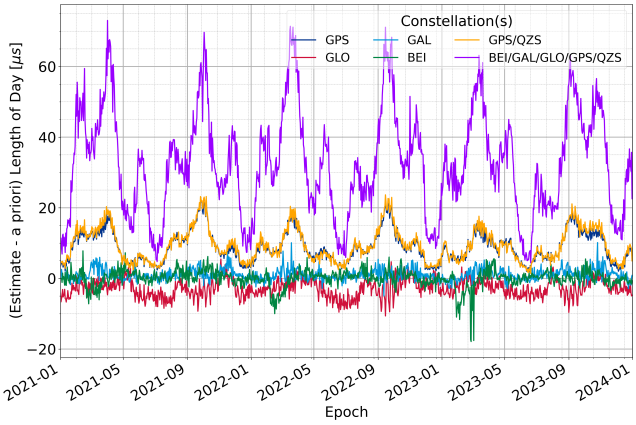

Figure 5.8: LOD estimates against a priori values

The LOD external comparison with the IERS EOP20C04 reference based on a 14-day moving average is shown in Figure 5.9, with a summary of the statistics in Table 5.3. All constellations seem to have a synchronised periodic variation with the same period as the differences between the DAILY and MGNSS sequences. The bias of the individual Galileo, GLONASS and Beidou constellations is positive, and close to null for the first two, while GPS alone shows a large negative bias. Furthermore, QZSS does not produce a major effect when combined with GPS, resulting in almost the same values as the individual GPS constellation due to the low number of QZSS satellites in the combination. As a result, the MGNSS combination also shows a negative bias, heavily influenced by GPS. Regarding the drift throughout the years, all constellations have a positive drift, which is again highly influenced by GPS, combined with QZSS, and Galileo alone. Additionally, the effect of combining the MGNSS results with other techniques in a multi-technique output can be seen in Figure 5.10, where the constant bias can be easily erased. However, the prevalence of a yearly drift reflects differences in the modelling which are harder to tackle.

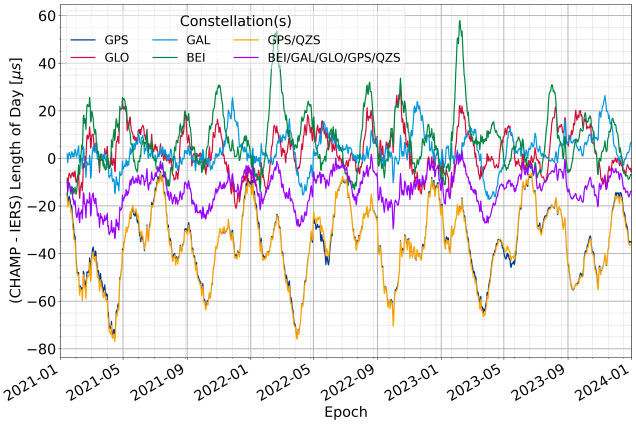

Figure 5.9: LOD estimated differences wrt. IERS EOP20C04

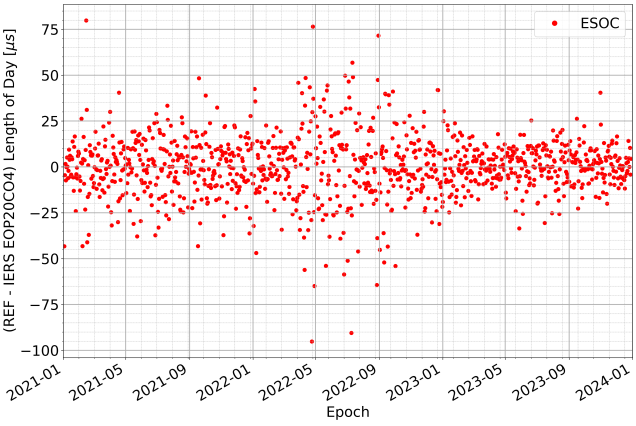

Figure 5.10: Comparison of internal ESOC reference wrt. IERS EOP20C04

Table 5.3: Main LOD statistics of individual and combined constellations compared against IERS EOP20C04

	Units	GPS	GLO	GAL	BEI	GPS/QZS	ALL
Mean/Bias	μs	-35.36	2.53	2.98	7.51	-35.84	-12.74
Std. dev.	μs	24.40	22.83	20.44	23.84	24.58	19.68
Drift	$\mu s/year$	2.20	0.42	1.86	0.59	2.45	2.45

Additionally, the relationship between solar declination and LOD variations was analysed to identify potential correlations. The only notable finding was the detection of a periodicity occurring six times per year, which did not provide further insight into the observed discrepancies in the LOD estimates. Overall, the GPS constellation displays distinct behaviour compared to other GNSS constellations, both combined with QZSS and as a standalone solution. The existence of a constant bias had been historically handled with corrections in the multi-techniques approach used by NSO to create and publish EOP estimates. However, when this behaviour is combined with the emergence of large drifts in the MGNSS LOD estimates, which were not identified in earlier analyses by NSO before 2021, the result indicates a potential anomaly in the GPS system's performance that affects the whole combination.

5.3.3 Polar Motion

The differences in the estimated values of the X and Y Polar Motion components, denoted as XPO and YPO, between the individual GNSS constellations and the combined MGNSS solution are illustrated in Figure 5.11 and Figure 5.12, respectively. The values are smoothed with a moving average of seven days over a three-year period to reduce short-term fluctuations and highlight longer-term trends. The plots highlight significant fluctuations in the polar motion estimates obtained with the GLONASS constellation, indicating potential challenges in its ability to consistently estimate polar motion components compared to the other constellations, the differences of which are one order of magnitude lower. The analysis reveals a three-times-per-year periodicity in the GLONASS differences, accompanied by an anomalous negative drift pattern in the Y component. The periodic fluctuations observed across all constellations reflect the influence of geophysical phenomena, such as the Chandler wobble and other seasonal variations, which inherently affect Earth's polar motion. The initial months of 2021 reflect the changes in the BeiDou constellation, the estimates of which stabilise once the constellation is complete. Additionally, GPS, combined with QZSS and in standalone configurations, jointly with Galileo, are the only constellations that present an invariable yearly pattern.

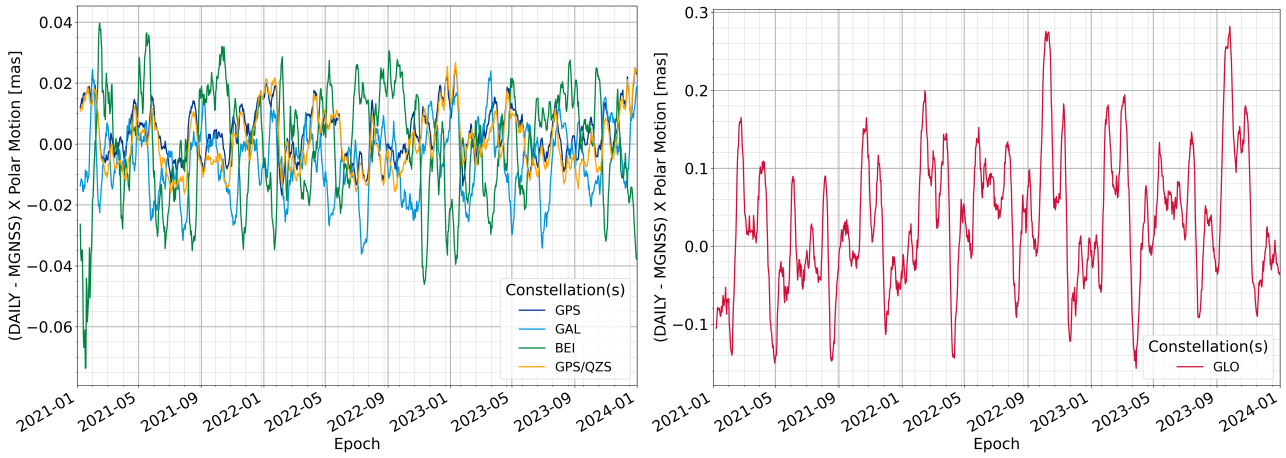

Figure 5.11: DAILY individual XPO differences wrt. the combined MGNSS solution

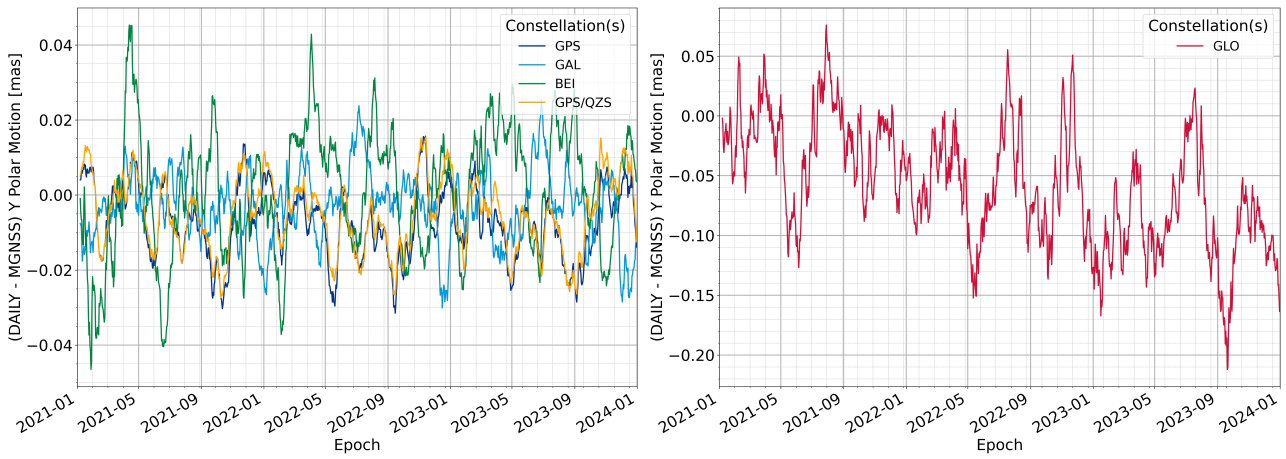

Figure 5.12: DAILY individual YPO differences wrt. the combined MGNSS solution

The standard deviations of the individual and combined solution estimates for XPO and YPO are presented in Figure 5.13 and Figure 5.14, respectively. Notably, the GLONASS deviations are highlighted, albeit without any discernible pattern. This behaviour is consistent with the large deviations observed in prior analyses, suggesting that GLONASS's performance may be inherently more variable compared to other constellations. Furthermore, the large initial differences in BeiDou estimates seen in 2021 can be attributed to the limited number of satellites and ground stations capable of receiving their signals at that time. As the number of BeiDou satellites increased and the network of receiving stations expanded, the standard deviations for BEI began to converge with those of Galileo, reaching a comparable level by 2022.

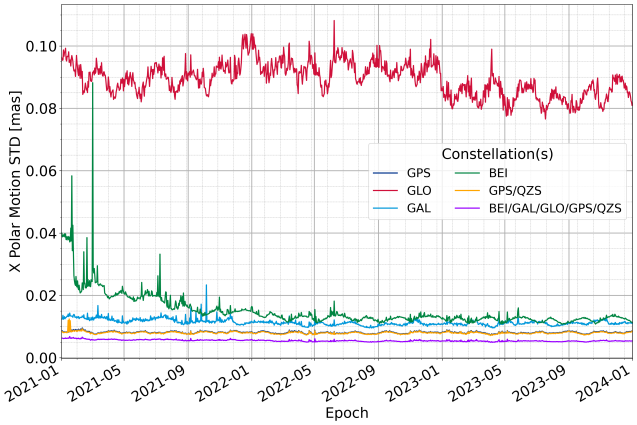

Figure 5.13: XPO standard deviation

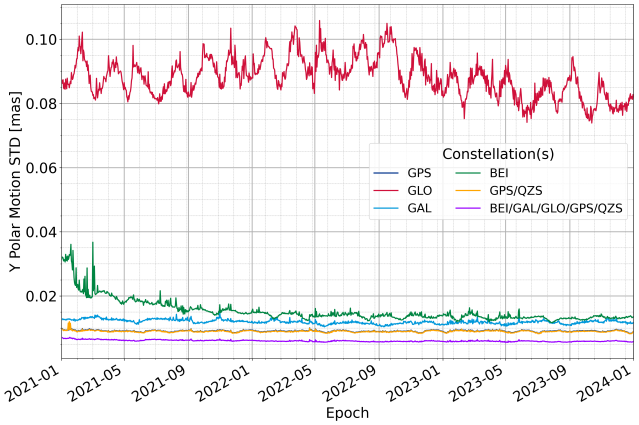

Figure 5.14: YPO standard deviation

The analysis of the differences between the estimated MultiArc and the a priori Bahn XPO and YPO values is shown in Figure 5.15 and Figure 5.16, respectively. In these figures, GLONASS also stands out, yet it reveals a different behaviour in its approach to XPO and YPO, as the differences do not exhibit uniform changes across both parameters.The XPO and YPO differences evolve independently, rather than in a correlated manner, suggesting that the ITRF alignment has a larger impact on the GLONASS estimates than on the other constellations.

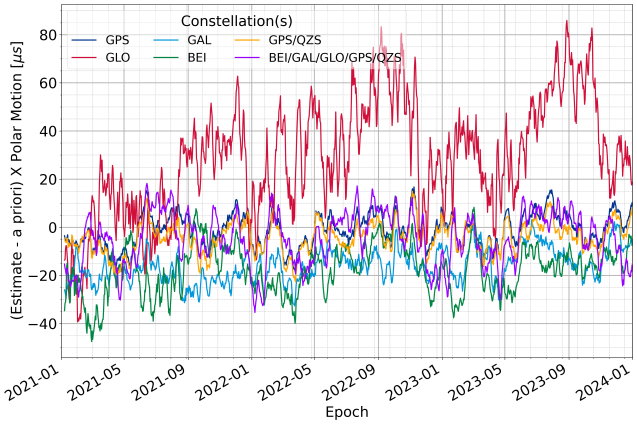

Figure 5.15: XPO estimates against a priori values

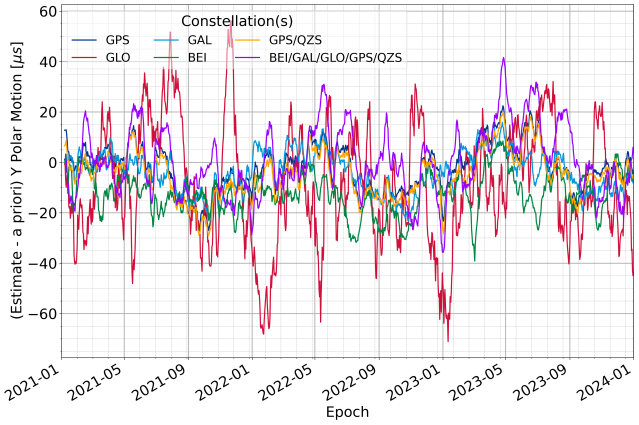

Figure 5.16: YPO estimates against a priori values

The XPO and YPO external comparison with the IERS EOP20C04 reference based on a 14-day moving average is shown in Figure 5.17 and Figure 5.18, with a summary of the statistics for both estimated parameters in Table 5.4. The differences in the estimation of the GLONASS constellation correspond to the same temporal pattern seen in the DAILY vs. MGNSS comparison, as the combined MGNSS bias is close to zero, specifically for the Y axis. Based on the statistics, GLONASS exhibits the highest variability and bias in both components, while Galileo demonstrates the most consistent performance with minimal bias and standard deviation.

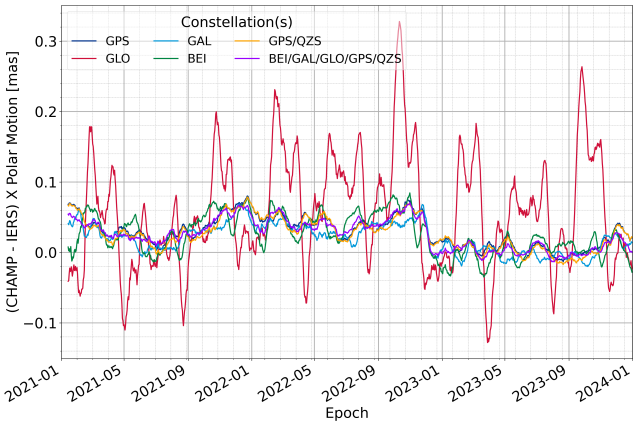

Figure 5.17: XPO estimated differences wrt. IERS EOP20C04

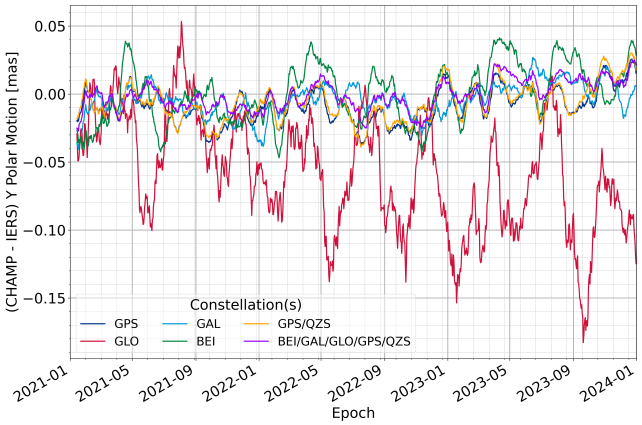

Figure 5.18: YPO estimated differences wrt. IERS EOP20C04

Table 5.4: Main XPO/YPO statistics of individual and combined constellations compared against IERS EOP20C04

	Variable	Units	GPS	GLO	GAL	BEI	GPS/QZS	ALL
Mean/Bias	XPO	*mas*	0.0296	0.0564	0.0204	0.0248	0.0267	0.0259
Std. dev.		*mas*	0.0260	0.1043	0.0272	0.0364	0.0266	0.0252
Drift		*mas/year*	-0.0132	0.0109	-0.0119	-0.0124	-0.0128	-0.0136
Mean/Bias	YPO	*mas*	-0.0085	-0.0588	-0.0039	0.0000	-0.0064	-0.0010
Std. dev.		*mas*	0.0185	0.0756	0.0204	0.0289	0.0189	0.0167
Drift		*mas/year*	0.0054	-0.0262	0.0062	0.0113	0.0062	0.0069

Additionally, the relationship between solar declination and X and Y polar motion component variations was analysed to identify potential correlations. As a result, no clear pattern or significant correlation was found to suggest a direct influence of solar declination on these parameters. Overall, the CHAMP estimated GLONASS constellation values show poor performance compared to the other constellations. However, as the standard deviation of GLONASS is much larger than the others, it is not expected to have a large weight in the combination.

5.3.4 Polar Motion Rates

The differences in the estimated values of the X and Y Polar Motion component rates, denoted as XPOR and YPOR, between the individual GNSS constellations and the MGNSS solutions are illustrated in Figure 5.19 and Figure 5.20, respectively. The values are smoothed with a moving average of seven days over a three-year period to reduce short-term fluctuations and highlight longer-term trends. GLONASS continues to exhibit significant fluctuations compared to the other constellations, but there is no visible drift in the X and Y component rate differences, as shown in Figure 5.19 and Figure 5.20.

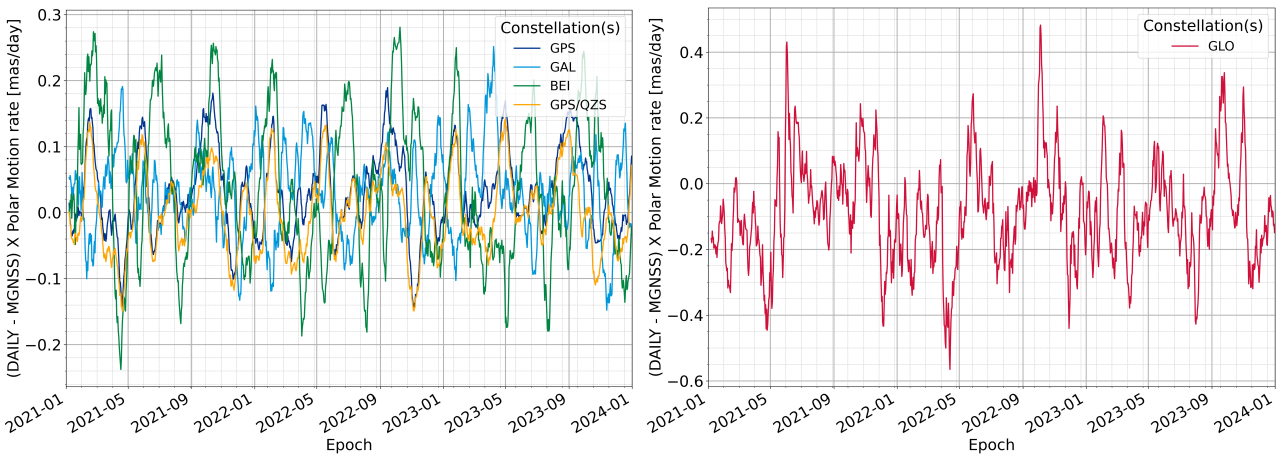

Figure 5.19: DAILY individual XPOR differences wrt. the combined MGNSS solution

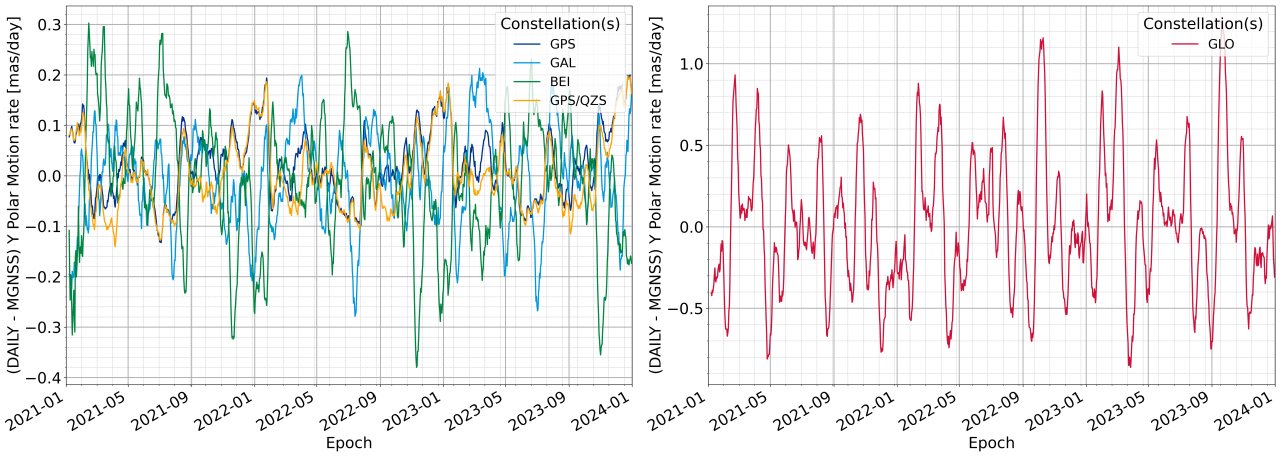

Figure 5.20: DAILY individual YPOR differences wrt. the combined MGNSS solution

The standard deviations of the individual and combined solution estimates for XPOR and YPOR are presented in Figure 5.21 and Figure 5.22, respectively. While the results are similar to the standard deviation of the poles, the rates show more variability. GLONASS presents large deviations in a wave-like pattern with a mean standard deviation value larger than the absolute difference of all other constellations. Additionally, Galileo and BeiDou show larger variability for the YPOR estimates. Finally, the GPS constellation standard deviation remains considerably constant as the lowest individual value for both rates, heavily influencing the combined solution, which results in a slightly smaller variation.

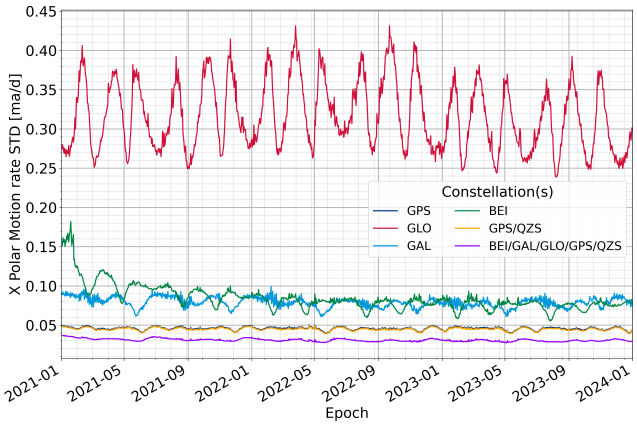

Figure 5.21: XPOR standard deviations

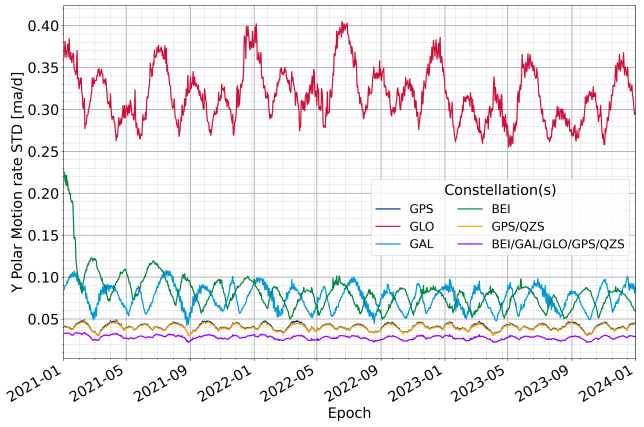

Figure 5.22: YPOR standard deviations

The analysis of the differences between the estimated MultiArc and the a priori Bahn XPOR and YPOR values is shown in Figure 5.23 and Figure 5.24, respectively. In this case, the combined solution is the one that shows the largest variability in both rates, indicating that the MNGSS estimates diverge from the a priori values following the stacked trends of all individual constellations except GLONASS in XPOR, and showing a clear yearly pattern in YPOR that is highlighted by a significant increase in values around the end of January of each year. Closely following these variations are the values of GLONASS, showing large amplitude peaks for XPOR.

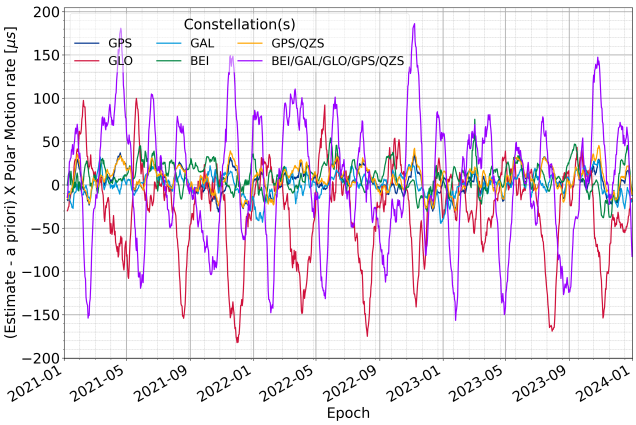

Figure 5.23: XPOR estimates against a priori values

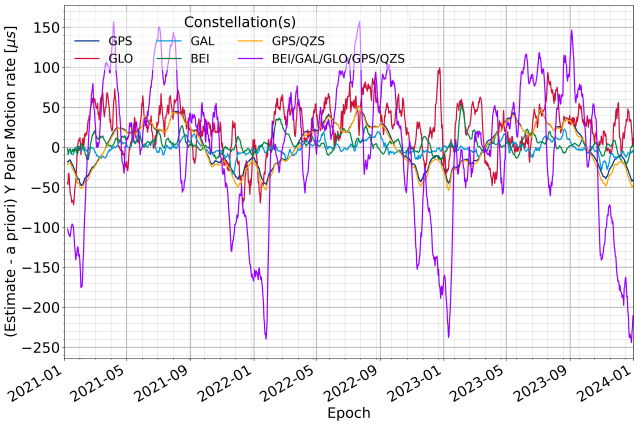

Figure 5.24: YPOR estimates against a priori values

The XPOR and YPOR external comparison with the IERS EOP20C04 reference based on a 14-day moving average is shown in Figure 5.25 and Figure 5.26, with a summary of the statistics for both estimated parameters in Table 5.5. Both X and Y axes show larger differences in the GLONASS constellations with a similar shape pattern, even if are more pronounced in the Y-axis. All other constellations seems to behave similarly among them.

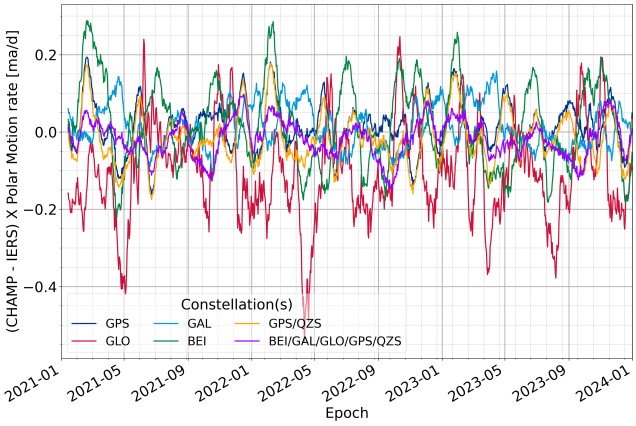

Figure 5.25: XPOR CHAMP products difference wrt. IERS EOP20C04

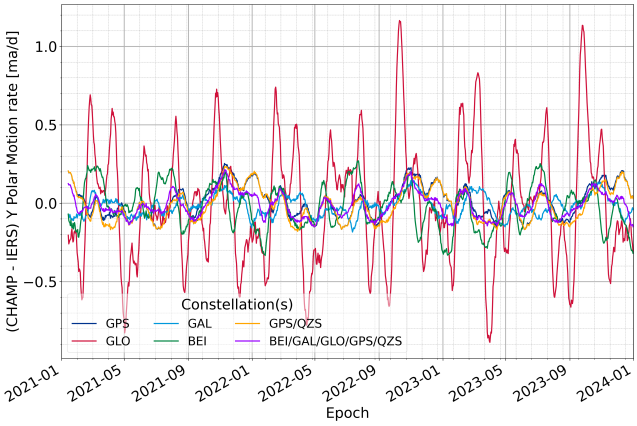

Figure 5.26: YPOR CHAMP products difference wrt. IERS EOP20C04

Table 5.5: Statistics of constellations compared against IERS

	Variable	Units	GPS	GLO	GAL	BEI	GPS/QZS	ALL
Mean/Bias	XPOR	*mas*	0.0151	-0.1055	0.0131	0.0204	-0.0159	-0.0164
Std. dev.		*mas*	0.1222	0.3220	0.1370	0.1920	0.1254	0.1119
Drift		*mas/year*	0.0043	0.0054	-0.0058	-0.0218	0.0016	-0.0019
Mean/Bias	YPOR	*mas*	0.0141	-0.0085	-0.0171	-0.0245	-0.0064	-0.0104
Std. dev.		*mas*	0.1449	0.5298	0.1353	0.2095	0.1480	0.1266
Drift		*mas/year*	0.0106	0.0218	0.0076	-0.0283	0.0102	-0.0024

The table shows the comparison of the polar motion component rates across GNSS constellations against IERS standards. The mean XPOR bias seems to be heavily influenced by GLONASS and the GPS/QZSS combination. In contrast, the YPOR combined mean is more balanced between the different individual constellations. Additionally, for both rates, the BeiDou constellation results seem to be the dominant influence in adding the drift to the combination. Overall, the CHAMP estimated GLONASS constellation rates also show poor performance compared to the other constellations. However, as the standard deviation of GLONASS is again much larger than the others, it is not expected to have a large weight in the combination.

5.4 Ground Station Coordinates

As the processing of GNSS data for Earth Orientation Parameters and precise orbit determination relies heavily on the accuracy of the input data, the role of ground stations is critical. The network of GNSS tracking stations, each providing precise measurements, serves as the backbone for multi-GNSS solutions. The Navigation Support Office relies on the stations of the IGS network (International GNSS Service, 2024a), as well as on ESA's GNSS Observation Network (Agency, 2024), for a global network. These stations contribute essential data to the generation of combined MGNSS products, enabling the refinement of satellite orbits, clocks, and other key parameters. Each station within the network can track and provide measurements for multiple GNSS constellations. Figure 5.27 illustrates the number of qualified and selected stations for each constellation that contribute to the DAILY solutions over time, with a maximum number of 200 stations per constellation for both the individual and combined solutions. This extensive station network of well-calibrated stations directly contributes to enhancing the quality of the GNSS products.

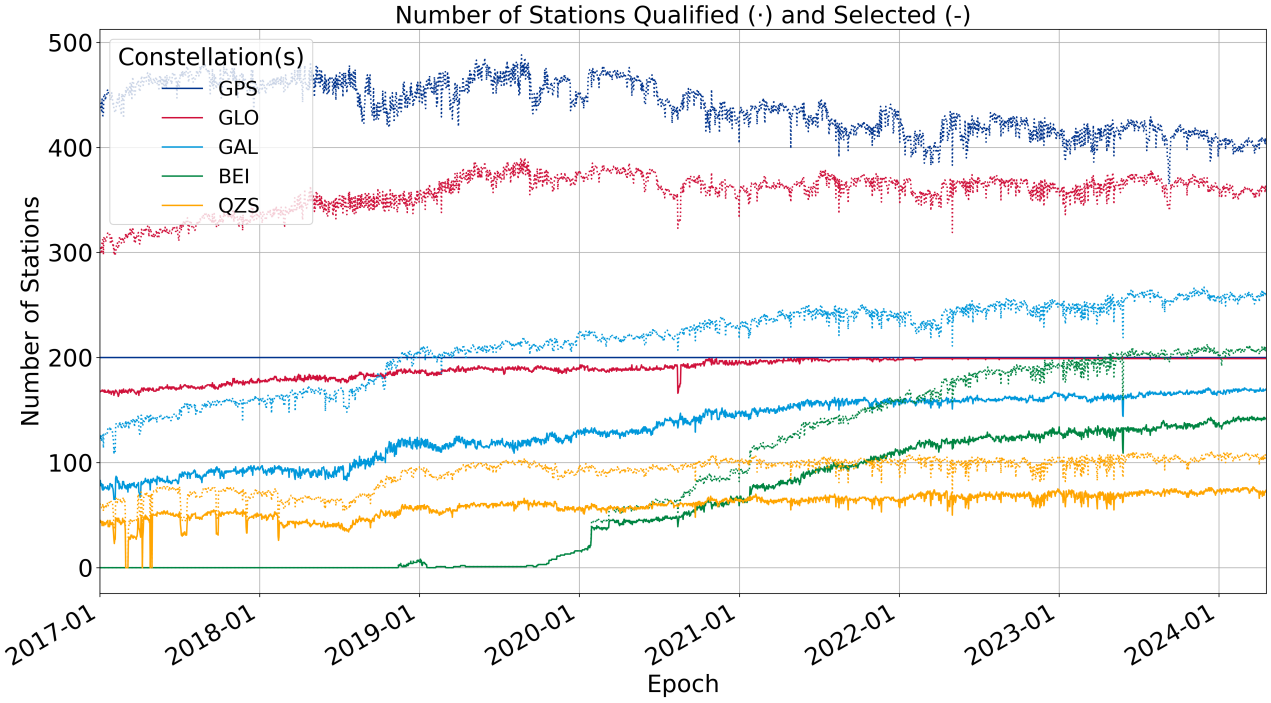

Figure 5.27: Qualified (···) and selected (—) ground stations for each individual constellation

Throughout the years, the IGS has made significant strides in expanding its station network and enhancing multi-GNSS tracking capabilities. One of the most impactful changes observed during the period under review is the considerable increase in the number of qualified and selected stations capable of tracking the BeiDou constellation. While this expansion improves the robustness of the individual BeiDou solutions and bolsters the performance of the entire MGNSS network, such a change could negatively influence the results if not properly accounted for, particularly in terms of biases or inconsistencies introduced by the newly added stations, which have nearly doubled in size. The shift from approximately 60 stations in 2022 to around 120 in 2023 for the selected stations might have a substantial impact on the MGNSS results and is further analysed in Section 6.2.1.

Once the stations are selected, the alignment with the International Terrestrial Reference Frame becomes a critical step, as described in Section 5.4.1. A detailed comparison of the scale values is performed to ensure consistency in the global reference frame. The 3D and East-North-Up (ENU) station coordinate differences are then thoroughly analysed in Section 5.4.2, where both the magnitude of the differences and their geographic distribution are considered. This analysis helps to identify any station outliers that may be contributing to the degradation of results, allowing for their exclusion or adjustment in subsequent processing. The continuous refinement of station selection and alignment ensures that only the most reliable data is used, which is crucial for maintaining the high standards of precision required for GNSS-based Earth orbit determination. Additionally, the initial analysis comparing individual and combined solutions for atmospheric delays and gradients revealed no significant differences, aside from a few outliers; thus, this aspect was not a priority for this research.

5.4.1 ITRF Alignment

The GNSS station coordinates are aligned to the International Terrestrial Reference Frame using a minimum constraint condition. This enforces No-Net-Translation and No-Net-Rotation constraints, ensuring that the station network remains fixed relative to the ITRF, without any unintended movement or rotation. These constraints are applied with tight control, using a standard deviation of $\sigma = 10^{-6}$ km for No-Net-Translation and $\sigma = 10^{-3}$ km for No-Net-Rotation, to maintain high precision in the alignment process. Once the rigid alignment constraints are defined, a Helmert transformation is applied to freely adjust the scale factor, correcting for any size discrepancies between the station positions and the reference frame. The scale differences over time between the individual constellation and the combined solution are shown in Figure 5.28, expressed in parts per billion (ppb). GLONASS shows pronounced scale variations compared to other constellations, with a clear annual pattern, evidencing that the alignment behaves differently for this constellation between the individual and combined solution. As the Helmert transformation aligns the GNSS station network to the ITRF by minimising the residuals between GNSS station coordinates and ITRF coordinates, this process could amplify GLONASS-specific scaling effects in the combined solution if GLONASS experiences unique biases or periodic variations that are not as pronounced in other constellations, leading to additional inconsistencies.

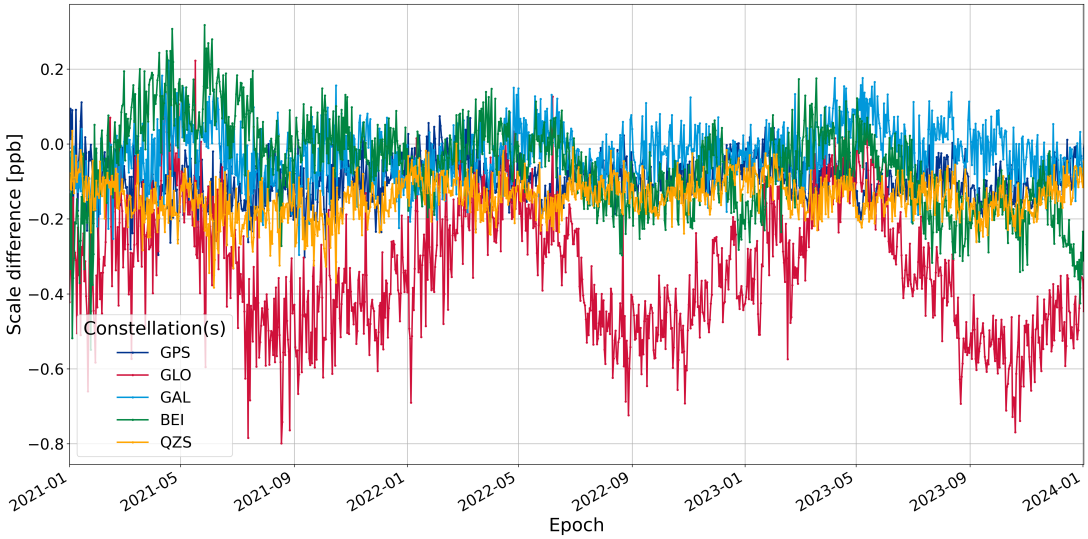

Figure 5.28: ITRF alignment individual constellation scale values wrt. combined MGNSS constellation

5.4.2 Station Coordinates

Following the alignment of station positions to the International Terrestrial Reference Frame, the subsequent comparison evaluates how well each individual solution conforms to the combined MGNSS solution, ensuring the stability of the station network. To achieve this, the root mean square values of the 3D positional differences over the 3-year period are calculated between each station in the individual and combined MGNSS solutions. These RMS values are depicted in a histogram in Figure 5.29 to analyse the distribution of the differences and help in the identification of potential outlier stations.

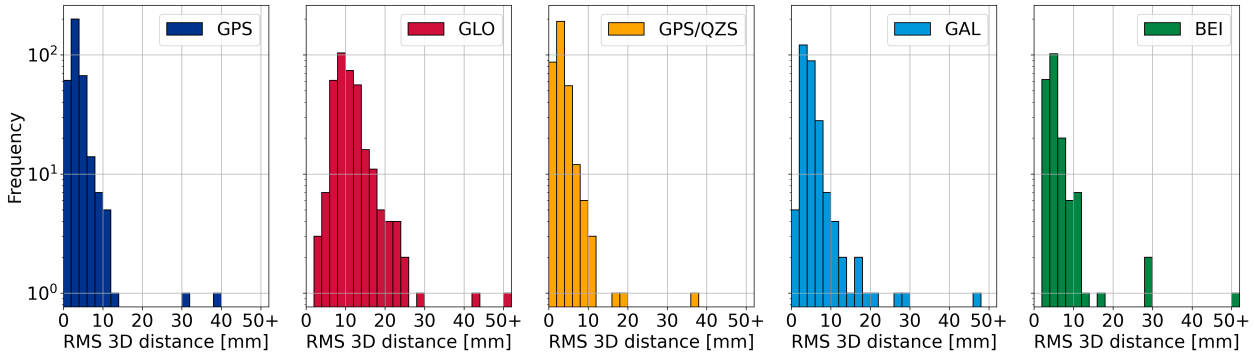

Figure 5.29: RMS 3D distance histograms between the individual and combined solutions

The constellation-specific results reveal varying degrees of station deviations above the 10 mm threshold. GPS, along with its combination with QZSS, demonstrates a highly stable network, with only 2.24% and 1.68% of stations, respectively, exceeding the 10 mm RMS difference, indicating strong consistency with the combined solution. Galileo and BeiDou show moderate consistency, with 5.30% and 5.94% of stations exceeding 10 mm, reflecting generally well-aligned networks with some notable discrepancies. In contrast, GLONASS exhibits significant deviations, with 50.00% of stations showing RMS differences greater than 10 mm, and 3.71% exceeding even 20 mm, which is consistent with the previously observed variations in scale during the ITRF alignment. Figure 5.30 further highlights that the majority of the positional errors arise from the Up direction in the East-North-Up (ENU) frame. This observation aligns with the scaling differences previously discussed, as vertical positioning is often more sensitive to such scale variations. Additionally, this pattern could potentially be linked to biases in the clock estimates, shown in the following Section 5.6, which would affect the vertical component more significantly than the horizontal components, further contributing to the discrepancies observed in the station positions.

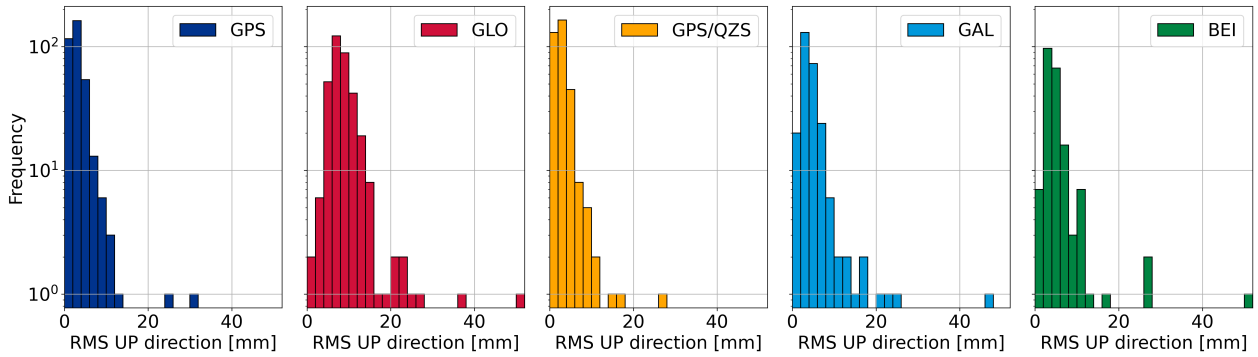

Figure 5.30: RMS UP distance histograms between the individual and combined solutions

The mean 3D distance RMS world map between the individual and combined solutions, as shown in Figure 5.31, reveals the spatial distribution of constellation-specific ground station outliers across the globe. Based on the previous histograms, values exceeding 16 mm are highlighted to emphasize stations that exhibit significant discrepancies, either consistently across all constellations or within a specific subset. This visualization draws attention to specific underperforming stations and identifies regions where GNSS alignment challenges are most pronounced. Notably, the highest concentration of these differences is located in the Asia-Pacific region, indicating a region-specific clustering of larger RMS values.

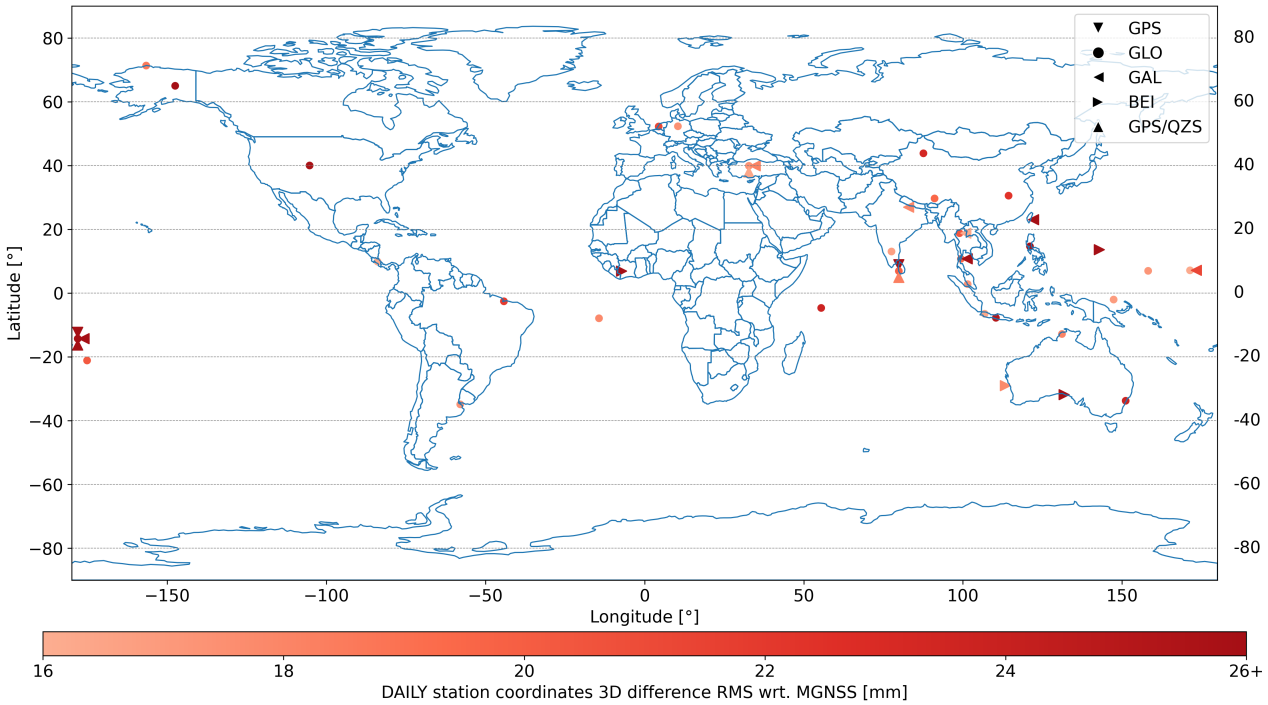

Figure 5.31: Mean 3D distance RMS world map between the individual and combined solutions

The ground stations showing larger 3D RMS differences between the DAILY and MGNSS coordinates for at least two constellations are detailed in Table 5.6.The table includes empty cells for stations that were not tracked by a particular constellation during the reprocessing period. Notably, the YAR300AUS station is only included in the solution on five distinct days, spread throughout the first half of 2022, and the ANKR00TUR station was decommissioned in 2022 (Royal Observatory of Belgium, 2024). An examination of the station hardware reveals that both SGOC00LKA and YAR300AUS are equipped with the JAVAD TRE-3 receiver and JAVAD Ring Antenna G5T, while YAR300AUS and JOG200IDN share the Septentrio PolarX5 receiver (International GNSS Service, 2024a). These similarities in hardware across stations suggest that the observed inter-constellation differences are unlikely to be hardware-related, at least in estimating the station coordinates. Additional anomalies are noted in station-specific constellations, with NCKU's Galileo and YKRO's BeiDou estimates showing clear signs of misbehaviour. This hints at potential issues with the specific frequency bands used by those constellations at these stations, possibly indicating signal interference or unmodelled biases affecting their performance.

A detailed analysis of the FTNA00WLF station, a representative station which has the highest 3D RMS differences between DAILY and MGNSS for all constellations, shows constant biases in the UP component of the station's height relative to the static IGS height value as of January 1st, 2021. Notably, the inclusion of QZSS in the GPS/QZSS combination leads to significant alterations in the shape of the height deviations, indicating that the additional QZSS signals could have an effect on the vertical positioning.

Table 5.6: Ground stations with largest 3D RMS coordinate differences between DAILY and MGNSS

				3D RMS [mm]				
Station	**LAT [deg]**	**LON [deg]**	**Height [m]**	**GPS**	**GLO**	**GAL**	**BEI**	**QZS**
FTNA00WLF	-14.31	-178.12	84.9	38.8	100.4	29.0	-	37.6
ANKR00TUR	39.89	32.76	974.8	13.8	17.4	18.1	-	18.3
CMUM00THA	18.76	98.93	308.962	10.6	20.4	16.3	-	10.2
WUH200CHN	30.53	114.36	25.8	11.5	22.3	7.9	12.9	10.7
SGOC00LKA	6.89	79.87	-78.5	30.2	19.9	6.3	6.3	18.3
YAR300AUS	-29.05	115.35	242.4	10.2	13.8	-	17.8	10.5
JOG200IDN	-7.76	110.37	174.4	11.8	25.1	13.2	5.7	9.1

5.5 Satellite Parameters

This section presents a comprehensive analysis of satellite-specific parameters, beginning with the assessment of satellite state vector parameters through overlap analysis. Satellite overlaps compare satellite positions and velocities at the boundaries of consecutive processing intervals, offering insights into the stability and accuracy of orbit solutions. The satellite overlaps for each individual constellation and the combined GNSS solution, as detailed in Section 5.5.1, provide insights into the consistency and alignment of these parameters across constellations. Additionally, estimates for the Empirical CODE Orbit Model parameters, which are essential for understanding non-gravitational forces acting on the satellites, are presented in Section 5.5.2. Finally, the empirical accelerations, capturing systematic forces at specific orbital frequencies, are included in Section 5.5.3.

5.5.1 Satellite Orbit

This section assesses the estimated satellite positions from the individual and combined solutions using orbit overlaps. These serve as a critical indicator for assessing the accuracy and consistency of satellite orbit solutions over consecutive time periods. In this case, the orbit overlaps are calculated by comparing the positions of a satellite at the boundaries of successive orbit arcs, spanning one day, to identify any discrepancies or discontinuities. Such overlaps provide a valuable means of evaluating the quality of orbit determination processes, as significant differences may indicate errors or inconsistencies in the modelling of satellite dynamics, force models, or observational data.

The nominal DAILY sequence only solves the SP3 orbit data before the ITRF alignemnt. Consequently, this process is adjusted to obtain orbit values both before and after the alignment. Each aligned MultiArc solution is subsequently propagated through an additional Bahn estimation, with all parameters fixed. Once the orbit values are derived for both the DAILY and MGNSS cases, the results are compared, Additionally, to provide a more detailed assessment of the error distribution, the individual RMS components in the Radial-, Along-,

and Cross-track directions are computed for 2023, which is a representative year for the current time interval. This facilitates a comprehensive examination of the orbit precision along each axis. To ensure the accuracy and reliability of these values, a dynamic outlier removal process has been implemented, with tailored settings applied to each constellation to optimally identify and exclude anomalies. These anomalies are defined as a combination of values larger than three standard deviations over the mean value, approximating to a normal distribution, and additional constellation-specific limits to account for possible sporadic satellite malfunctions. For instance, identifying the malfunction of the BEI-M215 satellite during 2023, and, subsequently, not adding it to the overall statistic. The comparative analysis of these values is illustrated on Figure 5.32 and Figure 5.33, respectively. Each column in the plot represents the DAILY solution for a specific year, distinguished by a unique colour to facilitate comparison across years. Overlaying these, the MGNSS solution is shown as a pale red hyphened column, indicating its inclusion within the combined solution.

The constellation-wise 3D RMS orbit overlaps plots illustrate the strong performance of GPS, Galileo, and BeiDou MEO satellites, which consistently exhibit lower RMS overlaps, indicating higher orbit determination precision. In contrast, GLONASS shows significantly higher RMS values, which can be attributed to a lack of integer ambiguity resolution and less accurate orbital models. Additionally, several GLONASS satellites are impacted by hardware failures, further affecting their orbit determination quality. For the IGSO and GEO satellites within BeiDou and QZSS, the orbit overlap performance is notably reduced, primarily due to their unique observation geometry, resulting from their higher altitude and geostationary nature. The use of 24-hour arcs is sub-optimal for these satellites, as this period coincides with their orbital period, leading to less accurate overlap results and overall orbit precision. As a result, the BEI-GEO satellites are not considered in the comparison. Interestingly, comparing the combined MGNSS against the individual DAILY solutions, Galileo's accuracy declines, while GPS and others maintain or even improve their performance, highlighting differences in the integration of various constellations. When considering just 2023 as a reference year, the differences in the three components can be compared for each individual and combined solution. As a result it can be seen that all satellites in medium Earth orbit accumulate the major differences in the along-track direction, while the satellites in IGSO highlight large differences in the radial direction. The decrease in accuracy for Galileo in the combined solution is slightly concentrated in the along-track direction, which is directly affected by variations in orbital speed and periodic alignment adjustments.

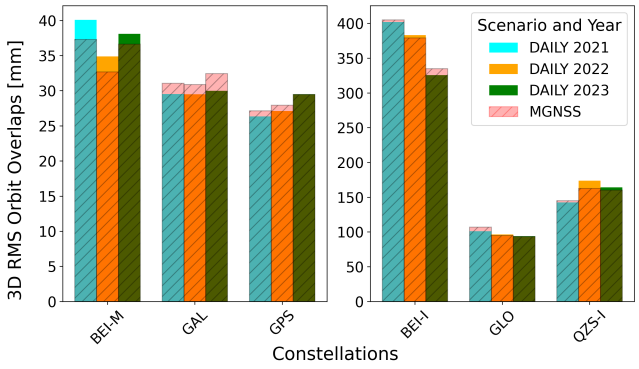

Figure 5.32: Constellation 3D RMS orbit overlaps

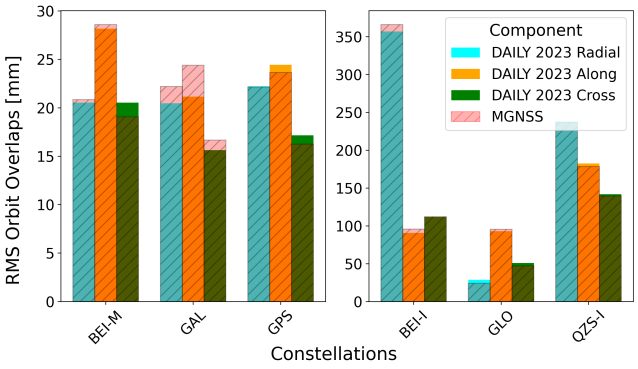

Figure 5.33: Component RMS orbit overlaps in 2023

5.5.1.1 GPS Constellation

The 3D orbit overlaps evolution for GPS satellites in both individual and combined solutions is depicted in Figure 5.34. This three-year visualisation provides a comprehensive perspective on the orbital performance of each GPS satellite. By tracking the evolution of individual satellites over time, potential anomalies or performance degradations can be easily pinpointed. Furthermore, the trends across different satellite blocks or orbital planes become more apparent, revealing insights into the relative stability and accuracy of each group. There is a noticeable decrease of accuracy in satellites such as GPS-44, GPS-59, GPS-61, and GPS-70, which correspond to the older GPS IIR and IIF blocks, particularly standing out in the final year of the analysis. This decline in precision is slightly mitigated after the combination of MGNSS solutions, although the aforementioned satellites continue to exhibit degraded performance. Despite this trend, certain satellites, like GPS-47, which was nearing the end of its lifecycle in 2022, demonstrate better-than-expected results. In contrast, the newest satellites from the IIIA block, including GPS-74 through GPS-79, consistently rank among the best orbit overlaps. As a result, this might indicate that there might be deficiencies in the modelling of the older GPS constellation blocks.

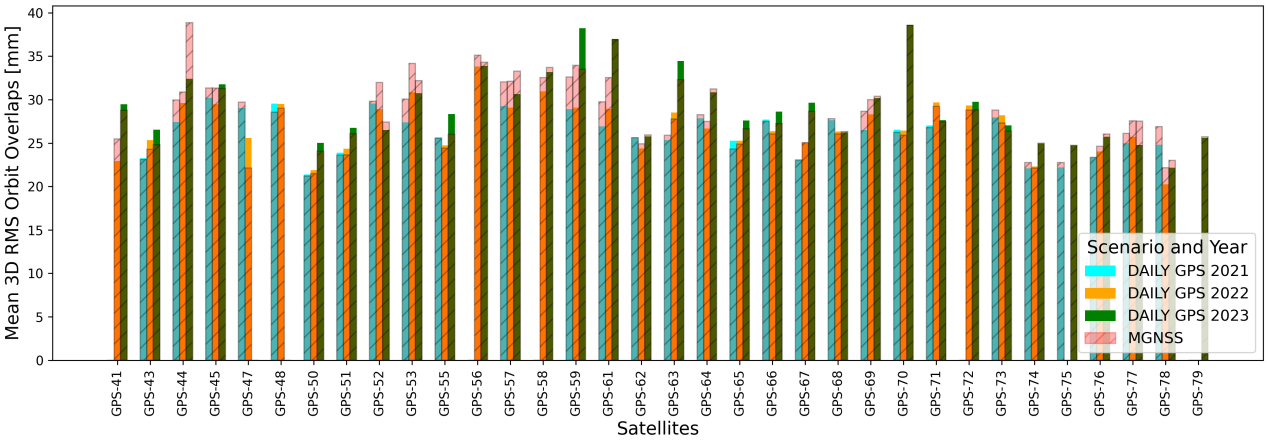

Figure 5.34: GPS 3D RMS orbit overlaps for the individual and combined solutions

5.5.1.2 GLONASS Constellation

The 3D orbit overlaps evolution for GLONASS satellites in both individual and combined solutions is depicted in Figure 5.35. The overall accuracy of the GLO satellites remains considerably stable during the 3-year interval, except for the older S-M block GLO-719, and the M block GLO-735 satellites, which have both greatly surpassed the projected operational lifespan of seven years. Additionally, the newer batch of GLONASS-K satellites, from GLO-702 to GLO-707, show better orbit overlaps for the combined solution, which could be attributed to a better modelling for the block K, as the latest GLONASS-M satellites launched after 2018, comprising GLO-757 to GLO-761, seem to have a degraded performance compared to the older satellites of the same block.

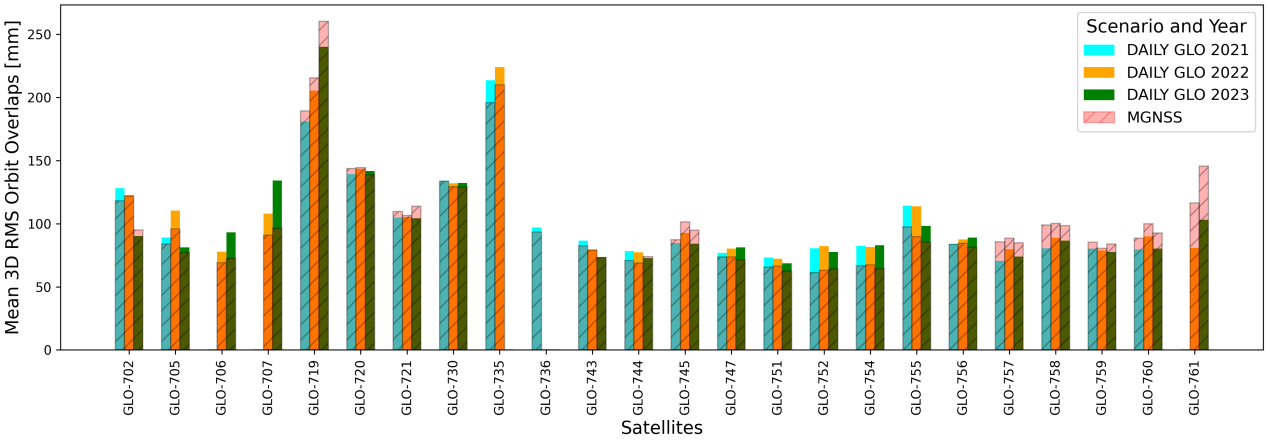

Figure 5.35: GLO 3D RMS orbit overlaps for the individual and combined solutions

5.5.1.3 Galileo Constellation

The 3D orbit overlaps evolution for Galileo satellites in both individual and combined solutions is depicted in Figure 5.36. Notably, the combined solution consistently shows worse overlap performance than the individual solution, suggesting that Galileo's independent models and parameters yield higher accuracy on their own. The stability of the 3D overlap values over the 3-year period, with only minor increases observed in 2023, reinforces the robustness of Galileo's individual orbit models and processing framework. When Galileo is combined with other constellations, each of which uses distinct models, reference frames, and sometimes differing assumptions, these differences introduce inconsistencies that degrade the solution's overall accuracy. This degradation in the combined setting indicates that Galileo's models and parameters are well-calibrated in isolation but are negatively affected by the alignment and harmonisation requirements of a multi-GNSS solution. Consequently, the results highlight the strong performance of Galileo's standalone models and underscore the challenges in achieving optimal integration within a combined framework.

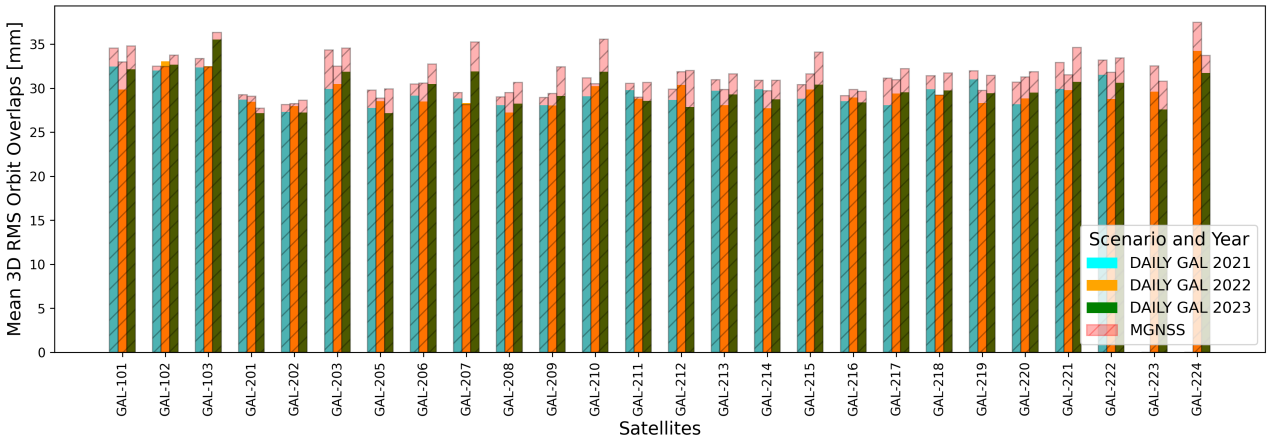

Figure 5.36: GAL 3D RMS orbit overlaps for the individual and combined solutions

5.5.1.4 BeiDou Constellation

The 3D orbit overlaps evolution for BeiDou satellites in both individual and combined solutions is depicted in Figure 5.37, which divides the constellation into BEI-M and BEI-I satellites, as their accuracy is heavily orbit-dependant. Geostationary BEI-G satellites are not considered due to their low accuracy. Overall, the BeiDou satellite orbit determination benefits from the combination, even for extreme cases such as in BEI-M215. With the current analysis, it was possible to see the initial malfunction of BEI-M215 already during 2023, before its announced degradation in accuracy in 2024 (Xia et al., 2024). Since the beginning of March 2024, BEI-M215 has one of its two solar panels no longer pointed towards the Sun, but perpendicular to the spacecraft-fixed X-axis. As such, there is no pitch motion of the panel around the Y-axis any more, and the pitch angle is kept fixed to 90 degrees. For this reason, the information of the year 2023 for this satellite is not taken into account for the whole constellation analysis. After spotting this issue in mid-2024, the Navigation Support Office has developed a new box-wing model for BEI-215 in order to alleviate the solar panel mismodeling, but it is out of the scope of this project. The BeiDou IGSO satellites show 3D RMS DAILY vs MGNSS differences among them that surpass 20 centimetres, evidencing that the different inclined orbits do not provide robust results with the current settings. Overall, there is a slightly worse performance in 2021 which can be attributed to the limited ground station network, which doubled in size during the interval of analysis.

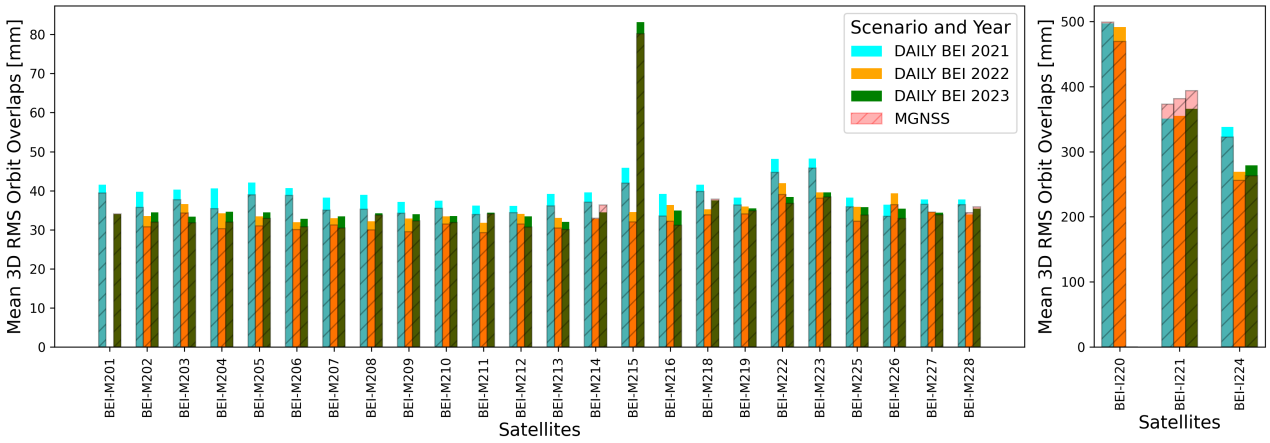

Figure 5.37: BEI 3D RMS orbit overlaps for the individual and combined solutions

5.5.1.5 GPS and QZSS Constellation Combination

The 3D orbit overlaps evolution for the GPS/QZSS combination in both this subgroup and the MGNSS solutions is depicted in Figure 5.35. The inclusion of QZSS into GPS does not seem to affect the GPS overlaps. This is a good indicator to verify that the combination of QZSS and GPS allows to merge QZSS data into the MGNSS solution without modifying the GPS standalone constellation. However, as seen with BeiDou, QZSS has the same issues in parametrising the arcs for the IGSO satellites, even if lower differences are seen in this case.

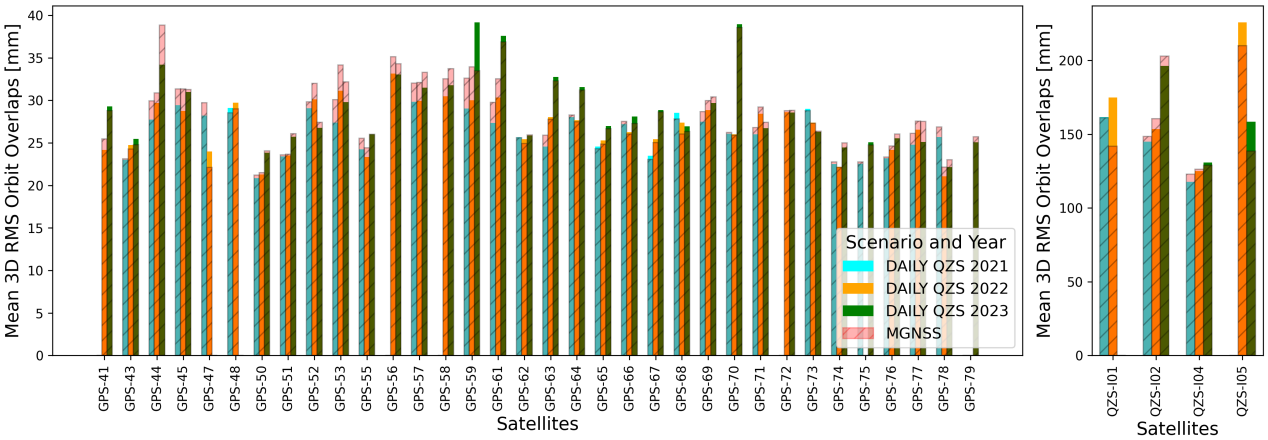

Figure 5.38: GPS/QZSS 3D RMS orbit overlaps for the individual and combined solutions

5.5.2 Empirical CODE Orbit Model

This section examines the estimated paramters of the Empirical CODE Orbit Model across the three principal axes of the DAILY and MGNSS solutions. The initial a priori model applied is the box-wing model, which offers a basic modelling estimation of non-gravitational perturbations, accounting for solar radiation pressure, Earth albedo and infrared radiation pressure, among other smaller effects.

thermal effects, and other non-gravitational perturbations.

Building on this foundation, ECOM introduces adjustable empirical parameters to absorb remaining non-gravitational modelling errors based on the observed motion of the satellites. These adjustments are crucial for enhancing the representation of perturbative forces experienced by different GNSS constellations, with refinements and added terms designed to address the unique behaviour and dynamics of each constellation. In this analysis, ECOM1 is used for both the individual and the combined solution, consisting of five components distributed across the satellite's axes, as explained in Section 3.6.1.4. The evolution of ECOM values for the representative GLO-719 satellite is shown in Figure 5.39. There are semi-annual patterns for all the estimates, indicating that the ECOM parameters are actively compensating for the mismodeling of non-gravitational forces. These patterns reflect the satellite's exposure to direct solar radiation pressure, variations in Earth's albedo and infrared radiation, and the effects of thermal and yaw attitude changes over time.

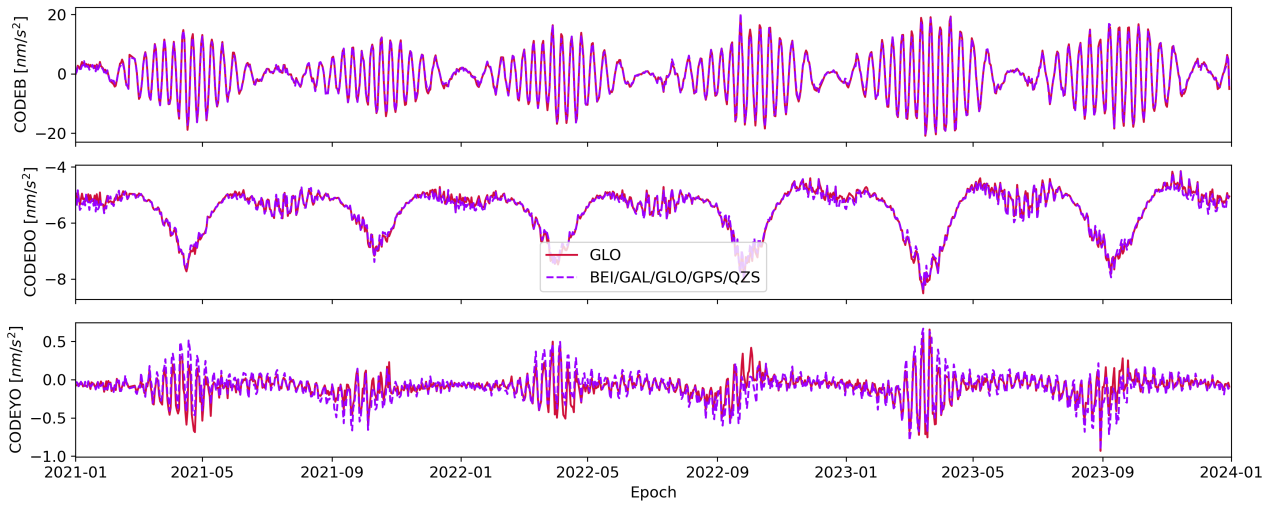

Figure 5.39: DAILY and MGNSS ECOM estimated parameters for GLO-719 satellite

The mean yearly ECOM1 parameters differences between the DAILY and MGNSS solutions for all constellations are shown in Figure 5.40. The sign of this absolute differences indicates whether the estimated accelerations increase or decrease compared to the MGNSS solution. Positive values reflect that the accelerations were higher in the individual solution, and vice versa. To better understand the relative impact of these differences, Figure 5.41 illustrates the percentage change with respect to the initial value, providing insight into the magnitude of the variations. A detailed look at the largest absolute differences, combined with their percentage change, highlights the most notable discrepancies in the B-axis across all constellations. On the Y-axis, although the percentage change is relatively high, the values are typically one to two orders of magnitude smaller, resulting in less significant overall differences in the solutions. This suggests that, while variations in the Y-axis are present, they do not have as strong an effect on the combined solution as those observed on the B-axis. Additionally, changes in the D-axis are only relevant for the GPS and GLONASS constellations. Overall, the reduction of the mean difference for GPS in the combined solution may indicate that combining constellations helps refine GPS-specific modelling, reducing the need for empirical accelerations to account for non-gravitational forces. This could imply that certain non-gravitational effects in the individual GPS solution may not be fully accounted for, whereas the combined approach compensates for these gaps, leading to a more balanced model.

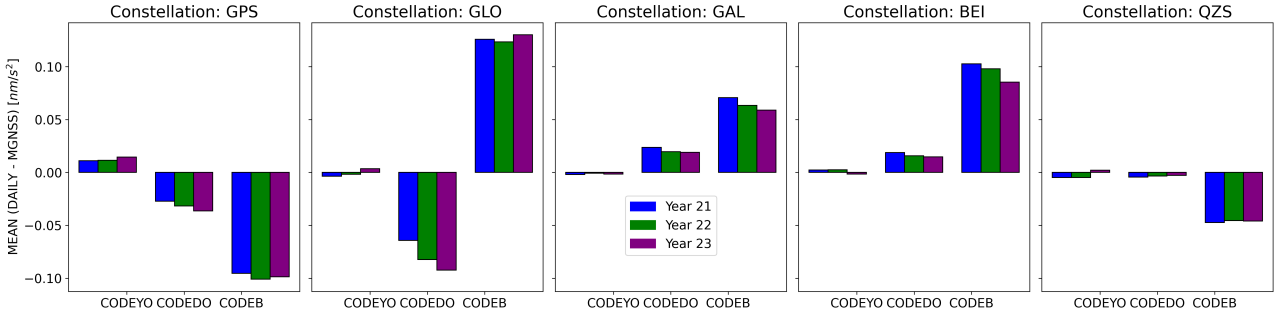

Figure 5.40: Mean DAILY vs. MGNSS ECOM differences

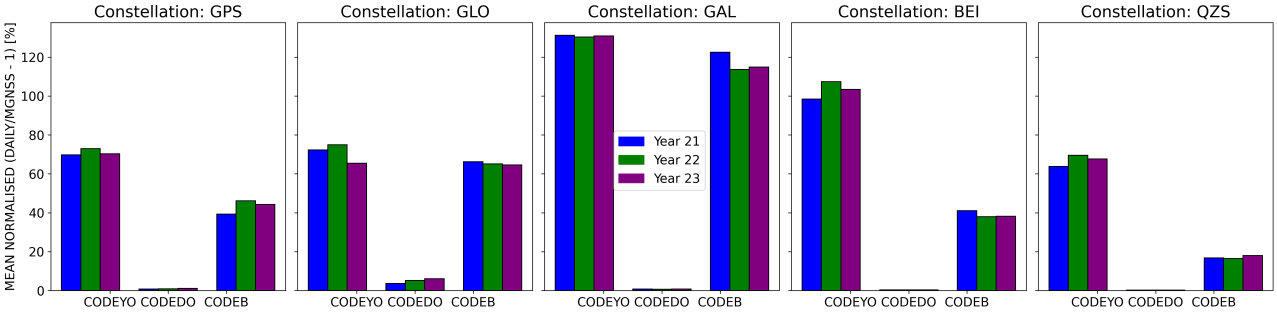

Figure 5.41: Mean DAILY vs. MGNSS ECOM differences normalised

The RMS differences between the DAILY and MGNSS ECOM parameters are notably higher for GLONASS, especially in the B-axis parameters, where the discrepancies increase significantly over the years, indicating a marked sensitivity in GLONASS to changes in modelling between individual and combined solutions. This behaviour suggests that GLONASS's orbit determination is more affected by the combination process. In contrast, the other constellations show relatively similar and stable RMS differences across the years, with smaller increases in the B-axis parameters. This indicates a more consistent and robust performance across these constellations, with fewer significant impacts from the combination process

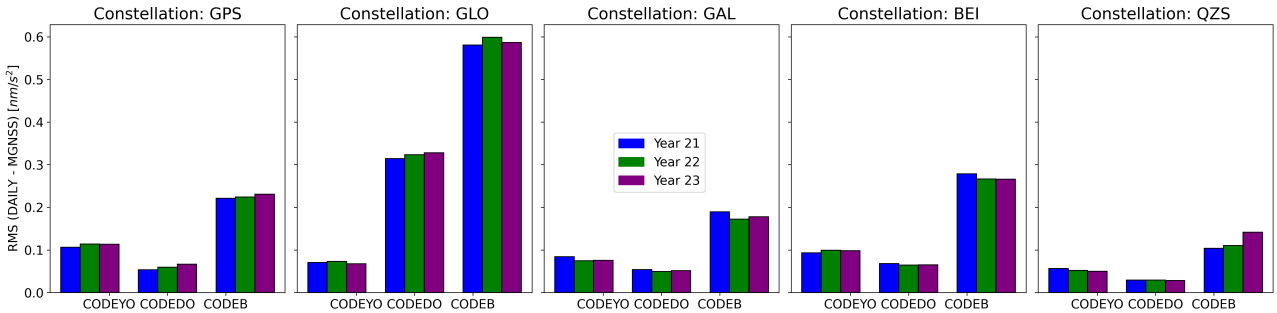

Figure 5.42: RMS DAILY vs. MGNSS ECOM differences

5.5.3 Empirical Accelerations

The empirical accelerations in the CHAMP framework are divided into the radial, along-track and cross-track directions. However, they are only implemented in the along-track direction. This section examines the differences in the empirical accelerations estimated parameters in the along-track direction between the DAILY and MGNSS solutions. As a representative example, the evolution of the CPR estimated parameters for the GPS-61 satellite is shown in Figure 5.43. Compared to the ECOM estimates, the semi-annual pattern is only visible in the CPR constant, while the sine and cosine terms to do show any periodicity. Regarding the constant term, the semi-annual pattern is more visible for GPS and QZSS, as the combined solution smoothes the results and brings the curve close to null.

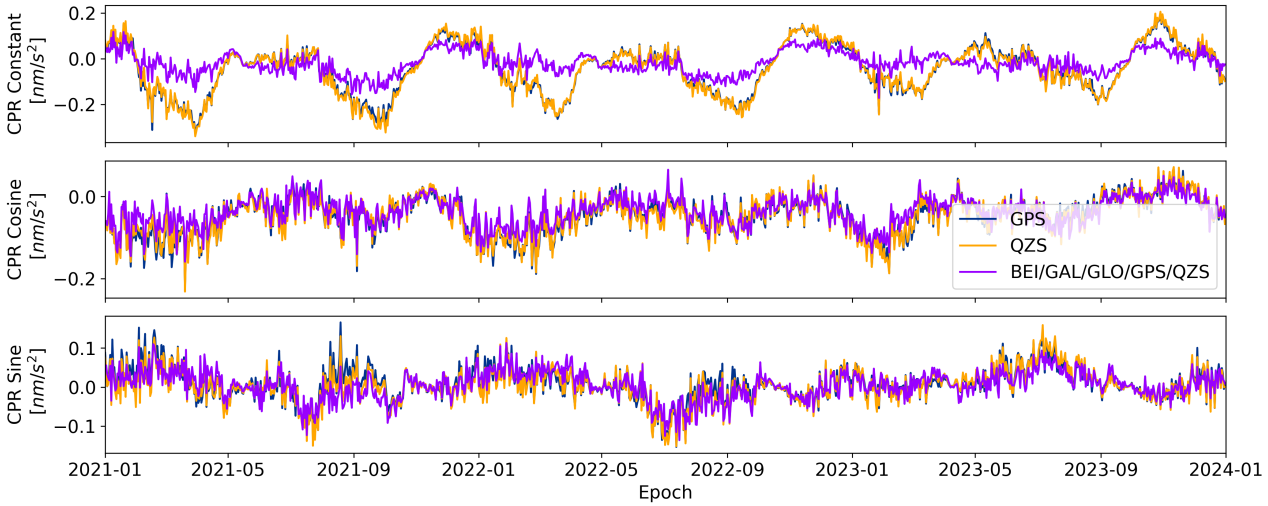

Figure 5.43: DAILY and MGNSS CPR estimated parameters in the along-track direction for GPS-61 satellite

The mean yearly CPR parameter absolute differences between the DAILY and MGNSS solutions for all constellations are shown in Figure 5.44, while the normalised relative differences are expanded in Figure 5.45. The absolute changes are relatively small except for the QZSS along-track offset values, which seem to increase during the three years of the study, highlighting the constant component changes. The largest normalised difference can be found for the GPS constant offset, even if these seem to decrease over time.

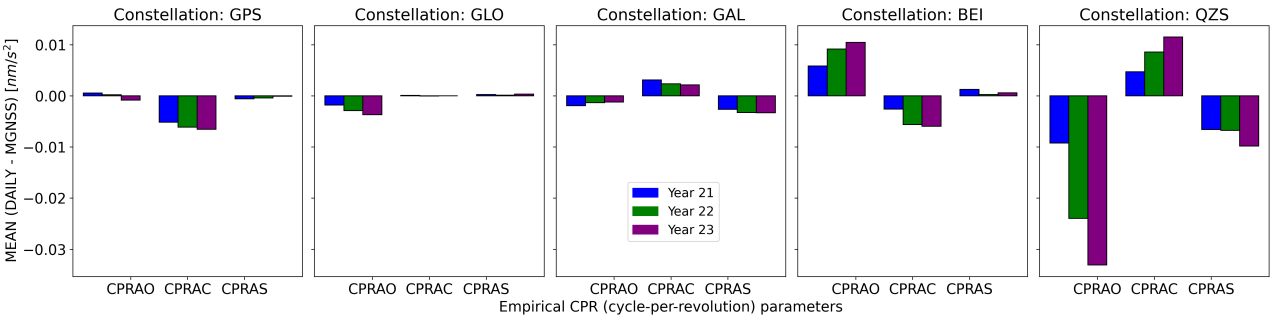

Figure 5.44: Mean DAILY vs. MGNSS CPR estimated parameter differences

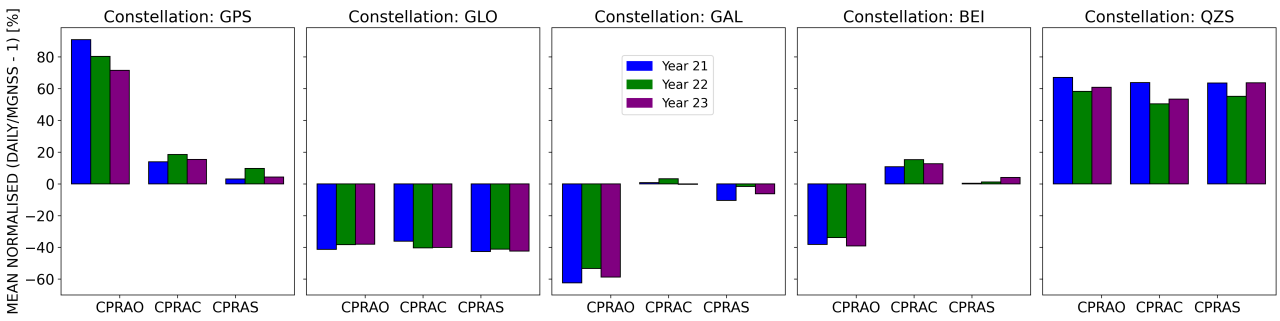

Figure 5.45: Mean DAILY vs. MGNSS CPR estimated parameter normalised differences

The RMS differences between the DAILY and MGNSS CPR parameters for each constellation are shown in Figure 5.46. Higher RMS values are evident in specific constellations, with more pronounced and generalised variations in the along-track offset. These differences may suggest areas where constellation-specific dynamics or unique characteristics influence CPR parameter performance over time, particularly for GPS, QZSS and BeiDou.

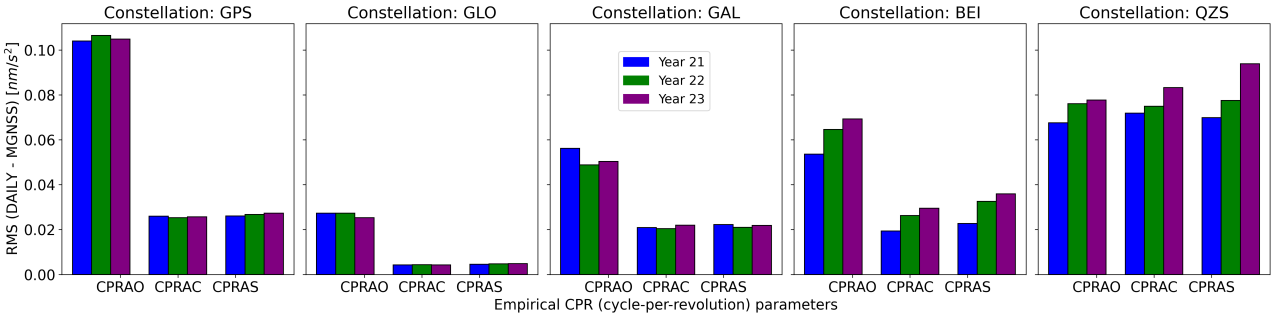

Figure 5.46: RMS DAILY vs. MGNSS CPR differences

5.6 Clock Parameters

This section introduces the analysis performed regarding clock variables, comprising receiver and transmitter clock biases, and the obtention of intersystem biases. As seen in the previous Section 4.2.4, the CHAMP ensemble of clocks can change on a daily basis between the different individual DAILY solution and between these and the MGNSS scenario. As a result, it is not possible to compare the different constellations throughout a large period of time without performing some conversion to the values. As such, a daily removal of the bias and drift of the difference between the individual and combined solution has been performed. However, the initial results were inconclusive, as the major differences were in the amplitude of the differences, which did not easily correlate with other parameters.

During the CHAMP parameter analysis, it was noted that the rejection rate for the combined CLOCK solution is approximately double that of the single-constellation solutions, going from approximately 1.5% to 3%. By comparing the clock estimates of single-constellation solutions, a pattern emerged that highlighted discrepancies in how clock biases, particularly sub-daily ISB jumps, are managed between these two solutions. The differences between the individual solutions and GPS, which is set as the clock reference, before removing the bias and drift are shown in Figure 5.47. In this picture the different daily inter-system clock biases can be seen in conjunction with areas were the different constellations rely on a different clock ensemble, which can be distinguished by the linear drift throughout one day. Consequently, once the inter-system bias with respect to GPS is applied to the other constellations on the same ground station for each day, all the clocks should be on the same reference. However, this is not always the case, as it can be seen on a zoomed view at end of December in Figure 5.48, leading to additional ISB jumps within the same day.

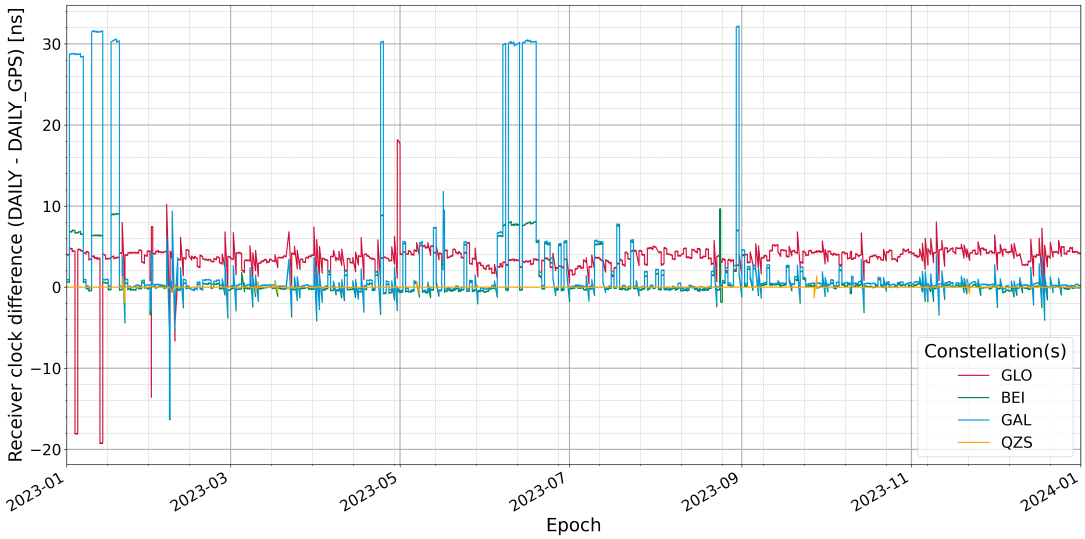

Figure 5.47: ESOC station receiver clock bias differences between individual solutions and GPS

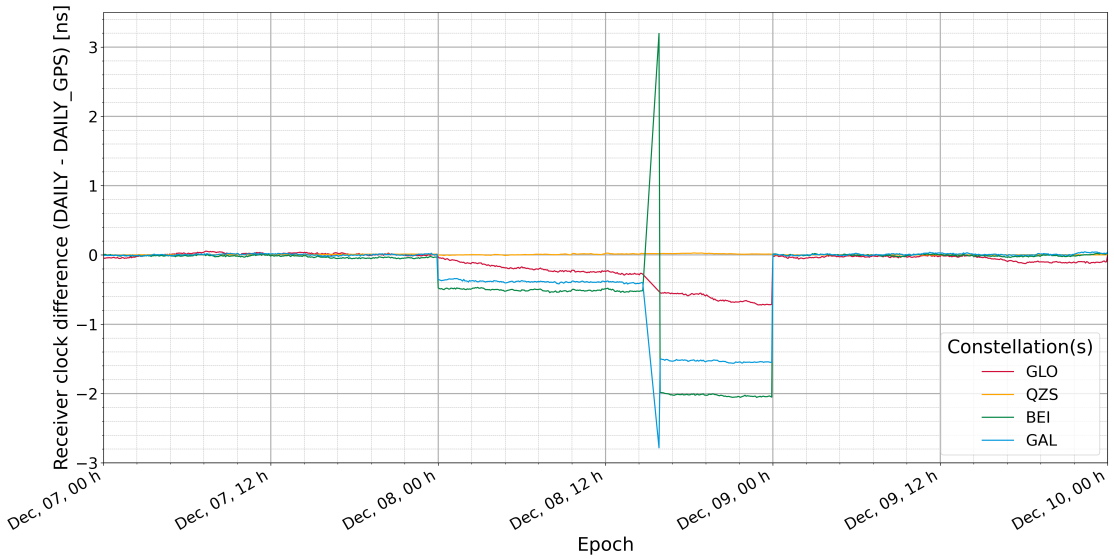

Figure 5.48: ESOC station receiver clock bias differences between individual solutions and GPS (ISB applied)

In the single-constellation solutions, individual station clocks can efficiently compensate for these sub-daily ISB jumps, ensuring that the observed variations do not significantly affect the results. Each station clock adjusts dynamically throughout the day to account for the ISB variations, thereby maintaining stable and reliable measurements. However, in the combined CLOCK solution, a more rigid approach is taken. Only one ISB parameter is used per constellation per day to account for these biases. Thus, this single parameter is insufficient to capture the sub-daily ISB variations observed in stations that experience multiple jumps throughout the day. As a result, the combined solution struggles to handle these fluctuations effectively, leading to higher rejection rates. Observations that do not conform to the single ISB value are rejected, causing an increased number of discarded data points. This issue is particularly evident in certain station clocks, where frequent sub-daily ISB jumps cause a significant portion of the observations to be excluded, further explaining the elevated rejection rates in the combined CLOCK solution. This discrepancy indicates that while the single-constellation solutions are more adaptive to temporal variations in station clocks, the combined solution's rigid approach to ISB management introduces inefficiencies, particularly when multiple ISB parameters per constellation per day are not allowed. Additionally, these differences could be related to the large discrepancies in the RMS values for the UP-component of certain stations, as shown in Figure 5.30. A mismodelling of the station biases would predominantly affect the vertical (UP) direction, resulting in larger differences and further contributing to the observed issues in the combined solution. This suggests that improving bias handling, particularly for stations with significant sub-daily ISB jumps, could mitigate the rejection rates and lead to more consistent results between the individual and combined solutions.

6 CHAMP Enhancements

This chapter delves into the inconsistencies found in the previous chapter between the individual constellation DAILY solutions and the combined MGNSS solution. The main focus of Section 6.1 is set on finding the root cause of the Length of Day inconsistencies between the different solutions, and their impact on the combined solution. For this purpose, Section 6.1.1 shows the effect of removing single constellations from the combination, showing that GPS is the main reason behind the LOD inconsistency. As a result, an analysis of the effect of the different blocks and orbital planes on the ECOM1 and empirical acceleration parameters is shown in Section 6.1.2, in order to find correlations between satellites and the inconsistencies. Once the empirical accelerations CPRs are seen to be correlated, the tuning of these is performed in Section 6.1.3. Furthermore, a different set of a priori non-gravitational GPS models are analysed in Section 6.1.4, while the best GPS individual solutions are then combined with the other nominal CHAMP constellations to produce new MGNSS solutions in Section 6.1.5. Finally, Section 6.2 introduces smaller tests done on the side of the overall analysis to see the effect of poor-behaving satellites and stations, while analysing the effect of constraining the number of ground stations.

6.1 Length of Day Inconsistencies

This section introduces the analysis and subsequent enhancements found for solving the inconsistencies in the LOD estimates between the individual and combined solutions. The effects of subtracting individual constellations from the combined solution are shown in Section 6.1.1, where the removal of the GPS constellation is seen to clearly enhance the combined solution, evidencing problem in the GPS constellation modelling. As a result, the effects of constraining or completely removing the empirical accelerations for the individual GPS constellation are researched in Section 6.1.3. Then, the effects of different a priori non-gravitational force models, in conjunction with empirical acceleration changes, in the individual GPS constellation are shown in Section 6.1.4. Finally, the combinations of a priori non-gravitational force models and empirical acceleration constraints in the individual GPS constellation that diverge the least from the IERS EOP20C04 reference are stacked with the nominal DAILY values of the other constellations in Section 6.1.5.

6.1.1 Removal of Individual Constellations from the Combined Solution

In order to test the impact of the different individual constellations in the combined solution, a new set of combinations are crafted, removing one constellation from MGNSS at a time, while keeping the others unchanged. For the GPS and QZSS individual case, both constellations are taken at the same time as the effect of the reduced number of QZSS satellites is seen to be minimal. The differences between the new constellation combinations and the original MGNSS in terms of LOD estimates are depicted in Figure 6.1. One of the major complications for this process was the removal of GPS from the combination, as the EPNS background of the CHAMP framework was initially designed so that the whole infrastructure always relies on GPS, stacking other normal equations of top to get a solution. As a result, the whole sequence of programmes had to be completely redesigned to allow other constellations to be the main one on top of which the others can be stacked, not only in the MGNSS sequence, but also in the way clocks and other references are defined in the DAILY sequence. For this purpose, Galileo was set as the new main constellation, while unlocking the possibility of using others in the future.

The elimination of GLONASS parameters from the stacked normal equation does not seem to be relevant to the combination, resulting in a maximum difference lower than $4\mu s$, as it could be expected based on the lower weight of the GLONASS observations and the larger standard deviations compared to the other constellations. In contrast, the elimination of both GPS and QZS from the combination results in a huge positive bias increase with a biannual pattern, as expected from the parameter analysis in Figure 5.2b, as these constellations behaved differently than the others while having a large weight in the combination. Additionally, the exclusion of either Galileo or BeiDou seems to have the opposite effect, giving even more weight to the negative GPS solution, which leads to an even more negative offset in the combined solution.

The comparison of the different MGNSS combinations with respect to the IERS EOP20C04 reference is shown in Figure 6.2, while the main statistics for each solution are summarised in Table 6.1. As seen with the previous analysis, the elimination of GPS and, subsequently, QZSS, reduces the bias almost completely. Thus, it can be ascertained that some kind of mismodeling in the GPS constellation leads to erroneous LOD estimates. Conversely, removing other constellations increases the bias in different ways, with the removal of Beidou

increasing it the most, by giving a larger weight to GPS constellation in the combined solution. In terms of standard deviation values, all the different combinations are considerably similar, with the interesting fact that removing Galileo or BeiDou seems to add more variability to the data, probably due to the increase in weight of GLONASS. However, even if the drift between the estimates and the reference is considerably reduced when removing GPS and QZSS, and slightly less when removing BeiDou, the prevalence of such a drift indicates that there are still further differences in the modelling which are not being accounted for.

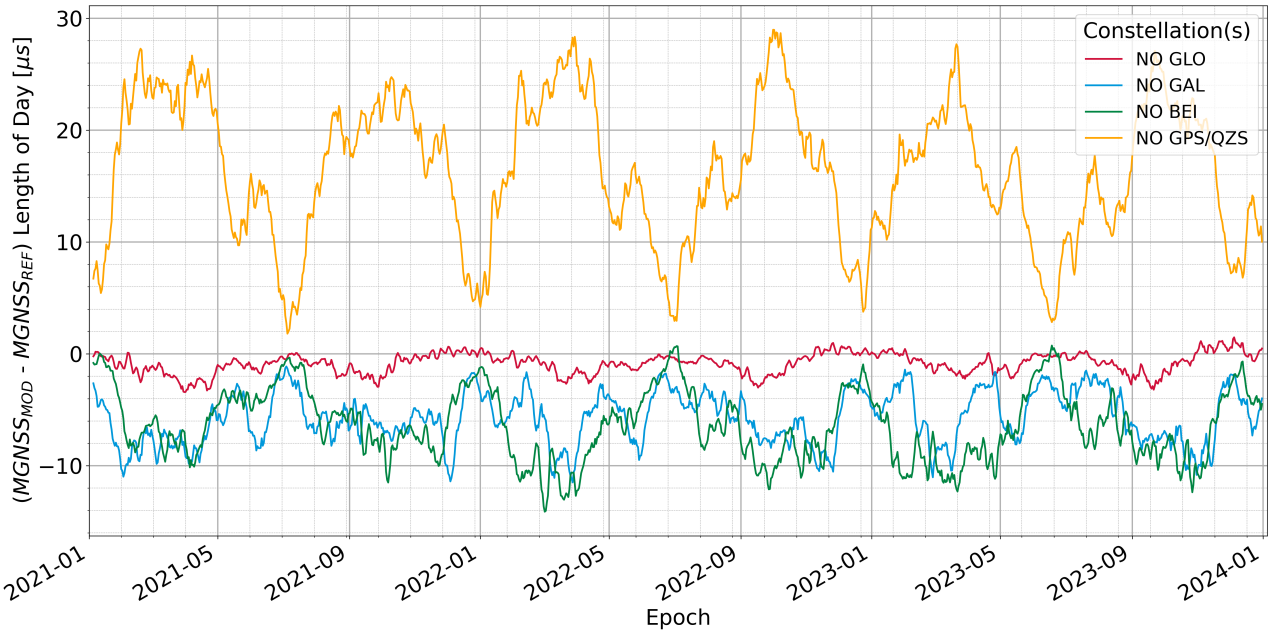

Figure 6.1: Length of day difference wrt. the nominal MGNSS (BEI/GAL/GLO/GPS/QZS) values

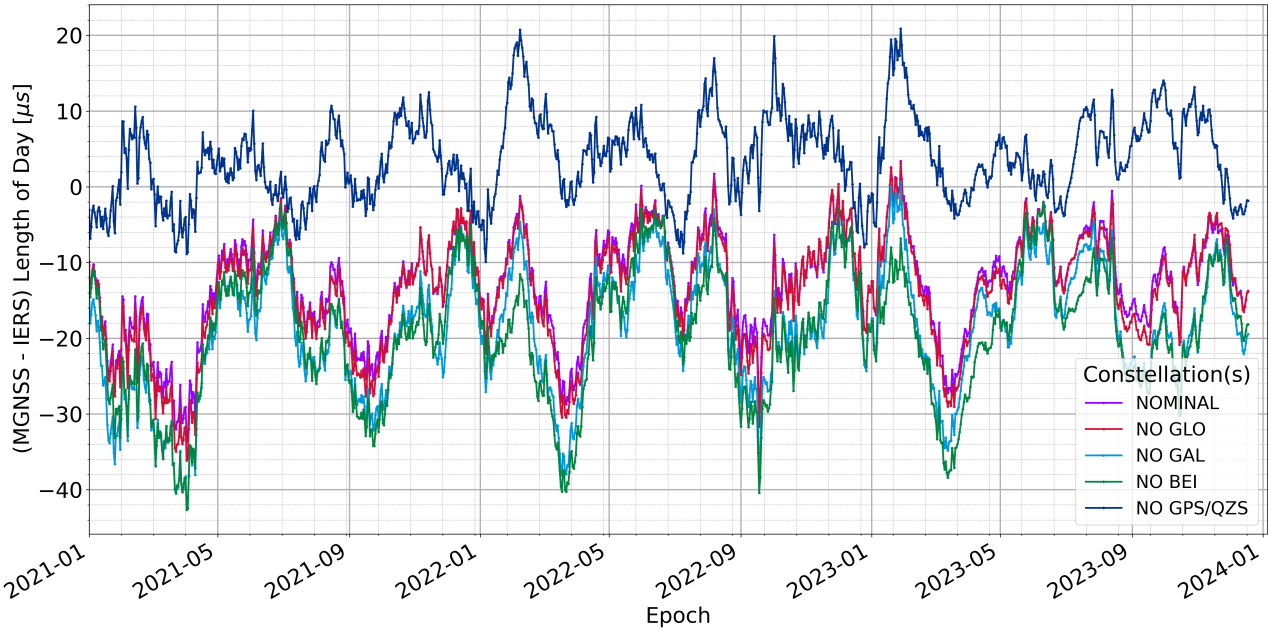

Figure 6.2: LOD MGNSS different combinations difference wrt. IERS EOP20C04

Table 6.1: Statistics of constellations compared against IERS

	Units	ALL	NO GLO	NO GAL	NO BEI	NO GPS/QZS
Mean/Bias	μs	-12.7354	-13.5877	-18.4735	-19.1208	3.6351
Std. dev.	μs	19.6824	19.9228	20.3621	20.4091	19.3827
Drift	$\mu s/year$	2.4420	2.6926	2.8110	1.9056	1.5373

A comparison of the satellite orbit overlaps of the different MGNSS combinations during the year 2023 is shown in Table 6.2, where the extraction of GPS and QZSS slightly improves the satellite overlaps with respect to the nominal MGNSS combination, except for the MEO satellites of BeiDou, which benefit from GPS remaining in the combination. However, removing either GLONASS, Galileo or Beidou from the combination always results in a degradation of the accuracy of the satellite orbit overlaps.

Table 6.2: MGNSS combinations - Satellite orbit overlaps comparison in 2023

Overlaps 3D RMS [mm]	ALL	NO GLO	NO GAL	NO BEI	NO GPS/QZS
GPS	30.6	31.1	31.1	31.0	-
GLO	93.4	-	93.7	96.9	93.0
GAL	35.2	35.3	-	35.2	34.5
BEI-M	36.9	37.1	37.2	-	37.6
BEI-I	274.2	276.7	276.5	-	271.0
QZS-I	157.8	159.2	157.9	158.2	-

The changes in the other estimated Earth Orientation Parameters are shown in Figure 6.3 and Figure 6.4, for the absolute pole differences, and in Figure 6.5 and Figure 6.6 for the differences in the pole rates. The whole duration of 2023 has been chosen as a representative comparison period as the differences in the nominal pole values behave differently than in the previous years. Overall, the bias and drift does not change significantly for the polar motion in the X axis, even if the removal of Galileo or BeiDou from the GNSS combination results in larger peaks, as this effect is seen on both positive and negative values. The same effect can be seen for the polar rates in both axes, to a lesser degree. However, the removal of BeiDou decreases the bias in the Y axis polar motion, while the removal of GPS has the opposite effect, showing a clear dependence on specific constellations.

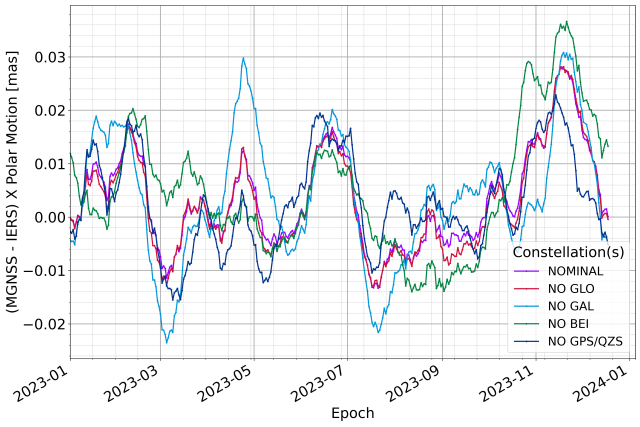

Figure 6.3: XPO difference wrt. IERS EOP20C04

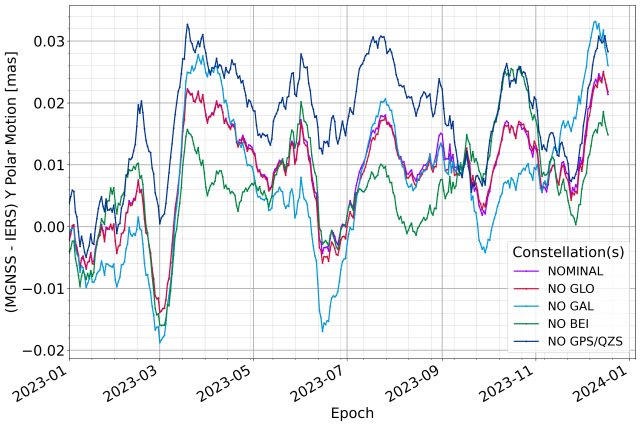

Figure 6.4: YPO difference wrt. IERS EOP20C04

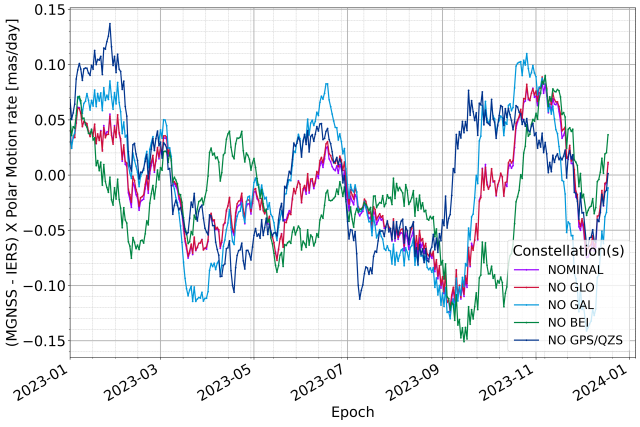

Figure 6.5: XPOR difference wrt. IERS EOP20C04

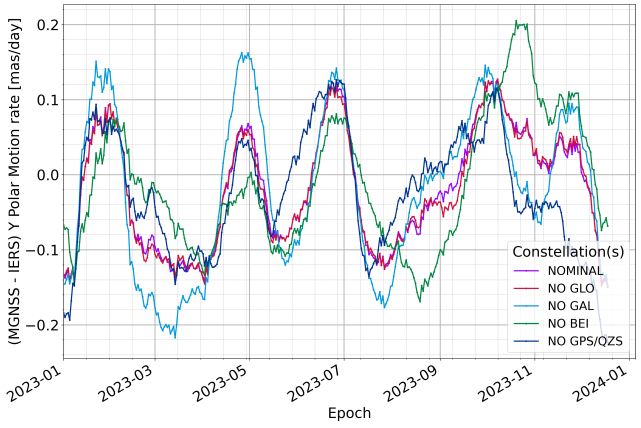

Figure 6.6: YPOR difference wrt. IERS EOP20C04

6.1.2 Influence of GPS Blocks and Orbital Planes

Based on the clear LOD inconsistency found for the GPS constellation estimates, a more detailed analysis of the different GPS blocks and orbital planes has been carried out to see the possible influence of the satellite geometry and position in the non-gravitational effects, namely the ECOM estimates, and the empirical accelerations.

6.1.2.1 Additional GPS ECOM Parameters Analysis

Following on the overall differences for each constellation, an analysis of the effect of the different blocks and orbital planes is performed. The differences in ECOM parameters for the different GPS blocks are shown in Figure 6.7. The comparison shows that the differences between the DAILY and MGNSS solution are almost constant in time for all block types. As such, if there is any mismodeling in the GPS solar radiation pressure that is being accounted for these parameters, it does not seem to be heavily influenced by the block type. Additionally, Figure 6.8 shows the differences in ECOM parameters for the different GPS planes, ordered from 1 to 6 from the smallest to the largest right ascension of the ascending node. For this analysis, planes 1 and 6, which are consecutive, seem to have smaller differences. Furthermore, the second plane seems to reduce the differences with time, while the fifth one increases. At the same time, the middle planes remain constant with time.

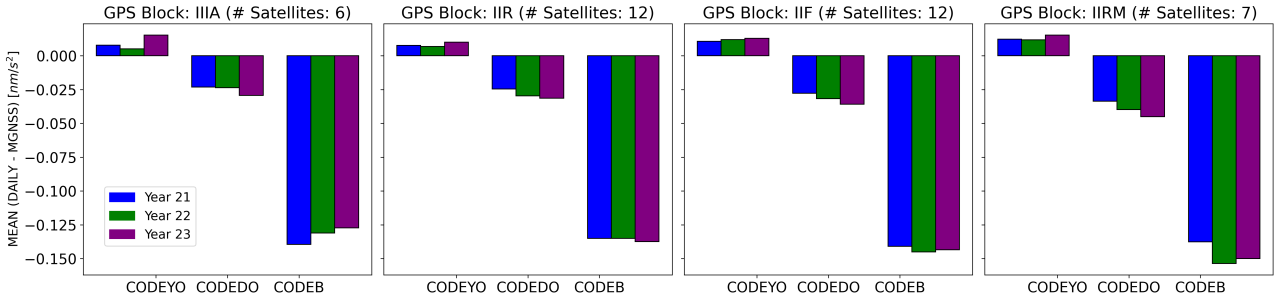

Figure 6.7: Mean DAILY vs. MGNSS ECOM differences ordered by GPS block

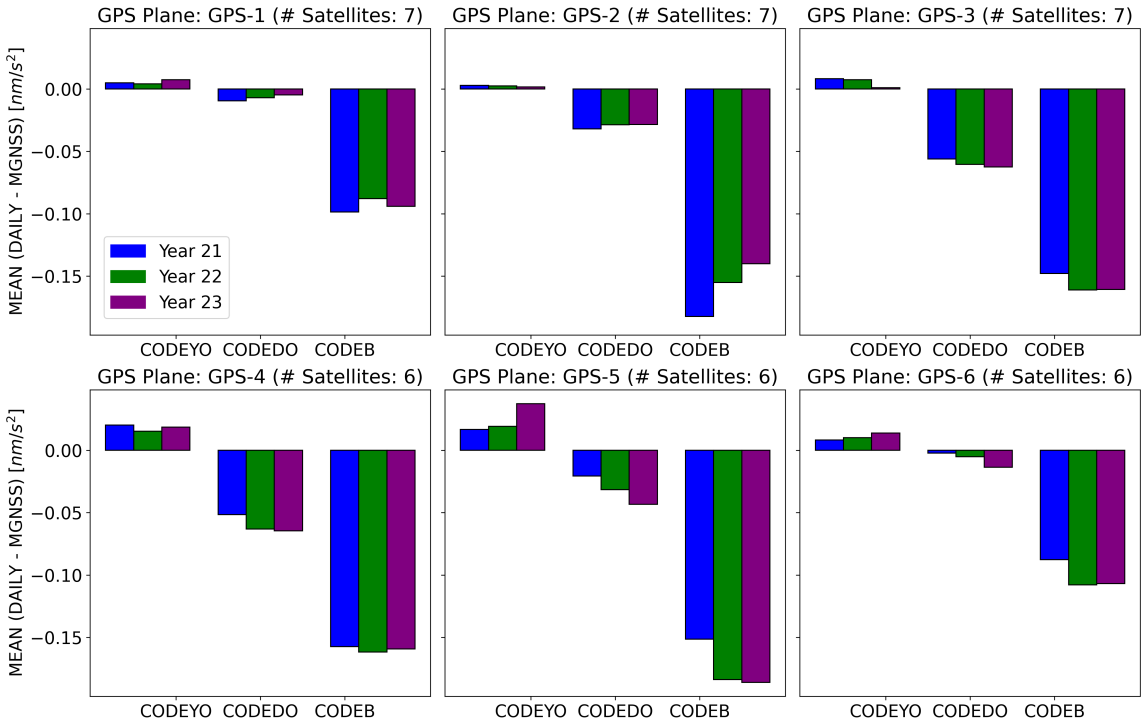

Figure 6.8: Mean DAILY vs. MGNSS ECOM differences ordered by GPS orbital plane

The large mean offset that was visible for the estimated ECOM parameters in the B-axis for the GPS constellation are further investigated per satellite, dividing the B-axis estimates into the three estimated parameters. The major differences are found for the offset and the cosine components, while the sine components changes are minimal. A large number of satellites from the different blocks seem to be enlarging the differences with time, while those that remain with the same value or reduce the difference are a minority. Thus, all GPS blocks seem to have the same issue.

6.1.2.2 Additional GPS Empirical Acceleration Analysis

Following on the overall differences for each constellation, an analysis of the effect of the different blocks and orbital planes is performed. The differences in CPR parameters for the different GPS blocks are shown in Figure Figure 6.9. Conversely to the ECOM estimates, the CPR estimates seem to vary differently for each block, even if the absolute values are considerably small. The latest GPS IIIA block differences increase considerably from 2021 to 2022 as most satellites from this group were being launched during these two years, and the effect on the combination had not been previously analysed. However, all blocks show small to no changes for the year 2022 onwards, showing that differences are maintained. Additionally, Figure 6.10 shows the differences in CPR parameters for the different GPS planes, ordered from 1 to 6 from the smallest to the largest right ascension of the ascending node. While planes 1 and 5 decrease the differences yearly, these values are regained by planes 2 and 6, while 3 and 4 remain considerably constant, or decrease slightly. This indicates that the empirical accelerations are considerably position-dependent, at least for four out of the six planes.

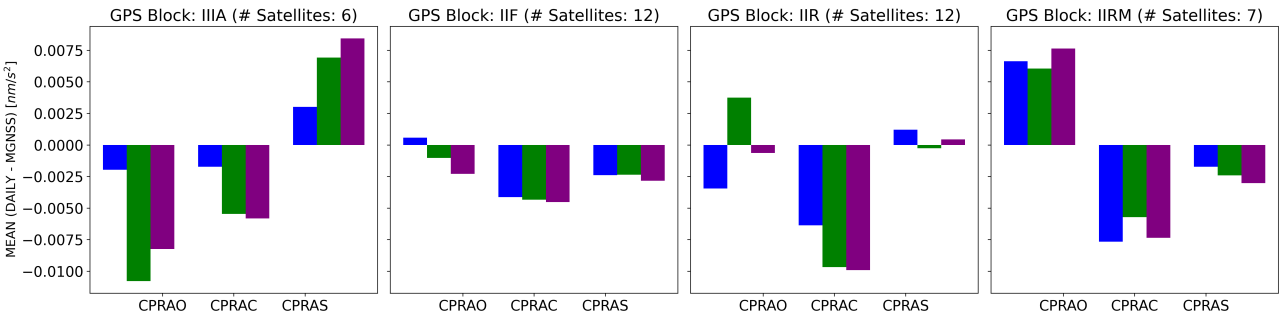

Figure 6.9: Mean DAILY vs. MGNSS CPR differences ordered by GPS block

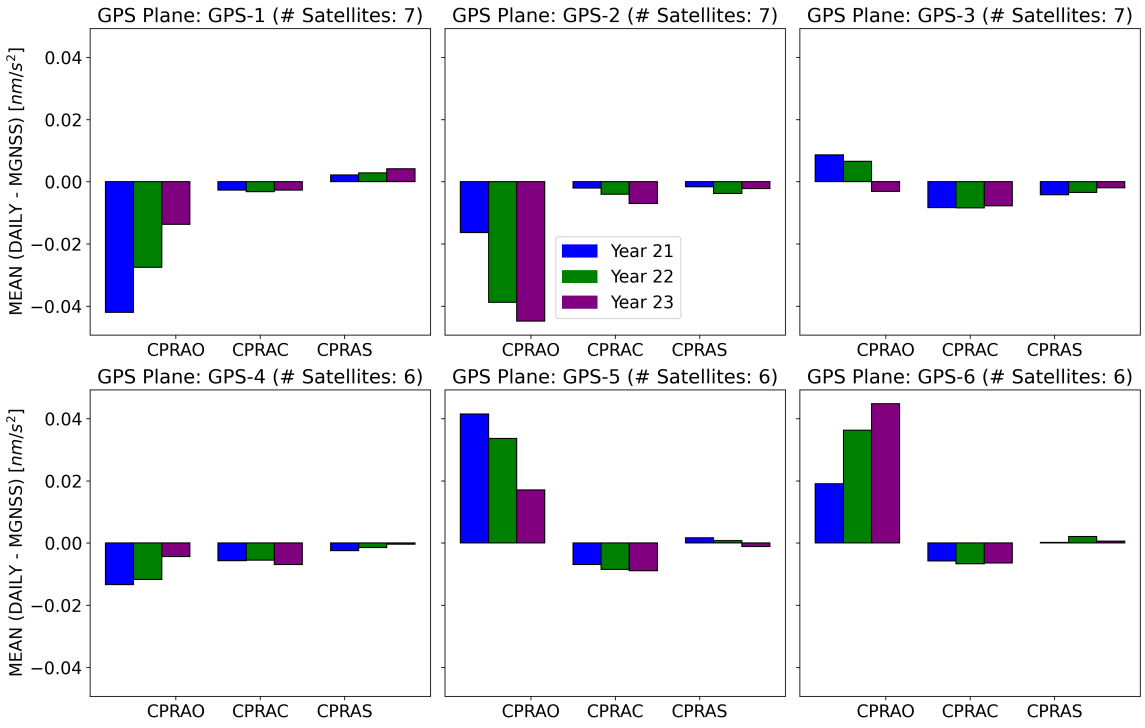

Figure 6.10: Mean DAILY vs. MGNSS CPR differences ordered by GPS orbital plane

6.1.3 Tuning of Empirical Accelerations

The empirical accelerations have shown to correlate with the LOD estimates. As a result, this section describes the impact of the tuning of the empirical acceleration constraints while using the nominal CHAMP box-wing model as an a priori for the solar radiation pressure, and the ECOM1 and CPR empirical estimates for further refinement. Table 6.3 collects the different constraints used, and also shows the satellite orbit overlap differences.

Table 6.3: GPS empirical acceleration configurations and metrics

CPR case	Nominal	Constrained	Removed
CPR constraint value $[km/s^2]$	10^{-13}	10^{-14}	0
3D RMS orbit overlaps $[mm]$	30.6	30.4	38.0

The differences between the estimated LOD parameters obtained with these three different empirical acceleration constraint settings and the IERS reference LOD values are depicted in Figure 6.11. It can be seen that implementing a tighter constraint or removing it altogether results in a better alignment with the IERS reference. As such, it indicates that the current CPR values do not align well with the problem dynamics. However, these empirical accelerations are still needed, as removing them results in an increase of the orbit overlaps 3D RMS of more than 7 mm, while the constrained values slightly improve the nominal results. This is particularly due to large unmodelled changes of solar radiation pressure during eclipse seasons and suggests that focusing on improved eclipse handling could eventually allow for the elimination of empirical accelerations for GPS, as seen with other internal projects related to Galileo within the Navigation Support Office, which would further enhance GPS LOD and improve overall precision.

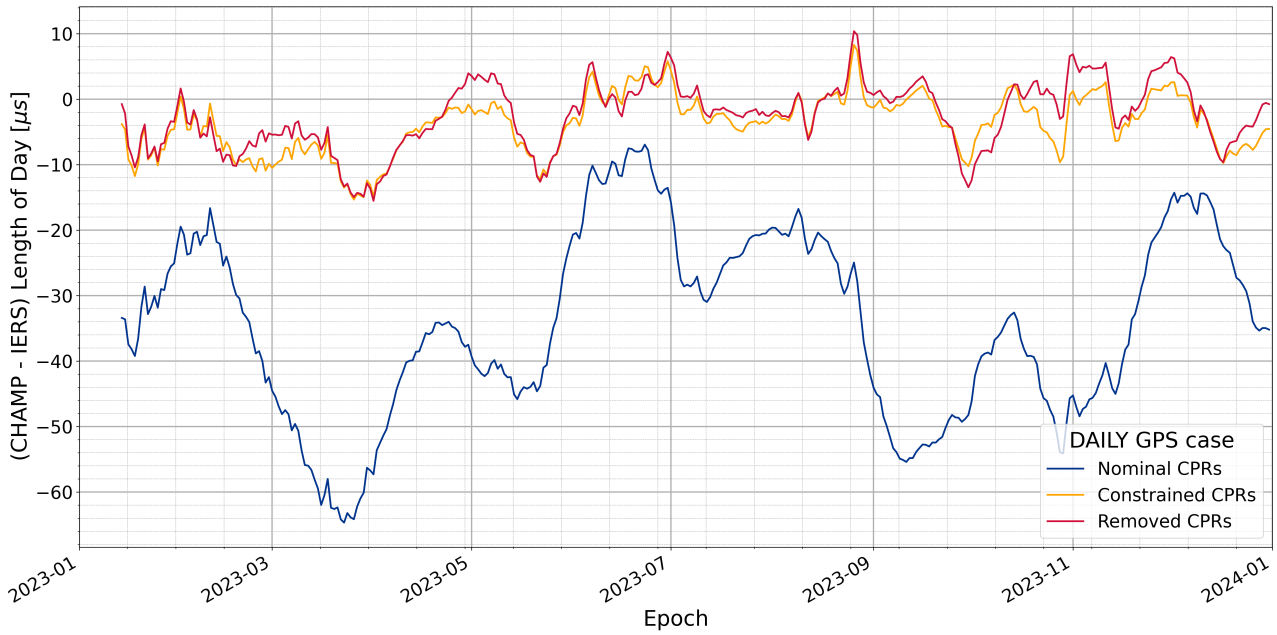

Figure 6.11: DAILY GPS LOD Box-Wing model differences wrt. IERS EOP20C04

The absolute pole differences between the three different GPS empirical acceleration constraint settings and the IERS reference LOD values are shown in Figure 6.12 and Figure 6.13. As the CPRs are there to account for unknown acceleration, it can be seen that both constraining and removing them affects differently over time, with no clear temporal patterns with respect to the nominal CPR values. Removing the constraint results in larger biases for both the polar motion values in both axes, making it an unfit solution. However, while the constraining effect leads to a similar bias for the X-axis, a clear negative offset is created on the Y-axis.

The pole rate differences between the three different GPS empirical acceleration constraint settings and the IERS reference LOD values are shown in Figure 6.14 and Figure 6.15. In this case, both the constrained and removed cases introduce a positive bias in the X-axis, even if the variability is smaller. Furthermore, the drift is common to all solutions in this axis. Additionally, the constrained and removed cases result in better estimates for the Y-axis in terms of bias, at the expense of a larger variability.

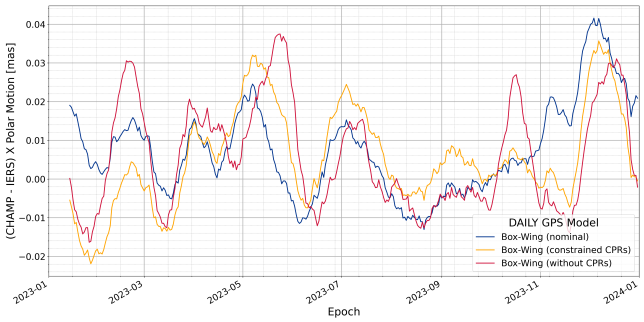

Figure 6.12: DAILY GPS XPO differences wrt. IERS EOP20C04

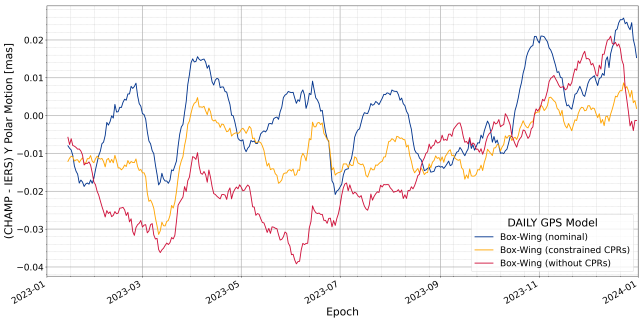

Figure 6.13: DAILY GPS YPO differences wrt. IERS EOP20C04

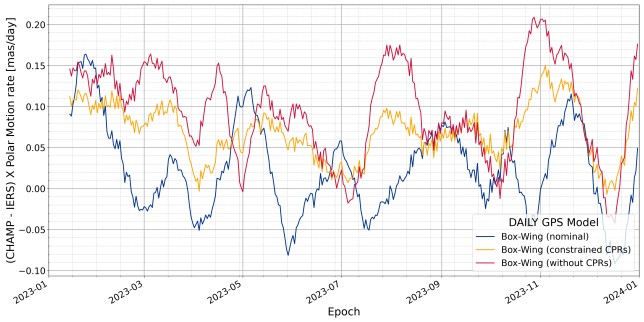

Figure 6.14: DAILY GPS XPOR differences wrt. IERS EOP20C04

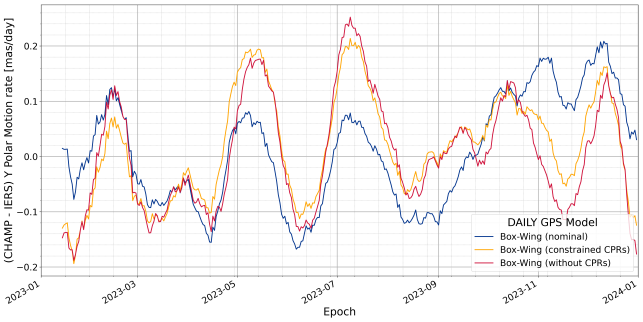

Figure 6.15: DAILY GPS YPOR differences wrt. IERS EOP20C04

6.1.4 Effects of Different A Priori Non-gravitational Models for GPS

In this section, the impact of using different a priori models instead of the nominal CHAMP box-wing model is analysed. First, the nominal model is introduced to characterise the different GPS blocks. These models are modified to try another box-wing configuration developed by TU Munich, followed by an assessment using the ROCK model. Finally, the impact of not using an a priori model is also investigated.

6.1.4.1 Nominal CHAMP GPS Box-Wing Model

The input characteristics needed by the model for each of the number of surfaces that make up the box-wing model for the specific GPS blocks in the combination are introduced in Table 6.4, Table 6.5 and Table 6.6. The attitude of the GNSS system is defined by the X, Y, and Z axes, where the Z-axis is oriented towards the Earth, and the Y-axis is the axis around which the solar panels rotate. In this configuration, the Y-panels are omitted and all surfaces are treated as flat plates. The Solar Array Front (SAF) is the side of the solar array that should be directed towards the Sun, while the Solar Array Back (SAB) is the opposite side. It was noted that the solar panels for the GPS block IIIA do not satisfy the condition $\alpha_{vis} + \delta_{vis} + \rho_{vis} = 1$.

Table 6.4: CHAMP Box-Wing model - GPS Block IIR satellites

		Visible spectrum			IR spectrum				
Surface	**A**(m^2)	α_{vis}	δ_{vis}	ρ_{vis}	α_{ir}	δ_{ir}	ρ_{ir}	**Thrust** (W)	**Reradiation**
+X	4.110	0.945	0.055	0	0.1	0.1	0.8	-	Yes
-X	4.110	0.945	0.055	0	0.1	0.1	0.8	-	Yes
+Z	4.25	0.940	0.06	0	0.1	0.1	0.8	85.0	Yes
-Z	4.25	0.940	0.06	0	0.1	0.1	0.8	-	Yes
SAF	13.92	0.707	0.044	0.249	0.1	0.1	0.8	-	No
SAB	13.92	0.707	0.044	0.249	0.1	0.1	0.8	-	No

Table 6.5: CHAMP Box-Wing model - GPS Block IIF satellites

		Visible spectrum			IR spectrum				
Surface	**A**(m^2)	α_{vis}	δ_{vis}	ρ_{vis}	α_{ir}	δ_{ir}	ρ_{ir}	**Thrust** (W)	**Reradiation**
+X	5.72	0.40	0.40	0.20	0.1	0.1	0.8	-	Yes
-X	5.72	0.40	0.40	0.20	0.1	0.1	0.8	-	Yes
+Z	5.40	0	0..3	0.7	0.1	0.1	0.8	249.0	Yes
-Z	5.40	0	0.3	0.7	0.1	0.1	0.8	-	Yes
SAF	22.25	0.770	0.034	0.196	0.1	0.1	0.8	-	No
SAB	22.25	0.770	0.034	0.196	0.1	0.1	0.8	-	No

Table 6.6: CHAMP Box-Wing model - GPS Block IIIA satellites

		Visible spectrum			IR spectrum				
Surface	**A**(m^2)	α_{vis}	δ_{vis}	ρ_{vis}	α_{ir}	δ_{ir}	ρ_{ir}	**Thrust** (W)	**Reradiation**
+X	7.50	0.440	0.460	0.100	0.440	0.460	0.100	-	Yes
-X	-	-	-	-	-	-	-	-	-
+Z	4.00	0.440	0.460	0.100	0.440	0.460	0.100	300.0	Yes
-Z	4.00	0.940	0.060	0	0.940	0.060	0	-	Yes
SAF	28.2	0.920	0	0.008	0.920	0	0.008	-	No
SAB	28.2	0.920	0	0.008	0.920	0	0.008	-	No

6.1.4.2 TUM Box-Wing A Priori Model for GPS

Specifying accurate box-wing properties for GPS satellites presents a significant challenge due to the limited availability of complete and accurate data. Unlike newer constellations, such as Galileo or BeiDou, where more comprehensive satellite metadata is available, GPS satellites, particularly older generations, lack full disclosure of critical parameters such as thermal and reflectivity characteristics. This incomplete data makes it difficult to model the precise impact of non-gravitational forces like solar radiation pressure or other thermal effects, which are essential for refining orbit determination and improving the overall accuracy of GPS solutions. For this purpose, a test with the estimated box-wing visible spectrum parameters of Duan and Hugentobler (2021) is performed. However, as the publication was initially written in 2019, it does not incorporate the modelling of the newest GPS block IIIA, and only the block IIR and IIF models are retrieved. However, these GPS models present certain limitations, as they do not fully adhere to physical expectations. In particular, unphysical negative optical estimates are observed for some surfaces, and the sum of the optical properties for the same surface does not meet the physical condition of equalling unity. One possible explanation given for these discrepancies is that the parameters for reflectivity and emissivity of the same surface are highly correlated, introducing systematic errors into the estimation. Additionally, since no constraints were imposed during the adjustment process, the estimates may be further contaminated, leading to results that lack physical coherence. As a result, while these values will still be used for modelling purposes, they should be interpreted cautiously due to their limited physical justification.

Consequently, a combination of the Box parameters of Duan and Hugentobler (2021), with the wing nominal parameters of CHAMP is used to create a new set of box-wing models, which are shown in Table 6.7 and Table 6.8 for the IIR and IIF blocks, respectively. In this case, the surface shape of the X surface is not flat, and the infrared spectrum has been set based on the values from the nominal CHAMP parameters.

Table 6.7: Modified TUM Box-Wing model - GPS Block IIR satellites

			Visible spectrum			IR spectrum				
Surface	**A**(m^2)	**Shape**	α_{vis}	δ_{vis}	ρ_{vis}	α_{ir}	δ_{ir}	ρ_{ir}	**Thrust** (W)	**Reradiation**
+X	4.110	0.258	0.730	0	0.175	0.1	0.1	0.8	-	Yes
-X	4.110	0	0.730	0	0.175	0.1	0.1	0.8	-	Yes
+Z	4.25	0	1.095	0	-0.137	0.1	0.1	0.8	85.0	Yes
-Z	4.25	0	0.935	0	0.096	0.1	0.1	0.8	-	Yes
SAF	13.92	0	0.707	0.044	0.249	0.1	0.1	0.8	-	No
SAB	13.92	0	0.707	0.044	0.249	0.1	0.1	0.8	-	No

Table 6.8: Modified TUM Box-Wing model - GPS Block IIF satellites

			Visible spectrum			IR spectrum				
Surface	**A(m^2)**	**Shape**	α_{vis}	δ_{vis}	ρ_{vis}	α_{ir}	δ_{ir}	ρ_{ir}	**Thrust (W)**	**Reradiation**
+X	5.72	0	0.262	0	0.255	0.1	0.1	0.8	-	Yes
-X	5.72	0	0.262	0	0.255	0.1	0.1	0.8	-	Yes
+Z	5.40	0	0.533	0	0.070	0.1	0.1	0.8	249.0	Yes
-Z	5.40	0	0.388	0	0.198	0.1	0.1	0.8	-	Yes
SAF	22.25	0	0.770	0.035	0.196	0.1	0.1	0.8	-	No
SAB	22.25	0	0.770	0.035	0.196	0.1	0.1	0.8	-	No

The results with the new box-wing model, with and without constraints in the CPRs, are shown in Figure 6.16, while the constraint values and the orbital overlap statistics are stated in Table 6.9. It can be seen that there is a considerable improvement in reducing the LOD bias already without any empirical acceleration constraints, reducing the variability of the results, even if the bias is not completely removed. After using tighter constraints for the empirical accelerations, as seen in the previous case with the nominal CHAMP model, the bias almost completely disappears. Additionally, there are further improvements in the orbit overlap statistics.

Table 6.9: GPS empirical acceleration and a priori configurations and metrics

A priori GPS model	**CHAMP Box-Wing Model**	**TUM Box-Wing Model**	
CPR case	Nominal	Nominal	Constrained
CPR constraint value [km/s^2]	10^{-13}	10^{-13}	10^{-14}
3D RMS orbit overlaps [mm]	30.6	30.3	29.7

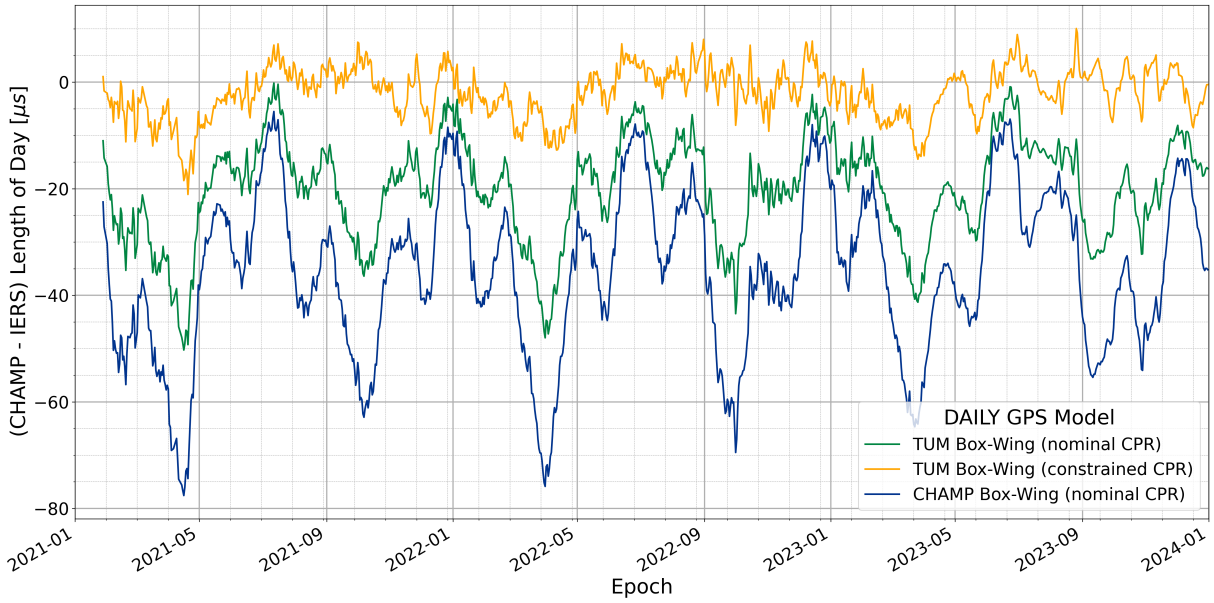

Figure 6.16: DAILY GPS LOD TUM Box-Wing model differences wrt. IERS EOP20C04

The pole absolute and rate difference statistics for the representative year 2023 between the different GPS a priori models and the IERS reference LOD values are shown in Table 6.10. The new TUM model with nominal empirical acceleration constraints reduces the bias of both the X-axis pole and the Y-axis pole rate, while increasing it for the other two, specifically in the case of the X-axis pole rate. Overall, the variability of the new TUM nominal model is reduced compared to the CHAMP model. The largest bias increase can be seen for the TUM model with constrained empirical accelerations in the X-axis polar motion rate, which increases more than 200% with respect to the nominal CHAMP value.

Table 6.10: LOD statistics of the DAILY GPS differences wrt. IERS EOP20C04

	Variable	Units	CHAMP nominal	TUM nominal	TUM constrained
Mean/Bias	XPO	*mas*	0.0079	0.0053	0.0075
Std. dev.			0.0175	0.0153	0.0151
RMS			0.0192	0.0162	0.0169
Mean/Bias	YPO	*mas*	0.0001	-0.0011	-0.0068
Std. dev.			0.0173	0.0152	0.0136
RMS			0.0173	0.0152	0.0152
Mean/Bias	XPOR	*mas/day*	0.0250	0.0418	0.0830
Std. dev.			0.1196	0.1131	0.1153
RMS			0.1222	0.1205	0.1420
Mean/Bias	YPOR	*mas/day*	0.0100	0.0055	0.0150
Std. dev.			0.1408	0.1190	0.1188
RMS			0.1412	0.1192	0.1198

6.1.4.3 ROCK Box-Wing A Priori Model for GPS

In this section, the CHAMP box-wing model is replaced with the ROCK model, as introduced by Dilssner and Springer (2024b) in the paper "Taming the Invisible" presented at the IGS Workshop 2024, ase previously seen in Section 3.6.1.6. This updated model offers significant improvements in the representation of non-gravitational forces acting on GNSS satellites, particularly for GPS. The ROCK model provides a more accurate depiction of spacecraft surface properties and external forces, enhancing orbit determination and satellite dynamics. The rock model applied in this work features individual models for each satellite, rather than a generalised type-based approach. These models are derived from empirical estimates specific to the year 2023, making them highly tuned to recent data. Consequently, satellites that were not active or lacked sufficient data during this year are not included in the model, limiting its applicability to those specific satellites. This lack of type-dependency poses challenges when attempting to extend the model to historical or future satellite missions, as it does not offer a theoretical foundation for broad application across different timeframes.

The results with the ROCK model, with and without constraints in the empirical accelerations, are shown in Figure 6.17, while Table 6.11 summarises the constraint values and the orbital overlap results of all the different cases. Compared to the nominal CHAMP and the modified TUM models, the nominal ROCK model slightly enhances the orbit overlaps, while the constrained case enhances the overlaps even more. As also seen with the other a priori models, the removal of the empirical accelerations degrades the overlap comparison, even if several millimetres less than the others. In this case, both the nominal and constrained CPR solutions heavily reduce the bias, with small differences between these two solutions. Thus, further constraining the bias does not seem to yield a better result, unless the CPRs are completely removed, in which case the bias is completely removed for the second half of the year.

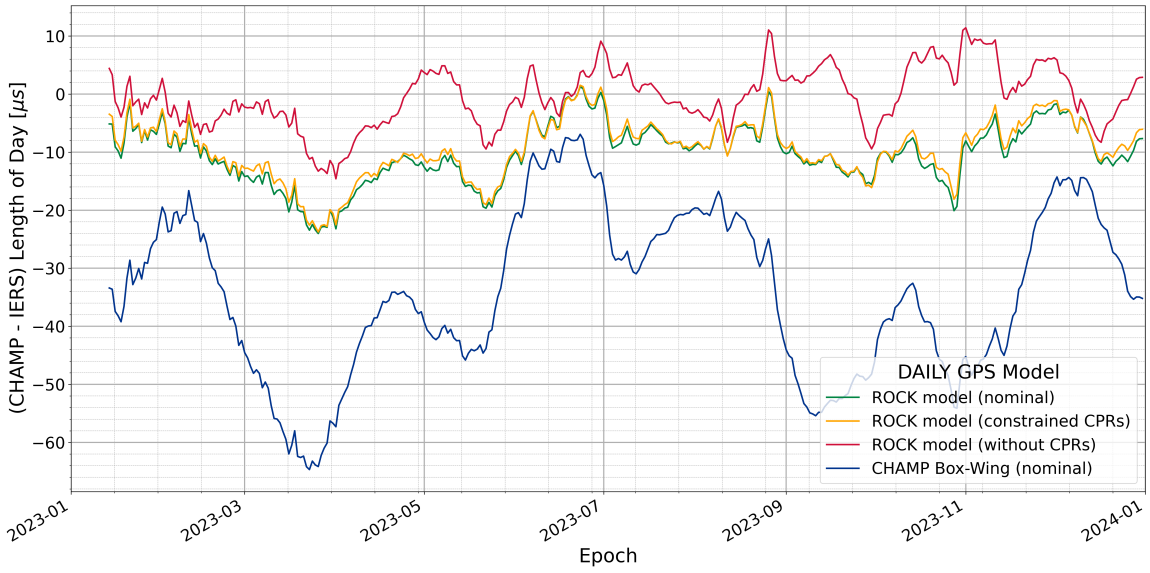

Figure 6.17: DAILY GPS LOD ROCK model differences wrt. IERS EOP20C04

Table 6.11: GPS empirical acceleration and a priori configurations and metrics

A priori GPS model	**CHAMP Box-Wing Model**	**ROCK Model**		
CPR case	Nominal	Nominal	Constrained	Removed
CPR constraint value $[km/s^2]$	10^{-13}	10^{-13}	10^{-14}	0
3D RMS orbit overlaps $[mm]$	30.6	30.0	29.4	32.6

The pole absolute and rate difference statistics for the representative year 2023 between the different GPS a priori models and the IERS reference LOD values are shown in Table 6.12. Overall, the bias gets slightly worse for all parameters except the X-axis polar motion, and no major differences are seen between the nominal, constrained and removed empirical accelerations except in the Y-axis polar motion rate, where the removed case is closer to the nominal CHAMP value. The variability increases for the polar motion values in both axes, while it decreases in both axes for the rates, except in the X-axis pole rate with removed empirical accelerations.

Table 6.12: LOD statistics of the DAILY GPS differences wrt. IERS EOP20C04

	Variable	**Units**	**CHAMP nominal**	**ROCK nominal**	**ROCK constrained**	**ROCK removed**
Mean/Bias	XPO	*mas*	0.0079	0.0041	0.0046	0.0072
Std. dev.			0.0175	0.0176	0.0173	0.0194
RMS			0.0192	0.0181	0.0179	0.0207
Mean/Bias	YPO	*mas*	0.0001	-0.0023	-0.0025	-0.0027
Std. dev.			0.0173	0.0181	0.0176	0.0194
RMS			0.0173	0.0183	0.0178	0.0196
Mean/Bias	XPOR	*mas/day*	0.0250	0.0371	0.0361	0.0371
Std. dev.			0.1196	0.1173	0.1157	0.1289
RMS			0.1222	0.1231	0.1212	0.1342
Mean/Bias	YPOR	*mas/day*	0.0100	-0.0214	-0.0229	-0.0113
Std. dev.			0.1408	0.1138	0.1147	0.1207
RMS			0.1412	0.1158	0.1170	0.1213

6.1.4.4 No A Priori Model for GPS

Once it has been seen that the different a priori models affect the individual GPS solution, the impact of not using any a priori model is also investigated. As a result, ECOM1 and empirical accelerations are applied directly without using a physical a priori model to analyse the absolute influence of the a priori model in the GNSS processing. Table 6.13 summarises the empirical acceleration constraint values and the orbital overlap results of all the different cases. It can already be seen that there is a generalised increase in the orbit overlaps for all solutions. Additionally, further constraining the solution seems to be worse, contrary to all the previous cases, which is a reasonable result as the parameters cannot accommodate the unknown differences which are estimated without a priori data. However, the fact that all the variants yield better results for the LOD estimates than the current box-wing model, as seen in Figure 6.18, shows that for GPS an improved a priori model and tuning of the empirical accelerations are required to improve the EOP estimates, without affecting the other variables in the estimation process.

Table 6.13: GPS empirical acceleration and a priori configurations and metrics

A priori GPS model	**CHAMP Box-Wing Model**	**No apriori Model**		
CPR case	Nominal	Nominal	Constrained	Removed
CPR constraint value $[km/s^2]$	10^{-13}	10^{-13}	10^{-14}	0
3D RMS orbit overlaps $[mm]$	30.6	43.1	43.9	45.5

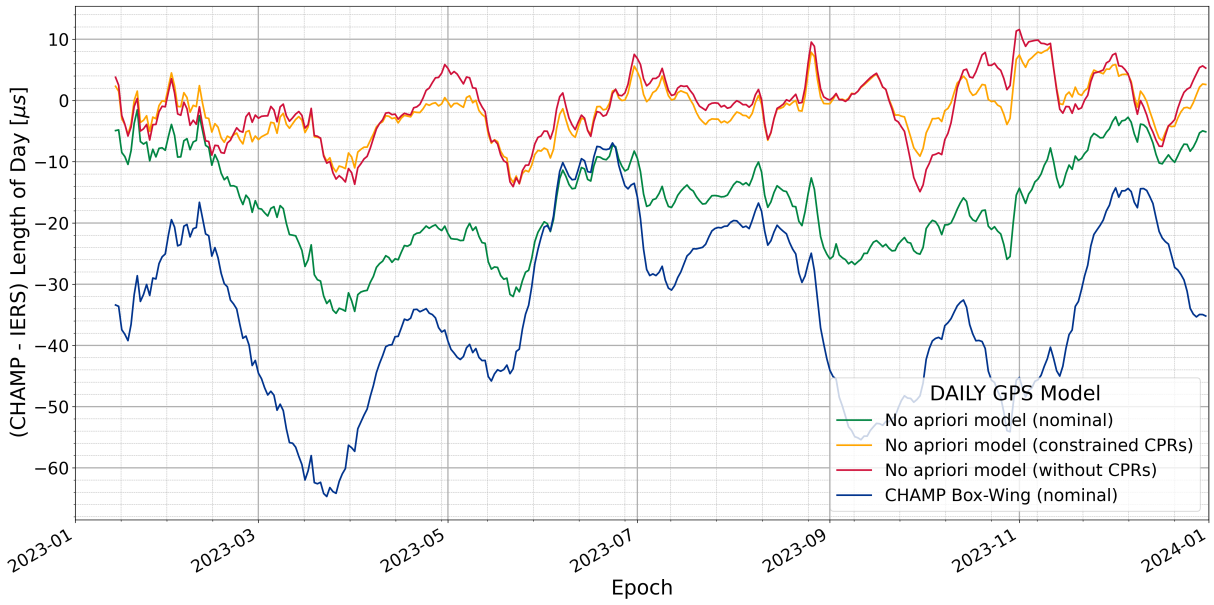

Figure 6.18: DAILY GPS LOD without apriori model differences wrt. IERS EOP20C04

6.1.5 Impact on the Combined Solution

Based on the best results of the individual GPS modifications of the previous section, the following section shows the results of combining the new individual GPS solutions with the other nominal CHAMP constellations into a new set of MGNSS scenarios. This process is started with the constrained CPR CHAMP solution in Section 6.1.5.1, followed by the modified TUM models in Section 6.1.5.2, and finishing with the constrained ROCK model results in Section 6.1.5.3.

6.1.5.1 CHAMP CPR Tighter-Constrained Box-Wing A Priori Model

The difference of the MGNSS CHAMP cases with nominal and tighter-constrained empirical accelerations with respect to the IERS EOP20CO4 reference are shown in Figure 6.19. Overall, a considerable improvement is reached with a considerably reduced bias, which is highlighted during the last two years. All other EOPs also result in better estimates than the original MGNSS case in terms of bias and drift with respect to IERS, evidencing the relevance of empirical accelerations in this setup.

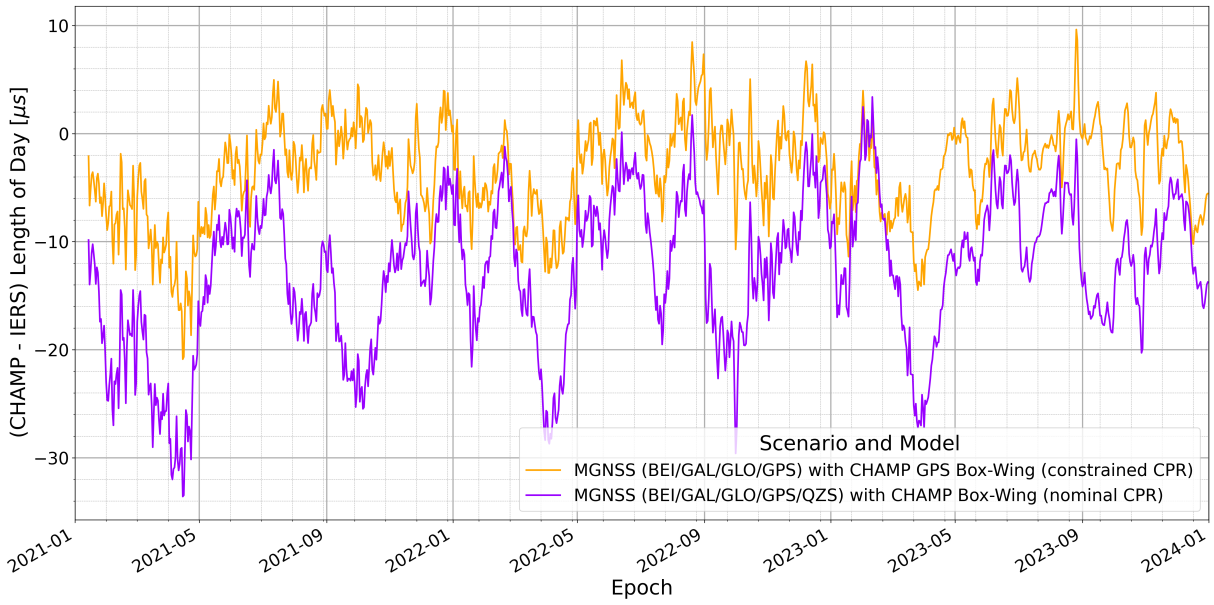

Figure 6.19: Effect of empirical acceleration on MGNSS LOD differences wrt. IERS EOP20C04

However, when taking into account all the different individual solutions that are stacked to obtain the new MGNSS solution, as shown in Figure 6.20, it can be seen that the combination almost completely relies on the GPS values, allowing limited variation coming from the other constellations. Thus, constraining the empirical accelerations influences the variance-covariance matrix of the a priori parameters in such a way that all the combination is heavily outweighed by the solution with smallest CPRs. This indicates that these empirical accelerations would need to be on a similar level for the other constellations to ensure a proper combination.

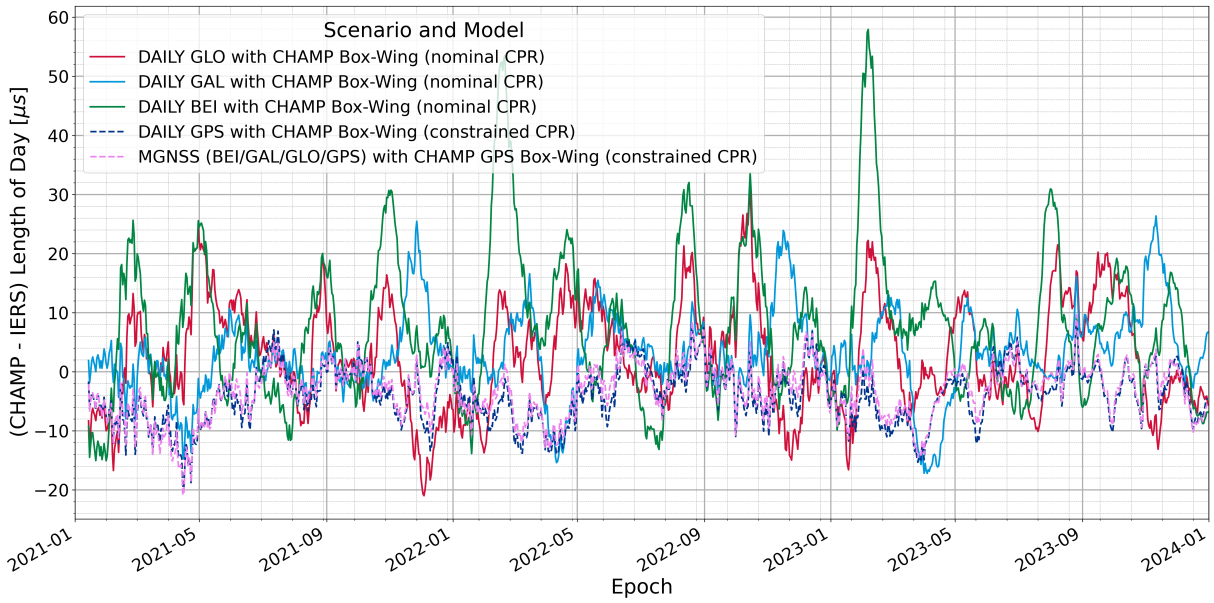

Figure 6.20: MGNSS solution combining the CPR constrained GPS CHAMP box-wing model with the nominal models for other constellations

6.1.5.2 TUM Box-Wing A Priori Model

The difference of the MGNSS CHAMP and TUM cases with nominal and tighter-constrained empirical accelerations with respect to the IERS EOP20CO4 reference are shown in Figure 6.21. A considerable improvement is also reached for the nominal TUM model, but still with a visible negative bias for the three-year period mean. This bias is further reduced when constraining the empirical accelerations, leading to an even smaller bias than the one found by constraining these accelerations in the nominal CHAMP model.

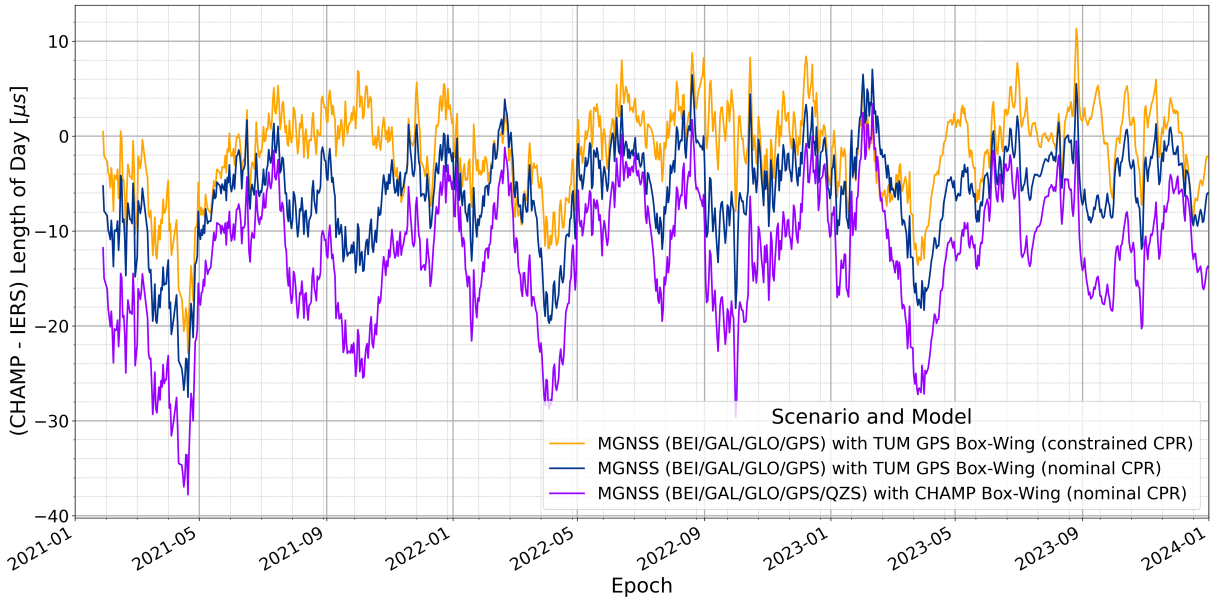

Figure 6.21: MGNSS solution combining the GPS TUM box-wing model with the nominal models for other constellations

All other EOPs also result in better estimates than the original MGNSS case for both TUM models in terms of bias and drift with respect to IERS, confirming that the nominal CHAMP box-wing model is suboptimal. The different individual solutions that are stacked to obtain the new MGNSS solution with nominal CPRs are shown in Figure 6.22, where the combination gives more weight to other constellations, bringing it further away from the still not perfect DAILY GPS values. Conversely, the LOD results of the different DAILY CHAMP nominal solutions combined with the new modified GPS TUM box-wing model with tighter constraints are shown in Figure 6.23. As the individual tighter constrained LOD GPS individual estimates had a smaller bias and drift, an additional improvement is reached with an almost null bias for the three-year period mean. However, as seen in the previous constrained case, all the EOPs values from the combination heavily weight the GPS individual constellation, adding limited variation coming from the other constellations.

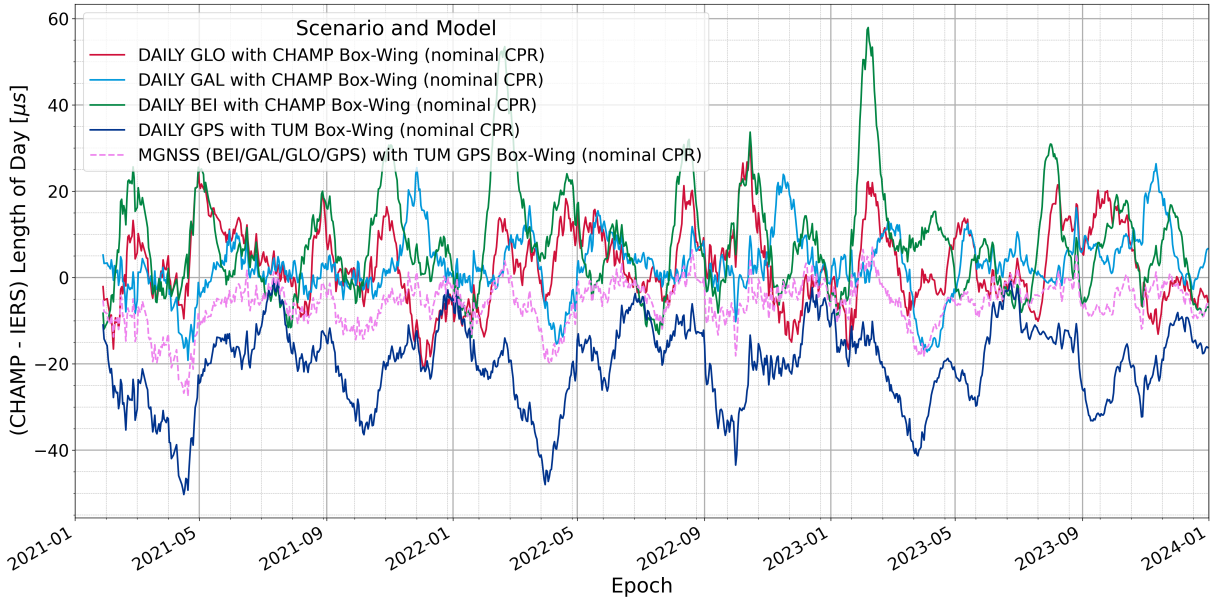

Figure 6.22: MGNSS solution combining the GPS TUM box-wing model with the nominal models for other constellations

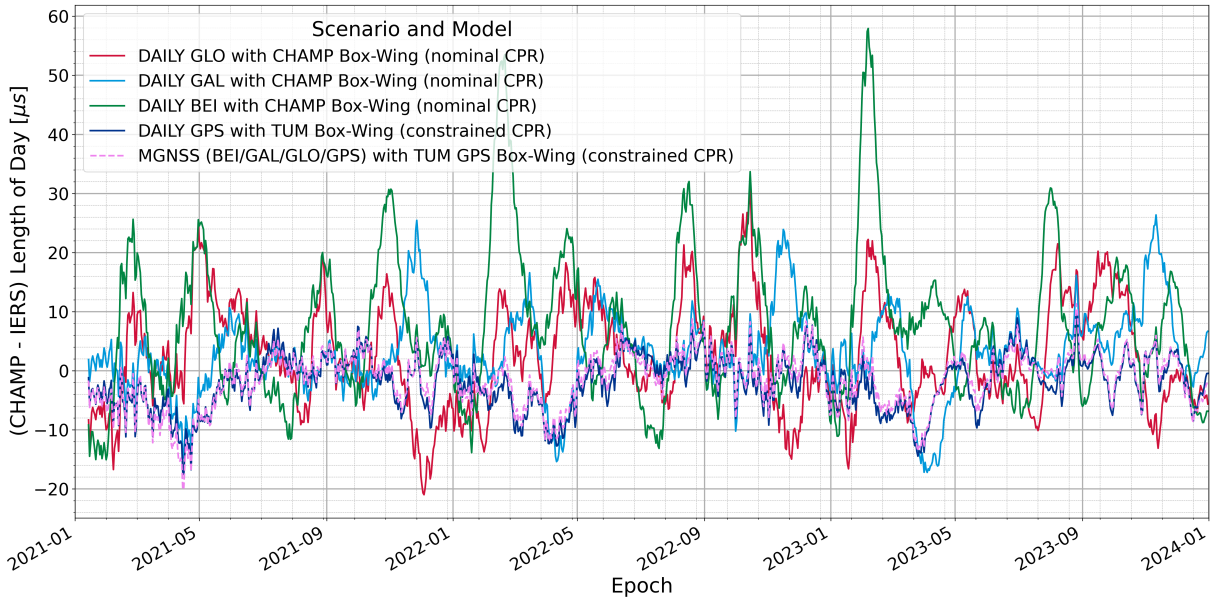

Figure 6.23: MGNSS solution combining the CPR constrained GPS TUM box-wing model with the nominal models for other constellations

6.1.5.3 ROCK Box-Wing A Priori Model

The difference of the MGNSS CHAMP and ROCK cases with nominal and tighter-constrained empirical accelerations with respect to the IERS EOP20CO4 reference are shown in Figure 6.24, respectively. A considerable improvement is also reached for the tighter-constrained ROCK model, but with a larger negative bias than the TUM model for the year 2023. All other EOPs also result in better estimates than the original MGNSS case in terms of bias and drift

The results of the different DAILY nominal CHAMP solutions combined with the new tighter-constrained GPS ROCK model are shown in Figure 6.25. A similar improvement to the previous constrained cases is reached, with a larger negative bias due to the large weight given to the GPS constellation, even if in this case the other constellations still modify slightly the combined solution.

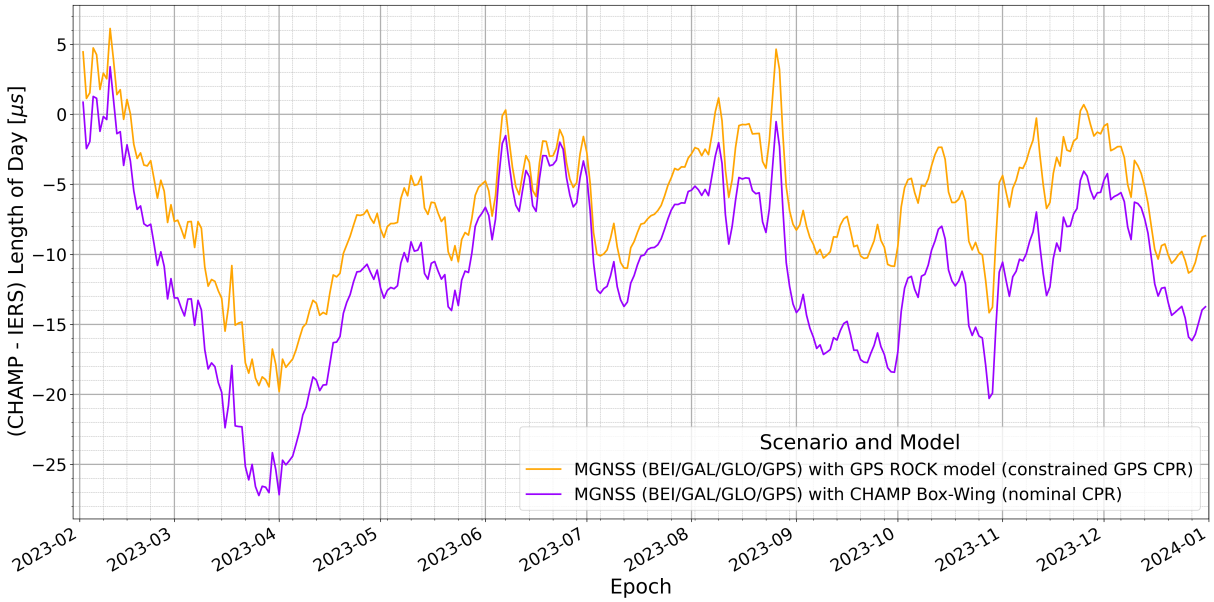

Figure 6.24: MGNSS solution combining the CPR constrained GPS ROCK model with the nominal models for other constellations

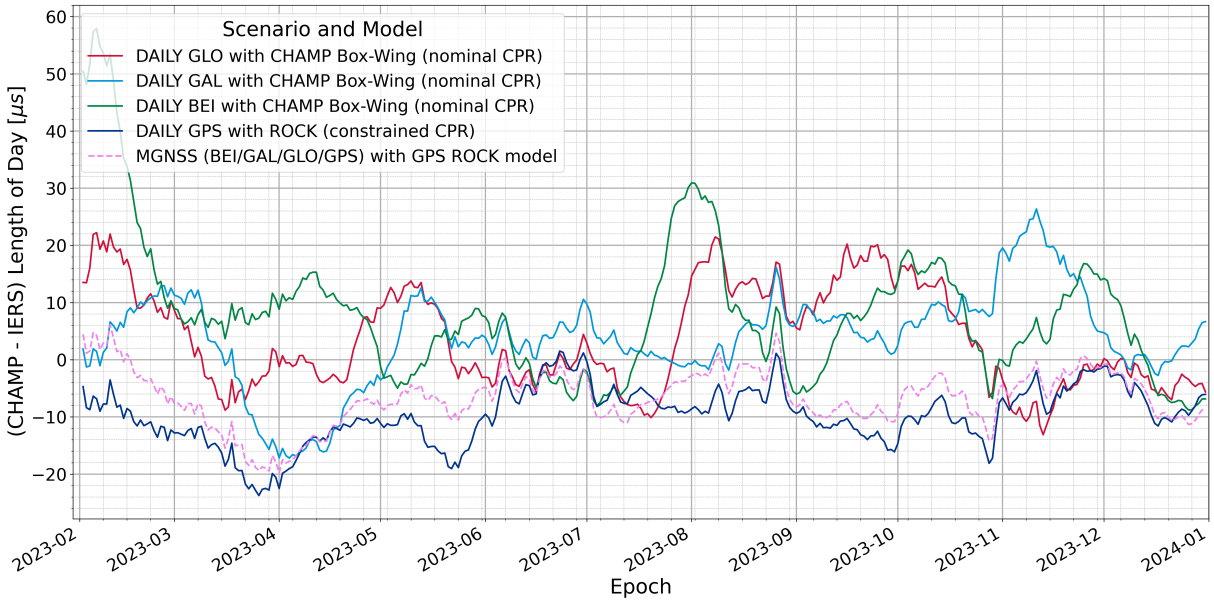

Figure 6.25: MGNSS solution combining the CPR constrained GPS ROCK model with the nominal models for other constellations

6.2 Further Analysis into Ground Stations and Satellites

This section introduces additional analysis performed regarding the ground stations and satellites of both the individual DAILY and combined MGNSS solutions. The reduction of the maximum number of stations to analyse the effect of the BeiDou station network growth is shown in Section 6.2.1, while the effects of removing poorly-behaving satellites or stations are shown in Section 6.2.2 and Section 6.2.3, respectively.

6.2.1 BeiDou Station Network Growth

As previously seen in the ground station analysis, BeiDou station network nearly doubled in size from 2021 to 2023, going from a mean number of 60 at the beginning, and reaching 120 stations during 2023. This large increase could potentially cause issues in the individual constellation that would propagate to the combination. To minimise the potential impact of this rapid station increase on the combined solution's accuracy, the number of stations was capped at 100 for the entire year 2023. By limiting the number of stations, the objective was to create a more controlled analysis environment where the station network remained constant throughout the analysis, thus reducing the variations caused by the increasing number of BeiDou-tracking stations. Additionally, this setup provided an opportunity to test the hypothesis that the fluctuations in station accuracy and combined solution quality could be attributed to the growing number of BeiDou-enabled stations. However, while the estimates of the other constellations changed with the reduction of observations coming from limiting the maximum number of ground stations, the results of combining BeiDou with the other capped constellations did not show a significant improvement or notable pattern changes related to the previously found inconsistencies. Thus, the hypothesis that the increasing number of BeiDou-tracking stations was a primary cause of the variation in station accuracy between the DAILY and MGNSS scenarios was therefore dismissed, as it does not appear to be the main driver behind the observed changes in accuracy.

6.2.2 Satellite Removal

In the satellite parameter analysis, certain satellites have been seen to degrade the quality of the overall results. For this reason, small tests removing the conflicting satellites have been performed to see the effect on both the individual and combined solution. Apart from the removal of the BEI-M215 satellite, which was already excluded in the 2023 analysis section, specific satellite groups have been removed. For instance, satellites such as GPS-44, GPS-70, GLO-719, GLO-735, and the IGSO satellites within the BeiDou constellation, were removed based on their poor performance in the initial analyses. The removal of these satellites resulted in slightly lower overlap values, indicating some improvement in orbit determination precision in both the individual and combined solutions. However, despite the marginal reduction in overlap errors, the overall variations in EOPs and other critical parameters remained largely unaffected. The changes observed were minimal, and the removal of these satellites did not lead to significant improvements in the quality of the combined solution. Furthermore, removing these satellites also reduces the available data pool, which could potentially hinder the robustness of the combined solution in certain cases, as fewer data points from critical constellations may lead to less accurate estimations in the overall system. While these trials highlight the potential benefits of removing underperforming satellites, the results suggest that such adjustments may not lead to substantial improvements within the scope of this thesis. Further analysis on a case-by-case basis could be pursued to assess specific satellite impacts more thoroughly. However, for the purposes of this research, the removal of these satellites did not yield meaningful enhancements to the overall MGNSS solution quality.

6.2.3 Ground Station Removal

In an effort to enhance the combined GNSS solution, an additional analysis was conducted, focusing on the exclusion of faulty stations exhibiting significant discrepancies between the individual and combined solutions, as shown in Table 5.6. The aim of this approach was to evaluate whether removing problematic stations could lead to an improvement in the overall precision and consistency of the combined solution. The process involved identifying stations with notable outliers in their performance and excluding them from the reprocessing in order to assess the impact on the combined results. However, despite these attempts, the results did not show any substantial improvement in the combined solution's accuracy. This is likely because, with the exception of a very small number of stations, the majority of the stations with significant differences between the individual and combined solutions belong to the GLONASS constellation. GLONASS, which typically has lower precision due to its known orbit determination challenges, is assigned lesser weight in the final combination. Therefore, the

exclusion of stations primarily affecting GLONASS did not result in notable changes in the overall accuracy of the combined solution. The relative insignificance of GLONASS in the final combination means that its influence on the total solution is limited, and thus, the new results aimed at stations mostly affecting GLONASS had only a minor effect. Further improvements in the overall combined solution would likely require addressing the intrinsic limitations of GLONASS or making advancements in its orbit and error models, as its contribution remains proportionally smaller compared to other constellations.

7 Conclusions and Recommendations

Throughout the preceding chapters, a comprehensive analysis has been conducted to address the inconsistencies and challenges in the processing of multi-GNSS solutions at the Navigation Support Office and how to potentially solve them. This concluding chapter summarises the main findings of the research and presents key recommendations for improving the Navigation Support Office multi-constellation GNSS accuracy and operational efficiency.

7.1 Conclusions

In this thesis, an in-depth examination was carried out on the ESA/ESOC multi-GNSS solutions, with a specific focus on refining the combined multi-constellation approach to enhance accuracy while maintaining operational efficiency. Central to this study was the analysis of inconsistencies within individual and combined GNSS solutions, alongside an investigation into their underlying causes and potential improvements to ensure consistency and reliability. Through this approach, insights were gained into the unique characteristics of individual constellations and the challenges inherent in their integration. The initial phase of the study focused on extracting all the estimated parameters of the individual and combined GNSS solutions from the novel Consolidated High Accuracy MGNSS Processing (CHAMP) framework. For this purpose, a new Python library was developed to efficiently extract all types of data from the operational pipeline and store the parameters of interest, seamlessly integrating into the NSO GNSS processing sequence pipeline. As a result, the new methodology not only reduces the overall file size requirements by eliminating the need for larger intermediate analysis files, but also allows to monitor data to find GNSS processing constellation inconsistencies. The following paragraphs summarise the principal conclusions drawn from this research.

One of the key findings of this thesis is found in the estimation of Earth Orientation Parameters. The analysis of the different individual solutions with respect to the combined solution showed that the estimation of the Length of Day was divided into two clear groups, where the GPS constellation and its combination with QZSS were behaving differently than the others. As a result, comparing with the IERS EOP20CO4 external reference, it was seen that GPS, and its combination with either QZSS or all the other constellations, diverged from the reference by a large bias, while the other individual constellations were mostly unbiased. Consequently, due to the small variance on the absolute parameters of the GPS constellation compared to the others, the combined LOD solution is heavily weighted by this constellation despite being the worst result compared to the external reference. Thus, this comparison evidenced the large reliance of CHAMP on suboptimal GPS modelling, which is not in line with the relative accuracy of the other constellations. Additionally, in terms of polar motion values and rates, it was seen that the GLONASS individual constellation diverged from all other constellations with respect to the IERS reference. However, as GLONASS observations are down-weighted from the start, the effect is not visible on the combined solution.

The analysis of the CHAMP ground station network has identified outlier stations based on the station position estimate differences between the individual and combined solutions, which are predominantly visible in the UP direction within the East-North-Up frame. While limiting or removing these stations from the GNSS processing can help enhance the robustness of the station network, smaller tests without the conflicting stations made it clear that ground station issues were not the primary source of the discrepancies in the combined solution. In addition, the analysis of the clock parameters uncovered sub-daily Intersystem Bias (ISB) jumps that were being inadequately managed in the combined solution, confirming that the inability to dynamically adjust ISB parameters for certain stations leads to an increased number of rejected observations in the combined solution, further impacting the combined overall performance.

The analysis of the CHAMP framework satellites comprised satellite orbits, Empirical CODE Orbit Model (ECOM) parameters and empirical accelerations, denoted as Cycle-per-Revolution (CPR) accelerations. The satellite orbits comparison between the individual and combined solutions, which relies on satellite orbit overlap statistics between successive days, highlighted the degradation of the Galileo orbit within the combination. Additionally, it was found that a specific satellite from BeiDou, BEI-M215, significantly contributed to the variations between individual and combined solutions from 2023 onwards, due to satellite malfunctioning that required changes in the specific satellite attitude, and it was subsequently removed from the statistics. The inclined geosynchronous orbit satellites also showed that the current 24h processing arcs are sub-optimal for these satellites, as this period coincides with their orbital period, leading to less accurate overlap results and overall orbit precision. The detailed examination of the estimated ECOM1 and empirical acceleration parameters,

that are used to absorb modelling deficiencies, further reinforced the idea that GPS modelling was problematic. The discrepancies of these parameters were tied to the improper modelling of non-gravitational forces, which correlate with the LOD issues.

Based on the analysis of the nominal CHAMP solutions, the next phase involved systematically removing constellations from the combination to isolate their effects on the estimated parameters. The results confirmed that GPS is the main driver of the inconsistencies in the Earth Orientation Parameters, and the degradation of the other constellations orbit overlaps. Additionally, the examination of the different GPS satellite blocks and orbital planes showed differences between these for the CPR accelerations, confirming different effects of the empirical accelerations based on the satellite geometry and position in space. Consequently, efforts were directed towards tuning the CPR parameters for GPS and refining the non-gravitational a priori models. The results demonstrated that carefully adjusting the CPR parameters could mitigate the observed biases and drifts in the GPS LOD estimates, and showed that the current CHAMP box-wing models for the GPS constellation were suboptimal. The alternative a priori models used relied on the ROCK model, which provides a more accurate depiction of spacecraft surface properties and external forces, featuring individual models for each satellite, rather than a generalised type-based approach, and an updated box-wing model based on the combination of the current parameters with those estimated by an analysis performed by TU Munich. The new a priori models resulted in an enhanced accuracy of the combined solution, while heavily reducing the LOD bias of the GPS constellations, indicating that enhancing the existing box-wing models could lead to a substantial improvement in the overall performance of the GPS constellation within the combined solution. However, even if the tightening of the CPRs for GPS is beneficial to the combined solution, due to the large weight of GPS in the combination, it has been seen that the already large weight of GPS increases even more, giving reduced freedom to the other constellations to contribute to the combined solution, degrading the consistency of the combination.

On the side, additional tests were conducted to remove outlier satellites and stations from the analysis to further refine the combination strategy. While these tests showed some minor improvements in orbit overlaps, particularly when removing a few older and poor performing satellites, the variations in EOPs and other critical parameters were minimal. Furthermore, the hypothesis stating that the increase of stations for BeiDou during the 3-year interval from the start 2021 to the end of 2023 could affect the processing results was dismissed, as no major differences were found between the individual and combined solution when constraining the maximum number of stations during the year 2023.

In conclusion, this thesis has underscored the critical impact of GPS modelling on the accuracy and consistency of multi-GNSS solutions, particularly in the estimation of Earth Orientation Parameters, such as the Length of Day. Through comprehensive analyses, it was determined that biases in GPS solutions heavily influence the combined multi-constellation result, revealing a disproportionate dependency on GPS due to its low variance but suboptimal non-gravitational force modelling. The targeted investigation into the root causes of these discrepancies, including constellation-specific issues in ECOM parameters, CPR accelerations, and a priori models, has provided valuable insights into the adjustments needed to mitigate LOD biases. Implementing enhanced CPR tuning and alternative a priori models, specifically the ROCK and refined box-wing models, has demonstrated substantial improvements in reducing GPS-related biases within the combined solution. Although these modifications improve GPS performance, they simultaneously increase the constellation's weight in the combination, thereby limiting the contribution of other constellations and posing new challenges in achieving a balanced, reliable integration. Overall, this research highlights promising avenues for refining the CHAMP framework's multi-GNSS solutions and sets a foundation for continued advancements in the Navigation Support Office GNSS processing accuracy and operational resilience.

7.2 Recommendations for Future Work

The primary recommendation for future work is the development of a new set of GPS box-wing models, either block or satellite specific, based on the different models and parameters analysed in this thesis. The impact of these models could now be analysed on all estimated parameters, comparing the individual and combined solutions, not only against each other, but also against the IERS EOP20CO4 external reference. Once this enhanced box-wing model is finalised, it will be essential to recalibrate and retune the constraints of the empirical accelerations not only for the new models, but also for all the constellations in order to make sure that the weighting scheme of the combination does not heavily rely on a unique constellation for the Length of Day estimates. With the new non-gravitational a priori models and empirical constraints, the next step would be to see the influence of the new Earth Orientation Parameter estimates inside ESA's Earth Rotation Parameter (ERP) project, which combines GNSS data coming from CHAMP with DORIS, VLBI, and SLR observations to produce enhanced ERP estimates.

Another recommendation for future work is to address the sub-daily Intersystem Bias jumps observed in the combined GNSS solution. These ISB variations currently impact the overall performance by increasing the number of rejected observations. A promising approach would be to develop a more dynamic ISB parameter adjustment method, allowing the GNSS processing system to adapt to ISB fluctuations more effectively. This could help maintain higher observation acceptance rates and improve the stability and accuracy of the combined solution

In addition, future work should include a thorough review of the stations and satellites selected for processing to ensure optimal performance. This includes an analysis of the optimal number of stations, balancing computational efficiency with accuracy requirements. By carefully evaluating which stations and satellites contribute most effectively to the combined solution, it would be possible to minimise inconsistencies and enhance the robustness of the GNSS processing. Regularly updating this selection based on performance criteria could further reduce the likelihood of outlier-induced biases and improve the stability and accuracy of the combined results.

Once the new models and constraint tuning are fully verified and validated, the processing methodology developed in this thesis will need to be integrated into the operational NSO GNSS pipeline, automating the conversion of all necessary intermediate files into accessible Python dataframes that optimise resource use and data handling. Routinely generating datasets containing all newly estimated parameters would facilitate the implementation of a quality indicator system, enabling continuous monitoring for outliers and early detection of model drift from its nominal path. Moreover, as these processes become standardised, AI and machine learning algorithms could play a pivotal role in automating the quality assurance, anomaly detection, and adaptive model refinement, ensuring an efficient and resilient GNSS processing framework for future operational demands.

Finally, integrating these refined processing techniques into the NSO workflow will enhance the accuracy and reliability of NSO GNSS products, which will subsequently contribute to the International GNSS Service. The updated models and reprocessing methods will elevate the overall quality of the combined solutions, supporting both future GNSS applications and international initiatives with advanced, dependable GNSS data products, thereby improving the global multi-GNSS combination.

Bibliography

Agency, E. S. (2024). *Esa's gnss observation network (egon)* [Accessed: 2024-10-05]. http://navigation-office.esa.int/ESA%27s_GNSS_Observation_Network_%28EGON%29.html (cit. on p. 60).

Agnew, D. C. (2024). A global timekeeping problem postponed by global warming. *Nature*, *628*(8007), 333–336. https://doi.org/10.1038/s41586-024-07170-0 (cit. on p. 51).

Arnold, D., Meindl, M., Beutler, G., Dach, R., Schaer, S., Lutz, S., Prange, L., Sośnica, K., Mervart, L., & Jäggi, A. (2015). Code's new solar radiation pressure model for gnss orbit determination. *Journal of Geodesy*, *89*(8), 775–791. https://doi.org/10.1007/s00190-015-0814-4 (cit. on p. 36).

Boehm, J., Heinkelmann, R., & Schuh, H. (2007). Short note: A global model of pressure and temperature for geodetic applications. *Journal of Geodesy*, *81*(10), 679–683. https://doi.org/10.1007/s00190-007-0135-3 (cit. on p. 14).

Boehm, J., Werl, B., & Schuh, H. (2006). Troposphere mapping functions for gps and very long baseline interferometry from european centre for medium-range weather forecasts operational analysis data. *Journal of Geophysical Research: Solid Earth*, *111*(B2). https://doi.org/https://doi.org/10.1029/2005JB003629 (cit. on pp. 14, 96).

Bruni, S., Mayer, V., Otten, M., & Schoenemann, E. (2022). ESA's Earth Rotation Parameter Service. *Proceedings of the 2nd Earth Orientation Parameters Prediction Comparison Campaign (2nd EOP PCC) Workshop*. http://navigation-office.esa.int/attachments/32834435/1/2nd_EOPPCC_ws_ESA.pdf (cit. on p. 51).

Bury, G., Sośnica, K., Zajdel, R., & Strugarek, D. (2020). Toward the 1-cm Galileo orbits: challenges in modeling of perturbing forces. *Journal of Geodesy*, *94*(2), Article 16, 16. https://doi.org/10.1007/s00190-020-01342-2 (cit. on p. 36).

Calian Group. (2024). *GNSS constellations, radio frequencies, and signals*. https://www.calian.com/advanced-technologies/gnss/information-support/gnss-constellations-radio-frequencies-and-signals/ (cit. on p. 6).

Charlot, P., Jacobs, C. S., Gordon, D., Lambert, S., de Witt, A., Böhm, J., Fey, A. L., Heinkelmann, R., Skurikhina, E., Titov, O., Arias, E. F., Bolotin, S., Bourda, G., Ma, C., Malkin, Z., Nothnagel, A., Mayer, D., MacMillan, D. S., Nilsson, T., & Gaume, R. (2020). The third realization of the international celestial reference frame by very long baseline interferometry. *A&A*, *644*, A159. https://doi.org/10.1051/0004-6361/202038368 (cit. on p. 29).

Chen, J. L., Wilson, C. R., Ries, J. C., & Tapley, B. D. (2013). Rapid ice melting drives earth's pole to the east. *Geophysical Research Letters*, *40*(11), 2625–2630. https://doi.org/https://doi.org/10.1002/grl.50552 (cit. on p. 51).

China Satellite Navigation Office. (2019). *The application service architecture of beidou navigation satellite system*. Retrieved February 15, 2024, from http://www.beidou.gov.cn/xt/gfxz/201912/P020191227337275341705.pdf (cit. on p. 7).

Curtis, H. D. (2013). *Orbital mechanics for engineering students*. Butterworth-Heinemann. (Cit. on p. 31).

Desai, S. D., & Sibois, A. E. (2016). Evaluating predicted diurnal and semidiurnal tidal variations in polar motion with gps-based observations. *Journal of Geophysical Research: Solid Earth*, *121*(7), 5237–5256. https://doi.org/https://doi.org/10.1002/2016JB013125 (cit. on p. 46).

Dilssner, F. (2010). Satellite antenna phase center variations of gps block iif satellites. *Inside GNSS* (cit. on p. 42).

Dilssner, F., & Springer, T. (2011). The glonass-m satellite yaw-attitude model. *Advances in Space Research*, *47*(1), 160–171. https://doi.org/https://doi.org/10.1016/j.asr.2010.09.007 (cit. on p. 42).

Dilssner, F., & Springer, T. (2024a). Glonass-k attitude: Rapid turning maneuvers and other deviations from ideal yaw steering. *GPS Solutions*. https://doi.org/10.21203/rs.3.rs-4102651/v1 (cit. on p. 42).

Dilssner, F., & Springer, T. (2024b). Taming the invisible: All-force radiation pressure modeling for multi-gnss. *IGS Workshop 2024, July 1-5, Bern, Switzerland*. https://files.igs.org/pub/resource/pubs/workshop/2024/IGSWS-2024-PY0202-Dilssner-Taming_the_Invisible.pdf (cit. on pp. 37, 81).

Duan, B., & Hugentobler, U. (2021). Enhanced solar radiation pressure model for gps satellites considering various physical effects. *GPS Solutions*, *25*(2), 42. https://doi.org/10.1007/s10291-020-01073-z (cit. on p. 79).

ESA Navigation Support Office. (2023). *Galileo precise orbit and clock determination, pod concept at esoc*. http://navigation-office.esa.int/attachments/32834975/1/Galileo_POD_IGSStop6_230523_FGini.pdf (cit. on p. 42).

European GNSS Service Centre. (2024). *Galileo satellite metadata* [Accessed: 2024-11-03]. https://www.gsc-europa.eu/support-to-developers/galileo-satellite-metadata (cit. on p. 42).

European Space Agency. (2009). *NAPEOS Math Models & Algorithms*. http://navigation-office.esa.int/attachments/32834429/1/NAPEOS_MathModels_Algorithms.pdf (cit. on pp. 11, 15, 26, 37, 39, 40).

European Space Agency. (2021). *Galileo future and evolutions*. Retrieved February 15, 2024, from https://gssc.esa.int/navipedia/index.php?title=Galileo_Future_and_Evolutions (cit. on p. 7).

European Space Agency. (2024a). *European space agency (esa)*. Retrieved October 27, 2024, from https://www.esa.int/ (cit. on p. 5).

European Space Agency. (2024b). *Ops-gn navigation support office*. Retrieved June 15, 2024, from http://navigation-office.esa.int (cit. on p. 40).

Gini, F., Mayer, V., Traiser, B., Springer, T., Dilssner, F., Sermanoukian, I., Schoenemann, E., & Enderle, W. (2024). Esa's new operational gnss processing approach for precise igs products [Poster Session 1, 01 July 2024, Bern]. *International GNSS Service Symposium and Workshop 2024* (cit. on pp. 40, 41, 45).

International GNSS Service. (2024a). *International gnss service - network* [Accessed: 2024-10-05]. https://network.igs.org/ (cit. on pp. 60, 63).

International GNSS Service. (2024b). *Mgex metadata* [Accessed: 2024-11-01]. https://igs.org/mgex/metadata/ (cit. on p. 42).

Kaplan, G. H. (2006). The iau resolutions on astronomical reference systems, time scales, and earth rotation models. *arXiv preprint astro-ph/0602086* (cit. on p. 29).

Kelly, M. (2012). *The earth's ionosphere: Plasma physics and electrodynamics* (Vol. 43). Elsevier. (Cit. on p. 13).

Kouba, J. (2009). A simplified yaw-attitude model for eclipsing gps satellites. *GPS Solutions*, *13*(1), 1–12. https://doi.org/10.1007/s10291-008-0092-1 (cit. on p. 42).

Leick, A., Rapoport, L., & Tatarnikov, D. (2015). *Gps satellite surveying*. John Wiley & Sons. (Cit. on p. 14).

Lemoine, J.-M., Biancale, R., Reinquin, F., Bourgogne, S., & Gégout, P. (2021). *Cnes/grgs rl04 earth gravity models and eigen-grgs.rl04.mean-field* [Accessed: 2024-10-13]. GRGS/CNES. https://grace.obs-mip.fr/variable-models-grace-lageos/grace-solutions-release-04/rl04-products-description/ (cit. on p. 32).

McCarthy, D. D., & Seidelmann, P. K. (2018). *Time: From earth rotation to atomic physics*. Cambridge University Press. (Cit. on p. 51).

Montenbruck, O., & Gill, E. (2001). *Satellite orbits: Models, methods, and applications* (Vol. 2). Springer. (Cit. on pp. 22, 31, 39).

Na, S.-H., Cho, J.-H., Baek, J., Kwak, Y., & Yoo, S.-M. (2012). Spectral analysis on earth's spin rotation for the recent 30 years. *Journal of the Korean Physical Society*, *61*. https://doi.org/10.3938/jkps.61.152 (cit. on p. 51).

Nelson, R. A., McCarthy, D. D., Malys, S., Levine, J., Guinot, B., Fliegel, H. F., Beard, R. L., & Bartholomew, T. R. (2001). The leap second: Its history and possible future. *Metrologia*, *38*, 509–529 (cit. on p. 51).

Petit, G., & Luzum, B. (2010). *IERS Conventions (2010)* (Technical Note No. 36). International Earth Rotation and Reference Systems Service (IERS). https://www.iers.org/SharedDocs/Publikationen/EN/IERS/Publications/tn/TechnNote36/tn36.pdf (cit. on pp. 30, 46, 95).

PosiTim. (2012). *PosiTim, High Accuracy GNSS Solutions and Services*. Retrieved March 15, 2023, from https://www.positim.com/ (cit. on p. 40).

QZSS Cabinet Office. (2020). *Quasi-zenith satellite system performance standard*. Retrieved February 15, 2024, from https://qzss.go.jp/en/technical/download/pdf/ps-is-qzss/ps-qzss-002.pdf (cit. on p. 7).

Reckeweg, F. (2020). *Integer ambiguity resolution for multi-gnss and multi-signal raw phase observations* [Doctoral dissertation, Technischen Universität Darmstadt]. https://dgk.badw.de/fileadmin/user_upload/Files/DGK/docs/c-849.pdf (cit. on pp. 8, 10).

Rotation, I. E., & (IERS), R. S. S. (2024). *Earth orientation data* [Accessed: 2024-11-03]. https://www.iers.org/IERS/EN/DataProducts/EarthOrientationData/eop.html (cit. on p. 51).

Royal Observatory of Belgium. (2024). *Euref permanent gnss network* [Accessed: 2024-10-05]. https://epncb.eu/ (cit. on p. 63).

Saastamoinen, J. (1972). Atmospheric correction for the troposphere and stratosphere in radio ranging satellites. *The use of artificial satellites for geodesy*, *15*, 247–251 (cit. on pp. 14, 96).

Sanz Subirana, J., Hernandez-Pajares, M., & Juan Zornoza, J. M. (2013). *Gnss data processing: Fundamentals and algorithms*. European Space Agency. (Cit. on pp. 4, 7–9, 13–17).

Schoenemann, E., Dilssner, F., Gini, F., Gonzalez, F., Seitz, M., Blossfeld, M., Springer, T., & Enderle, W. (2024). Esa antex: A consistent gnss satellite phase center model based on galileo ground calibration data. *International GNSS Service Symposium and Workshop 2024*. http://navigation-office.esa.int/attachments/83496549/1/IGSWS2024_ESAANTEX.pdf (cit. on p. 15).

Schönemann, E. (2014). *Analysis of gnss raw observations in ppp solutions* (Publication No. 42) [Doctoral dissertation, Technischen Universität Darmstadt]. (Cit. on p. 21).

Schutz, B., Tapley, B., & Born, G. H. (2004). *Statistical orbit determination*. Elsevier. (Cit. on pp. 9, 18, 19, 22, 39).

Sermanoukian, I. (2024). *E-TAC: ESA Precise Navigation System Test cases Automatic Comparison* (tech. rep.). TU Delft. (Cit. on p. 40).

Springer, T., Beutler, G., & Rothacher, M. (1999). A new solar radiation pressure model for gps satellites. *GPS Solutions*, *2*(3), 50–62. https://doi.org/10.1007/PL00012757 (cit. on p. 36).

Teunissen, P. J., & Montenbruck, O. (2017). *Handbook of global navigation satellite systems* (Vol. 10). Springer. (Cit. on pp. 4–11, 14–18, 27, 28, 32–34).

United Nations Office for Outer Space Affairs. (2018). *The interoperable global navigation satellite systems space service volume*. Retrieved February 15, 2024, from https://www.unoosa.org/res/oosadoc/data/documents/2018/stspace/stspace75_0_html/st_space_75E.pdf (cit. on p. 7).

Wu, J.-T., Wu, S. C., Hajj, G. A., Bertiger, W. I., & Lichten, S. M. (1993). Effects of antenna orientation on gps carrier phase. *Astrodynamics 1991*, 1647–1660 (cit. on pp. 15, 96).

Xia, F., Zhou, S., Lin, X., Hu, X., Liu, X., Jiang, N., & You, Y. (2024). Precise orbit determination for beidou-3 satellite with solar panel non-nominal orientation operations using telemetry information. *GPS Solutions*, *28*. https://doi.org/10.1007/s10291-024-01752-1 (cit. on p. 66).

A CHAMP Framework

A.1 CHAMP Models

A summary of the models used for relativity, gravitational perturbations, terrestrial reference frame definitions and atmospheric mapping can be found in the following Table A.1 to Table A.5, detailing the conventions and sources used for each model.

Table A.1: CHAMP Gravitational Models

Category	Topic	Description
Gravity field	Degree and order	12
Gravitational perturbations	Gravity field (Static)	Static gravity field model EIGEN.GRGS.RL04 C21 and S21 coefficients according to IERS 2010 conventions
	Gravity field (Time varying)	Annual and semi-annual terms of the degree and order two coefficients
	Solid Earth tides	Applied using IERS 2010 conventions
	Permanent tide (Tidal system)	Applied using IERS 2010 conventions
	Solid Earth pole tide	Applied using IERS 2010 conventions
	Ocean tides	Applied based on EOT11A model
	Ocean pole tide	Applied using IERS 2010 conventions Model for C21 and S21 terms only
	Lunar gravity	Only J2 effect considered
	Third bodies	JPL DE405: all planets, Sun and Moon

Table A.2: CHAMP General Terrestrial Reference Frame Models

Category	Topic	Description
Terrestrial Reference Frame	A priori frame	Predefined reference frame Applied ITRF2020 model
	Post seismic deformation	Deformations of the Earth's crust that occur after seismic events Applied ITRF2020 model
	Solid Earth tides	Deformations of the Earth's crust caused by the gravitational pull of the Moon and the Sun Anelastic Earth model applied using IERS 2010 routine DEHANTTIDEINEL.F (Petit and Luzum, 2010)
	Permanent tide	Constant deformation of the Earth's crust due to the gravitational forces of the Moon and the Sun (Zero-frequency contribution) Conventional tide-free approach (permanent tidal effects are included in the tide model but are removed from the site coordinates)
	Solid Earth Pole tide	Applied using IERS 2010 conventions to account for the deformation of the Earth's crust due to the movement of the Earth's rotational pole Additionally, mean pole effects are removed using the IERS 2010 mean pole model
	Ocean tides	Applied using IERS 2010 conventions to account for deformations of the Earth's crust due to the varying gravitational pull of the ocean's water Site-dependent amplitudes and phases (free ocean tide), with EOT11A model including joint mass centre of solid Earth and ocean correction. North/East/Up displacements using IERS routine HARDISP.F (Petit and Luzum, 2010)

Table A.3: CHAMP Atmosphere Models

Layers	Topic	Description
Troposphere	Hydrostatic a priori model	Predefined model for calculating tropospheric (Saastamoinen, 1972) Global Pressure and Temperature (GPT) Model
	Hydrostatic mapping function	Global Mapping Function (GMF) dry component used to map the hydrostatic dry delay to the satellite's line of sight (Boehm, Werl, and Schuh, 2006)
	Wet mapping function	Global Mapping Function (GMF) wet component used to map the delay due to water vapour in the atmosphere (Boehm, Werl, and Schuh, 2006)
	Gradient mapping functions	Variations in the atmosphere's refractivity with elevation angle e $\frac{1}{\sin(e)\cdot\tan(e)+0.0032}$
Ionosphere	First order effect	Accounted for by dual-frequency observations in linear combination.

Table A.4: CHAMP GNSS Antenna Models

Category	Topic	Description
GNSS Antenna Modeling	GNSS transmitting antenna	Data from esa23.atx Galileo antenna PCOs and PCVs fixed to ground calibration values
	GNSS receiving antenna	Data from igs20.atx ARP offsets, and elevation- and azimuth dependent PCVs applied
	Phase wind up	Applied according to Wu et al. (1993)

Table A.5: CHAMP Relativistic Models

Category	Topic	Description
Relativistic Model	Schwarzschild Terms	Applied to account for the curvature of space-time around a massive body.
	Lense-Thirring Precession	Applied using IERS 2010 conventions to account for the frame-dragging effect of rotating bodies.
	Geodetic (de Sitter) Precession	Applied using IERS 2010 conventions to account for space-time curvature caused by mass-energy.
	Relativistic Clock Effects	2nd order relativistic correction applied for non-zero orbit ellipticity to ensure time accuracy.
	Gravitational Time Delay	Applied using IERS 2010 conventions to account for the delay in signal travel time due to gravity.

A.2 CHAMP Programmes and Sequences

A summary of the programmes used within CHAMP sequences are shown in Table A.6, while the DAILY and MGNSS nominal sequences are detailed in Appendix A.2.1 and Appendix A.2.2, respectively.

Table A.6: CHAMP Source code programmes

Programme	Information
AmbFix.bin	Perform the integer ambiguity resolution of the GNSS phase ambiguities
Bahn.bin	Batch least-squares estimation (FLOAT and FIXED ambiguities)
BuildCat.bin	Makes a catalogue of the necessary files (e.g. RINEX observation files)
ClockComp.bin	Clock comparisons, aligning the clock to the reference one, if requested
ClockRef.bin	Generate new reference clock ensemble and apply to satellites/stations
ClockUpd.bin	Change clock format, time span or step size
CmdLine.tcl	Linux commands to execute within the tcl environment
Clock2Sp3.bin	Converts TCB to SP3 files
GnssObs.bin	Main pre-processing tool for GNSS observation
IgsAnaRep.bin	Tool to create an ASCII analysis report based on a residual file
Multiarc.bin	Normal equation stacking and coordinate alignment
Nav2Sp3.bin	Read navigation messages files and generate orbits and clocks
ObsNext.bin	Read and pre-process all non-GNSS observations (e.g. SLR, VLBI, DORIS)
OrbComp.bin	Comparison of one or multiple orbits based on two files
OrbUpd.bin	Orbit handling of files and formats
ParCompar.bin	Compare station position NEQ for common stations
Par2sinex.bin	Generate station position SINEX file
Par2tropo.bin	Conversion of format of parameters into the SINEX_TRO format
Tracksim.bin	Generate a simulation of the observations

A.2.1 CHAMP DAILY Sequence

Block	Programme	Mode	Parallelisation	Description
Start	CmdLine.tcl	START	NO	Create workspace directories Records the database used Links/Copies RINEXNAV/OBS files
A priori orbits and clocks based on input products	BuildCat.bin	BRDCFIT	NO	Catalogue RINEX NAV
	Nav2Sp3.bin	BRDCFIT	NO	Merge and Transform RINEX NAV to SP3
	OrbUpd.bin	BRDCFIT	NO	Cumulate BRDC SP3 with previously processed POD products. Result: get a priori orbit for every satellite and "robust" clocks.
	tracksim.bin	BRDCFIT	NO	SP3 to NTDF (Pseudo-observations)
	Bahn.bin	BRDCFIT-RAPID	NO	Interpolate cumulated a priori orbit (without considering clocks)
	ClockUpd.bin	BRDCFIT	NO	Cumulate BRDC TCB with previously processed POD products
	Clock2Sp3.bin	BRDCFIT	NO	Overwrite Clocks of BFIT SP3
Observation screening and Code-only solution	BuildCat.bin	GNSS	NO	Catalogue RINEX OBS
	GnssObs.bin	GNSS	NO	RTDC2NTDF, Screening based on code observations and meta information. Priority given to IGS20, ESOC UTC and TSD stations.
	ClockUpd.bin	GNSS	NO	Downsample TCB and RCB interval from 30s to 300sSelect single station reference. Orbits are estimated at 300s.
	ClockRef.bin	GNSS	NO	Determine Reference Station Clock and apply. Remove polynomial fit residuals.
FLOAT solution	Bahn.bin	FLOAT-GPS	YES	Estimation of EOP, Satellite, Station and GNSS Parameters (including ambiguities). IGSO and GEO only in FINALS GPS+QZS; only in FINALS
	Bahn.bin	FLOAT-GLO	YES	
	Bahn.bin	FLOAT-GAL	YES	
	Bahn.bin	FLOAT-BEI	YES	
	Bahn.bin	FLOAT-QZS	YES	
	CmdLine.tcl	PARALLELSTOP	NO	Step to stop parallelisation of previous steps
	ClockRef.bin	FLOAT-REF	YES	Generate new reference clock ensemble and apply
Ambiguity Fixing	AmbFix.bin	FIX-GPS	YES	Integer ambiguity resolution of the GNSS phase ambiguities and estimation of UPDs.
	AmbFix.bin	FIX-GAL	YES	
	AmbFix.bin	FIX-BEI	YES	
	AmbFix.bin	FIX-QZS	YES	
FIX solution RAPID & FINAL	CmdLine.tcl	PARALLELSTOP	NO	Step to stop parallelisation of previous steps
	Bahn.bin	FIX-GPS	YES	Estimation of EOP, Satellite, Station and GNSS Parameters.
	Bahn.bin	FIX-GAL	YES	
	Bahn.bin	FIX-BEI	YES	
	Bahn.bin	FIX-QZS	YES	
	ClockRef.bin	FIX-REF	NO	Generate new reference clock ensemble and apply
Compare solution	ClockComp.bin	QUAL	YES	Compares single constellation RCB against GPS RCB, step size 300s
	OrbComp.bin	QUAL	YES	Compares sp3 Orbit with to one of the day before, step size 900s
FIX solution FINALS	multiarc.bin	FIX-GPS	YES	ITRF alignment of single-constellation solutions (No-net rotation) because the single-constellation solutions do not share the same reference frame.
	multiarc.bin	FLOAT-GLO	YES	
	multiarc.bin	FIX-GAL	YES	
	multiarc.bin	FIX-BEI	YES	
	multiarc.bin	FIX-QZS	YES	
End	CmdLine.tcl	END	NO	Run autocheck script to ensure data completeness Copy relevant output to CHAMP processing storage
	CmdLine.tcl	STORELOG	NO	Store log files

Table A.7: CHAMP DAILY Sequence

A.2.2 CHAMP MGNSS Sequence

Block	Programme	Mode	Parallelisation	Description
Start	CmdLine.tcl	START	NO	Create workspace directories Records the database used Links/Copies DAILY-FINAL ntdf file
Stacking	ParUpd.bin	FIXED-MERGE	NO	Merges DAILY pneq and upds of single constellations
	multiarc.bin	FIXED-1D	YES	Merges normal equation (NEQ) files of single constellations
	multiarc.bin	FIXED-SNX	YES	Remove tropospheric parameters
	parCompar.bin	FIXED-QC	NO	Checks quality of NEQ against single constellation NEQ
	ClockUpd.bin	CLOCK	NO	Concentrates a priori clocks
	Bahn.bin	CLOCK	NO	Estimation of Clocks and ISB at 30 sec
Product generation	par2sinex.bin	GENPROD	YES	Writes SINEX file
	par2tropo.bin	GENPROD	YES	Writes TRO file
	IgsAnaRep.bin	GENPROD	YES	Writes 1D SUM File
	tracksim.bin	2DFIT	NO	SP3 to NTDF
	Bahn.bin	2DFIT	YES	Estimates a 2 Day orbit fit (day before and current day).
	Bahn.bin	3DFIT-WGT	YES	Estimates a 3 Day weighted orbitfit (day before, current, day after current).
	ClockRef.bin	CLOCK-ALIGN	NO	Determine Reference Station Clock from UTC list and predict
	ClockUpd.bin	GENPROD	YES	Writes CLK Rinexfile, RCB and TCB file with 30s interval
	OrbUpd.bin	GENPROD	YES	Writes ORB SP3 file
	Clock2Sp3.bin	GENPROD	NO	Converts TCB to SP3 (interval 05M)
	OrbComp.bin	QUAL	YES	Compares current orbit with the one before and with single constellations.
SLR process	BuildCat.bin	QUAL-SLR	YES	Catalogue SLR files
	ObsNext.bin	QUAL-SLR	NO	Convert np* to ntdf
	Bahn.bin	QUAL-SLR	YES	Estimates SLR residuals
End	CmdLine.tcl	END	NO	Run auto_check.csh Copy relevant output to CHAMPproc storage
	CmdLine.tcl	SUBMIT	NO	Compress and submit products
	CmdLine.tcl	STORELOG	NO	Store log files

Table A.8: CHAMP MGNSS Sequence